

¹ A Search in the Two-Photon Final State for
² Evidence of New Particle Production in pp
³ Collisions at $\sqrt{s} = 7$ TeV

⁴ Rachel P. Yohay
University of Virginia
`rpy3y@virginia.edu`

⁵ June 14, 2012

Contents

7	1	Introduction	2
8	2	Motivation for Physics Beyond the Standard Model	5
9	2.1	The Standard Model and Electroweak Symmetry Breaking	6
10	2.2	Implications of the Higgs Mechanism	10
11	2.3	Addressing Problems of the Standard Model with Supersymmetry . .	12
12	3	The Supersymmetric Extension to the Standard Model	16
13	3.1	Supermultiplet Representation	16
14	3.2	The Unbroken SUSY Lagrangian	17
15	3.3	Soft SUSY Breaking	23
16	3.4	Gauge-Mediated SUSY Breaking	26
17	3.5	Phenomenology of General Gauge Mediation	29
18	3.6	Experimental Status of SUSY	32
19	4	The Large Hadron Collider	38
20	4.1	Design Considerations and Performance Limitations	39
21	4.2	Beam Injection	42
22	4.3	Magnets and Cryogenics	44
23	4.4	Radiofrequency Cavities	47

²⁴	5 The Compact Muon Solenoid Experiment	49
²⁵	5.1 The Detectors and Their Operating Principles	53
²⁶	5.1.1 Tracking System	53
²⁷	5.1.2 Electromagnetic Calorimeter	62
²⁸	5.1.3 Hadronic Calorimeter	67
²⁹	5.1.4 Muon System	71
³⁰	5.2 Triggering, Data Acquisition, and Data Transfer	76
³¹	5.2.1 Level 1 and High Level Trigger Systems	76
³²	5.2.2 Data Acquisition System	80
³³	5.2.3 Data Processing and Transfer to Computing Centers	83
³⁴	6 Event Selection	86
³⁵	6.1 Object Reconstruction	87
³⁶	6.1.1 Photons	87
³⁷	6.1.2 Electrons	100
³⁸	6.1.3 Jets and Missing Transverse Energy	100
³⁹	6.2 HLT	106
⁴⁰	6.3 Event Quality	109
⁴¹	6.4 Photon Identification Efficiency	112
⁴²	6.4.1 Tag and Probe Method	114
⁴³	6.4.2 Photon Efficiency Scale Factor $\epsilon_e^{\text{data}}/\epsilon_e^{\text{MC}}$	119
⁴⁴	7 Data Analysis	123
⁴⁵	7.1 Control Samples	124
⁴⁶	7.2 Modeling the QCD Background	127
⁴⁷	7.2.1 Outline of the Procedure	127
⁴⁸	7.2.2 Reweighting	128
⁴⁹	7.2.3 Normalization	144

50	7.3	Modeling the Electroweak Background	147
51	7.4	Errors on the Background Prediction	151
52	7.5	Results	159
53	8	Interpretation of Results in Terms of GMSB Models	165
54	8.1	Simplified Models	165
55	8.2	Upper Limit Calculation and Model Exclusion	167
56	8.2.1	Signal Acceptance \times Efficiency	167
57	8.2.2	CL_s and the Profile Likelihood Test Statistic	171
58	8.3	Cross Section Upper Limits	179
59	8.4	Exclusion Contours	179
60	9	Conclusion	185
61	A	Monte Carlo Samples	187
62	A.1	List of Samples	187
63	A.2	Explanation of Naming Conventions	188

⁶⁴ Chapter 1

⁶⁵ Introduction

⁶⁶ Although the Standard Model of particle physics has passed every experimental test
⁶⁷ to date, it leaves some very fundamental questions unanswered. Why do particles have
⁶⁸ mass? Why are their masses so different? Up to what energy scale is the Standard
⁶⁹ Model a valid description of nature? Many competing theories have been proposed to
⁷⁰ answer these questions. Establishing the existence of any one of them requires careful
⁷¹ searches for deviations from Standard Model predictions of particle production or
⁷² decay rates. The stellar performance of the Large Hadron Collider, the 7 TeV center-
⁷³ of-mass energy proton collider located at the European Organization for Nuclear
⁷⁴ Research (CERN) in Geneva, Switzerland, presents a golden opportunity to do such
⁷⁵ a search for evidence of new physical phenomena.

⁷⁶ One nearly universal prediction of theories of physics beyond the Standard Model
⁷⁷ is that at a high enough collision energy, heavy particles introduced by the new theory
⁷⁸ will be produced. The heavy particles will then decay, leading to distinctive signatures
⁷⁹ in the hermetic detectors that completely surround the collision points. By comparing
⁸⁰ the observed rate of processes with a particular signature to the expected rate from
⁸¹ the Standard Model alone, the existence of a particular theory of new physics can be
⁸² confirmed or ruled out.

83 This thesis presents a search for evidence of new heavy particles decaying to a final
84 state with two photons, jets, and a striking momentum imbalance that implies the
85 existence of a new kind of particle that can easily pass through matter without leaving
86 a trace. The signature is motivated by theories that incorporate supersymmetry, a
87 new symmetry of nature that predicts supersymmetric antiparticles to the known
88 particles, just as charge symmetry predicts a positively charged antiparticle for every
89 negatively charged particle and vice versa. Supersymmetry can provide answers to
90 all of the questions posed in the first paragraph. Besides its theoretical motivation,
91 the choice of signature is also driven by the low rate of expected Standard Model
92 background.

93 The search is performed at the Compact Muon Solenoid experiment, a detector ca-
94 pable of identifying photons, electrons, muons, quark jets, τ leptons, and momentum
95 imbalances with high efficiency. The central feature of the experiment is a supercon-
96 ducting solenoid, which, at a length of 13 m and a diameter of 7 m [1], is one of the
97 largest superconducting magnets ever built. By bending the paths of charged parti-
98 cles in the final state under the Lorentz force, the magnetic field produced by the
99 solenoid allows charged particle momenta to be accurately measured. Highly granular
100 calorimeters sit inside the solenoid for the purpose of measuring the energy of neutral
101 final state particles.

102 This thesis is organized as follows. Chapters 2 and 3 motivate the search for physics
103 beyond the Standard Model and the specific signature of two photons, as well as give
104 an overview of the Standard Model and supersymmetric theoretical frameworks. A
105 description is given of the Large Hadron Collider in Chapter 4 and the Compact Muon
106 Solenoid detector in Chapter 5. Chapters 6 and 7 explain in detail the experimental
107 techniques used in the search. Chapter 6 shows how collisions that are likely to have
108 produced a new particle are selected from the enormous amount of data collected, then
109 Chapter 7 shows the data analysis in detail and presents the results. An interpretation

₁₁₀ of the results in terms of new physics models is given in Chapter 8. Finally, the thesis
₁₁₁ is concluded in Chapter 9.

¹¹² Chapter 2

¹¹³ Motivation for Physics Beyond the ¹¹⁴ Standard Model

¹¹⁵ In the 1960s, Sheldon Glashow, Steven Weinberg, and Abdus Salam proposed a math-
¹¹⁶ ematical framework that unified the electromagnetic and weak forces at an energy
¹¹⁷ scale in the hundreds of GeV/c, as well as a mechanism for breaking the electroweak
¹¹⁸ symmetry at low energies [2]. At the same time, Murray Gell-Mann introduced the
¹¹⁹ concept of quarks to describe hadron spectroscopy, a concept that would later grow
¹²⁰ into quantum chromodynamics (QCD), the full theory of the strong force [3]. These
¹²¹ two key developments motivated the unified representation of particle physics as a set
¹²² of fields whose dynamics are invariant under the Standard Model (SM) gauge group

$$SU(3)_C \otimes SU(2)_L \otimes U(1)_Y \quad (2.1)$$

¹²³ where $SU(3)_C$ describes the quark QCD interactions, $SU(2)_L$ describes the weak
¹²⁴ interactions among quarks and leptons, and $U(1)_Y$ describes the electromagnetic in-
¹²⁵ teraction.

¹²⁶ The Standard Model has been an extremely successful predictor of particle pro-
¹²⁷ duction and interaction cross-sections and decay rates, as well as of the exact masses

128 of the electroweak force carriers. The case for the validity of the Standard Model was
129 bolstered by the many precision QCD and electroweak measurements carried out at
130 the Large Electron-Positron (LEP) collider, which ran from 1989-2000 at center-of-
131 mass energies between 65 and 104 GeV/ c [4]. Figure 2.1 shows some of the highlights
132 of the LEP program.

133 However, there are still deep theoretical problems with the Standard Model,
134 stemming from the introduction of the Higgs scalar into the theory to break elec-
135 troweak symmetry [5]. Since the Higgs self-energy diagram is quadratically sensitive
136 to the ultraviolet cutoff scale, and assuming that there are no new important en-
137 ergy scales of physics between the weak scale ($\mathcal{O}(10^2 \text{ GeV}/c)$) and the Planck scale
138 ($\mathcal{O}(10^{19} \text{ GeV}/c)$), in order to be consistent with experimental measurements, this dia-
139 gram must include a remarkable 17-orders-of-magnitude cancellation that is otherwise
140 poorly motivated [6]. The quest to find new physics at an intermediate energy scale
141 between the weak and Planck scales, and thus extend the Standard Model, was the
142 driving force behind the construction of the Large Hadron Collider (LHC) in 2009,
143 the world's highest energy particle accelerator to date.

144 Section 2.1 of this chapter gives a brief overview of the Standard Model and
145 electroweak symmetry breaking. Sections 2.2 and 2.3 examine the issues raised by
146 electroweak symmetry breaking that the Standard Model is as yet ill-prepared to
147 address.

148 2.1 The Standard Model and Electroweak Symme- 149 try Breaking

150 All of the elementary matter particles (fermions)—quarks, charged leptons, and neutrinos—
151 can be put in fundamental representations of the SM gauge groups. The fermion con-
152 tent of the Standard Model is summarized in Table 2.1. The left-handed doublets are

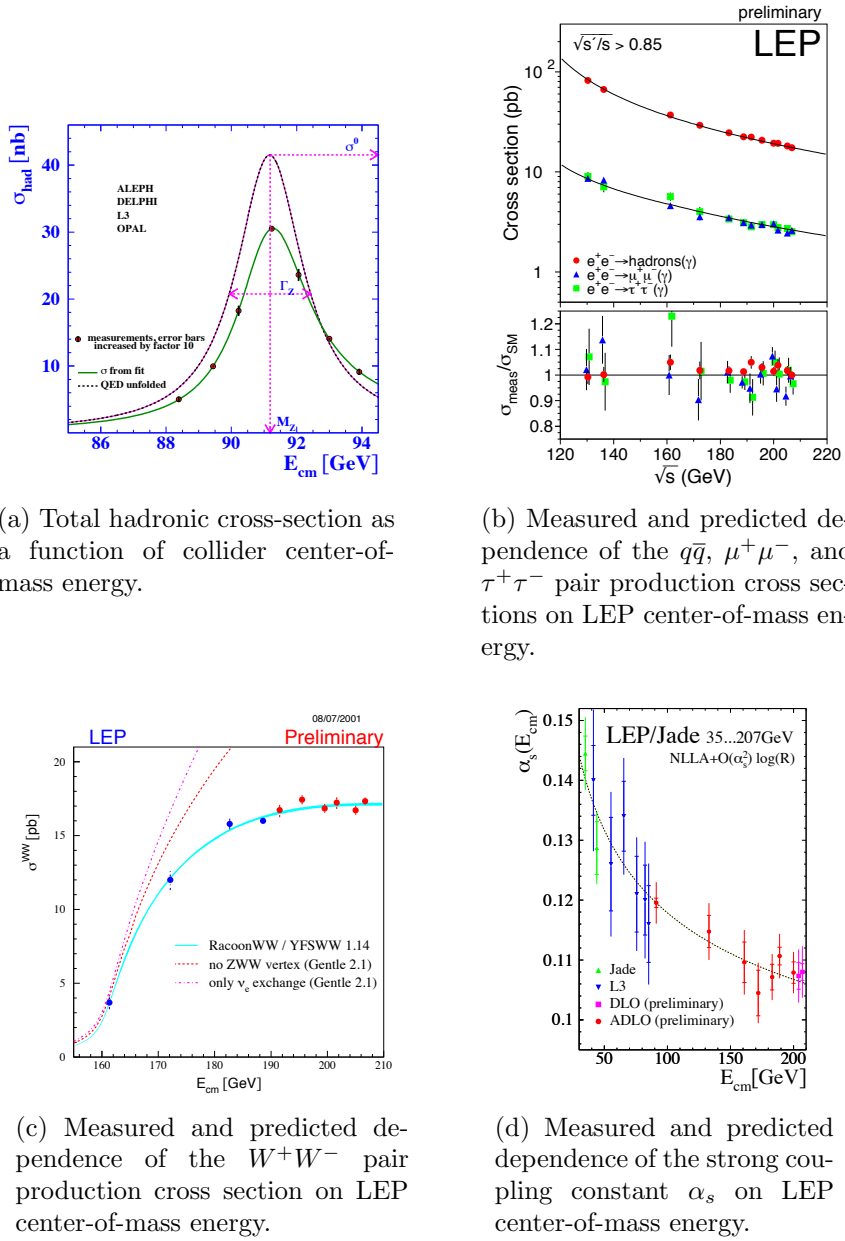


Figure 2.1: Selected LEP measurements demonstrating its contribution to the precise understanding of the Standard Model. Reprinted from ref. [4].

¹⁵³ analogous to the spinors of non-relativistic quantum mechanics, with the z component of “weak isospin” I_3 equal to $+1/2(-1/2)$ for the upper(lower) component of the ¹⁵⁴ doublet.
¹⁵⁵

Table 2.1: Fermion content of the Standard Model.

Type	Notation	Representation under $SU(3)_C \otimes SU(2)_L \otimes U(1)_Y$	Couples to
Left-handed quark doublet	$\begin{pmatrix} u_L \\ d_L \\ c_L \\ s_L \\ b_L \\ t_L \end{pmatrix}$	(3, 2, $\frac{1}{6}$)	g, W, Z, γ
Right-handed up-type quark singlet	$\begin{pmatrix} u_R^\dagger \\ c_R^\dagger \\ b_R^\dagger \end{pmatrix}$	($\bar{3}$, 1, $-\frac{2}{3}$)	g, γ
Right-handed down-type quark singlet	$\begin{pmatrix} d_R^\dagger \\ s_R^\dagger \\ t_R^\dagger \end{pmatrix}$	($\bar{3}$, 1, $\frac{1}{3}$)	g, γ
Left-handed lepton doublet	$\begin{pmatrix} \bar{\nu}_{eL} \\ e_L \\ \bar{\nu}_{\mu L} \\ \mu_L \\ \bar{\nu}_{\tau L} \\ \tau_L \end{pmatrix}$	(1, 2, $-\frac{1}{2}$)	W, Z, γ^a
Right-handed charged lepton singlet	$\begin{pmatrix} e_R^\dagger \\ \mu_R^\dagger \\ \tau_R^\dagger \end{pmatrix}$	($\bar{1}$, 1, 1)	γ

^aExcept for neutrinos, which have zero electric charge.

¹⁵⁶ There are two types of weak interactions: flavor-changing charged currents, in
¹⁵⁷ which an up-type and down-type quark or charged lepton and neutrino couple to
¹⁵⁸ a charged W , and neutral currents, in which a fermion couples to another of the
¹⁵⁹ same flavor and to a neutral Z . The charged current interaction is maximally parity
¹⁶⁰ violating—it only couples left-handed fermion doublets. The neutral current inter-
¹⁶¹ action has a term coupling left-handed doublets and a term coupling right-handed
¹⁶² singlets. There are no mass terms of the form $m_f^2(f_L \bar{f}_R + f_R \bar{f}_L)$ in the electroweak

₁₆₃ part of the Lagrangian, as these would violate gauge invariance [7]. The simplest
₁₆₄ way to link the left-handed and right-handed fermions is via a Yukawa interaction
₁₆₅ $-\xi [\bar{f}_R(\phi^\dagger f_L) + (\bar{f}_L \phi) f_R]$ where ϕ is a doublet of complex scalar fields [7].

₁₆₆ The fermion interaction part of the Lagrangian is [7]

$$\begin{aligned}\mathcal{L}_{\text{int}} = & \bar{f}_R i\gamma^\mu (\partial_\mu + i\frac{g_Y}{2} A_\mu Y) f_R \\ & + \bar{f}_L i\gamma^\mu (\partial_\mu + i\frac{g_Y}{2} A_\mu Y + i\frac{g_L}{2} \vec{\tau} \cdot \vec{b}_\mu) f_L\end{aligned}\quad (2.2)$$

₁₆₇ where g_Y and g_L are the electromagnetic and weak coupling constants, respectively;
₁₆₈ Y is the weak hypercharge; A_μ is the EM gauge field; \vec{b}_μ is a three-component
₁₆₉ vector of weak gauge fields; and $\vec{\tau}$ is a three-component vector of the three Pauli
₁₇₀ matrices. Before electroweak symmetry breaking, the three weak gauge fields and the
₁₇₁ one EM gauge field are massless. The three weak gauge fields correspond to the three
₁₇₂ generators (the Pauli matrices) of $SU(2)_L$. The one EM gauge field corresponds to the
₁₇₃ one generator (the real scalar Y) of $U(1)_Y$, where $Y = 2(Q - I_3)$ (Q is electric charge).
₁₇₄ For the $SU(3)_C$ part of the Lagrangian, there are eight massless gauge fields (the
₁₇₅ gluons) corresponding to the eight generators of $SU(3)_C$ (the Gell-Mann matrices).

₁₇₆ To break the electroweak symmetry implicit in the massless gauge bosons, a dou-
₁₇₇ blet of complex scalar fields (the Higgs) is introduced. It has a potential [7]

$$V(\phi^\dagger \phi) = \mu^2 \phi^\dagger \phi + |\lambda| (\phi^\dagger \phi)^2. \quad (2.3)$$

₁₇₈ Since $\mu^2 < 0$, the potential has the shape of a sombrero, as shown in Figure 2.2.
₁₇₉ At the minimum of the potential, the scalar fields are not zero, but have some positive
₁₈₀ vacuum expectation value (VEV) (it can be chosen such that one component is zero
₁₈₁ and the other is $\sqrt{-\mu^2/2|\lambda|}$). Nature spontaneously chooses one of the infinitely many

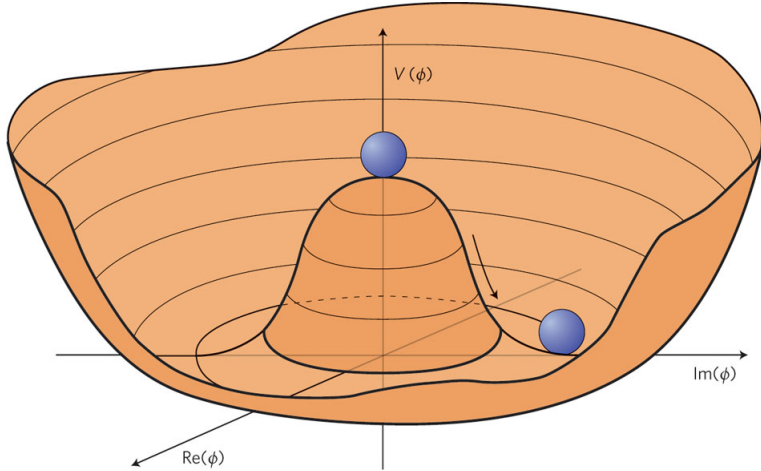


Figure 2.2: Higgs potential (the sombrero) as a function of the real and imaginary parts of the complex scalar field. The movement of the balls shows that the symmetry $\phi = 0$ is spontaneously broken, the stable vacuum state of nature being somewhere along the circle of minimum potential. Reprinted from Fig. 1 of ref. [8].

182 vacua along the circle of minimum V in $(\Re[\phi], \Im[\phi])$ space.

183 Expanding ϕ about its VEV v in the Lagrangian introduces one massive scalar, the
184 Higgs, and new mass terms for the gauge bosons. However, the terms with positive
185 mass are not the original b_1 , b_2 , b_3 , and A (spacetime indices dropped), but the
186 observable W^\pm and Z^0 . The W^\pm are linear combinations of b_1 and b_2 . The Z^0 is
187 one of the linear combinations of b_3 and A , the other being the massless photon γ .
188 After electroweak symmetry breaking (EWSB), the only remaining symmetry of the
189 vacuum is electric charge, because the value of the electric charge operator acting on
190 the Higgs VEV is zero. As expected, there is one massless photon in the SM to reflect
191 this symmetry. The SM fermions can also acquire masses as a by-product of the Higgs
192 mechanism via Yukawa terms.

193 2.2 Implications of the Higgs Mechanism

194 Before the formulation of the Higgs mechanism, physicists suspected that a heavy
195 boson mediated the weak force from observations of β decay, but had no way of

196 putting a mass term into the Lagrangian without breaking gauge symmetry. The
 197 Higgs mechanism of EWSB provided a way to generate masses for the $SU(2)_L$ gauge
 198 bosons. Furthermore, it predicted the W and Z masses in terms of g_L , g_Y , and v . g_L
 199 and g_Y could be measured in scattering experiments, and in 1983 the W and Z were
 200 first observed at the Super Proton-Antiproton Synchrotron (Sp \bar{p} S) at the European
 201 Organization for Nuclear Research (CERN) in Geneva, Switzerland [9, 10]. Crucially,
 202 the values of the coupling constants and the gauge boson masses predict that the
 203 Higgs VEV should be 246 GeV, so the Higgs mass should not be too much different
 204 than that if λ is to remain small enough to do perturbation theory [11].

205 The Higgs mechanism raises some interesting questions that cannot be immedi-
 206 ately answered by SM physics. First of all, why should μ^2 be negative? The form of
 207 the Higgs potential given in Eq. 2.3 is about the simplest renormalizable form that
 208 can be written for a scalar field, but the choice of $\mu^2 < 0$ is completely arbitrary.
 209 Second, how can the hierarchy problem be avoided?

210 The Higgs mass squared receives one-loop corrections from all the particles it
 211 couples to; namely, all particles with mass. Because the Higgs is a scalar particle, one-
 212 loop corrections are proportional to Λ_{UV}^2 , where Λ_{UV} is the ultraviolet cutoff energy of
 213 the loop integral. Λ_{UV} can be interpreted as the energy at which the SM can no longer
 214 describe particle physics and non-SM physics takes over. Ideally, Λ_{UV} is something
 215 like the Planck scale. However, taking $\Lambda_{\text{UV}} = M_{\text{Planck}}$ implies that in order to keep the
 216 Higgs mass of order a few hundred GeV, as required by experimental tests of EWSB, a
 217 very large and precise counterterm must be applied at all orders in perturbation theory
 218 to the bare m_H^2 . The quadratic sensitivity of the Higgs mass to the cutoff scale and the
 219 extremely fine-tuned counterterms it necessitates is called the hierarchy problem. SM
 220 fermions do not experience this problem because chiral symmetry prevents explicit
 221 fermion mass terms at any order, so by dimensional analysis, fermion masses can only
 222 be sensitive to $\ln \frac{\Lambda_{\text{UV}}}{\Lambda_{\text{other}}}$.

223 One of the most elegant ways to address these problems is to incorporate *super-*
224 *symmetry* (SUSY) into the SM. Supersymmetry is new fundamental symmetry of
225 nature between bosons and fermions, and will be discussed more thoroughly in Chap-
226 ter 3. The next section just briefly describes how supersymmetry can mitigate some
227 of the problems of the Higgs mechanism.

228 2.3 Addressing Problems of the Standard Model 229 with Supersymmetry

230 As in the ordinary Standard Model, the couplings and masses in supersymmetric
231 theory can be imposed at the supersymmetric scale and evolved down to the weak
232 scale by use of renormalization group equations. For many typical supersymmetric
233 scenarios (like the one shown in Figure 2.3), μ^2 is positive at the the supersymmetric
234 scale but runs negative at the weak scale, leading to precisely the conditions needed
235 for EWSB. This is a consequence of the fact that the evolution of m_H^2 depends on the
236 top quark Yukawa coupling, which, since the top is very heavy compared to the other
237 quarks ($m_t \sim 42m_b$, $m_t \sim 136m_c$ [13]), is large. In some sense, then, supersymmetry
238 not only provides the conditions for EWSB, but also explains why the top quark must
239 be so much heavier than the other quarks.

240 SUSY's greatest strength, however, comes from the way it elegantly solves the
241 hierarchy problem. The Higgs squared mass corrections from fermion loops take the
242 form [12]

$$\Delta m_H^2 = -\frac{|\lambda_F|^2}{8\pi^2} \Lambda_{\text{UV}}^2 + \dots \quad (2.4)$$

243 while the corrections from scalar loops would take the form [12]

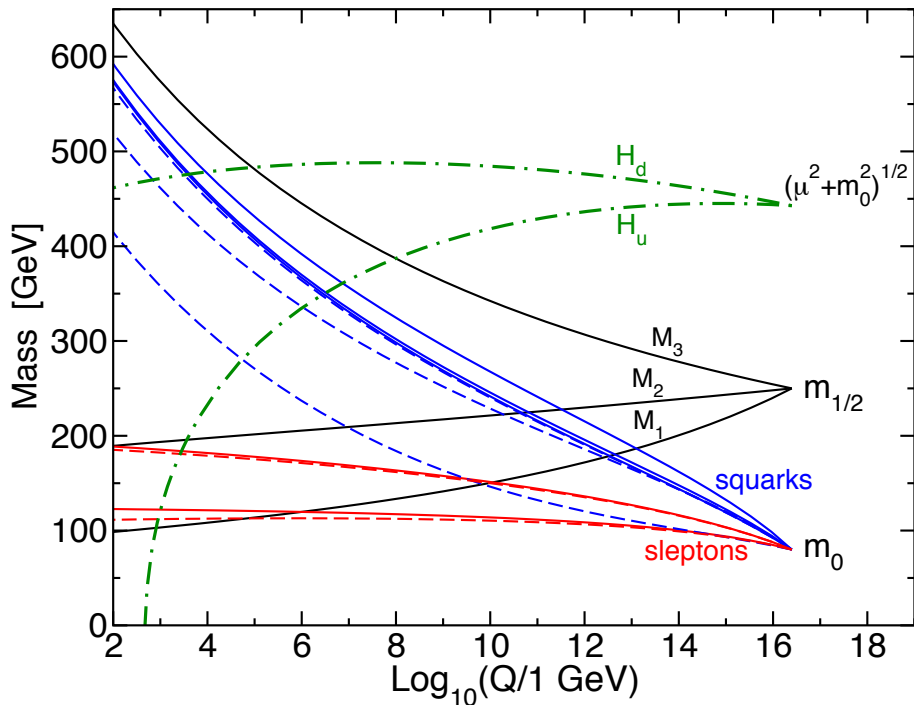


Figure 2.3: Predicted evolution of the free parameters of supersymmetry as a function of renormalization scale for a representative set of SUSY parameters. Note the dash-dotted line marked “ H_u ” that goes negative at ~ 1 TeV; this indicates μ^2 running negative. Reprinted from Fig. 7.4 of ref. [12].

$$\Delta m_H^2 = \frac{|\lambda_S|^2}{16\pi^2} \Lambda_{\text{UV}}^2 + \dots \quad (2.5)$$

where the ellipsis indicates terms proportional to $\ln \Lambda_{\text{UV}}$ that do not pose a problem for the validity of the SM up to the Planck scale. Since the fermion and scalar contributions have opposite signs, if each SM fermion were accompanied by two as-yet undiscovered scalar particles with $\lambda_S = |\lambda_F|^2$, then the problematic quadratic terms in Eqs. 2.4 and 2.5 would exactly cancel. This is precisely the foundation of supersymmetry: for each fermion, there is a supersymmetric partner boson. This would remove the hierarchy problem altogether, and is the main reason physicists are eager to find evidence for the existence of supersymmetry at the LHC.

In addition to providing some rationale for the Higgs mechanism, SUSY makes two other very desirable predictions. The first is that the strong, weak, and electromagnetic coupling constants will exactly unify at an energy scale of 10^{16} GeV/ c , as shown in Figure 2.4. Unification of forces is not required by any experimental consideration, but is an elegant result nonetheless. The second prediction of SUSY, explained in more detail in Sec. 3.5, is the existence of a new stable particle, undiscovered as of yet because of its extremely feeble interactions with ordinary matter. This particle might be what astronomers have observed as dark matter. In fact, regardless of any theory, searches for evidence of dark matter at colliders are well motivated by suggestions from astronomy that some or all of the dark matter should have a mass at the weak scale [14].

Everything discussed in this chapter assumes that the Higgs mechanism is indeed the origin of EWSB. It is important to remember that no experimental observation to date unequivocally establishes the existence of the Higgs scalar, although small excesses recently unearthed in the LHC data [15, 16] tentatively suggest a Higgs mass

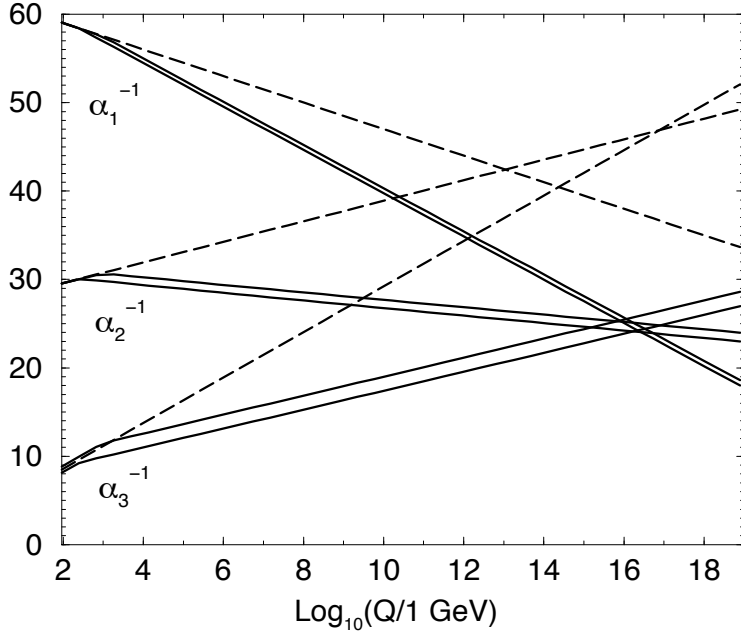


Figure 2.4: Inverse gauge couplings as a function of renormalization scale for the Standard Model assumption (dotted lines) and the SUSY assumption (solid lines; the double lines represent variations in SUSY parameters and in $\alpha_S(m_Z)$). Reprinted from Fig. 5.8 of ref. [12].

of ~ 125 GeV. The discovery of the Higgs scalar would place an important restriction on the types of SUSY theories that might be consistent with experiment. Operating at a 7 TeV center-of-mass energy, the LHC can thoroughly probe the scale of EWSB and the expected mass range of the Higgs, as well as the mass range of supersymmetric particles if SUSY is the solution to the hierarchy problem. Therefore, discovering or excluding SUSY is a key goal of the LHC physics program. The next chapter discusses SUSY more formally and shows what phenomenological consequences it entails.

²⁷⁴ Chapter 3

²⁷⁵ ²⁷⁶ The Supersymmetric Extension to the Standard Model

²⁷⁷ The following introduction to SUSY focuses primarily on the aspects of the formalism that are relevant to phenomenology. In particular, most of the details of SUSY breaking (about which there is little theoretical consensus) are omitted, except where they are relevant to experiment. The notation is similar to that used in refs. [6] and [12], and much of the information presented is culled from those references.

²⁸² 3.1 Supermultiplet Representation

²⁸³ The Standard Model is extended to include supersymmetry by the introduction of a supersymmetry transformation that takes fermionic states to bosonic states and vice versa. The resulting model is called the *supersymmetric Standard Model*. In analogy with the known symmetries of the Standard Model, the SUSY transformation has associated generators that obey defining commutation and anticommutation relations, and a fundamental representation. All SM particles and their *superpartners* fall into one of two *supermultiplet* representations. Using the property of SUSY that

$$n_F = n_B, \quad (3.1)$$

290 where n_F is the number of fermionic degrees of freedom per supermultiplet and n_B is
 291 the number of bosonic degrees of freedom, the two types of supermultiplets are

- 292 1. *Chiral supermultiplets*: Weyl fermions (two helicity states $\Rightarrow n_F = 2$) associated
 293 with complex scalar fields (with two real components $\Rightarrow n_B = 2$)
- 294 2. *Gauge supermultiplets*: Spin-1 vector bosons (two helicity states $\Rightarrow n_B = 2$)
 295 associated with Weyl fermions (two helicity states $\Rightarrow n_F = 2$)

296 In the gauge supermultiplet, the vector boson is assumed massless (i.e. before
 297 EWSB generates a mass for it). Since the superpartners to the SM particles have not
 298 yet been discovered, they must be significantly heavier than their SM counterparts.
 299 Unbroken SUSY predicts that the SM particles and their superpartners must have
 300 exactly the same mass, so ultimately a mechanism for SUSY breaking, in addition to
 301 EWSB, must be introduced to generate masses for the superpartners (see Sec. 3.3).
 302 Tables 3.1 and 3.2 show the chiral and gauge supermultiplets of the supersymmetric
 303 Standard Model, respectively. Note that the scalar partners to the SM fermions are
 304 denoted by placing an “s” in front of their names, while the chiral fermion partners
 305 to the SM gauge bosons are denoted by appending “ino” to their names.

306 3.2 The Unbroken SUSY Lagrangian

307 The first piece of the full unbroken SUSY Lagrangian density consists of the kinetic
 308 and interacting terms related to the chiral supermultiplets. As explained in Sec. 3.1, a
 309 chiral supermultiplet consists of Weyl fermions ψ (the ordinary fermion) and complex
 310 scalars ϕ (the sfermion). For a collection of such chiral supermultiplets, the Lagrangian
 311 is

Table 3.1: Chiral supermultiplets of the supersymmetric Standard Model. In the last column, the first number refers to the supermultiplet representation under $SU(3)_C$ (e.g. **3** means it has color charge and feels QCD), the second number refers to the representation under $SU(2)_L$ (e.g. **2** means it has weak isospin and feels the weak interaction), and the third number is the value of the hypercharge. A bar over a number refers to the adjoint representation. **1** means that the supermultiplet is not charged under that group, and thus does not feel the associated force (for example, the right-handed fermion singlets do not feel the weak interaction). Adapted from Table 1.1 of ref. [12].

Type of supermultiplet	Notation	Spin-0 component	Spin-1/2 component	Representation under $SU(3)_C \otimes SU(2)_L \otimes U(1)_Y$
Left-handed quark/squark doublet ($\times 3$ families)	Q	$(\tilde{u}_L \tilde{d}_L)$	$(u_L d_L)$	$(\mathbf{3}, \mathbf{2}, \frac{1}{6})$
Right-handed up-type quark/squark singlet ($\times 3$ families)	\bar{u}	\tilde{u}_R^*	u_R^\dagger	$(\overline{\mathbf{3}}, \mathbf{1}, -\frac{2}{3})$
Right-handed down-type quark/squark singlet ($\times 3$ families)	\bar{d}	\tilde{d}_R^*	d_R^\dagger	$(\overline{\mathbf{3}}, \mathbf{1}, \frac{1}{3})$
Left-handed lepton/slepton doublet ($\times 3$ families)	L	$(\tilde{\nu}_{eL} \tilde{e}_L)$	$(\bar{\nu}_{eL} e_L)$	$(\mathbf{1}, \mathbf{2}, -\frac{1}{2})$
Right-handed lepton/slepton singlet ($\times 3$ families)	\bar{e}	\tilde{e}_R^*	e_R^\dagger	$(\overline{\mathbf{1}}, \mathbf{1}, 1)$
Up-type Higgs/Higgsino doublet	H_u	$(H_u^+ H_u^0)$	$(\tilde{H}_u^+ \tilde{H}_u^0)$	$(\mathbf{1}, \mathbf{2}, \frac{1}{2})$
Down-type Higgs/Higgsino doublet	H_d	$(H_d^0 H_d^-)$	$(\tilde{H}_d^0 \tilde{H}_d^-)$	$(\mathbf{1}, \mathbf{2}, -\frac{1}{2})$

Table 3.2: Gauge supermultiplets of the supersymmetric Standard Model. Adapted from Table 1.2 of ref. [12].

Type of supermultiplet	Spin-1/2 component	Spin-1 component	Representation under $SU(3)_C \otimes SU(2)_L \otimes U(1)_Y$
Gluon/gluino	\tilde{g}	g	(8, 1, 0)
W/wino	$\widetilde{W}^\pm \widetilde{W}^0$	$W^\pm W^0$	(1, 3, 0)
B/bino	\tilde{B}^0	B^0	(1, 1, 0)

$$\begin{aligned} \mathcal{L}_{\text{chiral}} = & -\partial^\mu \phi^{*i} \partial_\mu \phi_i - V_{\text{chiral}}(\phi, \phi^*) - i\psi^{\dagger i} \bar{\sigma}^\mu \partial_\mu \psi_i - \frac{1}{2} M^{ij} \psi_i \psi_j \\ & - \frac{1}{2} M_{ij}^* \psi^{\dagger i} \psi^{\dagger j} - \frac{1}{2} y^{ijk} \phi_i \psi_j \psi_k - \frac{1}{2} y_{ijk}^* \phi^{*i} \psi^{\dagger j} \psi^{\dagger k} \end{aligned} \quad (3.2)$$

where i runs over all supermultiplets in Table 3.1, $\bar{\sigma}^\mu$ are the negative of the Pauli matrices (except for $\sigma^0 = \bar{\sigma}^0$), M^{ij} is a mass matrix for the fermions, y^{ijk} are the Yukawa couplings between one scalar and two spinor fields, and $V_{\text{chiral}}(\phi, \phi^*)$ is the scalar potential

$$\begin{aligned} V_{\text{chiral}}(\phi, \phi^*) = & M_{ik}^* M^{kj} \phi^{*i} \phi_j + \frac{1}{2} M^{in} y_{jkn}^* \phi_i \phi^{*j} \phi^{*k} \\ & + \frac{1}{2} M_{in}^* y^{jkn} \phi^{*i} \phi_j \phi_k + \frac{1}{4} y^{ijn} y_{klm}^* \phi_i \phi_j \phi^{*k} \phi^{*l}. \end{aligned} \quad (3.3)$$

The Lagrangian can also be written as the kinetic terms plus derivatives of the *superpotential* W :

$$\begin{aligned} \mathcal{L}_{\text{chiral}} = & -\partial^\mu \phi^{*i} \partial_\mu \phi_i - i\psi^{\dagger i} \bar{\sigma}^\mu \partial_\mu \psi_i \\ & - \frac{1}{2} \left(\frac{\delta^2 W}{\delta \phi^i \delta \phi^j} \psi_i \psi_j + \frac{\delta^2 W^*}{\delta \phi_i \delta \phi_j} \psi^{\dagger i} \psi^{\dagger j} \right) - \frac{\delta W}{\delta \phi^i} \frac{\delta W^*}{\delta \phi_i} \end{aligned} \quad (3.4)$$

³¹⁸ where

$$W = M^{ij} \phi_i \phi_j + \frac{1}{6} y^{ijk} \phi_i \phi_j \phi_k. \quad (3.5)$$

³¹⁹ The second part of the Lagrangian involves the gauge supermultiplets. In terms
³²⁰ of the spin-1 ordinary gauge boson A_μ^a and the spin-1/2 Weyl spinor gaugino λ^a of
³²¹ the gauge supermultiplet, where a runs over the number of generators for the SM
³²² subgroup (i.e. 1-8 for $SU(3)_C$, 1-3 for $SU(2)_L$, and 1 for $U(1)_Y$), this part of the
³²³ Lagrangian is

$$\mathcal{L}_{\text{gauge}} = -\frac{1}{4} F_{\mu\nu}^a F^{\mu\nu a} - i \lambda^a \bar{\sigma}^\mu D_\mu \lambda^a + \frac{1}{2} D^a D^a \quad (3.6)$$

³²⁴ where

$$F_{\mu\nu}^a = \partial_\mu A_\nu^a - \partial_\nu A_\mu^a + g f^{abc} A_\mu^b A_\nu^c \quad (3.7)$$

³²⁵ (g is the coupling constant and f^{abc} are the structure constants for the particular SM
³²⁶ gauge group),

$$D_\mu \lambda^a = \partial_\mu \lambda^a + g f^{abc} A_\mu^b \lambda^c, \quad (3.8)$$

³²⁷ and D^a is an auxiliary field that is introduced as a bookkeeping tool to keep the
³²⁸ fermionic and bosonic degrees of freedom equal both on- and off-shell. There is no
³²⁹ kinetic term for D^a in the Lagrangian, so therefore it does not propagate or represent

³³⁰ any real particle. Its equation of motion, from $\delta\mathcal{L}/\delta D^a = 0$, yields a simple algebraic
³³¹ expression for D^a that can be used to eliminate it from the Lagrangian if desired.

³³² To build a fully supersymmetric and gauge-invariant Lagrangian, the ordinary
³³³ derivatives in $\mathcal{L}_{\text{chiral}}$ (Eq. 3.2) must be replaced by covariant derivatives

$$D_\mu \phi_i = \partial_\mu \phi_i - ig A_\mu^a (T^a \phi)_i \quad (3.9)$$

$$D_\mu \phi^{*i} = \partial_\mu \phi^{*i} + ig A_\mu^a (\phi^* T^a)^i \quad (3.10)$$

$$D_\mu \psi_i = \partial_\mu \psi_i - ig A_\mu^a (T^a \psi)_i. \quad (3.11)$$

³³⁴ This leads to the full Lagrangian

$$\begin{aligned} \mathcal{L} &= \mathcal{L}_{\text{chiral}} + \mathcal{L}_{\text{gauge}} \\ &\quad - \sqrt{2} g (\phi^{*i} T^a \psi_i) \lambda^a - \sqrt{2} g \lambda^{\dagger a} (\psi^{\dagger i} T^a \phi_i) + g (\phi^{*i} T^a \phi_i) D^a \\ &= -\partial^\mu \phi^{*i} \partial_\mu \phi_i - i \psi^{\dagger i} \bar{\sigma}^\mu \partial_\mu \psi_i + ig \partial^\mu \phi^{*i} A_\mu^a (T^a \phi)_i - ig \partial_\mu \phi_i A^{\mu a} (\phi^* T^a)^i \\ &\quad - g^2 A^{\mu a} (\phi^* T^a)^i A_\mu^a (T^a \phi)_i - g \psi^{\dagger i} \bar{\sigma}^\mu A_\mu^a (T^a \psi)_i - V_{\text{chiral}}(\phi, \phi^*) \\ &\quad - \frac{1}{2} M^{ij} \psi_i \psi_j - \frac{1}{2} M_{ij}^* \psi^{\dagger i} \psi^{\dagger j} - \frac{1}{2} y^{ijk} \phi_i \psi_j \psi_k - \frac{1}{2} y_{ijk}^* \phi^{*i} \psi^{\dagger j} \psi^{\dagger k} \\ &\quad - \frac{1}{4} F_{\mu\nu}^a F^{\mu\nu a} - i \lambda^{\dagger a} \bar{\sigma}^\mu \partial_\mu \lambda^a - ig \lambda^{\dagger a} \bar{\sigma}^\mu f^{abc} A_\mu^b \lambda^c + \frac{1}{2} D^a D^a \\ &\quad - \sqrt{2} g (\phi^{*i} T^a \psi_i) \lambda^a - \sqrt{2} g \lambda^{\dagger a} (\psi^{\dagger i} T^a \phi_i) + g (\phi^{*i} T^a \phi_i) D^a. \end{aligned} \quad (3.12)$$

³³⁵ Writing out $F_{\mu\nu}^a$ and $V_{\text{chiral}}(\phi, \phi^*)$ explicitly combining the D^a terms using the equation
³³⁶ of motion $D^a = -g \phi^{*i} T^a \phi_i$, and rearranging some terms, the final unbroken SUSY
³³⁷ Lagrangian is

$$\begin{aligned}
\mathcal{L} = & -\partial^\mu \phi^{*i} \partial_\mu \phi_i - i\psi^{\dagger i} \bar{\sigma}^\mu \partial_\mu \psi_i \\
& - \frac{1}{4} (\partial_\mu A_\nu^a - \partial_\nu A_\mu^a) (\partial^\mu A^{\nu a} - \partial^\nu A^{\mu a}) - i\lambda^{\dagger a} \bar{\sigma}^\mu \partial_\mu \lambda^a \\
& - M_{ik}^* M^{kj} \phi^{*i} \phi_j - \frac{1}{2} M^{ij} \psi_i \psi_j - \frac{1}{2} M_{ij}^* \psi^{\dagger i} \psi^{\dagger j} \\
& + ig \partial^\mu \phi^{*i} A_\mu^a (T^a \phi)_i - ig \partial_\mu \phi_i A^{\mu a} (\phi^* T^a)^i - g \psi^{\dagger i} \bar{\sigma}^\mu A_\mu^a (T^a \psi)_i \\
& - ig \lambda^{\dagger a} \bar{\sigma}^\mu f^{abc} A_\mu^b \lambda^c \\
& - \frac{1}{4} g f^{abc} [(\partial_\mu A_\nu^a - \partial_\nu A_\mu^a) A^{\mu b} A^{\nu c} + A_\mu^b A_\nu^c (\partial^\mu A^{\nu a} - \partial^\nu A^{\mu a})] \\
& - \frac{1}{2} M_{in}^* y^{jkn} \phi^{*i} \phi_j \phi_k - \frac{1}{2} M^{in} y_{jkn}^* \phi_i \phi^{*j} \phi^{*k} \\
& - \frac{1}{2} y^{ijk} \phi_i \psi_j \psi_k - \frac{1}{2} y_{ijk}^* \phi^{*i} \psi^{\dagger j} \psi^{\dagger k} \\
& - \sqrt{2} g (\phi^{*i} T^a \psi_i) \lambda^a - \sqrt{2} g \lambda^{\dagger a} (\psi^{\dagger i} T^a \phi_i) \\
& - g^2 A^{\mu a} (\phi^* T^a)^i A_\mu^a (T^a \phi)_i - \frac{1}{4} g^2 f^{abc} A_\mu^b A_\nu^c f^{abc} A^{\mu b} A^{\nu c} \\
& - \frac{1}{4} y^{ijn} y_{kln}^* \phi_i \phi_j \phi^{*k} \phi^{*l} - \frac{1}{2} g^2 (\phi^{*i} T^a \phi_i)^2.
\end{aligned} \tag{3.13}$$

³³⁸ The above Lagrangian applies to chiral supermultiplets interacting with one kind
³³⁹ of gauge supermultiplet (i.e. one SM gauge group). In the general case, there are
³⁴⁰ additional terms corresponding to interactions with all three SM gauge groups.

³⁴¹ The following list gives a description of the terms in Eq. 3.13:

- ³⁴² • First two lines: kinetic terms for the four types of fields ϕ_i , ψ_i , A_μ^a , and λ^a
- ³⁴³ • Third line: mass terms for the ϕ_i and ψ_i (see Figs. 3.1(a) and 3.1(b))
- ³⁴⁴ • Fourth and fifth lines: cubic couplings in which ϕ_i , ψ_i , or λ^a radiates an A_μ^a (see
³⁴⁵ Figs. 3.1(c), 3.1(d), and 3.1(e))
- ³⁴⁶ • Sixth line: triple gauge boson couplings (see Fig. 3.1(f))
- ³⁴⁷ • Seventh line: triple sfermion couplings (see Fig. 3.1(g))

- 348 • Eighth line: cubic couplings in which ψ_i radiates a ϕ_i (see Fig. 3.1(h))
- 349 • Ninth line: ϕ_i - ψ_i - λ^a vertices (see Fig. 3.1(i))
- 350 • 10th line: A_μ^a - A_μ^a - ϕ_i - ϕ_i and quadruple gauge boson couplings (see Figs. 3.1(j)
351 and 3.1(k))
- 352 • 11th line: ϕ_i^4 vertices (see Figs. 3.1(l) and 3.1(m))

353 3.3 Soft SUSY Breaking

354 Since quadratic divergences in sfermion masses vanish to all orders in perturbation
355 theory in plain unbroken SUSY [12] due to the presence of gauge and Yukawa in-
356 teractions with the necessary relationships between coupling constants (i.e. chiral
357 symmetry inherited from the partner fermion protects the sfermion masses, as ex-
358 plained in Sec. 2.2), it is desirable that the terms that break SUSY not disturb this
359 property. In addition, SUSY should be broken spontaneously, as electroweak symme-
360 try is broken in the Standard Model, so that it is only made manifest at high energies.
361 To satisfy these constraints, SUSY-breaking terms are simply added to the unbroken
362 SUSY Lagrangian in Eq. 3.13 such that $\mathcal{L}_{\text{total}} = \mathcal{L}_{\text{unbroken}} + \mathcal{L}_{\text{breaking}}$. The coefficients
363 of terms in $\mathcal{L}_{\text{breaking}}$ must have positive mass dimension in order not to contribute
364 quadratically divergent loop corrections to the scalar masses (like the Higgs mass);
365 i.e. to not create a hierarchy problem (Sec. 2.2) for the scalars.¹ This form of SUSY

¹This point can be argued via dimensional analysis. Radiative corrections take the form Δm_S^2 , where m_S is the mass of the scalar particle in question. The dimensions of Δm_S^2 are mass². Δm_S^2 is proportional to some coupling constant or mass coefficient k multiplied by a function of Λ_{UV} , the high energy cutoff scale. The function of Λ_{UV} is determined by a loop integral, and thus typically takes the form Λ_{UV}^2 (quadratically divergent) or $\ln \frac{\Lambda_{\text{UV}}}{m_{\text{low}}}$ (logarithmically divergent, where m_{low} is some other lower-mass scale in the problem). Now, if k already contributes at least one power of mass to Δm_S^2 , then the high-energy behavior—the function of Λ_{UV} —can only contribute at most one power of the dimensionful parameter Λ_{UV} . However, there are typically no loop integrals that diverge linearly in Λ_{UV} , so by forcing k to have positive mass dimension, the form of the radiative corrections contributed by SUSY-breaking terms is limited to $\Delta m_S^2 \sim m_{\text{low}}^2 \ln \frac{\Lambda_{\text{UV}}}{m_{\text{low}}}$. In effect, the possibility of dangerous corrections proportional to Λ_{UV}^2 is excluded by dimensional analysis if the requirement that k contribute at least one power of mass is enforced.

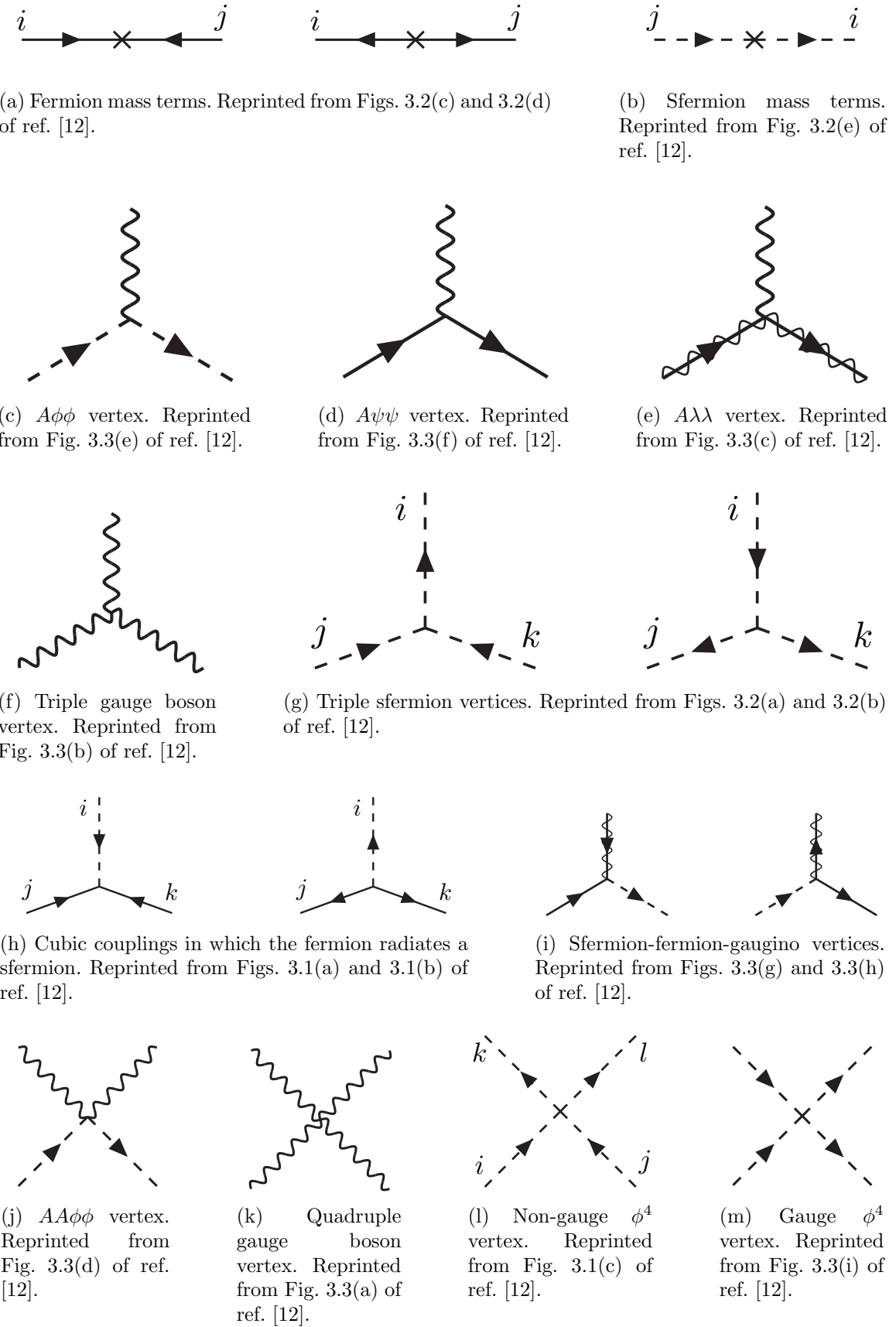


Figure 3.1: Interactions in the unbroken SUSY Lagrangian.

³⁶⁶ breaking is called *soft*, and all coefficients of soft SUSY breaking terms are expected
³⁶⁷ to be of order m_{soft} or m_{soft}^2 .

³⁶⁸ Soft SUSY breaking terms give masses to the sfermions and gauginos and introduce
³⁶⁹ a cubic sfermion vertex. The soft terms are given by

$$\begin{aligned} \mathcal{L}_{\text{soft}} = & -\frac{1}{2}(M_3\tilde{g}^a\tilde{g}^a + M_2\tilde{W}^a\tilde{W}^a + M_1\tilde{B}\tilde{B} + \text{h.c.}) \\ & - (a_u^{ij}\tilde{u}_{Ri}^*\tilde{Q}_j H_u - a_d^{ij}\tilde{d}_{Ri}^*\tilde{Q}_j H_d - a_e^{ij}\tilde{e}_{Ri}^*\tilde{L}_j H_d + \text{h.c.}) \\ & - m_{\tilde{Q}_{ij}}^2 \tilde{Q}_i^\dagger \tilde{Q}_j - m_{\tilde{L}_{ij}}^2 \tilde{L}_i^\dagger \tilde{L}_j \\ & - m_{\tilde{u}_{ij}}^2 \tilde{u}_{Ri} \tilde{u}_{Rj}^* - m_{\tilde{d}_{ij}}^2 \tilde{d}_{Ri} \tilde{d}_{Rj}^* - m_{\tilde{e}_{ij}}^2 \tilde{e}_{Ri} \tilde{e}_{Rj}^* \\ & - m_{H_u}^2 H_u^* H_u - m_{H_d}^2 H_d^* H_d - (b H_u H_d + \text{h.c.}) \end{aligned} \quad (3.14)$$

³⁷⁰ where a runs from 1-8 for \tilde{g}^a and from 1-3 for \tilde{W}^a , and i, j run over the three families.
³⁷¹ The color indices are not shown. The first line of Eq. 3.14 contains the gaugino mass
³⁷² terms. The second line contains cubic scalar couplings that contribute to mixing
³⁷³ between the left- and right-handed third generation sfermions (it is assumed in the
³⁷⁴ supersymmetric Standard Model that the a_u^{ij} , a_d^{ij} , and a_e^{ij} are negligible unless $i =$
³⁷⁵ $j = 3$). The third and fourth lines of Eq. 3.14 contain squark and slepton mass terms,
³⁷⁶ and finally the last line contains the Higgs mass terms.

³⁷⁷ Many viable models of achieving soft SUSY breaking have been studied over the
³⁷⁸ last 30 years. For an overview, see Sec. 6 of ref. [12]. However, this thesis will only cover
³⁷⁹ *gauge-mediated SUSY breaking* (GMSB), because the two-photon search performed
³⁸⁰ is far more sensitive to this model than to other models of SUSY breaking.

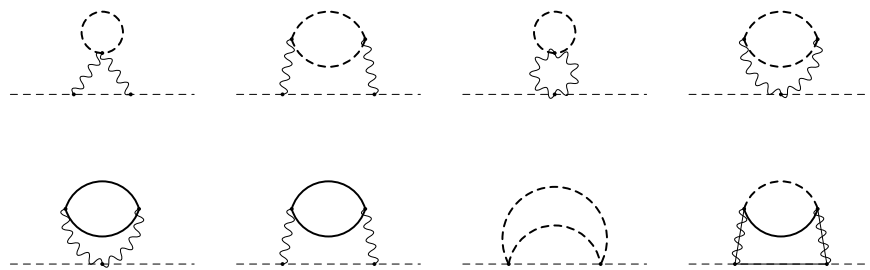
381 3.4 Gauge-Mediated SUSY Breaking

382 In gauge-mediated models [17], “hidden” fields spontaneously break the supersymme-
383 try of very heavy chiral *messenger* supermultiplets. There are a number of competing
384 models (see ref. [17]) that attempt to explain the precise mechanism of spontaneous
385 SUSY breaking, but fortunately the details of those models mostly decouple from the
386 phenomenology of GMSB. The messengers then communicate the SUSY breaking
387 to the sparticles via self-energy loop diagrams of gauge interaction strength (i.e. via
388 vertices like those shown in Figs. 3.1(c), 3.1(d), 3.1(i), 3.1(j), and 3.1(m), which are
389 proportional to the SM gauge couplings constants). The messengers are very heavy,
390 so they cannot be detected in current collider experiments. Feynman diagrams corre-
391 sponding to gaugino and sfermion mass terms are shown in Figure 3.2.

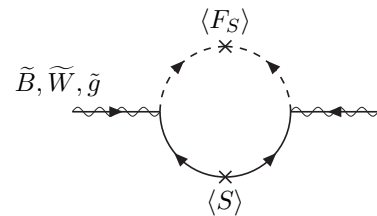
392 Historically, GMSB and gravity-mediated SUSY breaking, or mSUGRA [18], have
393 been the two most thoroughly experimentally studied scenarios of SUSY breaking.
394 One advantage of GMSB over mSUGRA is that it naturally suppresses flavor vio-
395 lation, a generic prediction of supersymmetry. Flavor violation is introduced in the
396 scalar³ couplings and sfermion mass terms of $\mathcal{L}_{\text{soft}}$ (second, third, and fourth lines of
397 Eq. 3.14). Since a_u^{ij} , a_d^{ij} , a_e^{ij} , $m_{\tilde{Q}ij}$, $m_{\tilde{L}ij}$, $m_{\tilde{u}ij}$, $m_{\tilde{d}ij}$, and $m_{\tilde{e}ij}$ are matrices in family
398 space, any nonzero off-diagonal elements will lead to mixing between sfermions of
399 different families. This can lead, for example, to contributions to the diagram $\mu \rightarrow e\gamma$
400 (Figure 3.3) exceeding the experimental bounds. To avoid this disaster, *universality*
401 conditions are assumed:

$$\mathbf{m}_{\tilde{\mathbf{Q}}}^2 = m_{\tilde{Q}}^2 \mathbf{1}, \mathbf{m}_{\tilde{\mathbf{L}}}^2 = m_{\tilde{L}}^2 \mathbf{1}, \mathbf{m}_{\tilde{\mathbf{u}}}^2 = m_{\tilde{u}}^2 \mathbf{1}, \mathbf{m}_{\tilde{\mathbf{d}}}^2 = m_{\tilde{d}}^2 \mathbf{1}, \mathbf{m}_{\tilde{\mathbf{e}}}^2 = m_{\tilde{e}}^2 \mathbf{1} \quad (3.15)$$

402 i.e. all sfermion mass matrices arising from the soft terms are assumed to be propor-
403 tional to the unit matrix $\mathbf{1}$, such that there can be no flavor mixing from these terms



(a) Sfermion mass terms. Heavy dashed lines denote messenger sfermions; solid lines denote messenger fermions. Reprinted from Fig. 6.4 of ref. [12].



(b) Gaugino mass term. The $\langle S \rangle$ part of the loop is a messenger fermion contribution; the $\langle F_S \rangle$ part is a messenger sfermion contribution. Reprinted from Fig. 6.3 of ref. [12].

Figure 3.2: Contributions to sfermion and gaugino masses from loop interactions with messenger particles in the GMSB framework.

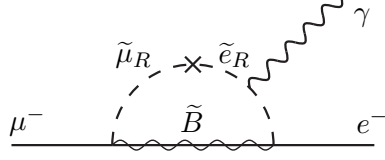


Figure 3.3: Possible contribution to $\mu \rightarrow e\gamma$ from $m_{\tilde{e}ij}$ soft term. Reprinted from Fig. 5.6(a) of ref. [12].

and contributions to flavor-changing processes are drastically reduced.² In mSUGRA models, universality is assumed from the beginning, while in GMSB it is a natural consequence of the fact that the sparticle-messenger vertices are the ordinary flavor-blind gauge couplings that prevent things like flavor-changing neutral currents.

In minimal GMSB (mGMSB), there are four messenger supermultiplets q, \bar{q}, l, \bar{l} providing the messenger (s)quarks and (s)leptons. There is one breaking scale Λ . The gaugino masses computed from diagrams like Fig. 3.2(b) are given by

$$M_a = \frac{\alpha_a}{4\pi} \Lambda \quad (3.16)$$

where a runs from 1-3 and the α_a are the SM gauge coupling constants. The sfermion masses computed from diagrams like Fig. 3.2(a) are given by

$$m_{\phi_i}^2 = 2\Lambda^2 \sum_{a=1}^3 \left(\frac{\alpha_a}{4\pi}\right)^2 C_a(i) \quad (3.17)$$

where $C_a(i)$ are group theory factors that are identical for all particles residing in the same type of supermultiplet (e.g. for all left-handed (s)quarks or left-handed (s)leptons). As explained in the previous paragraph, the gaugino and sfermion masses do not depend on fermion family.

²Universality also includes some assumptions about the form of a_{uij} , a_{dij} , and a_{eij} and the stipulation that the soft terms not introduce any CP-violating phases.

417 In recent years, much theoretical progress has been made in unifying models of
 418 gauge mediation and developing less restrictive models than mGMSB. *General gauge*
 419 *mediation* (GGM) [19] retains the essential features of mGMSB, such as flavor de-
 420 generacy and communication of SUSY breaking via messengers, but does not make
 421 assumptions about the specific messenger sector or SUSY breaking scale. Many dif-
 422 ferent collider final states can be interpreted in terms of GGM, and conversely, GGM
 423 implies a wealth of signatures, only a small fraction of which have been searched for
 424 at colliders [20, 21, 22]. The following section discusses the aspects of GGM collider
 425 phenomenology relevant to this thesis.

426 **3.5 Phenomenology of General Gauge Mediation**

427 The main distinguishing feature of all GMSB phenomenology is that the gravitino \tilde{G} is
 428 very light (eV-keV). In general, the gravitino mass is proportional to $\langle F \rangle / M_P$, where
 429 $\langle F \rangle$ is the vacuum expectation value (VEV) of a field F that spontaneously breaks
 430 SUSY in the vacuum state and M_P is the Planck mass. In GGM models, $\langle F \rangle \sim 10^8$
 431 GeV, leading to a very light gravitino. In contrast, mSUGRA predicts $\langle F \rangle \sim 10^{20}$
 432 GeV. The fact that the gravitino is so much lighter than any other particles in the
 433 supersymmetric Standard Model, and that it interacts only gravitationally (and thus
 434 extremely feebly), leads to two important phenomenological consequences:

- 435 1. All sparticle decay chains in GMSB end with the production of a gravitino.
 436 2. The gravitino escapes 4π , hermetic collider detectors without interacting, leav-
 437 ing a signature of “missing” momentum transverse to the beam direction.

438 Even if the gravitino were lighter than any other sparticle, but heavier than an
 439 ordinary SM particle, it still could not decay to the SM particle due to *R-parity*. R-
 440 parity is a conserved quantity of the supersymmetric Standard Model introduced to

441 enforce baryon and lepton number conservation, which would otherwise be generically
 442 allowed at levels in conflict with experiment (e.g. the non-observation of baryon-
 443 and lepton-number-violating proton decay). All sparticles have R-parity -1, while all
 444 ordinary SM particles have R-parity +1, and R-parity conservation dictates that at
 445 any vertex, the product of the R-parities of each leg must be +1. This leads to two
 446 more important consequences:

- 447 1. Since conservation of energy only allows it to decay to ordinary SM particles,
 448 but R-parity prevents a sparticle-particle-particle vertex, the *lightest supersym-
 449 metric particle* (LSP) must be absolutely stable. All sparticle decays proceed
 450 through the *next-to-lightest supersymmetric particle* (NLSP), which in turn de-
 451 cays to the LSP. The fact that it is stable and only gravitationally interacting
 452 makes the gravitino a candidate dark matter particle (see Sec. 3.6).
- 453 2. In colliders, sparticles are produced in pairs (particle + particle \rightarrow sparticle +
 454 sparticle).

455 In GMSB, then, the gravitino is the LSP. If the NLSP is a gaugino,³ then the
 456 possible decays depend on mixing among the gauginos. The four neutral gauginos
 457 $\tilde{H}_u^0, \tilde{H}_d^0, \tilde{B}, \tilde{W}^0$ mix into four *neutralino* mass eigenstates $\tilde{\chi}_1^0, \tilde{\chi}_2^0, \tilde{\chi}_3^0, \tilde{\chi}_4^0$, and the four
 458 charged gauginos $\tilde{H}_u^+, \tilde{H}_d^-, \tilde{W}^+, \tilde{W}^-$ mix into two *chargino* mass eigenstates $\tilde{\chi}_1^\pm, \tilde{\chi}_2^\pm$
 459 (two mass eigenstates each with two possible charges = four particles). In the limit
 460 that EWSB effects are small, the neutralino and chargino masses can be written as
 461 the gauge eigenstate masses plus a small perturbation:

³In principle, the NLSP could be anything, but in most popular GGM models, it is either a gaugino or a stau. The stau NLSP search is not the subject of this thesis, so it will not be considered in this section.

$$m_{\tilde{\chi}_1^0} = M_1 - \frac{m_Z^2 \sin^2 \theta_W (M_1 + \mu \sin 2\beta)}{\mu^2 - M_1^2} + \dots \quad (3.18)$$

$$m_{\tilde{\chi}_2^0} = M_2 - \frac{m_W^2 (M_2 + \mu \sin 2\beta)}{\mu^2 - M_2^2} + \dots \quad (3.19)$$

$$m_{\tilde{\chi}_3^0} = |\mu| + \frac{m_Z^2 (\text{sgn}(\mu) - \sin 2\beta)(\mu + M_1 \cos^2 \theta_W + M_2 \sin^2 \theta_W)}{2(\mu + M_1)(\mu + M_2)} + \dots \quad (3.20)$$

$$m_{\tilde{\chi}_4^0} = |\mu| + \frac{m_Z^2 (\text{sgn}(\mu) + \sin 2\beta)(\mu - M_1 \cos^2 \theta_W - M_2 \sin^2 \theta_W)}{2(\mu - M_1)(\mu - M_2)} + \dots \quad (3.21)$$

$$m_{\tilde{\chi}_1^\pm} = M_2 - \frac{m_W^2 (M_2 + \mu \sin 2\beta)}{\mu^2 - M_2^2} + \dots \quad (3.22)$$

$$m_{\tilde{\chi}_2^\pm} = |\mu| + \frac{m_W^2 \text{sgn}(\mu)(\mu + M_2 \sin 2\beta)}{\mu^2 - M_2^2} + \dots \quad (3.23)$$

462 where $\tan \beta = \langle H_u^0 \rangle / \langle H_d^0 \rangle$.

463 The two scenarios studied in ref. [22] are the following:

464 • **Bino NLSP:** $M_1 \sim$ few hundred GeV, $M_2, |\mu| \gg M_1$. All but the lightest
465 neutralino (Eq. 3.18) are effectively inaccessible at the LHC due to their large
466 masses. The NLSP can always decay to $\gamma + \tilde{G}$, and if it is heavy enough, to
467 $Z + \tilde{G}$ or $H + \tilde{G}$.

468 • **Wino NLSP:** $M_2 \sim$ few hundred GeV, $M_1, |\mu| \gg M_2$. The lightest neutralino
469 (Eq. 3.18) and the lightest chargino (Eq. 3.22) are nearly degenerate in mass,
470 and are the only two particles to play a role at the LHC. The decays described
471 in the previous bullet point can happen, as well as chargino decays to $W + \tilde{G}$.

472 The search described in this thesis is optimized for the classic bino NLSP decay $\gamma + \tilde{G}$,
473 but sensitivity to the wino co-NLSP scenario is also studied (see Chapter 8).

474 Since strong production of SUSY particles, for instance via $gg \rightarrow \tilde{g}\tilde{g}$, dominates
475 over electroweak production, for instance via $q\bar{q} \rightarrow \tilde{\chi}_1^\pm \tilde{\chi}_1^\mp$, at the LHC due to the
476 enhanced gg parton luminosity over the $q\bar{q}$ parton luminosity, early LHC searches are
477 particularly sensitive to light squarks and gluinos. General gauge mediation makes no

⁴⁷⁸ a priori restrictions on the mass splitting between the strongly interacting sparticles
⁴⁷⁹ and the weakly interacting sparticles, so models with light squarks and gluinos are
⁴⁸⁰ viable. In fact, such models could not be probed as well at the Tevatron⁴ as they are
⁴⁸¹ at the LHC due to the aforementioned parton luminosities.

⁴⁸² Typical LHC signatures of the bino and wino NLSP scenarios are shown in Fig-
⁴⁸³ ure 3.4.

⁴⁸⁴ 3.6 Experimental Status of SUSY

⁴⁸⁵ Collider searches for evidence of supersymmetry began in earnest in the 1980s [24]
⁴⁸⁶ and continue to this day. Most recently, the LHC and Tevatron experiments have set
⁴⁸⁷ the strictest limits on a variety of SUSY breaking scenarios, including GMSB and
⁴⁸⁸ mSUGRA.

⁴⁸⁹ Figure 3.5 shows the current limits set by the CMS experiment on the mSUGRA
⁴⁹⁰ model (with $\tan \beta = 10$) in the m_0 - $m_{1/2}$ plane. (Note that although the plot is trun-
⁴⁹¹ cated at $m_0 = 1000 \text{ GeV}/c^2$, some searches are sensitive out to $m_0 \sim 2000 \text{ GeV}/c^2$.)
⁴⁹² Although the LHC has pushed m_0 above $\sim 1 \text{ TeV}/c^2$ for $m_{1/2}$ up to $\sim 400 \text{ GeV}/c^2$,
⁴⁹³ casting some doubt onto the theory's prospects for solving the hierarchy problem,
⁴⁹⁴ there is still a sizable chunk of mSUGRA parameter space that is not ruled out by
⁴⁹⁵ collider experiments. Furthermore, parts of the CMS unexplored regions overlap with
⁴⁹⁶ areas allowed by astrophysics experiments [25].

Removed

⁴⁹⁷ Figure 3.6 shows the most up-to-date limit (using 1 fb^{-1} of integrated luminosity CMS
⁴⁹⁸ collected by the ATLAS experiment [27] at the LHC) on the Snowmass Points and Moriond
⁴⁹⁹ Slopes (SPS) model of mGMSB, dubbed SPS8 [28]. In general, the lifetime of the result
⁵⁰⁰ lightest neutralino in GMSB models can take on any value between hundreds of
⁵⁰¹ nanometers to a few kilometers depending on the mass of the lightest neutralino and

⁴Located on the Fermilab site in Batavia, Illinois, the Tevatron was a proton-antiproton collider operating at 1.96 TeV center-of-mass energy. The Tevatron ran from 1987 to 2011 [23].

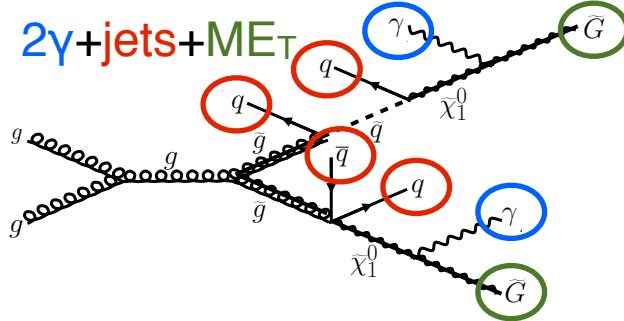
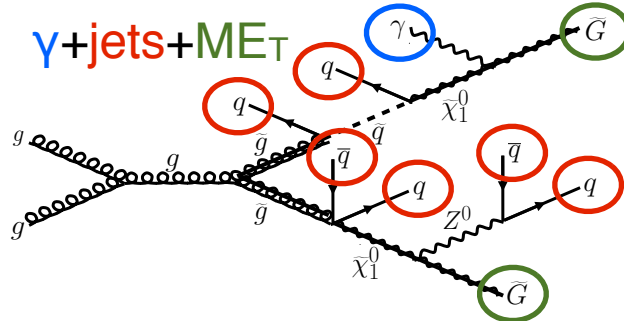
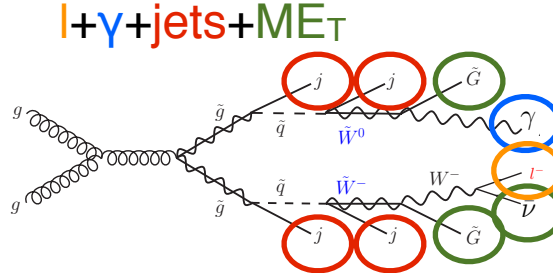
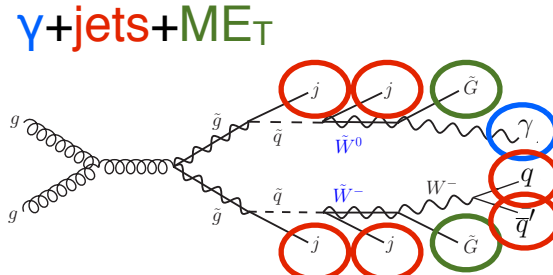
(a) Two gluinos each decay via $\tilde{\chi}_1^0 \rightarrow \gamma \tilde{G}$.(b) One gluino decays via $\tilde{\chi}_1^0 \rightarrow \gamma \tilde{G}$, the other via $\tilde{\chi}_1^0 \rightarrow Z(\rightarrow q\bar{q})\tilde{G}$.(c) One gluino decays via $\tilde{\chi}_1^0 \rightarrow \gamma \tilde{G}$, the other via $\chi_1^\pm \rightarrow W^\pm(\rightarrow l^\pm \nu_l)\tilde{G}$.(d) One gluino decays via $\tilde{\chi}_1^0 \rightarrow \gamma \tilde{G}$, the other via $\chi_1^\pm \rightarrow W^\pm(\rightarrow q\bar{q}')\tilde{G}$.

Figure 3.4: Typical LHC signatures of the bino and wino NLSP scenarios.

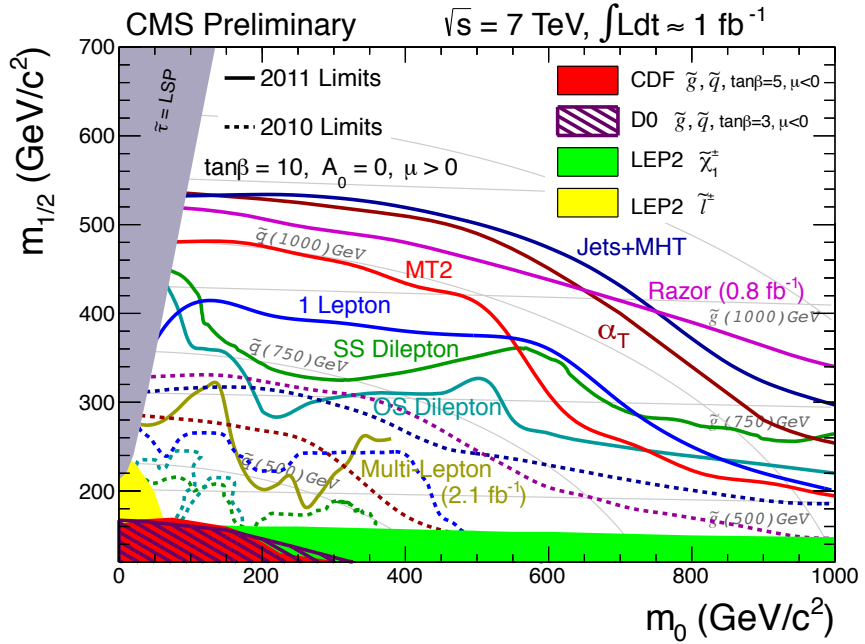


Figure 3.5: CMS limits on mSUGRA with $\tan\beta = 10$, corresponding to a model with third-generation squarks and sfermions somewhat lighter than their first- and second-generation counterparts. The limits set by individual searches are shown as separate colored lines. Solid lines refer to 2011 searches (i.e. using an integrated luminosity of $\sim 1 \text{ fb}^{-1}$), while dashed lines refer to 2010 searches ($\sim 36 \text{ pb}^{-1}$). Reprinted from ref. [26].

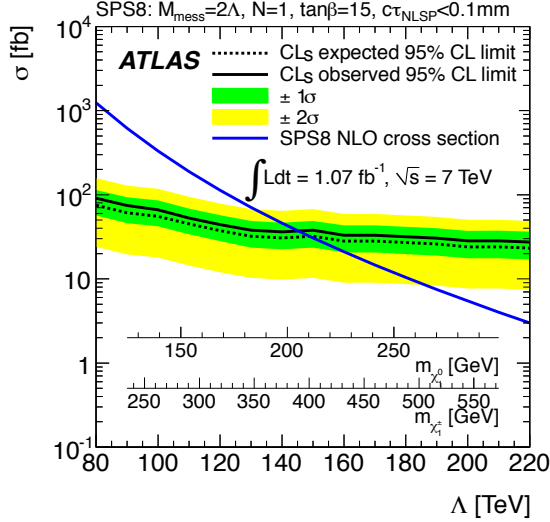


Figure 3.6: ATLAS cross section upper limit on the SPS8 [28] model of mGMSB as a function of SUSY breaking scale Λ , lightest neutralino mass $m_{\tilde{\chi}_1^0}$, or lightest chargino mass $m_{\tilde{\chi}_1^\pm}$. Values of Λ , $m_{\tilde{\chi}_1^0}$, or $m_{\tilde{\chi}_1^\pm}$ below the intersection point between the blue (predicted SPS8 cross section) and black (observed cross section upper limit) curves are excluded. The model parameters listed above the plot are defined in Secs. 3.4 and 3.5, except for τ_{NLSP} , which is the neutralino lifetime. Reprinted from ref. [20].

502 the SUSY breaking scale [12]. The search published in ref. [20] (from which Fig. 3.6 is
 503 culled) considers only *prompt* neutralino variants, i.e. with neutralino lifetime short
 504 enough that the distance traveled by the neutralino before decay cannot be resolved
 505 by the detector. The most recent limits on non-prompt SPS8-style neutralino models
 506 were set by the Collider Detector at Fermilab (CDF) collaboration with 570 pb^{-1} ,
 507 and are shown in Figure 3.7 [21].

508 Finally, if the gravitino is to make up some or all of the dark matter, constraints
 509 on the form of gauge mediation must come from cosmological considerations and
 510 astronomical observations. The gravitino in gauge mediation models is usually very
 511 light ($\mathcal{O}(\text{eV-MeV})$) because it is proportional to the SUSY breaking scale divided
 512 by the Planck mass, and in GMSB the breaking scale is typically only of order a
 513 few hundred TeV ([12] and Sec. 3.5). A light, highly relativistic dark matter particle
 514 might have been produced, for instance, in the early, radiation-dominated period
 515 of the universe [30]. This *warm dark matter* (WDM) may be responsible for all of

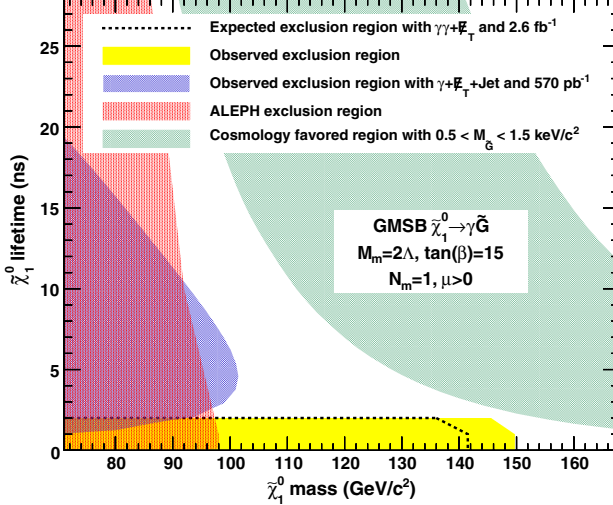


Figure 3.7: CDF exclusion contour in the $\tau_{\tilde{\chi}_1^0}$ - $m_{\tilde{\chi}_1^0}$ plane, where $\tau_{\tilde{\chi}_1^0}$ is the lifetime of the neutralino. Reprinted from ref. [21].

the dark matter needed to account for galactic structure, or it may share the duties with *cold dark matter* (CDM, weakly interacting particles with masses in the GeV range). In any viable model, the predicted relic density of the dark matter species must match the observed value of $\Omega h^2 \sim 0.1$ [31]. For many GMSB models, this measurement constrains the gravitino mass to the keV range [32]. This constraint, however, does not translate into a very strong bound on the lifetime of the lightest neutralino. Using the following equation (taken from [32]):

$$\tau_{\tilde{\chi}_1^0} \sim 130 \left(\frac{100 \text{ GeV}}{m_{\tilde{\chi}_1^0}} \right)^5 \left(\frac{\sqrt{\langle F \rangle}}{100 \text{ TeV}} \right)^4 \mu \text{m} \quad (3.24)$$

and applying the gravitino mass constraint $\sqrt{\langle F \rangle} \lesssim 3000 \text{ TeV}$ (cf. the first paragraph of Sec. 3.5 with $m_{\tilde{G}} \sim \text{keV}$) and $m_{\tilde{\chi}_1^0} = 100 \text{ GeV}$, the upper bound on the neutralino lifetime is 100 meters. For $\sqrt{\langle F \rangle} \sim 100 \text{ TeV}$, the neutralino lifetime is detectable on collider time scales.

Recently, a lower bound on the WDM particle mass in either pure warm or mixed warm and cold dark matter scenarios was set using observations of the Lyman- α forest. For pure WDM, $m_{\text{WDM}} > 8 \text{ keV}$, while for some mixed WDM-CDM scenarios,

530 $m_{\text{WDM}} > 1.1\text{-}1.5 \text{ keV}$ [30, 33]. These bounds and others have motivated the develop-
531 ment of more complicated gauge mediation models [33].

532 However, rather than focus on a specific GMSB model, of which there are many,
533 the search detailed in the following chapters is interpreted in a minimally model
534 dependent way. With this approach, the results can be applied to many competing
535 models. The remainder of this thesis is devoted to the experimental details of the
536 search, analysis strategy, and presentation of the results. The work described in this
537 thesis forms the basis for the CMS public result “Search for Supersymmetry in Events
538 with Photons and Missing Energy” [29], published in April 2012 (see Chapters 7 and 8
539 for results). Ref. [29] contains the best limits on bino-like NLSP and wino-like NLSP
540 GGM models to date.

541 **Chapter 4**

542 **The Large Hadron Collider**

543 At a 2010-2011 energy of 3.5 TeV/beam (7 TeV/beam design [34]) and maximum
544 instantaneous luminosity of $3.55 \times 10^{33} \text{ cm}^{-2} \text{ s}^{-1}$ [35] ($10^{34} \text{ cm}^{-2} \text{ s}^{-1}$ design [34]),
545 the CERN Large Hadron Collider (LHC) is the highest energy and highest intensity
546 proton-proton collider ever built. Its purpose is to allow the four LHC experiments to
547 explore TeV scale physics. For CMS and ATLAS, this implies examining the origins of
548 EWSB via searches for the SM Higgs boson and physical phenomena not predicted by
549 the SM that may explain the mass hierarchy in the SM. It also includes searches for
550 possible dark matter candidates that are often proposed to have masses at the weak
551 scale. The LHC needs to provide high energy proton collisions because the masses
552 of the sought-after particles are higher than those already incorporated into the SM.
553 It must also provide an unprecedented collision rate because signatures of the Higgs
554 boson and physics beyond the SM are very rare compared to SM processes.

555 The rest of this chapter is devoted to an overview of the LHC machine. Sec-
556 tion 4.1 gives the overall layout of the machine and design choices made in light of
557 energy and luminosity demands. Section 4.2 describes the LHC injection scheme. The
558 different types of magnets and their functions is illustrated in Section 4.3, and finally
559 the radiofrequency cavities are covered in Section 4.4. Unless otherwise noted, all

560 information in this chapter comes from ref. [34].

561 4.1 Design Considerations and Performance Lim- 562 itations

563 The layout of the 26.7-km long [36] LHC ring, located \sim 100 m underground on the
564 border between France and Switzerland northwest of Geneva, is shown in Figure 4.1.
565 The two circulating beams of protons travel in opposite directions, colliding only at
566 the experimental points. There are eight straight sections, each \sim 528 m long, and
567 eight arcs, each made of 23 106.9-m long arc cells. Beam crossings occur in four of
568 the straight sections. The arcs contain six 14.3-m long dipole magnets, the cryogenics
569 to cool the magnets, and short straight sections (SSS) with focusing and corrector
570 magnets. The high luminosity experiments CMS and ATLAS are located diametrically
571 opposite each other on the ring, ensuring that in principle each should receive the
572 same integrated luminosity from the LHC.

573 To achieve a maximum energy per beam of 7 TeV, the peak magnetic field pro-
574 duced by the dipole magnets must be 8.33 T, demanding the use of superconducting
575 technology. Due to the like charges of the two beams, two separate magnet systems
576 and evacuated beam pipes must be used to accelerate the protons in opposite direc-
577 tions. Space limitations in the LHC tunnel, which was previously used for the LEP
578 collider, prevent the installation of two separate rings of magnets, so each dipole in-
579 stead contains two beam pipe bores and two sets of superconducting coils to produce
580 two fields in opposite directions. In order to safely operate the magnets at 8.33 T,
581 the cryogenic bath temperature is chosen to be 1.9 K, colder than any other acceler-
582 ator cryogen and well below the critical temperature of the niobium-titanium (NbTi)
583 superconducting wires of 9.2 K [39]. The extremely low bath temperature leads to
584 a lessened heat capacity in the wires and consequently a lower energy threshold for

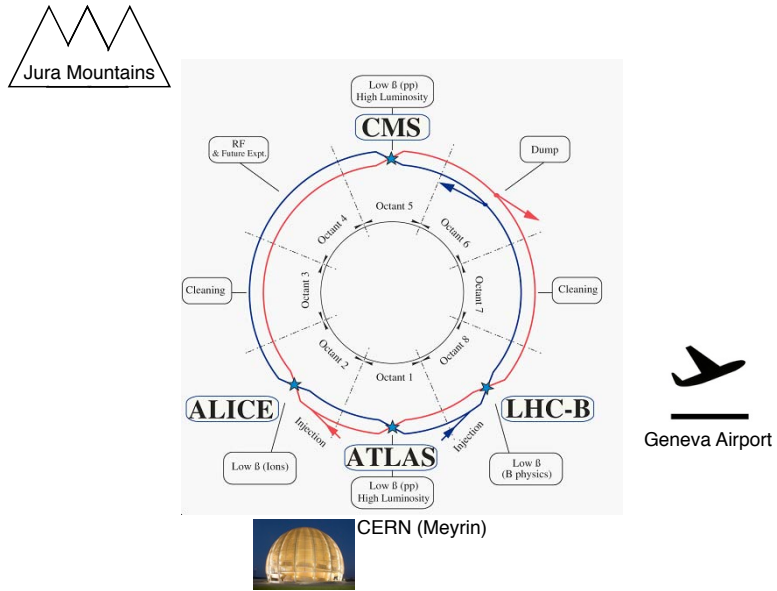


Figure 4.1: Bird's-eye view of the LHC ring, showing the locations of the experiments and local landmarks. Arrows show the beam direction. The ring figure is reprinted from Fig. 2.1 of ref. [34]. The CERN Globe of Innovation photo comes from ref. [37] and the airplane cartoon comes from ref. [38].

585 triggering a quench, so movements and heat dissipation within the cables must be
 586 controlled more tightly than in previous accelerators.

587 The LHC beams are arranged in bunches of protons, with each bunch separated
 588 by an integer multiple of the 25 ns minimum bunch spacing. The machine luminosity
 589 L is given by

$$L = \frac{N_b^2 n_b f_{\text{rev}} \gamma_r}{4\pi \epsilon_n \beta^*} F \quad (4.1)$$

590 where N_b is the number of protons per bunch (squared for the two beams), n_b is
 591 the number of bunches per beam, f_{rev} is the bunch revolution frequency, γ_r is the
 592 relativistic γ of the protons, ϵ_n is the normalized transverse beam emittance, β^* is
 593 the value of the β function at the collision point, and F is a geometrical factor less
 594 than one related to the *crossing angle* of the bunches with respect to the horizontal

595 (ATLAS) or vertical (CMS) planes and the beam size. The normalized transverse
 596 beam emittance is a measure of the RMS spread of the beam in the plane transverse
 597 to its direction of motion, irrespective of its energy. A smaller emittance implies that
 598 particles are squeezed into a smaller area in phase space, leading to larger luminosity.
 599 The β function is defined as the square of the transverse beam size divided by the
 600 emittance. It describes the oscillations of the transverse beam size as a function of
 601 position in the ring. To achieve high luminosity, β^* is the minimum of the β function,
 602 and it is related to the focusing strength of the triplet magnets near the interaction
 603 points. In accelerating sections of the ring, the β function gets large so that the proton
 604 momenta may be more uniform. Each piece of the luminosity is limited by safety or
 605 design considerations.

606 Above some saturated bunch intensity, nonlinear beam-beam interactions experi-
 607 enced by the protons during collisions cause the luminosity to scale as N_b , not N_b^2
 608 [40]. The scale of these interactions is set by N_b/ϵ_n , and the size of the beam pipe and
 609 maximum β function limit ϵ_n to $3.75 \mu\text{m}$. Instabilities are also introduced through
 610 interactions between the protons and the wall of the beam pipe that scale with the
 611 beam current. Last but not least, the beam dump and magnet safety systems limit the
 612 total stored energy in the ring. For these reasons, the maximum number of bunches
 613 is limited to 1.15×10^{11} . In bunches of this proton multiplicity, the average num-
 614 ber of proton-proton collisions per bunch crossing, or *pileup*, in CMS and ATLAS is
 615 approximately 20. This unprecedented level of pileup poses unique triggering, event
 616 reconstruction, and analysis challenges for the experiments.

617 n_b can range from zero to 2808 and had a maximum of ~ 1400 in 2011, corre-
 618 sponding to 50 ns bunch spacing. f_{rev} is set by the circumference of the ring to 11.2
 619 kHz [41]. γ_r is set by the beam energy, which was 3.5 TeV in 2011.

620 The mechanical aperture of the triplet assemblies of quadrupole magnets limit
 621 the minimum β^* to 0.55 [41] and maximum crossing angle to $285 \mu\text{rad}$ [41] at the

The LHC injection complex

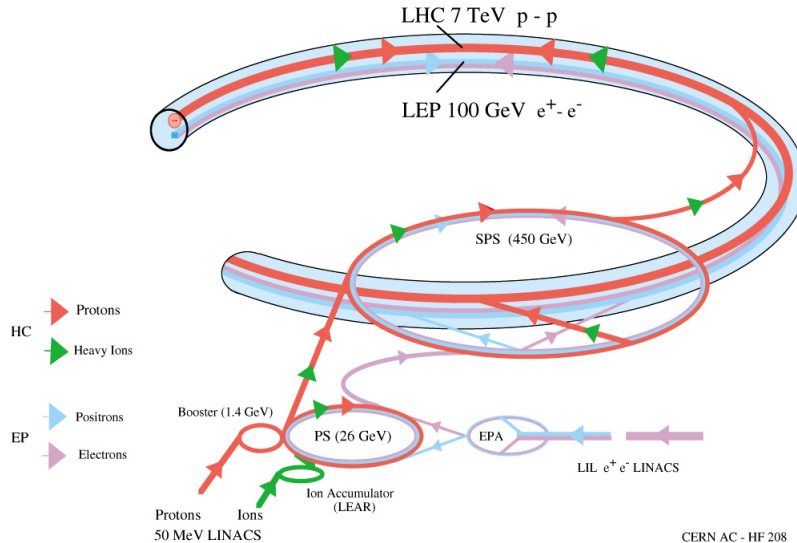


Figure 4.2: Overview of the LHC injector complex at CERN [42].

622 interaction points. The purpose of the crossing angle is to prevent parasitic collisions
 623 in the 23-m length of shared beam pipe upstream and downstream of the interaction
 624 points.

625 4.2 Beam Injection

626 The ultimate source of protons for the LHC is a bottle of hydrogen connected to the
 627 CERN Linac2 linear accelerator, which accelerates the protons up to 50 MeV. From
 628 there they enter the Proton Synchrotron Booster (PSB), which accelerates them to
 629 1.4 GeV, and then the Proton Synchrotron (PS) itself, which brings them to 25 GeV.
 630 The Super Proton Synchrotron (SPS) is the next stage, accelerating the protons to
 631 an energy of 450 GeV. Finally, they leave the SPS and enter the LHC, where they are
 632 accelerated to the desired beam energy (3.5 TeV in 2011). An overview of the LHC
 633 injector complex is shown in Figure 4.2.

634 The 25-ns spaced bunches (or 50 ns for 2011 operation) are produced in trains
 635 of 72 in the PS via a process of splitting six initial bunches into 12 smaller bunches

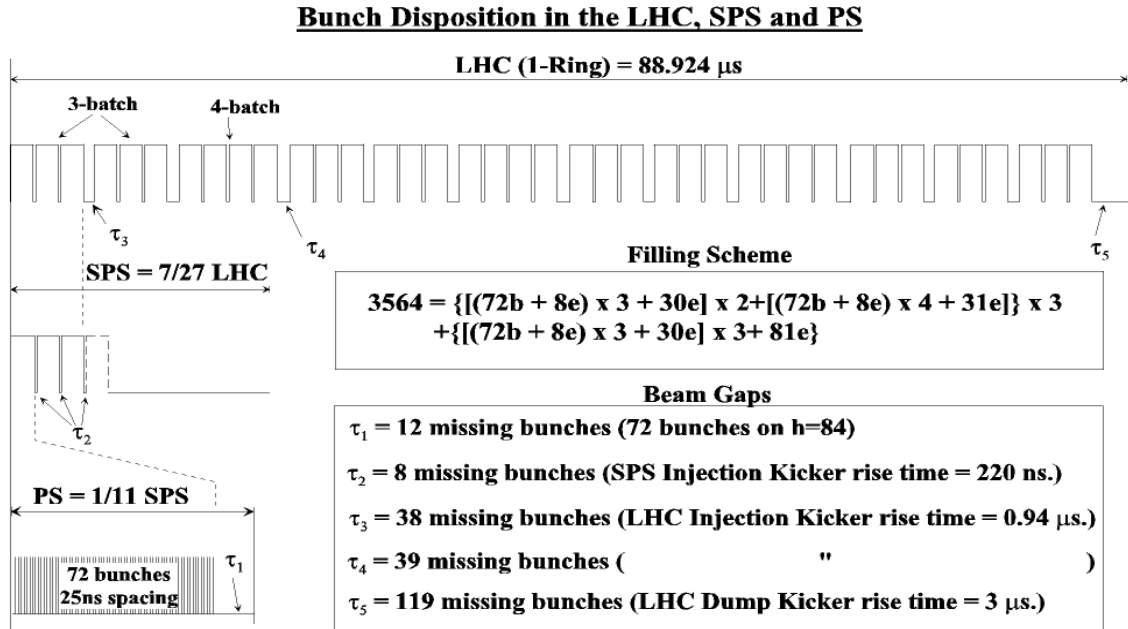


Figure 4.3: LHC injection scheme. Reprinted from Fig. 12.2 of ref. [34].

636 at specified points along the ring. At the end of each train is a 300 ns (12 bunch)
 637 gap, which is an artifact of the splitting process. The SPS is limited by its maximum
 638 allowed bunch intensity to storing three or four PS trains at a time. There is an 220
 639 ns (8 bunch) gap at the end of each train due to the SPS injection kicker rise time.
 640 The LHC is filled three or four trains at a time from the SPS. At the end of each
 641 three-train and four-train group is a gap of 0.94 μ s (38 or 39 bunches) due to the
 642 LHC injection kicker rise time. Finally, at the end of an entire 88.924- μ s long LHC
 643 orbit is a gap of 3 μ s (119 bunches), known as the *abort gap*, to allow for the LHC
 644 dump kicker rise time. The injection scheme is shown in Figure 4.3.

645 LHC injection occurs at points 2 and 8. At the intersection of the SPS-LHC
 646 transfer line and the LHC beam pipe are five septum magnets that deflect the bunches
 647 12 mrad horizontally into orbit. The septum magnets have a gap into which the
 648 beam is injected as well as two separate holes for the circulating beams, as shown in
 649 Figure 4.4. Four kicker magnets then deflect the bunches 0.85 mrad vertically into
 650 orbit. The kicker magnets supply a pulsed magnetic field with a 0.94 μ s rise time

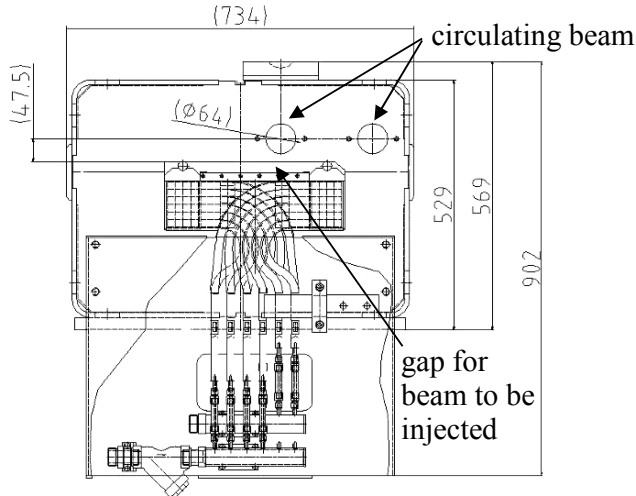


Figure 4.4: Cross-sectional view of septum magnet (beam direction is into or out of the page) showing the holes for the circulating beams and the separate gap for injected particles. Reprinted from Fig. 11.2 of ref. [34].

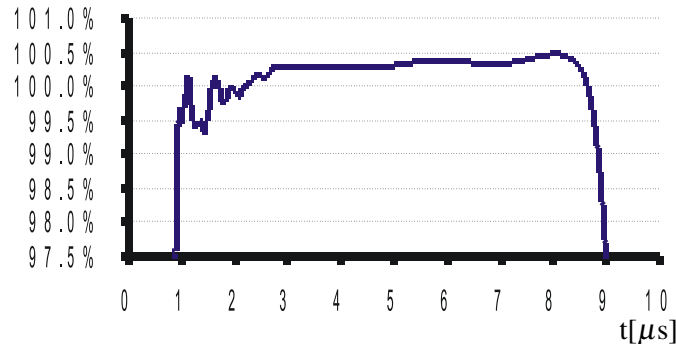


Figure 4.5: LHC injection kicker pulse shape. The y -axis measures percentage of maximum current. Reprinted from Fig. 11.7 of ref. [34].

651 (see Fig. 4.3) and a 5.84(7.86) μs flat top for three-train(four-train) injection (see
 652 Figure 4.5). To limit emittance growth at injection due to over- or under-kicking the
 653 injected bunches such that they miss the core of the LHC orbit, the kicker current is
 654 limited to $< 0.5\%$ flat top ripple in any direction.

655 4.3 Magnets and Cryogenics

656 There are 1232 twin-bore dipole magnets along the LHC ring used for establishing
 657 the circular orbit of the protons. They consist of two evacuated beam pipes, each

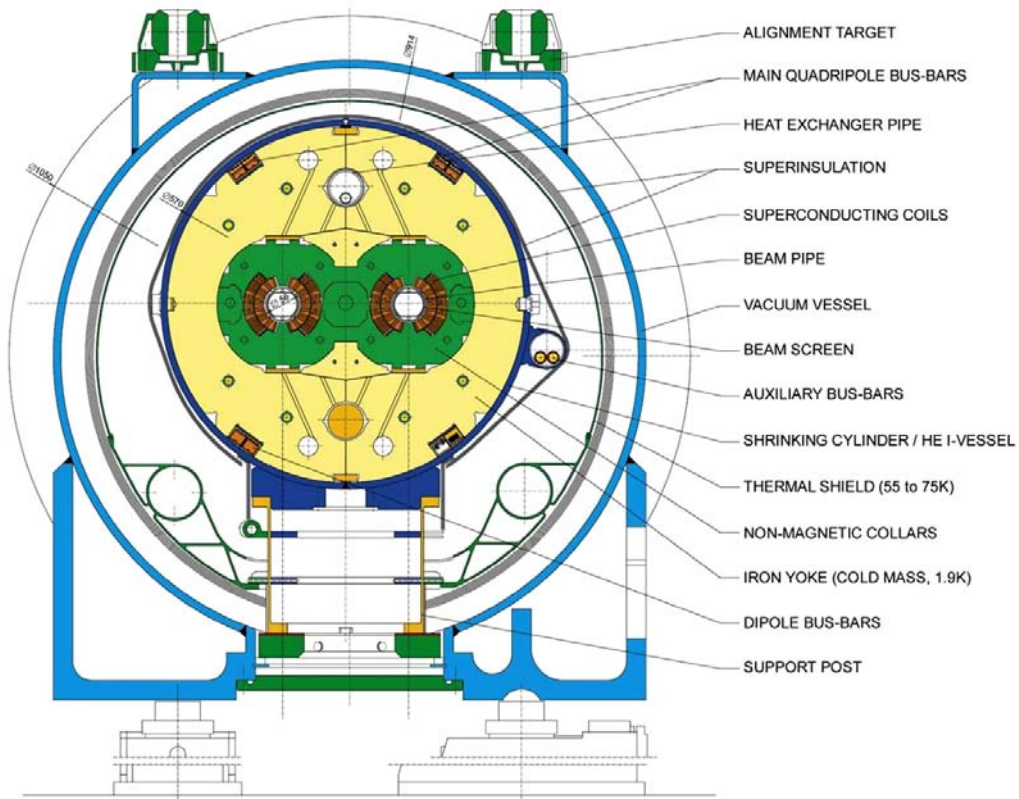


Figure 4.6: Cross-sectional view of LHC dipole + cryostat. Reprinted from Fig. 3.3 of ref. [34].

658 flanked by its own set of superconducting coils, inside an iron yoke which serves as
 659 the 1.9 K cold mass. The entire assembly sits inside a helium vessel, which is itself
 660 surrounded by a vacuum chamber thermally insulating the cold mass from the room
 661 temperature LHC cavern. The entire dipole + cryostat device is ~ 16.5 m long and
 662 weighs about 27.5 t. A cross-sectional view of the dipole is given in Figure 4.6.

663 To provide a centripetal Lorentz force on the protons, the dipole field points
 664 vertically up or down, depending on the sense of the beam. The magnetic field lines for
 665 a single beam pipe are shown in Figure 4.7. Figure 4.8 shows the coil windings in two
 666 bores. To provide the correct field direction, the coils are wound around blocks that
 667 are ~ 14 m long (the length of the dipole), so that each winding has a circumference
 668 of ~ 28 m.

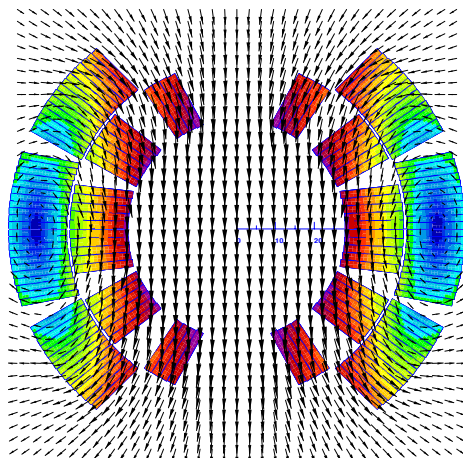


Figure 4.7: Magnetic field lines of the dipole field. The beam direction is into the page. Reprinted from Fig. 4 of ref. [43].

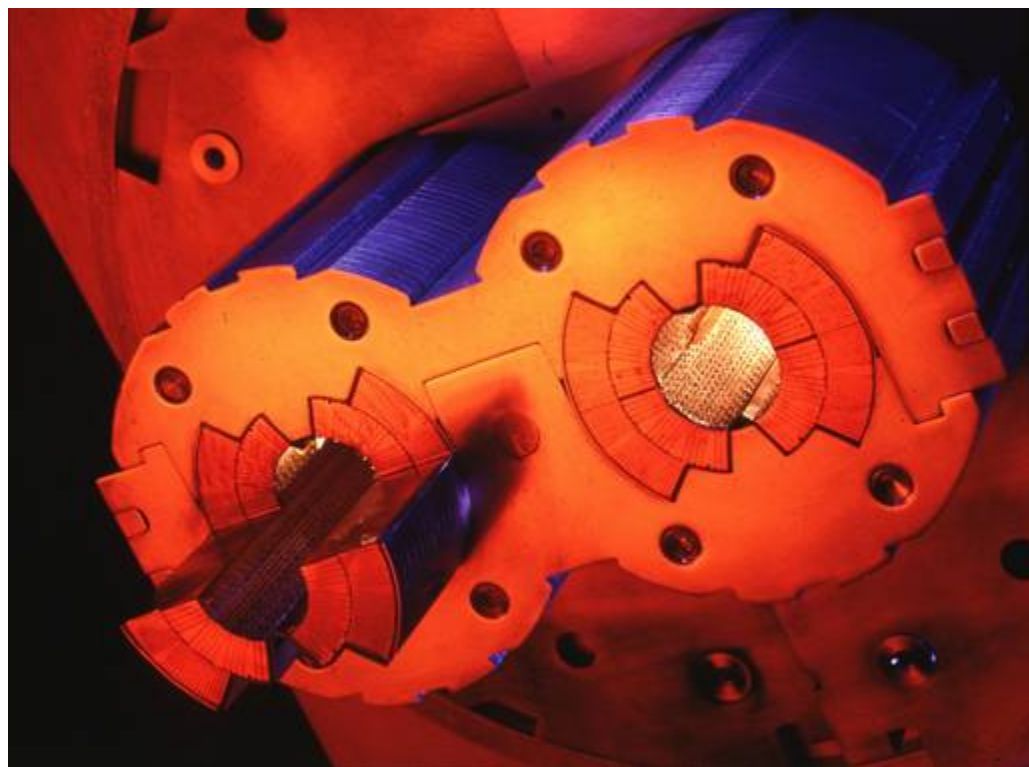


Figure 4.8: Superconducting coils in a twin-bore dipole [44].

669 In addition to the dipoles, a number of different types of orbit corrector magnets
 670 are installed throughout the ring. The main quadrupole magnets, as well as higher
 671 order field corrector magnets, are located in the arcs and short straight sections. The
 672 function of these magnets is to provide fine grained control over the magnetic field
 673 in order to keep the bunches in the proper orbit and control the emittance and β
 674 functions.

675 In the straight sections, there are four specialized types of magnets related to SPS
 676 extraction and bringing the beams into collision. Matching section quadrupoles near
 677 the transfer lines help to match the injected bunch orbit to the circulating bunch orbit.
 678 Dispersion suppressors, consisting of dipoles and quadrupoles, help to reduce beam
 679 dispersion near the collision points due to off-momentum protons. Matching section
 680 separation dipoles control the separation between the two beams near the collision
 681 points. The magnets that perform the final squeeze of the beams before collision,
 682 called the low- β inner triplets, must provide a very high field gradient of 215 T/m,
 683 withstand a high radiation dose, and sustain high heat loads in the superconducting
 684 coils.

685 The superfluid helium cryogen is delivered to the magnets via a distribution line
 686 from the main refrigerator. A cross section of the LHC tunnel, showing the cryogen
 687 delivery apparatus for a dipole, is shown in Figure 4.9.

688 4.4 Radiofrequency Cavities

689 LHC bunches are captured and accelerated in 400 MHz superconducting radiofre-
 690 quency (RF) cavities. 400 MHz defines the bunch length of $\lesssim 2$ ns. As bunches pass
 691 through the cavities, the oscillating electric field is at its peak and accelerates the
 692 protons through a potential difference of 2 MV per cavity (16 MV per turn). The
 693 finite bunch length is due to particles that arrive out of phase with the electric field

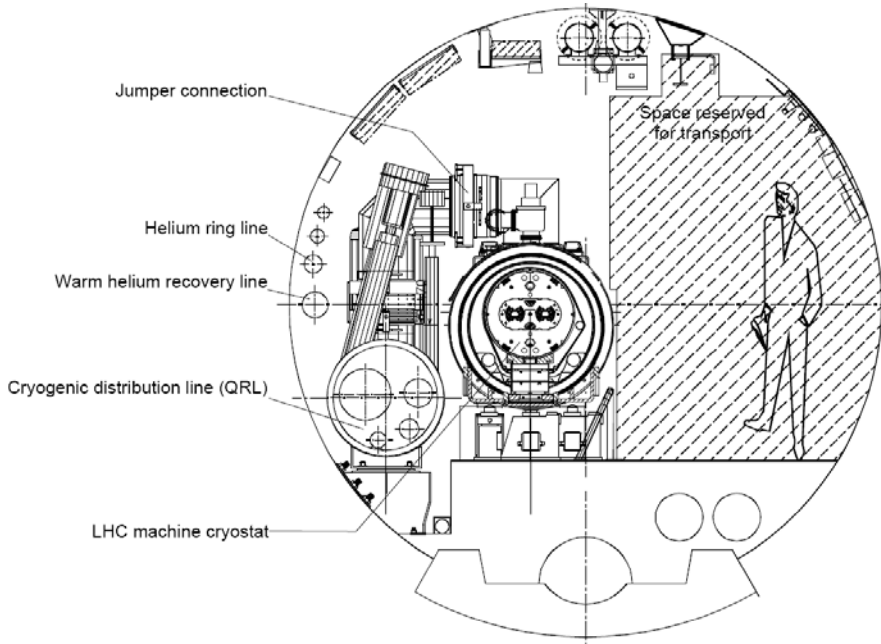


Figure 4.9: Cross section of the LHC tunnel, showing the cryogen delivery apparatus for a dipole. Reprinted from Fig. 7.1 of ref. [34].

694 due to deviations in their momenta from the nominal. During a ramp of the beam
 695 energy from 450 GeV to 3.5 or 7 TeV, bunches repeatedly travel around the ring, re-
 696 ceiving an energy kick each time, until the desired energy is reached. Feedback from
 697 the RF accelerating system causes an increase in magnet current to keep the bunches
 698 in a fixed orbit.

699 Superconducting material (niobium) coats the cylindrical walls of the cavity. RF
 700 power is coupled to the cavity via a klystron. The RF electric field standing wave is set
 701 up across the cavity in the beam direction. The transverse magnetic field dissipates
 702 some energy into the walls, but much less than in a normal conducting cavity.

703 **Chapter 5**

704 **The Compact Muon Solenoid**
705 **Experiment**

706 The Compact Muon Solenoid (CMS) detector sits at point 5 of the LHC ring, diamet-
707 rically opposite the ATLAS detector at point 1. It is a 4π hermetic general purpose
708 detector, meaning that it has the capability to detect charged and neutral hadrons,
709 photons, electrons, muons, taus, neutrinos, and non-Standard-Model particles pre-
710 dicted to escape the detector with good efficiency over a large range of rapidity.
711 Its main distinguishing feature is a superconducting solenoid that provides a 3.8T
712 magnetic field parallel to the beam line. This strong magnetic field allows precise de-
713 termination of the momentum and charge of muons and electrons up to a momentum
714 of ~ 1 TeV.

715 The origin of the CMS coordinate system is at the nominal interaction point. The
716 y -axis points skyward, the x -axis points towards the center of the LHC ring, and
717 the z -axis points counterclockwise along the LHC ring. r denotes radial distances
718 from the beam line, ϕ is the azimuthal angle measured with respect to the positive
719 x -axis, and θ is the polar angle measured with respect to the positive z -axis. The
720 *pseudorapidity* η is defined as $\eta = -\ln \tan(\theta/2)$, and is a good approximation to

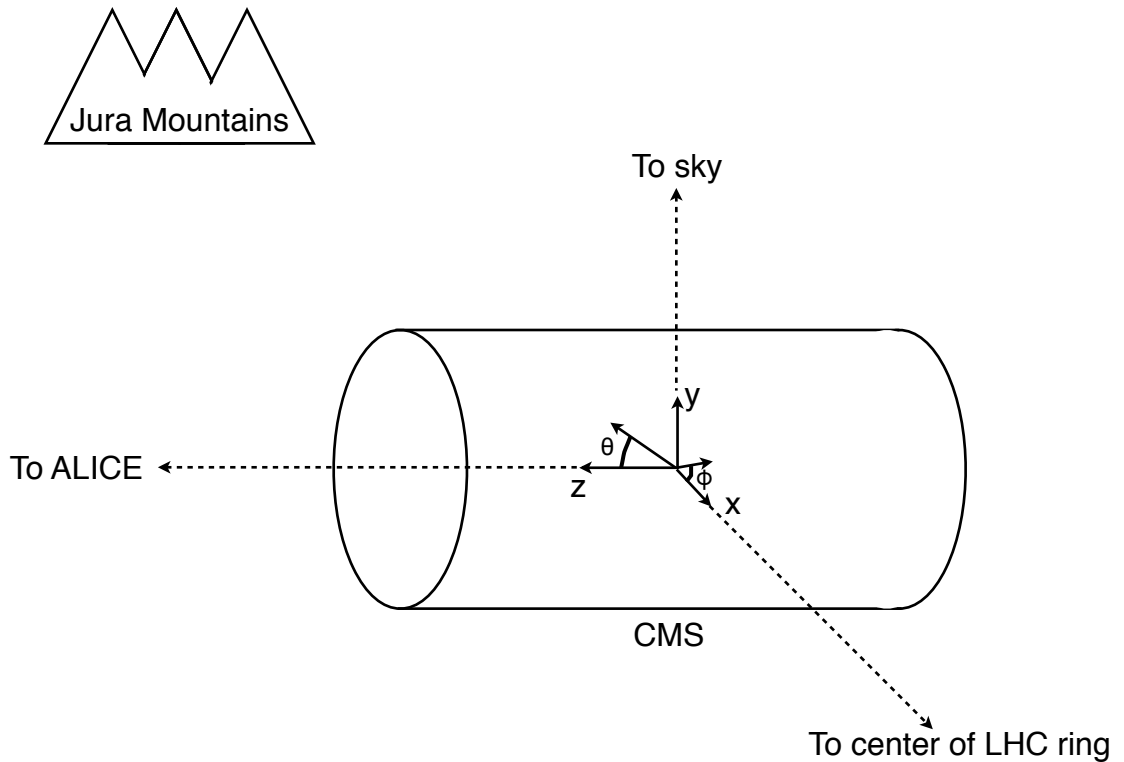


Figure 5.1: CMS coordinate system.

721 rapidity $y = (1/2) \ln((E + p_z c)/(E - p_z c))$ for relativistic particles. The transverse
 722 momentum and energy (p_T and E_T) of a particle are defined as $p_T = p \cos \phi$ and
 723 $E_T = E \cos \phi$, where p and E are the magnitude of the particle's momentum vector
 724 and the particle's total energy, respectively. A depiction of the CMS coordinate system
 725 is shown in Figure 5.1.

726 The CMS sub-detectors are arranged in concentric cylindrical layers, plus “end-
 727 caps,” around the beam line, as shown in Figure 5.2. Closest to the beam line are
 728 three layers of silicon pixel detectors, with the innermost at radius 4.4 cm and out-
 729 ermost at radius 10.2 cm [45]. Including the pixel endcaps, the total pixel coverage

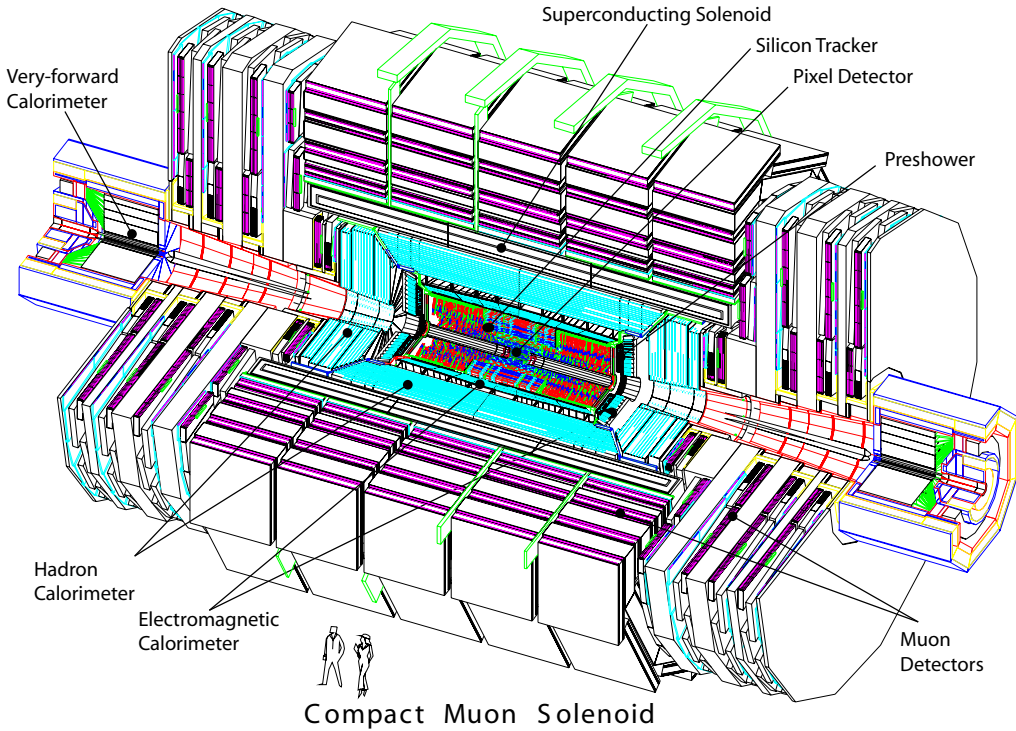


Figure 5.2: Cutaway view of CMS. Reprinted from Fig. 1.1 of ref. [45].

730 extends to $\eta = 2.5$ [45]. The pixel detector plays an important role in determining the
 731 proton-proton interaction position (*beam spot*) and the impact parameters of charged
 732 particle trajectories, and is critical for the measurement of decay positions some dis-
 733 tance from the beam spot (*displaced vertices*), such as those due to the showering and
 734 hadronization of a b quark.

735 The 10 next layers of CMS are comprised of silicon microstrip detectors, with the
 736 outermost layer at a radius of 1.3 m from the beam line [45]. As for the pixel detectors,
 737 the silicon strip endcaps extend tracking coverage to $\eta = 2.5$. The silicon microstrip
 738 layers are the workhorse of the CMS tracking system, and provide excellent charged
 739 particle momentum resolution and track finding efficiency.

740 Outside the tracking detectors are the calorimeters, starting with the single-layer
 741 lead tungstate crystal electromagnetic calorimeter at a radius of 1.3 m from the beam
 742 line (location of crystal front faces) [45]. Each crystal is 23 cm long, corresponding

743 to 25.8 radiation lengths (X_0) [45]. The crystal dimensions are such that most of one
 744 electromagnetic shower, and no more, can be contained in a single crystal, leading to
 745 excellent energy resolution for photons and electrons. The electromagnetic calorime-
 746 ter radial and endcap layers cover a pseudorapidity range up to 3.0. A lead/silicon
 747 sampling calorimeter sits in front of the crystal endcaps to provide better rejection
 748 of neutral pions.

749 The last layer of calorimetry inside the solenoid is the brass/scintillator sampling
 750 hadronic calorimeter, which has a radial extent from 1.77-2.95 m [45]. The hadronic
 751 barrel and endcap calorimeters cover up to $|\eta| = 3.0$, while the iron/quartz-fiber for-
 752 ward hadronic calorimeter covers the region $3.0 \leq |\eta| \leq 5.2$.¹ There is one more
 753 layer of hadronic calorimetry outside the solenoid in $|\eta| < 1.3$ which, together with
 754 the layers inside the solenoid, provides approximately 12 hadronic interaction lengths
 755 of instrumented absorber. Because of its large $|\eta|$ coverage and depth, the hadronic
 756 calorimeter provides good missing transverse energy resolution and accurate measure-
 757 ments of high energy jets.

758 The iron return yoke of the solenoidal magnetic field is interleaved with muon
 759 detectors from 4.1-7.4 m in r and 6.6-10.6 m in z , providing muon detection up to
 760 $|\eta| = 2.4$ [45]. In the barrel region of $|\eta| < 1.2$, drift tubes are used to read out the
 761 muon tracks, while in the endcaps cathode strip chambers are used. Due to their
 762 speed, resistive plate chambers are used throughout the muon system to provide
 763 an independent trigger and timing measurement. Combining the tracker and muon
 764 system hits, the momenta and charge of muons up to $p_T = 1$ TeV can be precisely
 765 reconstructed.

766 A longitudinal quarter cross-sectional view of CMS is shown in Figure 5.3. The
 767 remainder of this chapter is devoted to explaining the CMS subdetectors and readout

¹The Centauro and Strange Object Research (CASTOR) and Zero Degree Calorimeter (ZDC) detectors provide additional calorimetry beyond $|\eta| = 5.2$. However, they are mainly used in the heavy ion and diffractive physics programs of CMS, and play no role in the detection of heavy SUSY particles. Therefore, they will not be discussed here.

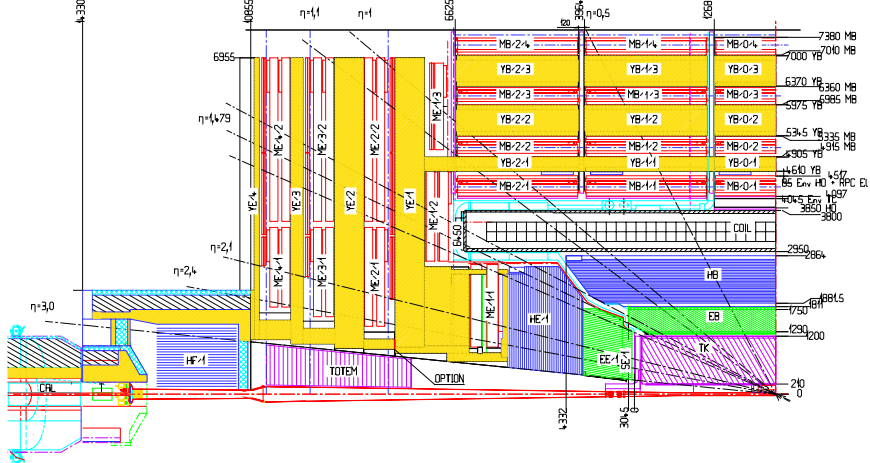


Figure 5.3: Longitudinal quarter cross-sectional view of CMS. The nominal interaction point is at the lower right-hand corner of the drawing. The tracker is shown in purple diagonal hashing, the electromagnetic calorimeter in green, the hadronic calorimeter in blue, and the muon stations in red. The solenoid is shown in black and white and labeled COIL, and the magnet return yoke is shown in yellow. Radial and longitudinal distances are measured in millimeters. Reprinted from Fig. CP 1 of ref. [46].

systems. Section 5.1 describes the subdetector technologies and performance benchmarks, while Section 5.2 details the CMS trigger and data acquisition systems and framework for promptly reconstructing and transferring data worldwide. For a thorough description of CMS, see ref. [45]. Unless otherwise noted, all information in this chapter comes from ref. [45].

5.1 The Detectors and Their Operating Principles

5.1.1 Tracking System

Given the LHC design instantaneous luminosity, efficient reconstruction of charged particle tracks from transverse momenta of 1 GeV up to 1 TeV can only be achieved with a low occupancy tracker. For $r < 10$ cm, the hit rate density is highest, leading to the choice of $100 \mu\text{m} \times 150 \mu\text{m}$ silicon pixel sensors for hit detection. For $20 \text{ cm} < r < 110 \text{ cm}$, the lower hit rate allows the use of silicon strips, with length along z of

order centimeters and length along the $r \cdot \phi$ curve of order hundreds of microns. This design leads to a pixel hit occupancy of $\sim 10^{-4}$ /pixel/BX and a strip hit occupancy of $\sim 10^{-2}$ /pixel/BX, where BX refers to 1 LHC bunch crossing.

As radiation dose from hadrons accumulates over the lifetime of the tracker, silicon leakage current through the semiconductor junctions increases, heating up the sensors. Since the leakage current itself depends on temperature, this can lead to *thermal runaway* that damages the detector. To avoid this, the tracker must be cooled to approximately -10°C . Operating at this temperature, the signal:noise ratio in the silicon sensors is 10:1, and should remain at that level over the 10-year lifetime of the tracker.

At its thickest ($|\eta| \sim 1.5$), the tracker depth (including services) is $\sim 1.8X_0$, and the depth falls off to $\sim 1X_0$ in thinner areas. Unfortunately, the large mass of the tracker degrades somewhat the performance of the electromagnetic calorimeter behind it, as $\sim 50\%$ of photons will convert to e^+e^- pairs in the tracker.

Pixel Detector

A longitudinal quarter view of the three barrel pixel (BPix) layers and two forward pixel (FPix) disks is shown in Figure 5.4. There are 768 BPix modules in total. Each BPix layer is divided into 32 ϕ -wedges, with eight modules per wedge arranged end-to-end in z . The ϕ -wedges operate nearly independently in terms of clock and readout. Each FPix disk consists of 24 ϕ -wedges, with pie-shaped modules attached to the front and back of the disk, for a total of 192 modules. The front- and back-side modules of the FPix disks are constructed of different sized *plaquettes*, or multi-pixel sensor chips, such that the gaps in the front-side module are covered by plaquette area in the back-side module and vice versa. An illustration of the BPix and FPix mechanical layouts is given in Figure 5.5.

Since the electric field in the depletion region of the BPix sensors is perpendicular

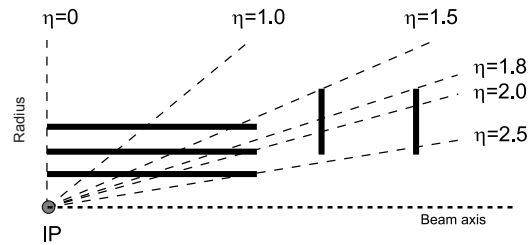
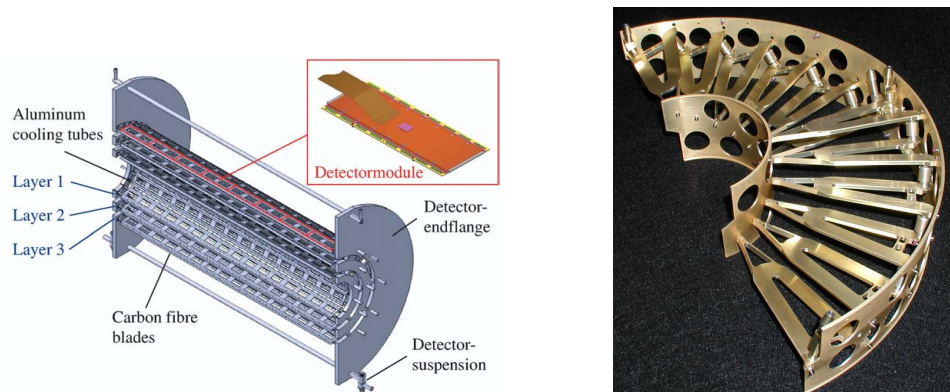


Figure 5.4: Longitudinal quarter view of the pixel detector. Reprinted from Fig. 3.6 of ref. [45].



(a) Cutaway view of the barrel pixel layers, showing the three layers and the eight end-to-end modules along z . Reprinted from Fig. 3.11 of ref. [45].

(b) Half-disk of the forward pixel detector, showing the 12 pie-shaped module mounts. Reprinted from Fig. 3.15 of ref. [45].

Figure 5.5: BPix and FPix mechanical structures.

806 (i.e. pointing along r) to the magnetic field of CMS (i.e. pointing along z), the charge
 807 carriers in the silicon experience a Lorentz drift along ϕ . The multi-pixel sensor pitch
 808 is such that this causes the charge from one particle hit to be shared among multiple
 809 pixels. Particle hits are reconstructed reading out the analog pixel signal and inter-
 810 polating between signals in multiple pixels. This method achieves a $15\text{-}20 \mu\text{m}$ spatial
 811 resolution, which is comparable to the sensor pitch. To induce this effect in FPix,
 812 the sensor wedges are tilted by the approximate BPix Lorentz angle of 20° [47] with
 813 respect to the y -axis.

814 Each multi-pixel sensor consists of an array of 52×80 n-type pixels implanted onto
 815 an n-type substrate with $320 \mu\text{m}$ thickness. The other face of the substrate is covered
 816 with a thin layer of p-type semiconductor. Except for the outer edges, which are held
 817 at ground potential to prevent sparking between the sensor edges and the connected
 818 readout chip [48], the p-side is reverse biased at 150 V (BPix) or 300 V (FPix). The
 819 pixels are held at ground potential. A particle entering through the p-side will cause
 820 a burst of current to flow across the p-n junction. The charge will be collected by the
 821 pixels, which are bump-bonded to the readout. The BPix and FPix sensors employ
 822 slightly different technologies for electrically isolating the individual pixels, but both
 823 rely on the idea of surrounding the pixels with a p-type material to provide a p-n
 824 junction that acts as a barrier to current flow.

825 Each 52×80 pixel sensor is bump bonded to a readout chip (ROC). The ROCs
 826 provide zero suppression and amplify, buffer, and communicate the signals from the
 827 sensors. A single token bit manager (TBM) controls ~ 16 ROCs in the barrel or ~ 24
 828 ROCs in the endcaps. Its purpose is to distribute the clock and trigger to the ROCs
 829 (the latter initiates a transmission of the signal further upstream to be assembled
 830 into the full event readout of CMS). The clock and trigger are supplied by the pixel
 831 front end controller (pFEC), which interfaces to the central clock and data acquisition
 832 systems. Analog signals that are collected from the pixel front ends are digitized by

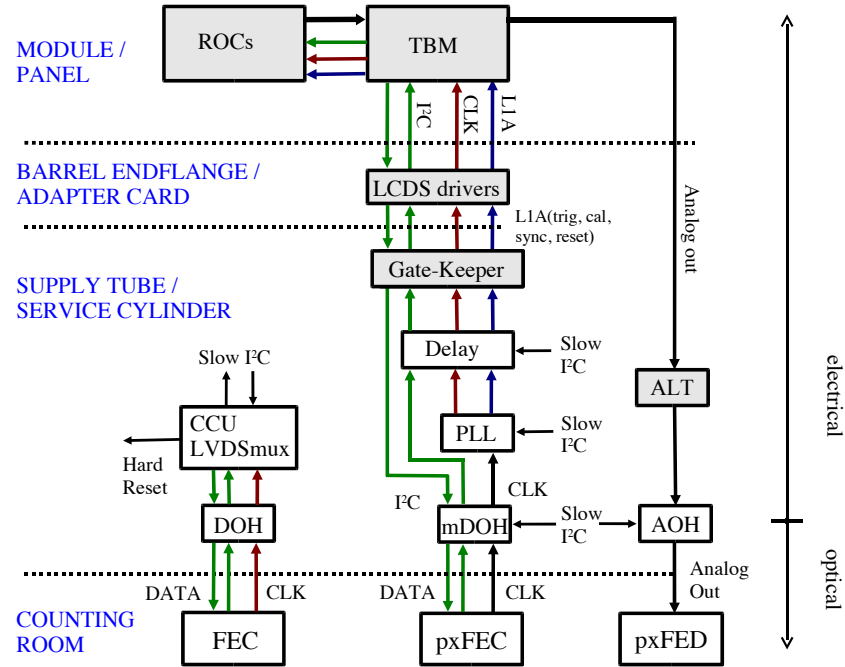


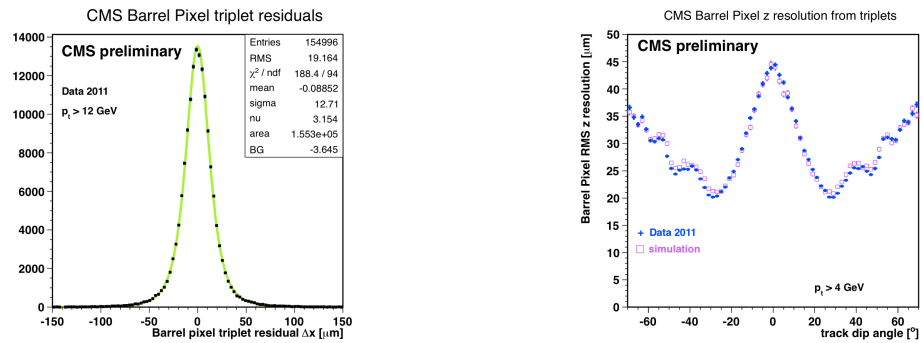
Figure 5.6: Pixel control and readout system. Reprinted from Fig. 3.9 of ref. [45].

833 the pixel front end digitizer (pxFED). A diagram of the readout system is shown in
 834 Figure 5.6.

835 Figure 5.7 shows some results highlighting the performance of the pixel detector.

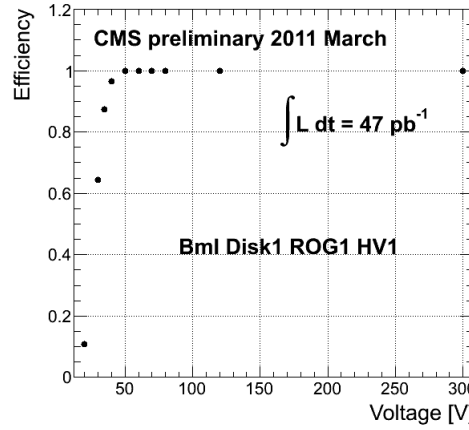
836 Silicon Strip Tracker

837 The silicon strip tracker is divided into four parts: the inner barrel (TIB) and inner
 838 disks (TID), covering the radial extent $20 \text{ cm} < r < 55 \text{ cm}$ and z extent $80 \text{ cm} <$
 839 $|z| < 90 \text{ cm}$; and the outer barrel (TOB) and endcap (TEC), covering the radial
 840 extent $61 \text{ cm} < r < 108 \text{ cm}$ and z extent $124 \text{ cm} < |z| < 282 \text{ cm}$. A number of the
 841 tracker layers and endcaps hold double-sided strip modules (shown as double lines
 842 in Figure 5.8), with the rear module tilted at an angle of 100 mrad with respect to
 843 the front module, to provide a measurement in two coordinates. There are a total of
 844 15,148 modules in the tracker, arranged as shown in the longitudinal cross-sectional
 845 view of Fig. 5.8. For the TIB and TOB, the modules are arranged in straight rows



(a) BPix hit resolution in the $r \cdot \phi$ coordinate [49].

(b) BPix hit resolution in the z coordinate vs. track dip angle, showing the effect of charge sharing on resolution [50].



(c) Pixel reconstruction efficiency vs. bias voltage for a group of three wedges in FPix [51].

Figure 5.7: Pixel detector performance highlights.

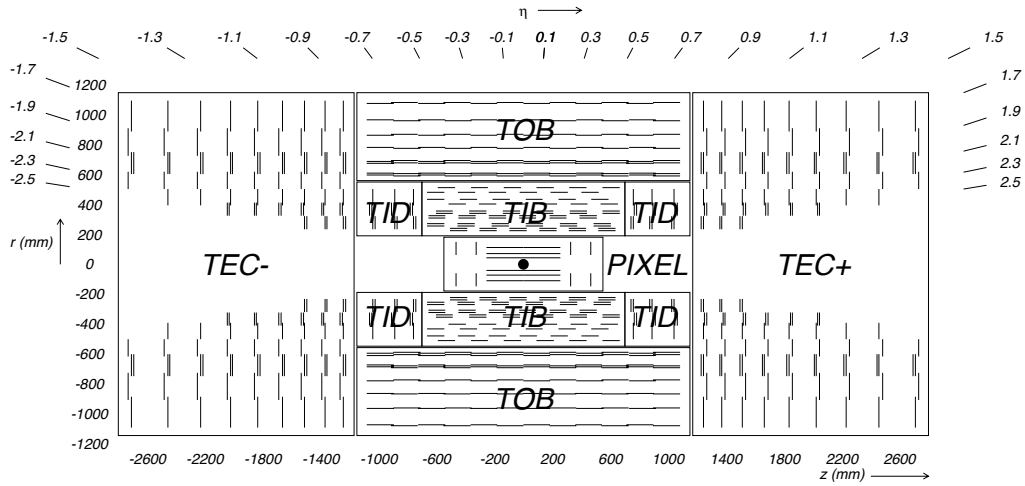


Figure 5.8: Longitudinal cross section of the silicon strip detector. Reprinted from Fig. 3.1 of ref. [45].

846 end-to-end along z , with repeating rows covering the full 2π extent in ϕ . In each of the
 847 TID disks, the modules are arranged into three concentric circular rings of increasing
 848 r . In the TEC, the modules are affixed to ϕ -wedges called *petals*. One side of the TEC
 849 and its petal structure is shown in Figure 5.9.

850 Like the pixels, the strip sensors generate a signal when current flows across a
 851 p-n junction in response to interaction with a charged particle. Whereas the pixels
 852 are n-type implants on an n-type substrate, with a solid p-type rear layer to which
 853 the high voltage is connected, the strips are p-type implants on an n-type substrate,
 854 with a solid n-type rear layer connecting to the high voltage. The p-n junction in the
 855 strip sensors is at the strip-substrate boundary, whereas in the pixel sensors it is at
 856 the boundary between the rear layer and the substrate. Each sensor has either 512
 857 or 768 electrically isolated strips, with pitch varying from 80-205 μm depending on
 858 location. Strip lengths in z range from ~ 10 to ~ 25 cm. Thin (320 μm) sensors are
 859 used in the TIB, TID, and inner four rings of the TEC, while thick (500 μm) sensors
 860 are used in the TOB and the outer rings of the TEC. The thicker sensors compensate
 861 for the increased strip capacitance (and hence electronics noise) of the longer strips
 862 in the outer layers/disk of the tracker such that strip signal:noise is maintained above

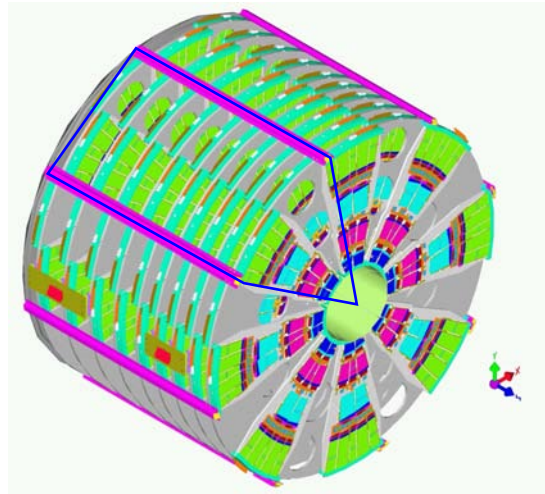


Figure 5.9: View of one tracker endcap, with the outline of a petal shown in blue. There are nine petals per wedge-shaped sector (one per TEC disk). Reprinted from Fig. 3.30 of ref. [45].

863 10 everywhere.

864 The strips are wire bonded to a front end readout chip called the APV25. The
865 APV25 amplifies and shapes the strip signals before sending the full analog pulse
866 information to an APVMUX, which multiplexes the output of two APV25s. Then,
867 the electrical signal from the APVMUX is sent differentially a few centimeters to an
868 optical driver, where it is converted to an optical signal and sent to one of the 450
869 front end drivers (FEDs). The FEDs convert the signal back to an electrical pulse
870 and digitize it for use in the global event assembly. As for the pixels, analog readout
871 is used on detector so that hit reconstruction may benefit from charge sharing.

872 Clock, trigger, and control signals are sent from the front end controllers (FECs)
873 to phase locked loop (PLL) chips on the front ends. The FECs interface to the global
874 clock and trigger system. Four or six APV25s, an APVMUX, and a PLL chip all sit on
875 a *hybrid*, two which one thin or two thick sensors are also affixed. The sensor-hybrid
876 combination and its frame form a module. Figure 5.10 shows a diagram of a module,
877 while Figure 5.11 shows a block diagram of the strip readout architecture.

878 As an example of the strip capabilities, strip hit resolution and signal:noise mea-

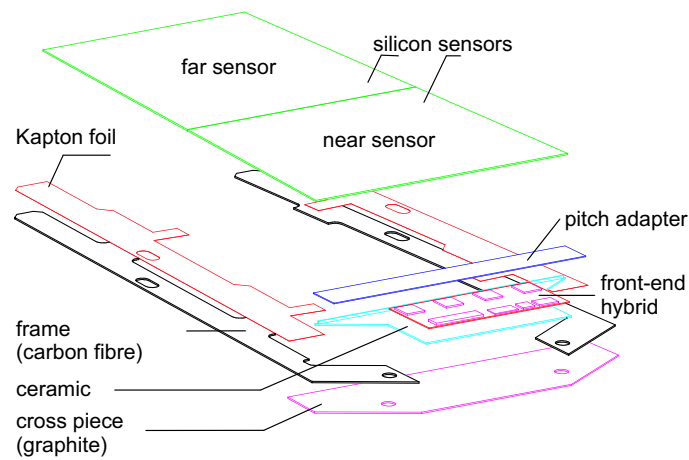


Figure 5.10: Exploded view of a strip module with two sensors. Reprinted from Fig. 3.22 of ref. [45].

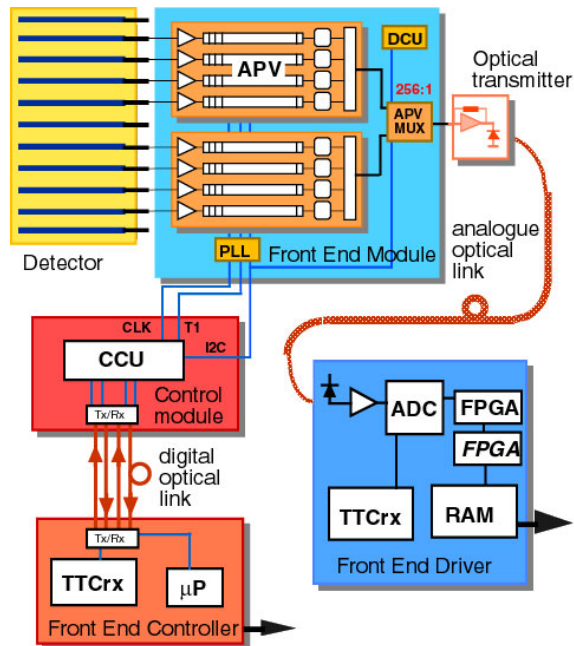


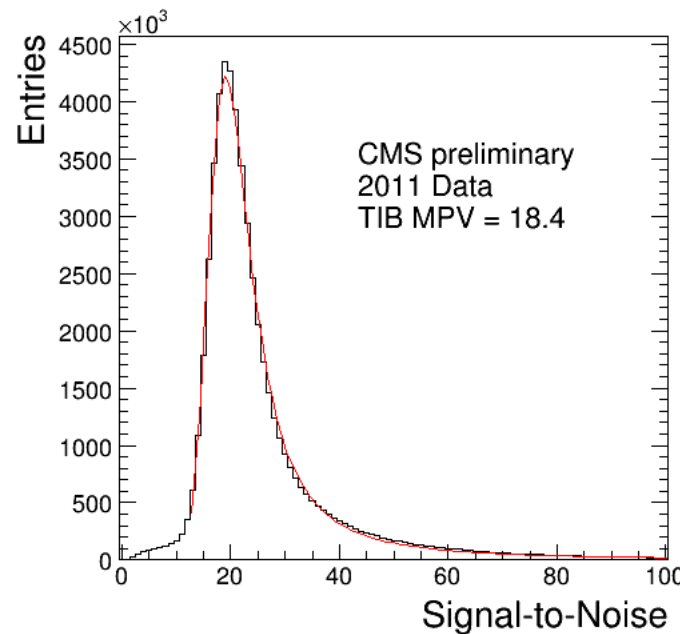
Figure 5.11: Block diagram of the strip readout architecture. Reprinted from Fig. 3.20 of ref. [45].

surements are shown in Figure 5.12. The entire pixel + strip tracker has been used successfully in the reconstruction of primary and secondary vertices, electrons, muons, tau decays, and charm and bottom hadron decays. In addition, the superior performance of the tracker over the hadronic calorimeter for low energy charged hadrons has been exploited in the the particle flow jet and \cancel{E}_T reconstruction technique (see Sec. 6.1.3). The CMS silicon strips, as well as the pixels, are well aligned and operating at close to design performance.

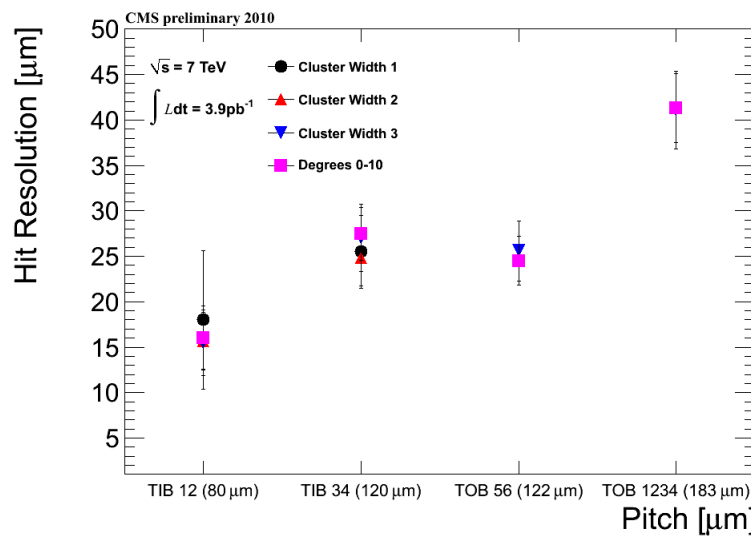
5.1.2 Electromagnetic Calorimeter

The electromagnetic calorimeter (ECAL) is composed of 68,524 lead tungstate (PbWO_4) crystals, divided into one barrel (EB) layer and two endcap (EE) disks. In EB, there are 1700 crystals per *supermodule* (SM), arranged in a 20×85 grid in $\phi \times \eta$. Two SMs are laid out end-to-end to form one row at fixed ϕ , with a total of 18 rows needed to cover the entire 2π extent in ϕ . The SMs may be operated independently. In EE, the independent unit is a wedge-shaped sector, with nine sectors covering each endcap side. The 7,324 EE crystals are divided approximately evenly between the 18 EE sectors. A two-layer preshower detector is placed in front of the EE disks, each layer consisting of a lead absorber followed by 1.9 mm pitch silicon strip detectors (the strips in the first layer are rotated 90° with respect to the second layer). The ECAL layout is shown in Figure 5.13.

The electromagnetic energy resolution can be parametrized as $(\sigma/E)^2 = (S/\sqrt{E})^2 + (N/E)^2 + (C)^2$, where S characterizes the size of photostatistical fluctuations, N characterizes the contribution from electronics noise, and C is a constant accounting for imperfect intercalibration between crystals, non-uniformity of crystal performance, and incomplete shower containment within one crystal. The design goal of the ECAL is to achieve $C = 0.5\%$. Therefore, fast, dense, and relatively radiation hard PbWO_4 was chosen as the crystal material. When a photon or electron strikes the crystal, it



(a) TIB signal:noise [52].



(b) TIB and TOB hit resolution as a function of strip pitch [53].

Figure 5.12: Strip detector performance highlights.

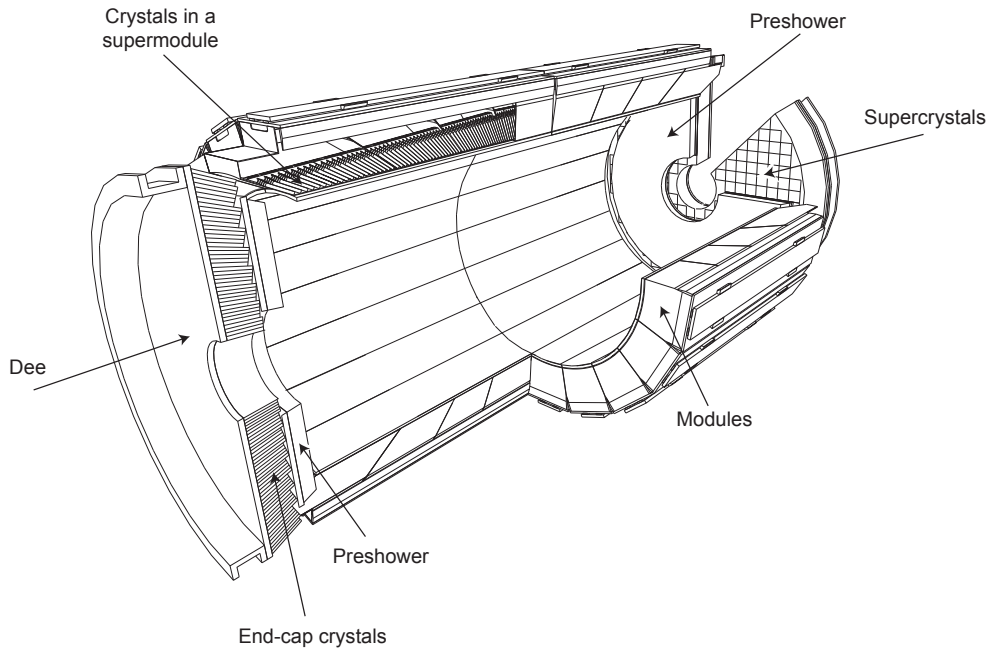


Figure 5.13: Layout of the ECAL detector. Reprinted from Fig. 4.5 of ref. [45].

905 initiates an electromagnetic (EM) shower. Due to the density, short radiation length,
 906 and small Molière radius of PbWO_4 , nearly the entirety of an EM shower can be
 907 contained in a single 23-cm long crystal with front face dimensions $2.2 \text{ cm} \times 2.2 \text{ cm}$.
 908 The crystals scintillate in the blue-green part of the spectrum, emitting $\sim 80\%$ of the
 909 scintillation light within 25 ns. Light is transmitted along the length of the crystals
 910 and collected at the rear with avalanche photodiodes (semiconductor diodes) in EB or
 911 vacuum phototriodes (conventional photomultipliers) in EE. Since the light output is
 912 low and varies with temperature, the crystals must be kept precisely at 18°C . The EB
 913 and EE crystals, which are slightly tapered to match the lateral shower development,
 914 are shown in Figure 5.14.

915 For each trigger, 10 samples, each separated by 25 ns, are read out. The 10-sample
 916 pulse is amplified and shaped by a multi-gain preamplifier (MGPA) residing on a very
 917 front end (VFE) card serving five crystals. The MGPA can switch between gains 1,
 918 6, and 12 to avoid saturation of the electronics, and affords a dynamic range up to

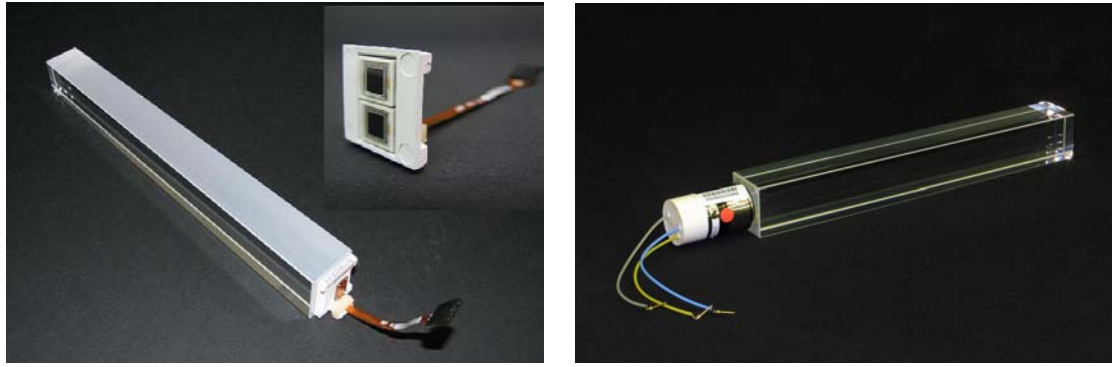


Figure 5.14: Left: EB crystal with attached APD. Right: EE crystal with attached VPT. Reprinted from Fig. 4.2 of ref. [45].

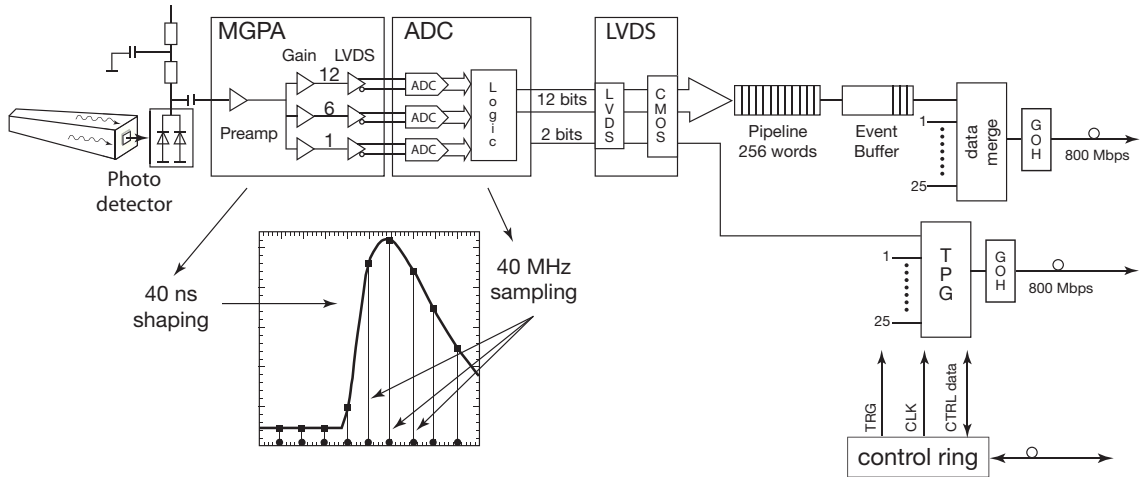


Figure 5.15: Flow chart of the crystal readout, showing the 10-sample pulse shape. Reprinted from Fig. 4.9 of ref. [45].

919 3 TeV. The samples are digitized on the VFE card, then sent to the front end (FE)
 920 card serving five VFEs. Digitized samples are buffered in the FE card until receipt
 921 of a trigger, when they are sent over an optical link to the data concentrator card
 922 (DCC) that interfaces to the global DAQ. The DCC interfaces to the *selective readout*
 923 processor, which decides whether a crystal should be read out with or without zero
 924 suppression based on its proximity to a high-energy hit. The clock is transmitted to
 925 the FE cards from the Clock and Control System (CCS) boards. A flow chart of the
 926 crystal readout is given in Figure 5.15.

At each bunch crossing, the trigger concentrator cards (TCC) of the ECAL compute *trigger primitives* from 5×5 non-overlapping transverse energy sums (in the endcaps the geometry is not always 5×5). This information, along with a special bit in EB only characterizing the transverse shower profile that is used for rejection of anomalous APD hits (see Sec. 6.1.1), is transmitted from the TCCs to the synchronization and link boards (SLBs), and then on to the global trigger system. The trigger decision is communicated to the DCCs, which request the buffered data from the front ends if the decision is affirmative.

Despite the radiation hardness of lead tungstate relative to other types of crystals, it still suffers from transparency loss due to radiation-induced lattice damage, as shown in Figure 5.16. In addition, any unforeseen change in the gains of the MGPAs and VPTs, or in the pedestal levels, will degrade the energy resolution. For this reason, a continuously running calibration system is installed with the ECAL. The system makes use of the LHC abort gaps to read out the pedestal levels, test pulses fired into the MGPAs, and laser (EB and EE) or LED (EE only) pulses fired into the crystals at regular intervals. Laser and LED events are used to compute corrections to the crystal gains for transparency loss, while the other types of calibration events serve to monitor changes in the electronics performance due to magnetic field or high voltage cycling. The mean time between transparency measurements is ~ 40 minutes. Figure 5.17 shows the architecture of the laser monitoring system.

The current ECAL energy resolution is somewhat worse than the design goal of 0.5%. An incomplete understanding of (a) the transparency loss and (b) the photon conversion and electron bremsstrahlung processes in the $\sim 1X_0$ of tracker material in front of the ECAL are the main limiting factors in improving the resolution. However, as more data accumulate, more refined models of transparency loss and EM interactions in the tracker can be built, leading to better resolution. Energy resolution vs. $|\eta|$ can be seen in Figure 5.18.

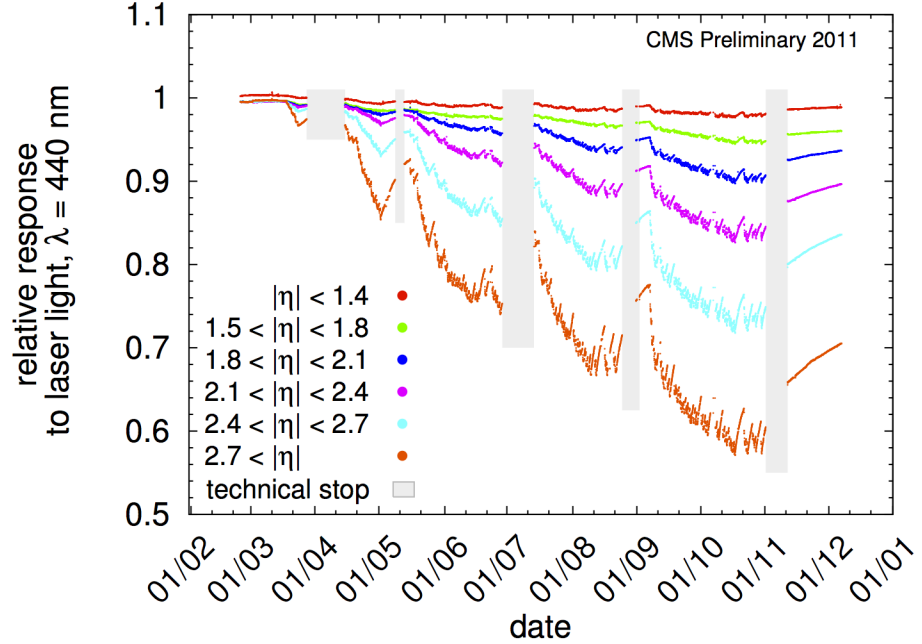


Figure 5.16: Relative response of the crystals to blue laser pulses from February 1, 2011 to January 1, 2012 [54]. Technical stops, during which the LHC is turned off for maintenance and development, are shown in gray. These periods of inactivity correspond to growth in the crystal response, as radiation damage recovery occurs.

954 The 10-sample readout coupled with the fast scintillation time of lead tungstate
 955 allows for a very precise reconstruction of the time of ECAL hits. ECAL timing is used
 956 for searches for long-lived particles that decay to photons or jets, such as long-lived
 957 neutralinos in GMSB [?]. Figure 5.19 shows the timing resolution in EE.

958 5.1.3 Hadronic Calorimeter

959 The CMS hadronic calorimeter (HCAL) has four parts: HCAL barrel (HB), HCAL
 960 endcap (HE), and HCAL outer (HO), which all utilize the same brass absorber /
 961 plastic scintillator sandwich technology; and HCAL forward (HF), which is a Čerenkov
 962 detector made of quartz fibers. A quarter longitudinal cross-sectional view of HCAL
 963 is shown in Figure 5.20. Like EB, HB is formed of 36 ϕ -wedges (18 cover 2π in positive
 964 η , 18 cover 2π in negative η). Each wedge is divided into 16 along η and four along
 965 ϕ , for a total of 64 readout towers per wedge (compare 1700 individually read out

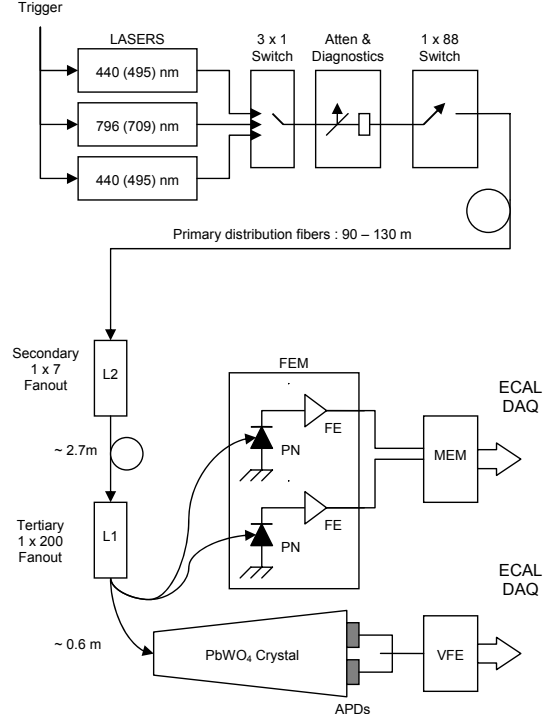


Figure 5.17: Architecture of the laser monitoring system. Reprinted from Fig. 4.16 of ref. [45].

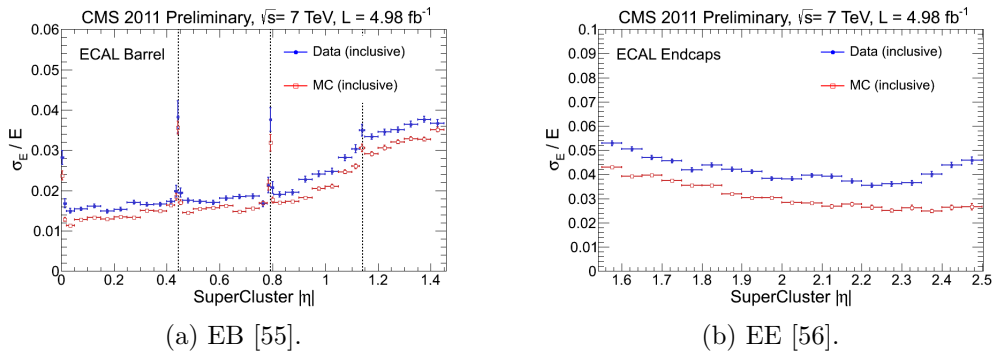


Figure 5.18: Energy resolution vs. $|\eta|$ for Z decay electrons for data (filled blue circles) and MC (empty red squares). The dotted lines show the locations of module gaps (three per SM).

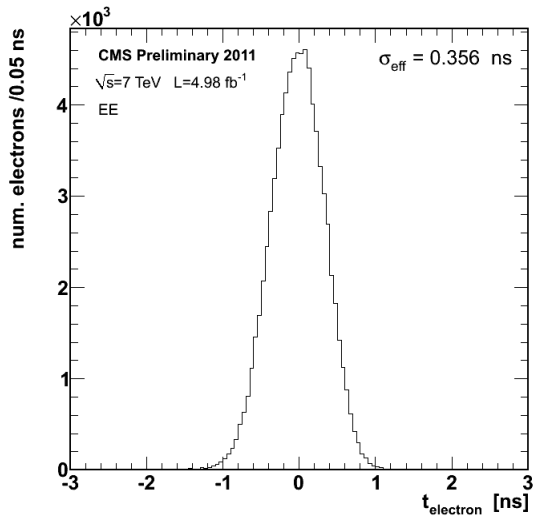


Figure 5.19: Distribution of reconstructed times of Z decay electrons in EE [57].

966 crystals per EB wedge). HE is divided into 36 ϕ -wedges containing 38 readout towers
 967 each. HO consists of five rings around HB and HE distributed symmetrically along z .
 968 There are 72 ϕ -slices per ring, with each ϕ -slice further divided into 5, 6, or 8 along
 969 z depending on ring. The HF fibers are distributed within the steel absorber. HF is
 970 divided into 18 ϕ -wedges per endcap side, each containing 24 readout towers. All HB
 971 towers have a single readout channel except for the two in each wedge at highest $|\eta|$,
 972 which are segmented into two longitudinal layers for readout. In HE, all towers have
 973 two longitudinal readout layers, except for the three rings of towers closest to the
 974 beam line, which have three. There are also two longitudinal depths of HF fibers.

975 HB, HE, and HO are all sampling calorimeters consisting of alternating layers of
 976 brass absorber and plastic scintillator. The absorber initiates the hadronic shower,
 977 and as shower particles travel through the scintillator the scintillation light is read
 978 out by wavelength-shifting (WLS) fibers connected to the scintillator tiles.² The full
 979 development of the shower is sampled by the layers of instrumented scintillator. The
 980 scintillator tiles are staggered so that there are no cracks in coverage along the direc-

²By contrast, in the ECAL, the crystal material acts as both absorber and scintillator, greatly reducing the contribution to energy resolution from sampling fluctuations.

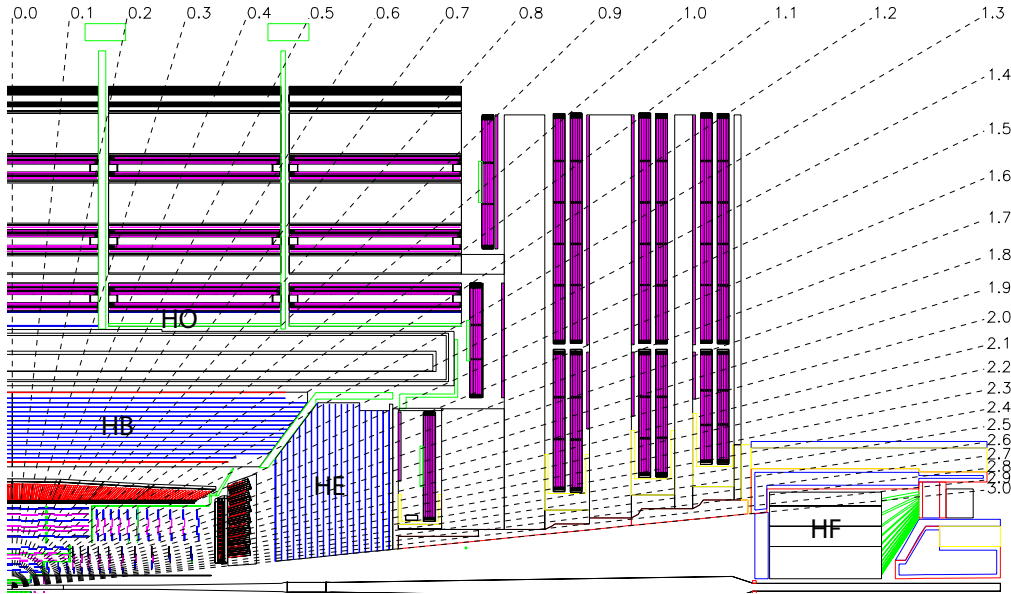


Figure 5.20: Quarter longitudinal cross-sectional view of HCAL (and muon stations in purple). Reprinted from Fig. 5.1 of ref. [45].

tion projected back to the beam spot. Light output from all tiles in a single readout tower is collected via the WLS fibers and merged into a single signal that is amplified by a hybrid photodiode (HPD). A diagram of the optical readout of HB (similar for HE and HO) is shown in Figure 5.21.

Due to the extremely harsh radiation environment near the beam line, HF is constructed of a 1.2-m thick, 1.7-m long ring of steel absorber with radiation hard quartz fibers distributed within the steel and running parallel to the beam line. Hadronic showers develop in the steel and are sampled in the quartz fibers when charged shower particles hit the the fibers and emit Čerenkov light. The light is transmitted by total internal reflection down the fibers to a photomultiplier tube (PMT), where the signals from all fibers in an HF tower are merged into one. Since only relativistic particles emit Čerenkov light in these fibers, it is mostly the EM component of the hadronic shower, consisting of neutral pions decaying to photons that interact electromagnetically with the absorber, that is sampled [58]. The charged hadrons produced in hadronic showers are typically too slow to generate Čerenkov light. Figure 5.22

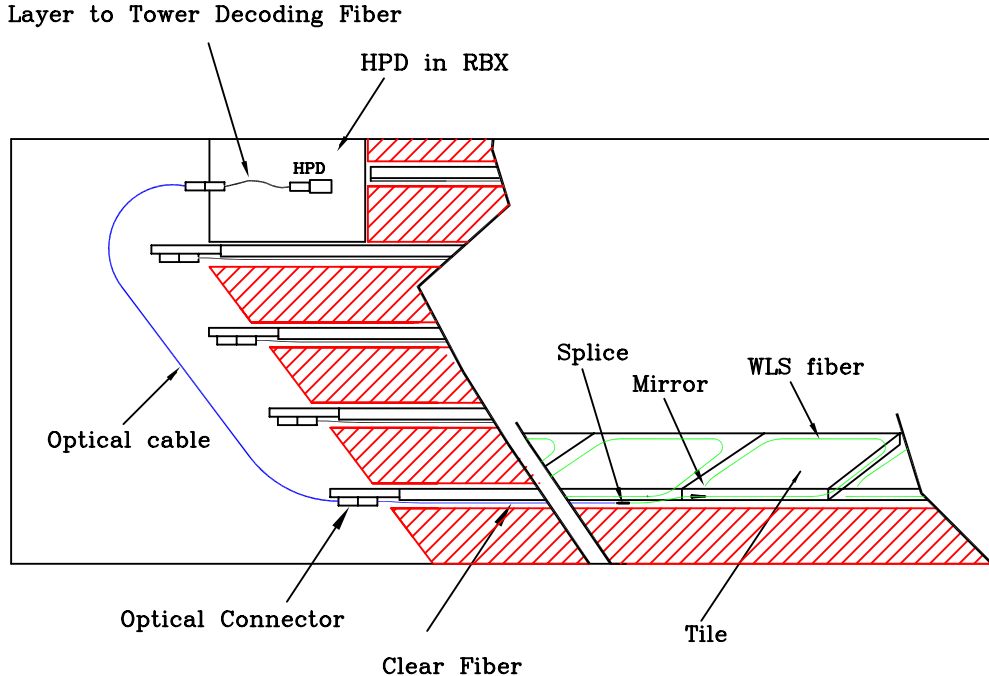


Figure 5.21: Diagram of the optical readout of HB. Reprinted from Fig. 5.7 of ref. [45].

996 shows a cross-sectional view of one side of HF.

997 Electrical signals from either HPDs (HB/HE/HO) or PMTs (HF) are digitized on
 998 the front ends by means of a fast charge-integrating ADC. The digitized signals are
 999 sent off-detector to the HCAL Trigger/Read-Out (HTR) boards, where they await a
 1000 trigger decision. If the trigger is accepted, the signals are sent on to the HCAL data
 1001 concentrator cards (DCCs), which interface to the global DAQ system. HCAL trigger
 1002 primitives, consisting of transverse energy sums over an entire tower, are calculated
 1003 in the HTR boards and sent to the global trigger system.

1004 Selected HCAL performance results can be seen in Figure 5.23.

1005 5.1.4 Muon System

1006 Beginning at a radius of ~ 10 interaction lengths from the beam line, where all parti-
 1007 cles except muons should have been stopped by the HCAL, are the muon chambers,
 1008 interspersed with the iron return yoke of the CMS magnetic field. Three technologies

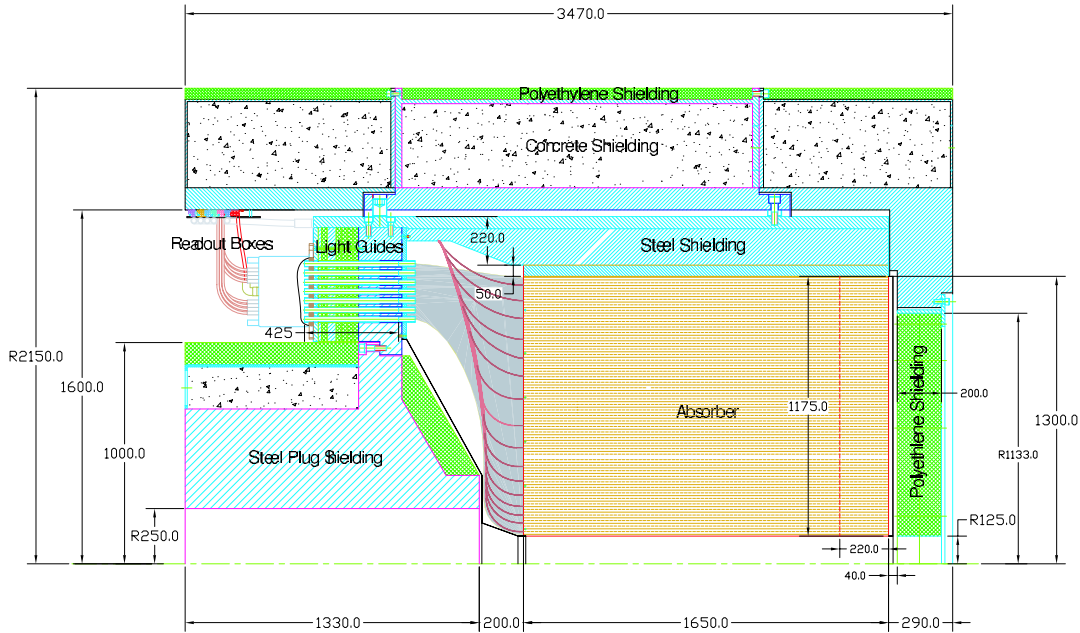
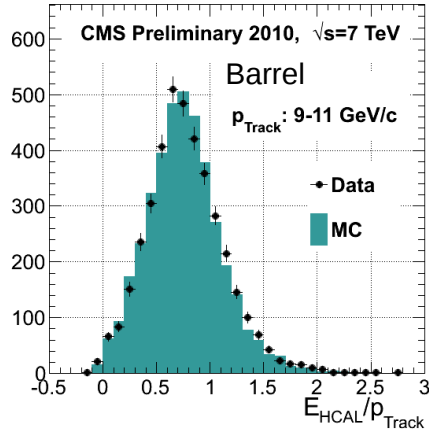


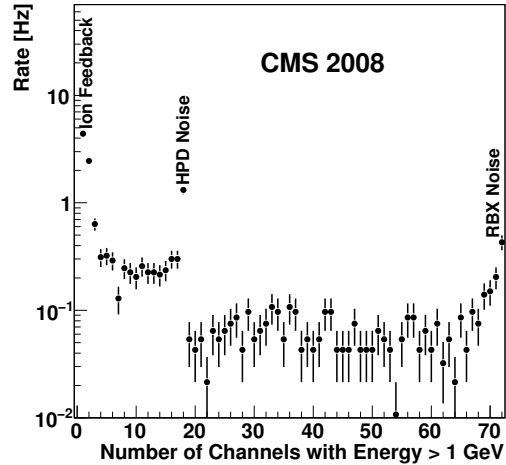
Figure 5.22: Cross-sectional view of one side of HF. The z -axis is horizontal. Reprinted from Fig. 5.28 of ref. [45].

1009 are employed: drift tubes in the barrel section (MB), cathode strip chambers (CSCs)
 1010 in the endcap section (ME), and resistive plate chambers (RPCs) in both sections to
 1011 provide an independent trigger with superior time resolution. There are four barrel
 1012 layers of stations extending out to $|\eta| = 1.2$. Each endcap consists of five disks of
 1013 stations as shown in Figure 5.24b, covering $1.4 < |\eta| < 2.4$. RPCs populate the barrel
 1014 and endcap muon systems alongside the DT chambers and CSCs. Since they have
 1015 time resolution much better than a few ns, they are used to assign the bunch crossing
 1016 of muon tracks and provide a p_T trigger with sharp turn-on.

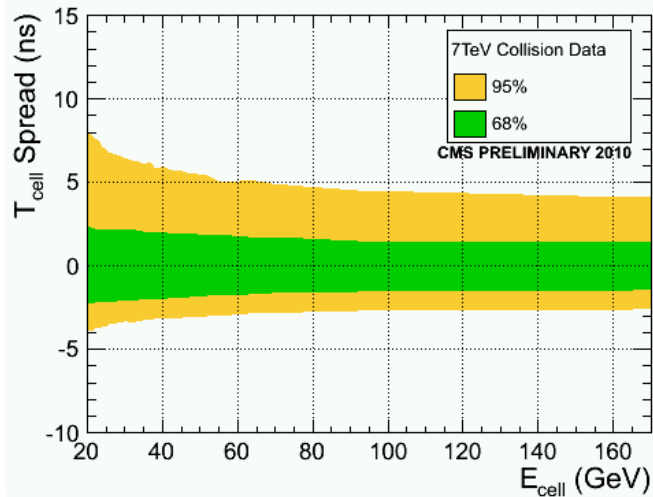
1017 Each DT chamber consists of two $r \cdot \phi$ superlayers (SLs) and optionally one z
 1018 SL (in all chambers except those in the fourth layer). The SLs contain four rows of
 1019 drift tubes, with the rows staggered such that there are no gaps in the coverage. The
 1020 $r \cdot \phi$ SLs have the tube axis parallel to the beam line, while the z SL is perpendicular
 1021 to the beam line. The tubes are ~ 2.4 m in length and $13 \text{ mm} \times 42 \text{ mm}$ in cross
 1022 section. Each chamber therefore records eight $r \cdot \phi$ tracking points and optionally four



(a) Data/MC comparison of HB response to charged tracks of 9-11 GeV/c momentum [59].

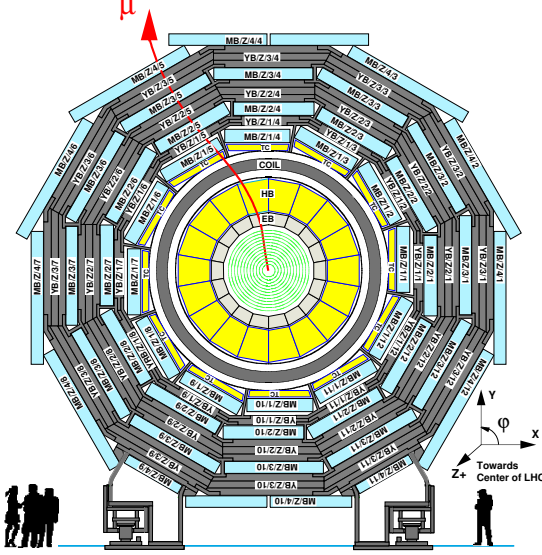


(b) Distribution of tower multiplicity, clearly showing three peaks in rate corresponding to noise sources (see Sec. 6.3) [100].

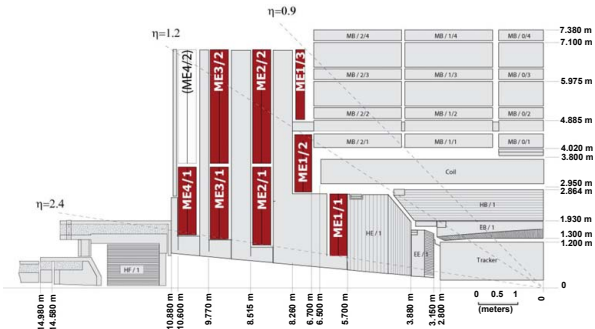


(c) Timing resolution vs. tower energy [59].

Figure 5.23: Selected HCAL performance results.



(a) One of the five wheels of MB, showing the four layers of muon stations. The five wheels are spaced symmetrically in z about $z = 0$. As a muon traverses the muon detectors, its curvature in the transverse plane changes direction and magnitude due to the magnetic field in the return yoke, which is of opposite sign and reduced strength relative to the field within the solenoid volume. Reprinted from Fig. 7.3 of ref. [45].



(b) Quarter longitudinal cross section of CMS highlighting the location of the ME disks. Reprinted from Fig. 7.47 of ref. [45].

Figure 5.24: View of the MB and ME layout in CMS.

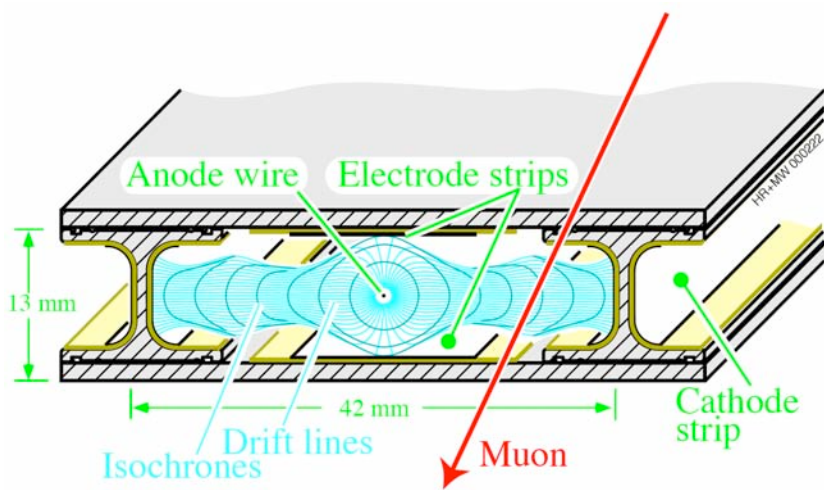


Figure 5.25: Electric field lines within a drift tube as well as the contours of equal drift time. Reprinted from Fig. 7.5 of ref. [45].

1023 z tracking points. The tubes are filled with an 85%Ar + 15% CO₂ gas mixture. An
 1024 anode wire at 3600 V runs the length of the tube, while the walls are covered with
 1025 electrodes held at 1800 V or -1200 V depending on wall. When a muon passes through
 1026 the tube, it ionizes the gas atoms. The liberated electrons drift along the electric field
 1027 lines created by the electrodes to the anode, which is read out. Figure 5.25 shows
 1028 the electric field lines within a drift tube as well as the contours of equal drift time.
 1029 The maximum drift time is 380 ns.

1030 CSCs consist of alternating layers of cathode strips (four planes oriented along r)
 1031 and anode wires (three planes oriented along ϕ). A 40%Ar + 50%CO₂ + 10%CF₄ gas
 1032 mixture fills the space between two successive planes, forming six gas gaps. When a
 1033 muon ionizes the gas atoms, the positive ions drift toward the anode and are read
 1034 out to provide a measurement of r , just as in the DTs. However, an image charge is
 1035 induced on the cathode strips, which is also read out to provide a measurement of ϕ .
 1036 The wires are spaced 3.2 mm apart. The cathode strips have pitch varying from 8.4
 1037 mm at the end closest to the beam line to 16 mm at the other end, and are spaced
 1038 0.5 mm apart. A trapezoidal CSC is shown in Figure 5.26.

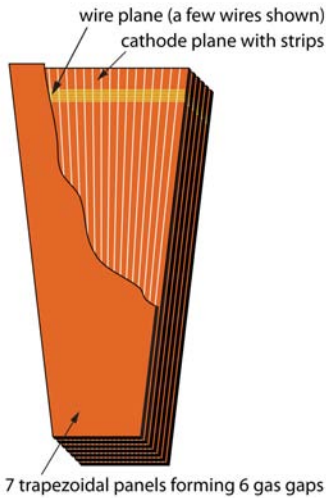


Figure 5.26: CSC wedge, showing the cathode and wire planes. Reprinted from Fig. 7.49 of ref. [45].

1039 Track stubs from the muon system are combined with tracks from the tracking
 1040 system to form more precise muon tracks than either system could form alone, as
 1041 shown in Figure 5.27. This leads to extremely good di-muon invariant mass resolution
 1042 (Figure 5.28) over a large p_T range.

1043 **5.2 Triggering, Data Acquisition, and Data Trans-** 1044 **fer**

1045 **5.2.1 Level 1 and High Level Trigger Systems**

1046 The Level-1 (L1) trigger system, which encompasses dedicated hardware processors
 1047 to construct trigger objects (typically high p_T jets, electrons, photons, taus, and
 1048 muons) out of the calorimeter and muon hits, distributes a L1 accept or reject to all
 1049 subdetectors at the LHC bunch crossing frequency of 40 MHz. Further data filtering
 1050 is performed by the High Level Trigger (HLT) system, a farm of ~ 1000 commercially
 1051 available processors running a slimmed down version of the CMS event reconstruction

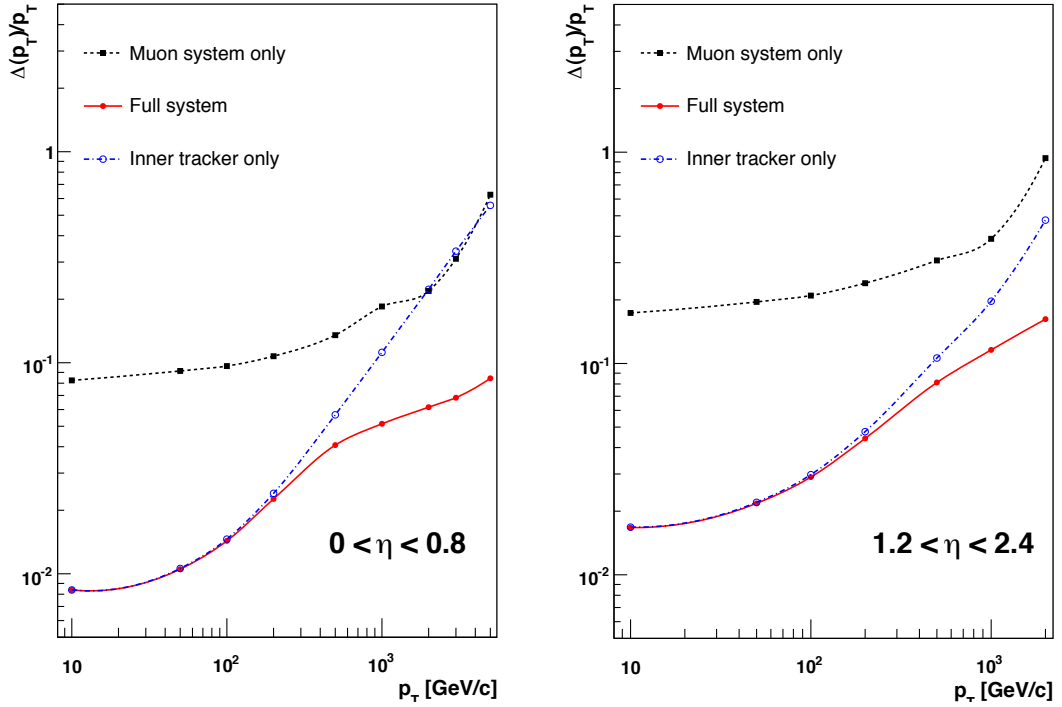


Figure 5.27: Muon p_T resolution as a function of muon p_T for tracker information only (blue), muon information only (black), and both tracker and muon information combined (red). Reprinted from Fig. 1.2 of ref. [45].

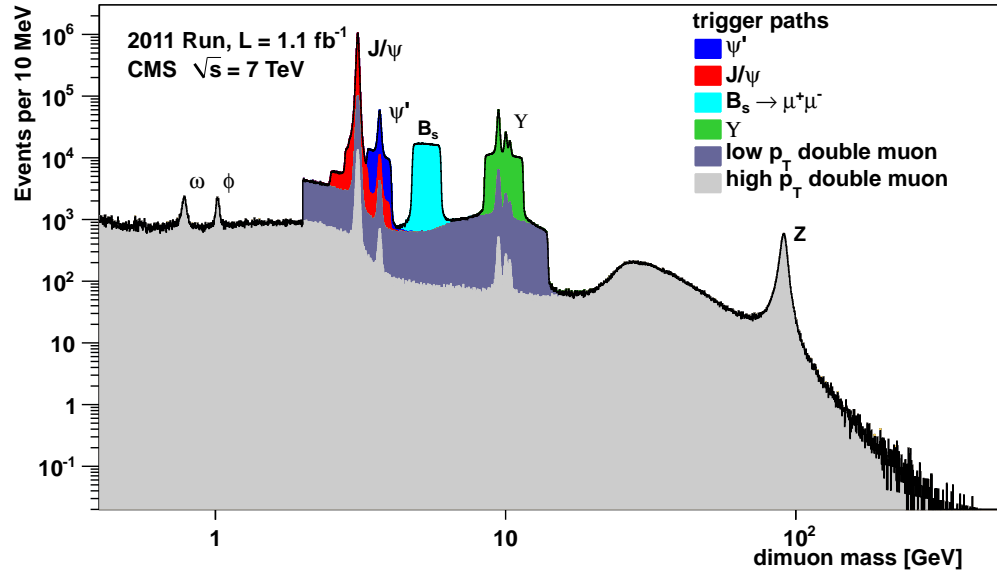


Figure 5.28: Di-muon invariant mass spectrum broken down by trigger path [60]. The light(dark) gray regions show the contribution from high- p_T (low- p_T) di-muon triggers. Note that no $B_s \rightarrow \mu^+\mu^-$ decays have been observed [61]; the light blue region just shows the amount of triggers dedicated to the $B_s \rightarrow \mu^+\mu^-$ search.

1052 software CMSSW. The data rate received by the HLT is ~ 100 kHz; the output rate of
 1053 events permanently written to disk is ~ 100 Hz. An L1 trigger *latency* (time between
 1054 the collision and the distribution of the L1 decision to the subdetectors) of $3.2\ \mu\text{s}$ is
 1055 achieved via the use of fast electronics and sufficiently deep buffers to pipeline trigger
 1056 primitives waiting to be analyzed. This latency corresponds to the length of the LHC
 1057 abort gap, so in principle CMS may be operated with zero *dead time* (during which
 1058 LHC bunches are missed because the L1 system is blocked while processing other
 1059 triggers).

1060 At the bottom, the L1 trigger consists of trigger primitive generators (TPGs) in
 1061 the calorimeter and muon systems that send E_T sums or muon track stubs to the
 1062 regional calorimeter trigger (RCT) or muon track finders, respectively. The EB TPG
 1063 also sends a *fine grain veto bit* [63], which encodes information about the EM shower
 1064 pattern in the 5×5 array of crystals, and is used to reject anomalous signals (see
 1065 Sec. 6.1.1). The RCT, DT track finder (DTTF), and CSC track finder (CSCTF) sort
 1066 and rank the regional trigger primitives based on p_T and quality. The ranked RCT
 1067 candidates and muon track stubs are sent to the global calorimeter trigger (GMT)
 1068 and global muon trigger (GMT), respectively, where high-level objects like isolated
 1069 and non-isolated muons and EM candidates, jets, taus, and \cancel{E}_T are constructed from
 1070 all the regional inputs and ranked. Calorimeter isolation sums for muons are also
 1071 sent from the RCT to the GMT. The highest ranked global objects are sent to the
 1072 global trigger (GT), which sits at the top of the L1 trigger. The GT issues the final
 1073 L1 accept or reject to all subdetectors based on a comparison of the GMT and GCT
 1074 candidates with the requirements of its programmed trigger menu. A block diagram
 1075 of the L1 trigger is shown in Figure 5.29.

1076 A region in the RCT consists of a matrix of 4×4 trigger towers. A trigger tower
 1077 in EB/HB is one HCAL tower + the 5×5 matrix of ECAL crystals in front of it;
 1078 in EE/HE the idea is similar but the counting of crystals and HE towers is slightly

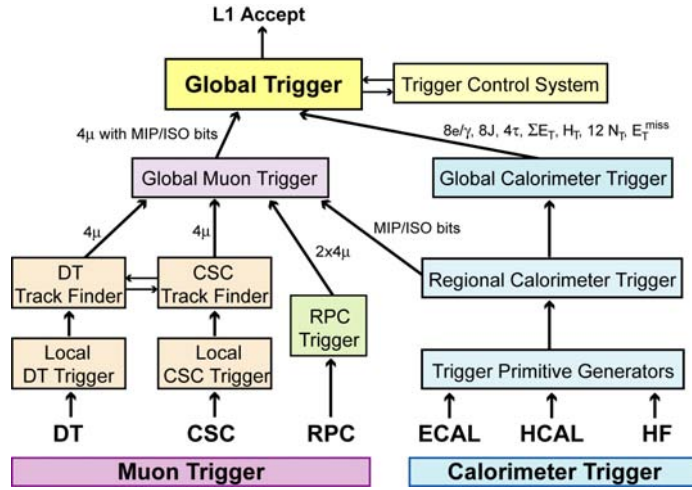


Figure 5.29: Block diagram of the L1 trigger. Reprinted from Fig. 8.1 of ref. [45].

more complicated. An EM RCT candidate is built around a high E_T seed tower. The E_T of the candidate is the sum of the tower E_T and the E_T of its highest- E_T broad side neighbor (see Figure 5.30 for a definition of the broad side neighbors). Two isolation criteria are defined based on (a) the ratio of the EM energy to the HCAL energy in the tower and (b) the shower shape. For a non-isolated EM candidate, the highest- E_T broad side neighboring tower must pass these two isolation criteria; for an isolated EM candidate, all eight neighboring towers must pass the criteria, and there must also be at least one quiet corner with the E_T of all five towers in the corner below some threshold (see Fig. 5.30). The process is repeated until four isolated and four non-isolated EM candidates are found, starting with the highest- E_T tower in the region and moving down in tower E_T . An RCT region is flagged as consistent with tau decay only if the pattern of tower transverse energy sums defines at most a 2×2 matrix of energetic towers within the 4×4 RCT region.

From the tower transverse energy sums, eight EM candidates, and tau flag received from each RCT, the GCT computes the total E_T in the calorimeter (and the total E_T above some programmable threshold, called H_T), and the \cancel{E}_T . It also classifies the towers into jets and determines the globally highest ranked isolated and non-isolated

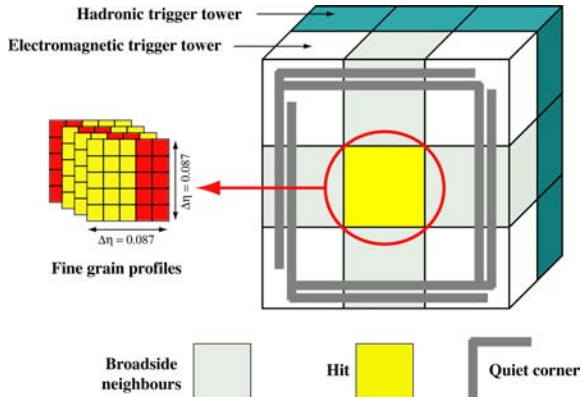


Figure 5.30: Geometry of an EM RCT candidate. Reprinted from Fig. 8.2 of ref. [45].

1096 EM candidates. The jet finding uses a clustering algorithm based on the energy of a
 1097 sub-cluster with respect to its neighbors [62]. Jets are classified as tau decays if all
 1098 of the RCT regions participating in the jet clustering had energy patterns consistent
 1099 with tau decay. Counts of jets above 12 different programmable E_T thresholds are
 1100 calculated. The jet counts, energy sums, E_T , and highest ranked EM candidates
 1101 are sent to the GT, where the final L1 decision is taken and transmitted to the sub-
 1102 detectors. The GT can execute a maximum of 128 trigger algorithms in parallel. If
 1103 any one of these algorithms yields an accept, the event is accepted, and all trigger
 1104 information is sent on to the HLT for further filtering. The double-photon HLT paths
 1105 used in this analysis (see Sec. 6.2) require isolated L1 seeds (i.e. EM candidates built
 1106 by the RCT) with $E_T > 12$ or 20 GeV, depending on path.

1107 No muon triggers are used in the two-photon analysis. A description of the muon
 1108 trigger system can be found in ref.[45].

1109 5.2.2 Data Acquisition System

1110 The CMS data acquisition (DAQ) system takes event fragments (calorimeter hits,
 1111 track hits, etc.) from each of the 626 subdetector front end drivers (FEDs), assembles
 1112 them into a data structure representing the full event, and sends the event on to

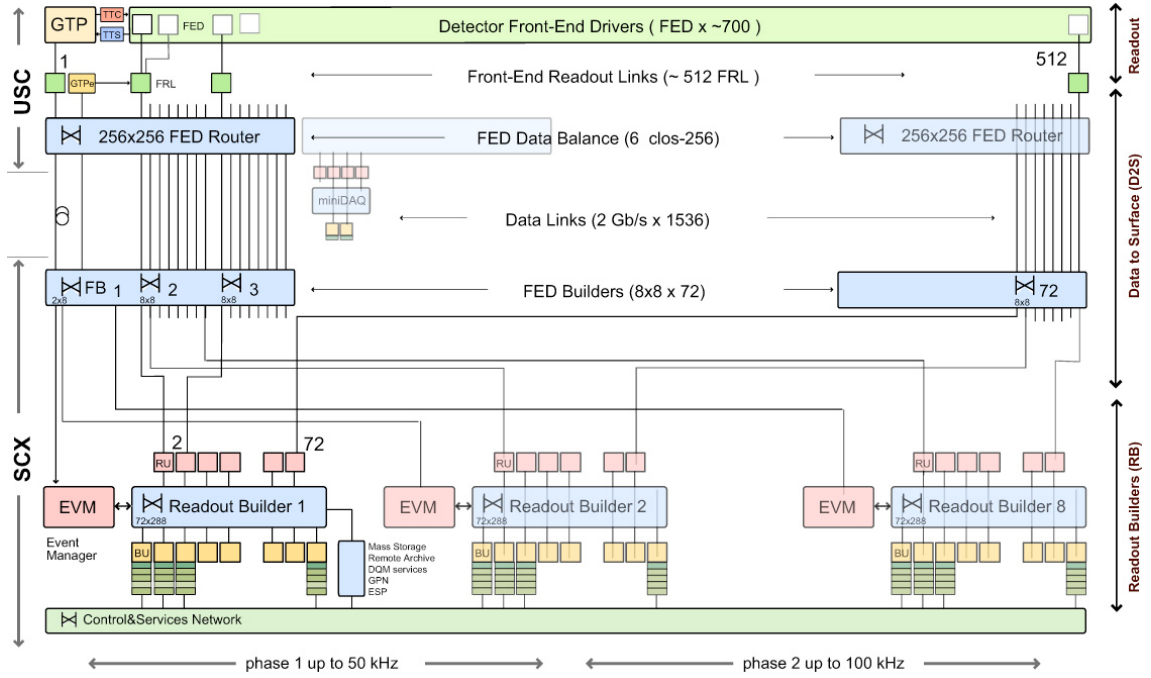


Figure 5.31: Diagram of the DAQ system. The identical event builder systems, shown as inputs and outputs to the boxes labeled “Readout Builder 1”, “Readout Builder 2”, etc., represent the eight slices. Within one slice, data can flow from the detector front ends to the readout systems to the builder network (which assembles the event fragments) to the filter systems (HLT) independently of the other slices. Reprinted from Fig. 9.8 of ref. [45].

the HLT for further filtering. The DAQ must operate at an input rate of ~ 100 GB/s, corresponding to an input rate from the L1 trigger of ~ 100 kHz. To facilitate expansion of the system as the need arises, the DAQ is composed of eight nearly independent slices. Each slice functions as a smaller version of the whole DAQ that can handle an input event rate up to ~ 12.5 kHz. A diagram of the DAQ system, showing schematically the eight slices, is given in Figure 5.31.

Data from the front ends is collected by the FEDs and pushed to the front end readout links (FRLs), which may take inputs from up to two FEDs simultaneously. The FRLs check for transmission errors, generate event fragments with size ~ 2 kB, buffer the fragments in 64 kB memories, and finally send them to the FED builders. The FEDs, FRLs, and FED builders are located in the underground control room.

1124 The 72 FED builders each construct one ~ 16 kB *super-fragment* from the input
 1125 event fragments, then send the super-fragment on to a readout unit (RU) located in
 1126 the surface control room ~ 80 m away. Super-fragments belonging to the same event
 1127 are sent to RUs in the same DAQ slice. There are 72 RUs per readout builder, one
 1128 for each super-fragment of an event, with each DAQ slice built around one readout
 1129 builder (see Fig. 5.31). Each readout builder hosts a number of builder units (BUs)
 1130 that perform the final integration of super-fragments into complete events.

1131 Resource brokers (RBs) in the HLT filter farm request complete events from the
 1132 BUs and distribute those events to the filter units (FUs) for HLT selection. If an
 1133 event passes any one of the HLT paths in the predefined menu, it is sent back to
 1134 the RB for transfer to the storage manager (SM). The SM nodes transfer accepted
 1135 events to the CERN Tier-0 prompt reconstruction facility for unpacking of the raw
 1136 data into ROOT [64] files that can be accessed by physicists wishing analyze the data.
 1137 The lag time between recording of an event in the DAQ and availability of the fully
 1138 reconstructed event for analysis is typically 48 hours.

1139 If the buffers of the upstream DAQ elements (the filter farm, readout builders,
 1140 FED builders, or FRLs) are full, those elements will not request new events from
 1141 downstream. This can lead to a buildup of events in the downstream element buffers,
 1142 *back-pressuring* all the way down to the FEDs themselves. The CMS trigger throttling
 1143 system (TTS) consists of dedicated lines between the FEDs and the GT for the
 1144 purpose of sending predefined signals to the GT about the state of the FED buffers.
 1145 If the buffer of a particular FED is getting full, it can alert the GT to reduce the
 1146 trigger rate so as to prevent FED buffer overflows and loss of time synchronization
 1147 between event fragments. The TTS latency is $\sim 1\mu\text{s}$. Causes of back-pressure (hence
 1148 dead time) include: problems with the FED electronics (in this case, the upstream
 1149 elements request events but the FEDs have trouble sending them), increases in the
 1150 L1 accept rate (perhaps due to a noisy detector channel) beyond what the upstream

1151 DAQ elements can handle, increases in the event size due to high pileup or a poor
 1152 quality beam that scrapes against the beam pipe, failures of the DAQ transmission
 1153 lines or DAQ hardware such that events are not requested from the FEDs fast enough,
 1154 or bottlenecks at the SM nodes or filter farm due to hardware failures or large event
 1155 sizes.

1156 All components of the DAQ, from the FEDs up to the SMs, are controlled by
 1157 cross-platform DAQ (XDAQ) [65] processes, or *executives*. The Simple Object Access
 1158 Protocol (SOAP) [66] protocol is used to transmit control and monitoring data be-
 1159 tween XDAQ-enabled devices and to the end user, who can view the running of a
 1160 XDAQ executive via a Web interface called HyperDAQ [67]. The Run Control and
 1161 Monitoring System (RCMS) handles the configuration and control of all XDAQ exec-
 1162 utives via a hierarchical structure. At the top of the hierarchy is the Level-0 *function*
 1163 *manager* (FM), controlling the Level-1 sub-detector FMs, which in turn control their
 1164 Level-2 system-specific XDAQ executives. The central DAQ and L1 trigger each have
 1165 their own Level-1 FM. A unit of data acquisition, called a *run*, may be configured,
 1166 started, and stopped by an end user interacting with the RCMS Web interface.

1167 5.2.3 Data Processing and Transfer to Computing Centers

1168 Data leaving the filter farm are grouped into datasets based on HLT path, i.e. there
 1169 are different datasets for events passing diphoton triggers, jet triggers, muon + elec-
 1170 tron triggers, etc. At the Tier-0 facility, the datasets go through three levels of
 1171 processing to create three *data tiers*. The first layer produces RAW data by unpack-
 1172 ing the detector byte streams sent from the DAQ and L1 trigger into data structures
 1173 holding the ADC counts recorded for each channel of the detector, digitized trigger
 1174 primitives, and the L1 decision. A single event has ~ 1.5 MB of RAW data. The next
 1175 layer of processing is the reconstruction, which forms channel energies in GeV, ap-
 1176 plies calibrations, and creates high-level objects like photons, electrons, muons, taus,

jets, E_T , and charged tracks. The RECO data tier occupies ~ 0.5 MB per event.
 Finally, analysis object data (AOD) is a subset of the RECO data, comprising the
 high-level objects but usually excluding the individual channel hit information if it is
 not associated to a physics object. This tier occupies ~ 0.1 MB per event. One copy
 of the RAW data is stored permanently at CERN and another copy is distributed
 amongst the Tier-1 facilities (see below) for permanent storage. Changes in the re-
 construction algorithms periodically require reprocessing of the RAW data to form a
 new RECO tier. In general, only the AOD tier is available to physicists wishing to
 perform analyses due to the smaller size and faster replication and transfer time of
 AOD with respect to RAW or RECO.

There are three tiers of computing and data storage sites within the Worldwide
 LHC Computing Grid (WLCG) [68]. The tier closest to CMS is Tier-0, which is
 located at CERN and performs archiving of the RAW data, prompt reconstruction
 of the data within ~ 48 hours of its being collected, and transferral of copies of the
 RECO datasets to Tier-1 facilities. There are a few Tier-1 centers worldwide, hosted
 by national computing facilities and laboratories. They store parts of the RAW dataset
 and copies of the RECO datasets, participate in subsequent reconstruction passes
 after the prompt reconstruction at Tier-0, and ship AOD datasets upon request to the
 Tier-2 centers. Analysts interact primarily with the Tier-2 centers, which store AOD
 datasets and run batch processing queues for running analysis jobs over the datasets.
 Different layers of WLCG software control data transfer between sites, data storage,
 and batch processing. A diagram of the WLCG tier system is given in Figure 5.32.

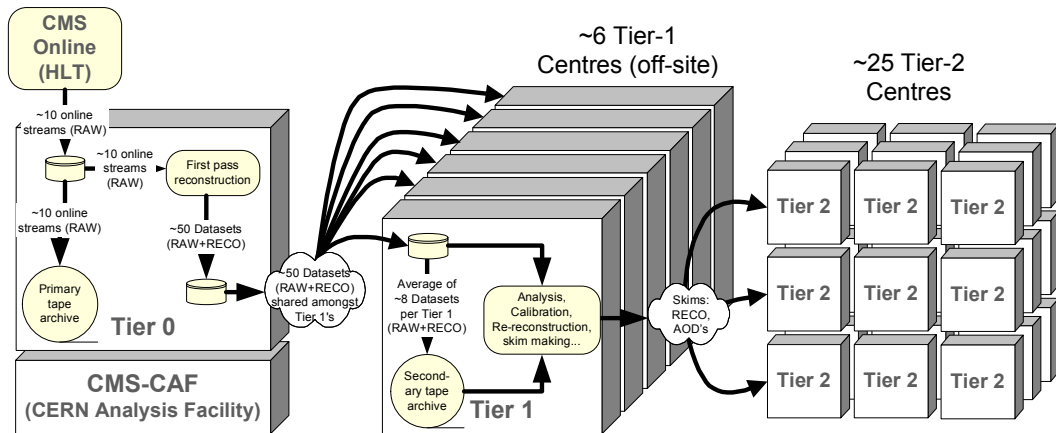


Figure 5.32: Diagram of the WLCG tier system showing data archival and reconstruction at each tier along with data transfer between tiers. Reprinted from Fig. 11.2 of ref. [45].

1199 **Chapter 6**

1200 **Event Selection**

1201 In keeping with the phenomenology described in Sec. 3.5, the candidate GGM events
1202 selected in this search consist of two high- E_T photons and a significant momentum
1203 imbalance transverse to the beam, indicating the production of an escaping gravitino.
1204 This momentum imbalance is usually referred to as *missing transverse energy* and is
1205 denoted by the symbols \cancel{E}_T or ME_T . The GGM signature is shown in Figure 6.1.

1206 However, in order to use real CMS data (as opposed to simulation) to derive
1207 predictions for the backgrounds to the search, *control samples* that are not expected
1208 to contain any GGM signal events and are distinct from the *candidate* two-photon
1209 sample must be collected from the LHC data. These samples consist of different
1210 numerical combinations of photons, electrons, and jets, and are explained in more
1211 detail in Chapter 7. Since this search is performed in the high- E_T tail of the \cancel{E}_T
1212 distribution, where adequate detector simulation is very difficult, it is advantageous
1213 to use *data-driven* background estimates, which capture the true detector response,
1214 over numbers derived from simulation.

1215 In the following sections, the reconstruction of photons, electrons, jets, and \cancel{E}_T
1216 is explained. Sec. 6.1 begins with an explanation of the high level reconstruction.
1217 It is followed by Sec. 6.2, which describes the triggers used to collect the candidate

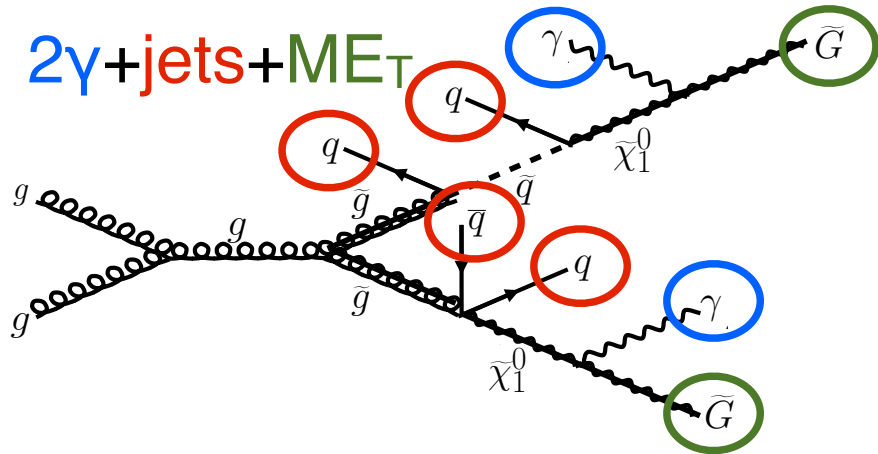


Figure 6.1: Two gluinos each decay via $\tilde{\chi}_1^0 \rightarrow \gamma \tilde{G}$.

and control samples. Sec. 6.3 describes event cleaning cuts that are applied to the candidate and control samples. Finally, the chapter concludes with a measurement of the photon identification efficiency in Sec. 6.4.

6.1 Object Reconstruction

This section describes the *offline* object reconstruction, i.e. the reconstruction of particle objects from events that have already been triggered and written to permanent storage, as opposed to the building of trigger objects explained in Secs. 5.2.1 and 6.2.

6.1.1 Photons

Uncalibrated EB/EE Hits

Photon reconstruction begins with the ADC count value for each of the 10 recorded time samples per ECAL crystal per trigger. To construct an *uncalibrated hit*, the gain (1, 6, or 12; see Sec. 5.1.2) of each sample is determined and the ADC count value scaled appropriately. The pedestal is estimated from the average of the first three samples, which, for a properly timed in hit, should contain no signal. This

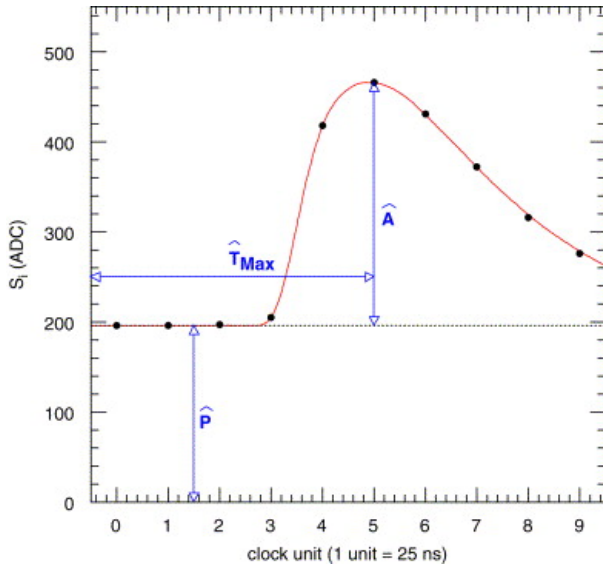


Figure 6.2: Typical ECAL channel pulse shape. \hat{P} is the pedestal value, \hat{A} is the pulse amplitude, and \hat{T}_{\max} is the hit time. The red line is the assumed pulse shape from which the weights are derived. Reprinted from ref. [69].

pedestal value is subtracted from the rest of the samples. Finally, the amplitude of the pulse is reconstructed using a predetermined weight for each sample [69]. The weights correspond to the pulse shape expected from the MGPA and shaping circuit response. The time of the hit is also reconstructed using the ratios between neighboring time samples [70]. A typical ECAL channel pulse shape is shown in Figure 6.2.

Calibrated EB/EE Hits

In the next phase of the photon reconstruction, calibrations are applied to the uncalibrated hits to form *calibrated hits* with energy measured in GeV. Channels are excluded from seeding calibrated hits if

- they are excessively noisy,
- they are stuck in fixed gain (i.e. the MGPA gain does not change properly to avoid saturation),
- they are totally dead,

- 1245 • they have one or more neighboring dead channels, or
 1246 • they do not have good trigger primitives (i.e. trigger primitive is missing, satu-
 1247 rated, or *spike-like*; cf. Secs. 5.1.2 and 5.2.1).

Added

1248 *ECAL spikes* are hits in which low energy protons and heavy ions from jets ionize this
 1249 in the sensitive volume of the EB APD (Sec. 5.1.2), causing the APD to register a para-
 1250 fake large-amplitude hit. Because they are not the result of a real electromagnetic graph
 1251 shower, spikes tend to be isolated. They may also appear to arrive early or late with and the
 1252 respect to the nominal bunch crossing. Most spikes are reconstructed with a hit time next
 1253 ~ 10 ns earlier than real EM hits because unlike real hits, whose pulse shapes include about
 1254 the time constant associated with crystal scintillation, the reconstructed spikes only spikes
 1255 involve the rise time of the electronics. There also is a long tail of late arriving spikes
 1256 due to slow neutrons from jets [71].

1257 Because of their particular timing and topological characteristics, cuts have been
 1258 developed to effectively identify and reject spike-like hits. This analysis utilizes both
 1259 the “Swiss cross” cut $1 - E_4/E_1 > 0.95$, where E_1 is the energy of the spike candidate
 1260 crystal and E_4 is the sum of the energies in the four crystals whose edges are next to
 1261 the four edges of the spike candidate crystal, and a timing cut $t \geq 3$ ns, to flag spikes.
 1262 More information about these cuts can be found in ref. [71]. A simpler algorithm
 1263 using the fine grain veto bit of the ECAL L1 TPG (Sec. 5.2.1) is used to reject spikes
 1264 at the trigger level.

1265 In addition to the trigger primitives, no uncalibrated hits that are spike-like are
 1266 eligible for calibration. The calibrations applied are corrections to account for crystal
 1267 transparency and VPT photocathode loss (leading to signal loss), measured continu-
 1268 ously by the laser/LED system; energy intercalibrations (relative energy calibration
 1269 between crystals); absolute scale calibrations between ADC counts and GeV;¹ and

¹The ADC-GeV scale factors (one for EB and one for EE) are defined such that the sum of fully calibrated and scaled hits in a particular 5×5 cluster of crystals (plus the associated energy deposited in ES) is 50 GeV for a 50 GeV incident unconverted photon [72].

1270 time intercalibrations (relative time calibration between crystals).

1271 The ECAL crystals were pre-calibrated before installation in CMS using labora-
 1272 tory light yield and photodetector gain measurements [73]. In addition, some EB and
 1273 EE crystals were intercalibrated using test beams [74], and all EB crystals were inter-
 1274 calibrated with cosmic ray muons [75]. EE precalibrations were validated with LHC
 1275 *splash events* in 2009 [75, 76], in which the beam was dumped onto a collimator ap-
 1276 proximately 150 meters upstream of CMS, causing a spray of muons to enter CMS at
 1277 one endcap and exit at the other. Splash events were also used to derive time intercal-
 1278 ibration constants. Before colliding beam operations commenced, the intercalibration
 1279 precision was estimated to be 0.5%-2.2% in EB and 1%-5% in EE [77].

1280 Three calibration methods were employed once colliding beam operations began:

- 1281 • ϕ symmetry relative calibration between crystals, exploiting the azimuthal sym-
 1282 metry of CMS
- 1283 • π^0 and η relative calibration between crystals, using the diphoton decays of
 1284 these particles
- 1285 • E/p absolute calibration, comparing the momentum measured in the tracker p
 1286 to the energy measured in the ECAL E of a sample of electrons from Z decay

1287 By September 2011, the intercalibration precision in EB was measured to be be-
 1288 tween 0.3% and 1.1% using the π^0/η method [78]. Figure 6.3 shows the improvement
 1289 in Z reconstruction from pre-LHC calibration constants to the latest π^0/η -derived
 1290 constants.

1291 Calibrated ES Hits

Added

1292 ES calibrated hits are formed from the three samples read out per sensor. Just as in the paren-
 1293 case of EB/EE crystals, ES uncalibrated hits are gain-adjusted, pedestal-subtracted, thetical
 1294 remark

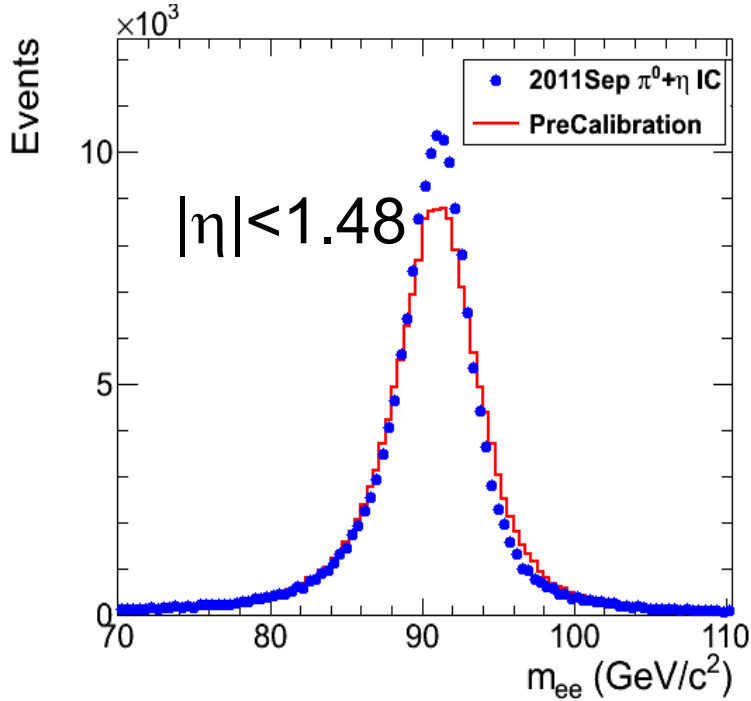


Figure 6.3: Z peak reconstructed using pre-LHC calibration constants (red) or September 2011 π^0/η -derived intercalibration constants (blue). Reprinted from ref. [78].

1294 and reconstructed using weights. To make a calibrated ES hit, intercalibration con-
 1295 stants, angle correction constants (for the non-uniformity of sensor angle with respect
 1296 to the vertical across ES), and a MIP-GeV absolute scale factor are applied.

1297 **Clustering**

1298 After calibrated ECAL hits are formed, they must be clustered into shapes that
 1299 represent the energy deposit from a single particle. *Basic clusters* are formed around
 1300 seed hits, defined as a hit that

- 1301 • has calibrated $E_T > 1(0.18)$ GeV in EB(EE),
- 1302 • does not originate from a dead channel or one with faulty hardware,
- 1303 • is not poorly calibrated,

- 1304 • was reconstructed with the standard algorithm (i.e. not a special recovery algo-
 1305 rithm for channels with subpar data integrity),
- 1306 • is not saturated,
- 1307 • is not spike-like, and
- 1308 • is in time (EB).

1309 EB basic clusters are formed around the seeds via the *hybrid* algorithm, while EE
 1310 basic clusters are formed with the `multi5x5` algorithm [79]. In addition to handling
 1311 non-radiating electrons and unconverted photons, both algorithms are designed to also
 1312 recover all of the energy associated with electron bremsstrahlung deposits and photon
 1313 conversions. The geometry of the CMS magnetic field means that bremsstrahlung
 1314 and conversions will tend to spread the shower out in ϕ , not η . Both algorithms
 1315 work by forming basic clusters around seeds, then combining the basic clusters into
 1316 *superclusters* (SC) by searching in a window extended in the ϕ direction for all basic
 1317 clusters consistent with bremsstrahlung radiation from the primary electron, or with
 1318 a photon conversion. Figure 6.4 illustrates the hybrid algorithm in EB. In EE, the
 1319 energy deposited in ES must also be added into the total clustered energy sum.

1320 Figure 6.5 shows the effect of superclustering on $Z \rightarrow ee$ reconstruction.

1321 **Supercluster Corrections**

1322 The total clustered ECAL energy is defined as

$$E = F \times \sum_{i=1}^{n_{\text{crystal}}} G \times c_i \times A_i \quad (6.1)$$

1323 where G is the ADC-GeV or MIP-GeV scale factor, c_i are the intercalibration con-
 1324 stants, A_i is the uncalibrated hit amplitude in ADC counts, and F is a SC correction

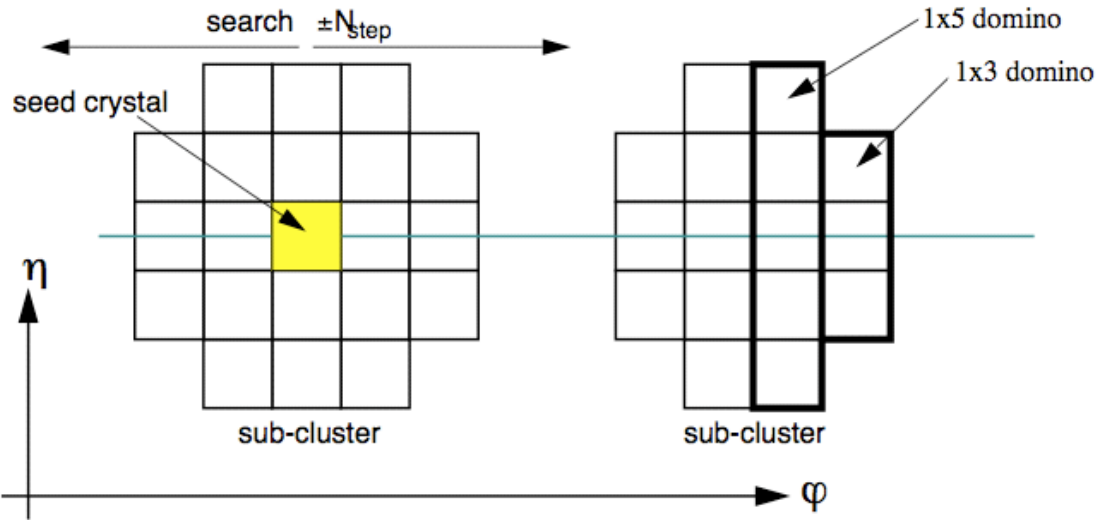


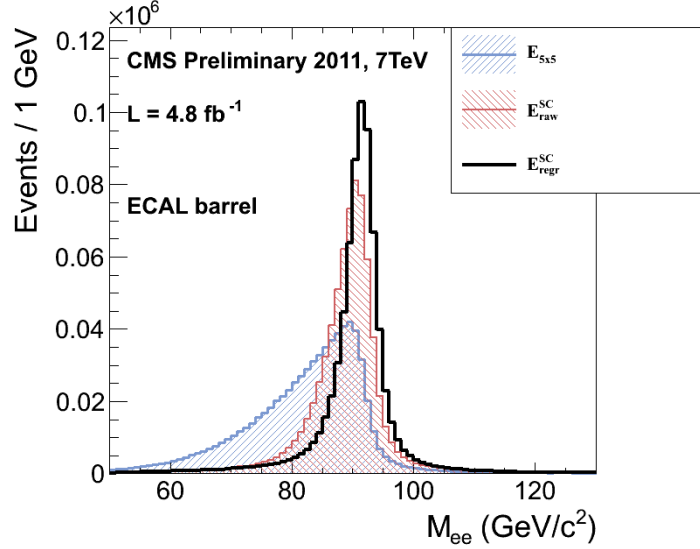
Figure 6.4: Hybrid algorithm in EB. The shower extent is constant in η (five crystals), but spreads out in ϕ as the two sub-clusters (or basic clusters) are grouped into the same supercluster. The maximum extent in ϕ is 17 crystals. Reprinted from ref. [79].

1325 factor. G and c_i were explained in Sec. 6.1.1. F is a product of three factors for hybrid
 1326 SCs (two for `multi5x5` SCs in EE, items 2 and 3 below) [79]:

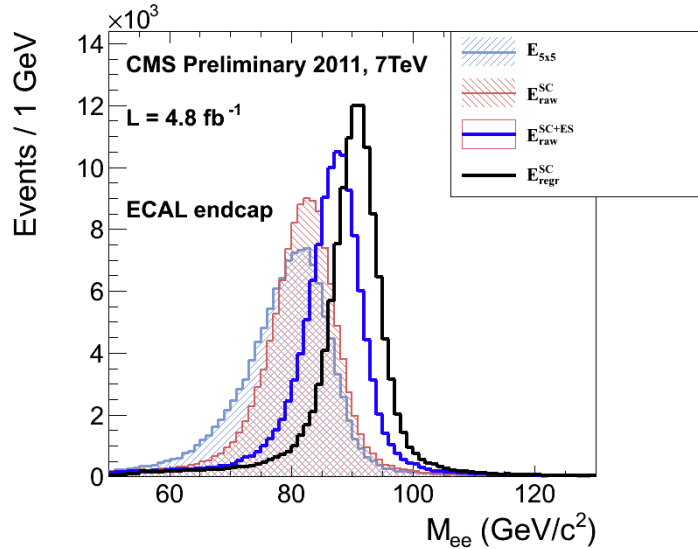
- 1327 1. $C_{\text{EB}}(\eta)$, which compensates for lateral energy leakage due to the crystal off-
 1328 pointing in EB only. These corrections are taken from MC simulation [79] and
 1329 were confirmed in test beams [74].
- 1330 2. $f(\text{brem})$, which corrects for biases in the clustering algorithms for showers char-
 1331 acterized by differing amounts of bremsstrahlung. These corrections are taken
 1332 from MC simulation [79].
- 1333 3. Residual correction $f(E_T, \eta)$, due to the variation in η of detector material
 1334 traversed by a primary electron or photon, and to any residual E_T dependence
 1335 of the reconstruction. These corrections are determined from MC and validated
 1336 on $Z \rightarrow ee$ data samples [80].

Changed

1337 As a benchmark of ECAL calibration performance, the extra energy smearing in
 1338 MC needed to achieve data/MC agreement in the Z width was between $\sim 0.9\%$ (in



(a) EB.



(b) EE.

Figure 6.5: Z peak reconstructed in the dielectron channel for different kinds of clustering. The constituent hits were calibrated with the best available intercalibrations and laser calibrations as of December 2011. The light blue histogram shows the reconstruction using a 5×5 energy sum, the red histogram shows the reconstruction using the SC energy for crystals only (the dark blue histogram in the EE plot adds in the energy from ES), and the black histogram shows the reconstruction after the SCs are corrected using a multivariate method [?]. Reprinted from Fig. 30 of ref. [?].

1339 the central part of EB for electrons with little bremsstrahlung) and $\sim 3.3\%$ (in the
1340 outer part of EE for heavily radiating electrons) [81].

1341 **From Supercluster to Photon**

1342 The CMS photon object is any SC with $E_T > 10$ GeV and $H/E < 0.5$, unless the SC
1343 $E_T > 100$ GeV, in which case the H/E requirement is dropped. H/E is defined as the
1344 ratio of energy in the HCAL in a 0.15 cone around the SC centroid, directly behind
1345 the SC, to the SC energy. SCs with $R9 > 0.94(0.95)$ in EB(EE), where $R9$ is defined
1346 as the ratio of the energy in the central 3×3 cluster of crystals divided by the SC
1347 energy $E_{3 \times 3}/E_{\text{SC}}$, are the best calibrated and most accurate type of electromagnetic
1348 shower. Therefore, for these objects, the photon energy is defined as the energy sum
1349 of the fully calibrated hits in the central 5×5 cluster around the seed (with $C_{\text{EB}}(\eta)$
1350 applied for EB photons). For all other SCs, the photon energy is equal to the fully
1351 corrected SC energy (cf. Sec. 6.1.1).

Reorganized

1352 In this search, candidate photons and *fake photons* (f , “fakes”) are further selected next 3
1353 according to the criteria listed in Table 6.1. Fakes are used in the determination of para-
1354 the QCD background, as explained in Chapter 7. graphs;

Table 6.1: Selection criteria for photons and fakes. “Pixel seed,” I_{comb} , and $\sigma_{i\eta i\eta}$ are edited
defined in the text.

Variable	Cut (γ)	Cut (f)
SC $ \eta $	< 1.4442	< 1.4442
H/E	< 0.05	< 0.05
$R9$	< 1	< 1
Has pixel seed	No	No
$I_{\text{comb}}, \sigma_{i\eta i\eta}$	< 6 GeV AND < 0.011	$(\geq 6 \text{ AND } < 20 \text{ GeV}) \text{ OR } \geq 0.011$

1355 I_{comb} is defined as

Updated

effective

area

$$I_{\text{comb}} = I_{\text{ECAL}} - 0.093\rho + I_{\text{HCAL}} - 0.0281\rho + I_{\text{track}} \quad (6.2)$$

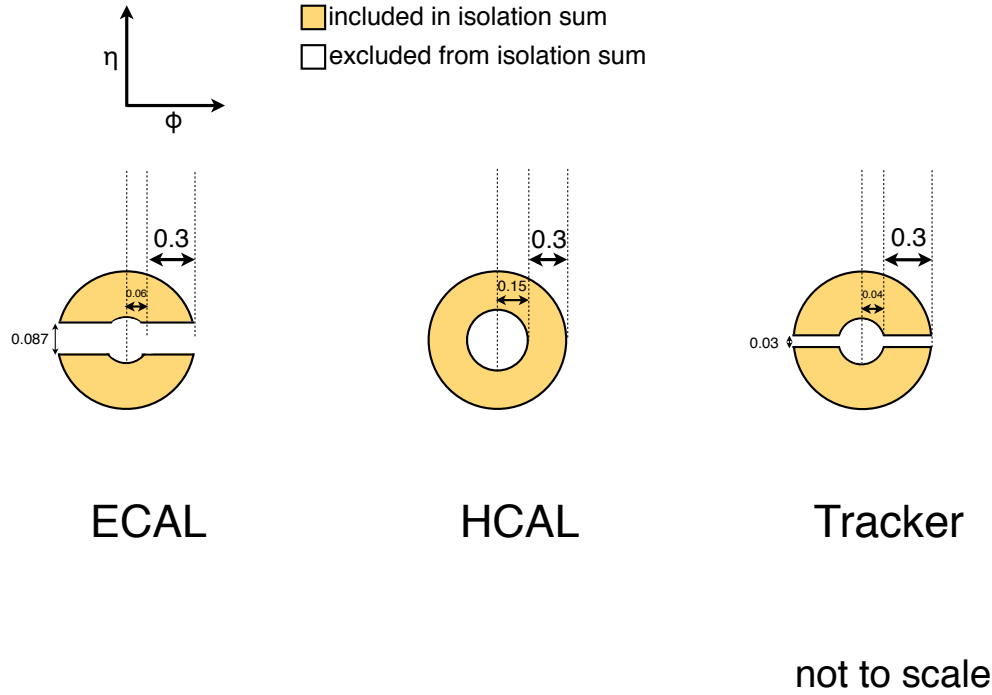


Figure 6.6: ECAL, HCAL, and track isolation cones.

1356 where I_{ECAL} , I_{HCAL} , and I_{track} are E_T sums in the annular regions defined in Figure 6.6
 1357 and ρ is the average pileup energy density in the calorimeters (per unit $\eta \cdot \phi$, or unit
 1358 calorimeter surface area) as measured with the Fastjet algorithm [82, 83]. ρ is constant
 1359 over the η range of the calorimeter. Note that the ECAL and track isolation veto
 1360 strips at constant η ensure that the isolation cuts are similarly efficient for converted
 1361 photons, radiating electrons, and unconverted photons.

1362 $\sigma_{i\eta i\eta}$ is the log energy weighted extent of the shower in η and is defined as

Added

$$\sigma_{i\eta i\eta} = \frac{\sum_{i=1}^{25} w_i (\eta_i - \bar{\eta})^2}{\sum_{i=1}^{25} w_i} \quad (6.3)$$

$\sigma_{i\eta i\eta}$

defini-
tion

1363 where the sums run over the 5×5 matrix of crystals surrounding the seed, $w_i =$
 1364 $\max(0, 4.7 + \ln(E_i/E))$, E_i is the energy of the i^{th} crystal, E is the total energy in the

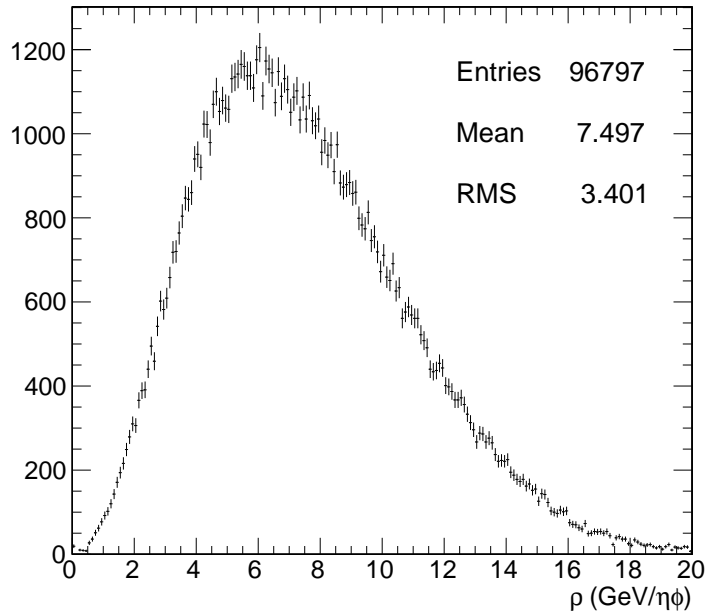


Figure 6.7: ρ distribution for a sample of two-photon events, with at least one 40 GeV and one 25 GeV photon, passing the selection requirements in Table 6.1 and the trigger requirements in Table 6.3. This sample covers the full 2011 dataset of 4.7 fb^{-1} .

1365 25 crystals, η_i is the offset in η of the i^{th} crystal from the seed, and $\bar{\eta}$ is the weighted
 1366 average η of the 25 crystals (using the w_i as weights) [84]. Changed

1367 Figure 6.7 shows the ρ distribution for a sample of two-photon events, with at average
 1368 least one 40 GeV and one 25 GeV photon, passing the selection requirements in ρ ; up-
 1369 Table 6.1 and the trigger requirements in Table 6.3. This sample represents the full dated
 1370 2011 dataset of 4.7 fb^{-1} . Since the average ρ is $\sim 7.5 \text{ GeV}$, and there is a long tail fig. 6.7
 1371 above this average value, it is necessary to subtract pileup energy from the ECAL
 1372 and HCAL isolation cones to recover otherwise clean photons in events with large
 1373 pileup. The ECAL and HCAL *effective areas* of 0.093 and 0.0281, respectively, are
 1374 calculated by fitting the average ECAL or HCAL isolation energy vs. ρ in a sample
 1375 of $Z \rightarrow ee$ events to a straight line. The slope of the line—which has the units of $\eta \cdot \phi$,
 1376 or area—is the effective area. New

1377 The cut on combined isolation of 6 GeV (Table 6.1) is the result of an S/\sqrt{B}

S \sqrt{B} Vs ComblsoDR03

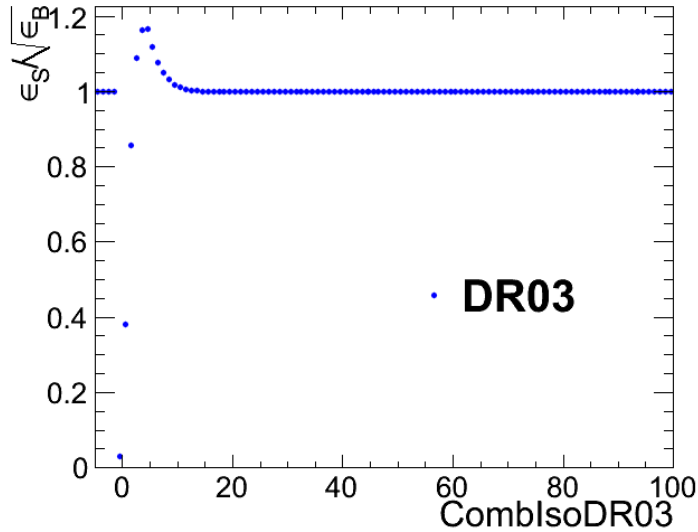


Figure 6.8: S/\sqrt{B} (S and B defined in the text) vs. I_{comb} . “DR03” in the legend indicates that this combined isolation was calculated in $\Delta R = 0.3$ cones, as used throughout this analysis. Reprinted from Fig. 7 of ref. [85].

optimization procedure [85]. S is a sample of photons in simulated GGM events that are products of neutralino decay, while B is a sample of photons matched to generated hadronic jets in simulated QCD events. Figure 6.8 shows the value of S/\sqrt{B} vs. combined isolation, in particular the pronounced peak around 6 GeV.

The upper bound on fake photon combined isolation guarantees that poorly isolated dijet events, with \cancel{E}_T resolution dissimilar to the candidate diphoton events, do not enter the ff sample. The exact value of 20 GeV (cf. Table 6.1) arises from a low- \cancel{E}_T $ff/\gamma\gamma \chi^2$ optimization procedure [85]. Figure 6.9 shows the value of the Neyman’s χ^2 between the ff and $\gamma\gamma \cancel{E}_T$ distributions, truncated at either 25 or 50 GeV, vs. upper bound on fake combined isolation. As shown in the figure, 20 GeV keeps the χ^2 small while also being large enough that a sufficient number of ff events may be collected.

Finally, a “pixel seed” is defined as a hit in the pixel detector consistent with a

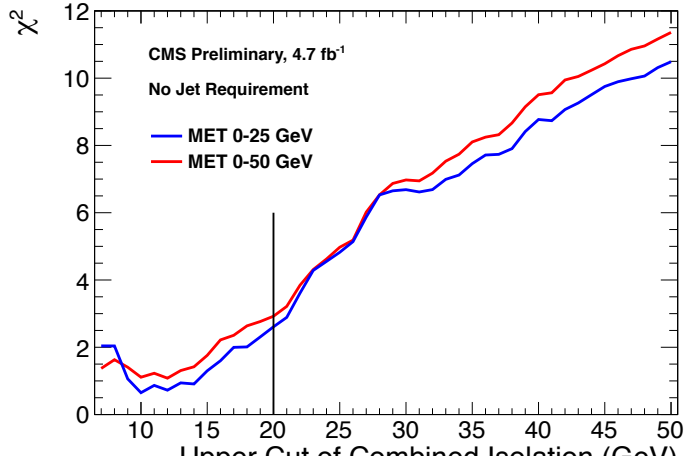
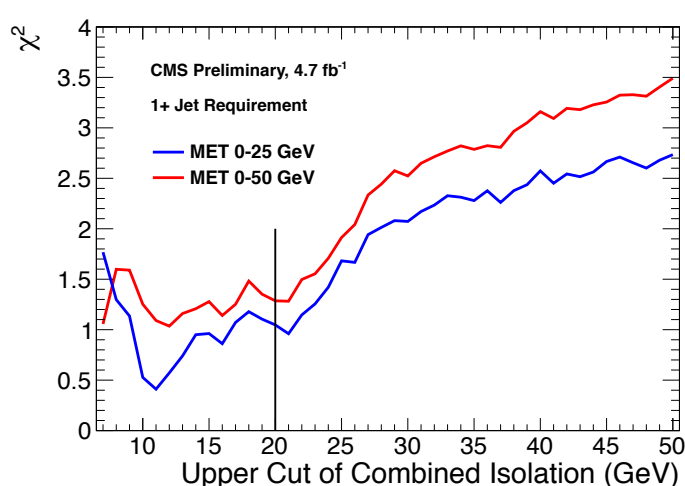
(a) Events with ≥ 0 jets.(b) Events with ≥ 1 jet.

Figure 6.9: Neyman's χ^2 between the ff and $\gamma\gamma$ \cancel{E}_T distributions, truncated at either 25 (red) or 50 (blue) GeV, vs. upper bound on fake combined isolation. A jet is defined as in Table 6.2, but with the ΔR cleaning criteria of Table 6.2 applied to the two primary EM objects and all additional electrons, photons, and fake photons. The full reweighting and normalization procedure is employed in the \cancel{E}_T calculation (see Sec. 7.2). Reprinted from Fig. 9 of ref. [85].

1391 track extrapolated from the position of the ECAL SC back to the primary vertex.
1392 Real photons, having no charge and therefore no bending in the magnetic field, should
1393 not have a pixel seed.

1394 6.1.2 Electrons

1395 Electrons are reconstructed identically to photons, except that in the electron case
1396 the presence of a pixel seed is enforced, rather than vetoed.² Photons and electrons
1397 are defined by very similar criteria so that $Z \rightarrow ee$ events can be used to model
1398 the QCD background in the two-photon sample without introducing any bias in the
1399 electron energy measurement (cf. Sec. 7.2).

1400 6.1.3 Jets and Missing Transverse Energy

1401 Particle Flow

1402 In this analysis, jets and \cancel{E}_T are formed from *particle flow* (PF) candidates. The parti-
1403 cle flow algorithm [89, 90] uses information from all CMS subdetectors to reconstruct
1404 as accurately as possible the positions and momenta of all visible jet constituents,
1405 exploiting the fine granularity of the tracker and ECAL to achieve a greatly improved
1406 momentum resolution over calorimeter-only jets [91]. The PF algorithm is summa-
1407 rized below [92].

1408 1. Reconstruct the fundamental detector objects via iterative procedures

- 1409 • Tracks in the inner silicon layers
 - 1410 – High efficiency and low fake rate for charged hadrons in jets

2In many CMS analyses, electrons are reconstructed very differently from photons. In particular, a special tracking algorithm [88] is used to best follow a radiating electron. However, in this analysis, the electron tracking is not used.

- 1411 – Relaxed primary vertex constraint allows photon conversions, parti-
 1412 cles originating from nuclear interactions in the silicon, and long-lived
 1413 particles to be reconstructed
- 1414 • Calorimeter clusters
- 1415 • Muon tracks in the outer muon layers
- 1416 2. Create a “block” of linked fundamental objects
- 1417 • Link silicon tracks to calorimeter clusters via $\Delta R_{\text{track-cluster}}$ (account for
 1418 electron bremsstrahlung)
- 1419 • Link clusters in one calorimeter layer to clusters in a separate layer via
 1420 $\Delta R_{\text{cluster-cluster}}$
- 1421 • Link silicon tracks to muon tracks via global track χ^2
- 1422 3. ID the particles in the block
- 1423 • If global (silicon + muon layers) muon p_T is compatible with silicon track
 1424 p_T , ID as a muon and remove corresponding tracks from block
- 1425 • ID electron tracks via special algorithm and removed all corresponding
 1426 tracks and cluster from block
- 1427 • Remove fake tracks from the block
- 1428 • Allow multiple tracks to be associated to one HCAL cluster, but not mul-
 1429 tiple HCAL clusters to be associated to one track—for each track, keep
 1430 only the HCAL cluster link that is closest in ΔR to the track
- 1431 • If the cluster energy is significantly larger then the energy of the linked
 1432 tracks, ID as a PF photon or PF neutral hadron
- 1433 • If the cluster is not linked to a track, ID as a PF photon or PF neutral
 1434 hadron

- 1435 • If the cluster energy is smaller than the energy of the linked tracks, ID
 1436 each track as a PF charged hadron

1437 **Jets**

1438 PF candidates are clustered into jets by means of the anti- k_T algorithm with $R = 0.5$
 1439 [93]. In this algorithm, all possible pairs of PF candidates i, j are looped over, and
 1440 the pairs that minimize the distance variable

$$d_{ij} = \frac{\Delta R_{ij}^2}{R^2 \max(k_{Ti}^2, k_{Tj}^2)} \quad (6.4)$$

1441 are clustered together, where k_{Ti} is the transverse momentum of PF candidate i . The
 1442 process is repeated, using the pairwise-clustered PF candidates as input objects to
 1443 the next round of clustering, until $d_{ij} > 1/k_{Ti}^2$ for all pairs of clustered PF candidates
 1444 [94]. An illustration is given in Figure 6.10. The anti- k_T algorithm is infrared and Added
 1445 collinear safe, leading to well-behaved theoretical predictions and ease of comparison refer-
 1446 between data and MC simulation. It also tends to form circular jets, making it easy ence to
 1447 for experimental effects such as expected out-of-cone energy and fiducial acceptance Fig. 6.10
 1448 to be measured or simulated. For these reasons, the anti- k_T jet clustering algorithm
 1449 was chosen for this analysis.

1450 Once jets are found, they must be corrected for biases in the energy measurement
 1451 due to non-compensation [95], invisible energy (lost to overcoming nuclear binding
 1452 energy, in neutrinos, or in unclustered muons, for example) [95], detector geometry
 1453 and cracks [96], zero suppression and trigger inefficiencies [97], pileup, and effects of
 1454 the clustering algorithm [96]. Four multiplicative correction factors are applied to the
 1455 raw jet four-momentum p_μ^{raw} [91]:

- 1456 • $C_{\text{offset}}(p_T^{\text{raw}})$, which accounts for extra energy due to noise, pileup, and the un-

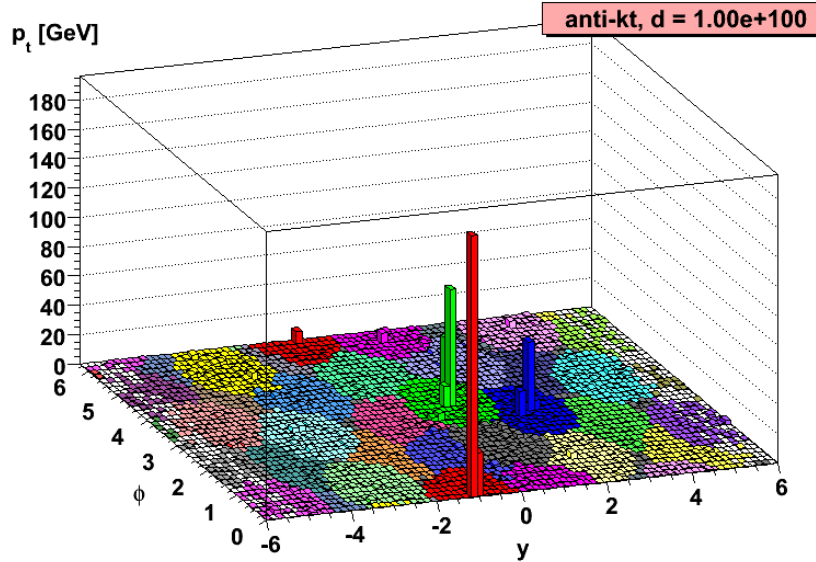


Figure 6.10: Example event display showing jets clustered via the anti- k_T algorithm. y is pseudorapidity. Reprinted from slide 85 of ref. [94].

- 1457 derlying event;
- 1458 • $C_{\text{MC}}(C_{\text{offset}}p_T^{\text{raw}}, \eta)$, which is derived from MC and accounts for most of the p_T
1459 and η dependence;
- 1460 • $C_{\text{rel}}(\eta)$, which accounts for the remaining differences in uniformity over the
1461 entire calorimeter between data and MC; and
- 1462 • $C_{\text{abs}}(C_{\text{rel}}C_{\text{MC}}C_{\text{offset}}p_T^{\text{raw}})$, which accounts for the remaining differences in linear-
1463 ity over the full p_T range between data and MC.

1464 Figure 6.11 shows the total jet energy correction factor $C_{\text{offset}}C_{\text{MC}}C_{\text{rel}}C_{\text{abs}}$ vs. η
1465 for jets reconstructed with the anti- k_T algorithm, $R = 0.5$. The PF jet corrections
1466 are more uniform across η than those of CALO jets (composed of simple calorimeter
1467 towers) or JPT jets (Jet Plus Tracks; composed of calorimeter energies replaced,
1468 where possible, with matching track p_T) [98]. In addition, for p_T in the range 30-200
1469 GeV and $|\eta|$ up to 2.0, the PF jet energy correction uncertainty is lower than that of
1470 the other two types of jets, and never exceeds $\sim 3\%$ [91]. The superior performance

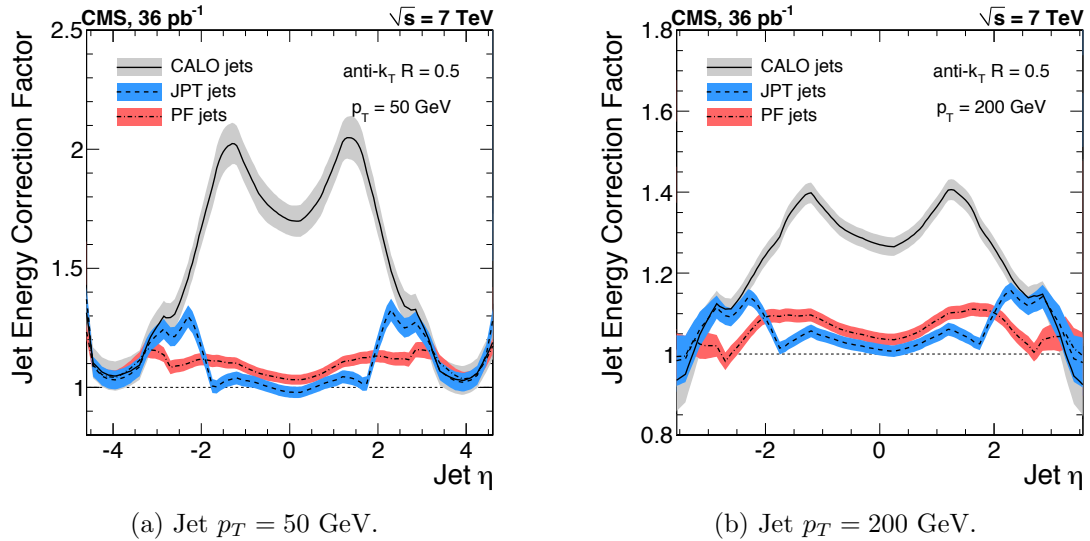


Figure 6.11: Total jet energy correction factor $C_{\text{offset}}C_{\text{MC}}C_{\text{rel}}C_{\text{abs}}$ vs. η , including uncertainty band, for jets reconstructed with the anti- k_T algorithm, $R = 0.5$. Reprinted from Fig. 26 of ref. [91].

¹⁴⁷¹ of PF jets motivates their use in this search.

¹⁴⁷² In this analysis, candidate and QCD control events are binned by number of jets
¹⁴⁷³ satisfying the criteria in Table 6.2.

¹⁴⁷⁴ Missing Transverse Energy

¹⁴⁷⁵ To be consistent with the jet reconstruction, \cancel{E}_T in this analysis is also reconstructed
¹⁴⁷⁶ from PF candidates. Raw \cancel{E}_T is defined as

$$\cancel{E}_{T\text{raw}} = \left| - \sum_{i=1}^{n_{\text{PF}}} \vec{p}_{Ti} \right| \quad (6.5)$$

¹⁴⁷⁷ where n_{PF} is the number of PF candidates in the event. $\cancel{E}_{T\text{raw}}$ may be corrected for
¹⁴⁷⁸ the same effects that necessitate jet corrections, since $\cancel{E}_{T\text{raw}}$ is usually the result of jet
¹⁴⁷⁹ mis-measurement (except, of course, in electroweak physics processes that include an
¹⁴⁸⁰ energetic neutrino, or SUSY production). CMS *Type-I* \cancel{E}_T corrections simply involve

Table 6.2: Definition of HB/HE hadronic jets.

Variable	Cut
Algorithm	L1FastL2L3Residual corrected PF
p_T	$> 30 \text{ GeV}$
$ \eta $	< 2.6
Neutral hadronic energy fraction	< 0.99
Neutral electromagnetic energy fraction	< 0.99
Number of constituents	> 1
Charged hadronic energy	$> 0.0 \text{ GeV}$ if $ \eta < 2.4$
Number of charged hadrons	> 0 if $ \eta < 2.4$
Charged electromagnetic energy fraction	< 0.99 if $ \eta < 2.4$
ΔR to nearest PF electron ^a , muon ^b , or one of the two primary EM objects	> 0.5

^aA PF electron is defined as an electron reconstructed with the PF algorithm [86] with $p_T > 15 \text{ GeV}$, $|\eta| < 2.6$, and $(I_{\text{charged}} + I_{\text{photon}} + I_{\text{neutral}})/p_T < 0.2$, where $I_{\text{charged}}(I_{\text{photon}})(I_{\text{neutral}})$ is the sum of PF charged hadron(PF photon)(PF neutral hadron) momenta in a $\Delta R = 0.4$ cone around the PF electron.

^bMuons are reconstructed [87] from a combination of muon station and inner tracker hits. Here, a muon must have track $\chi^2 < 10$, at least one good muon station hit, inner track transverse impact parameter $< 0.02 \text{ cm}$, inner track longitudinal impact parameter $< 0.5 \text{ cm}$, $p_T > 15 \text{ GeV}$, $|\eta| < 2.6$, and $(I_{\text{ECAL}} + I_{\text{HCAL}} + I_{\text{track}})/p_T < 0.2$, where $I_{\text{ECAL}}(I_{\text{HCAL}})(I_{\text{track}})$ is the sum of ECAL(HCAL)(track) momenta in a $\Delta R = 0.3$ cone around the muon.

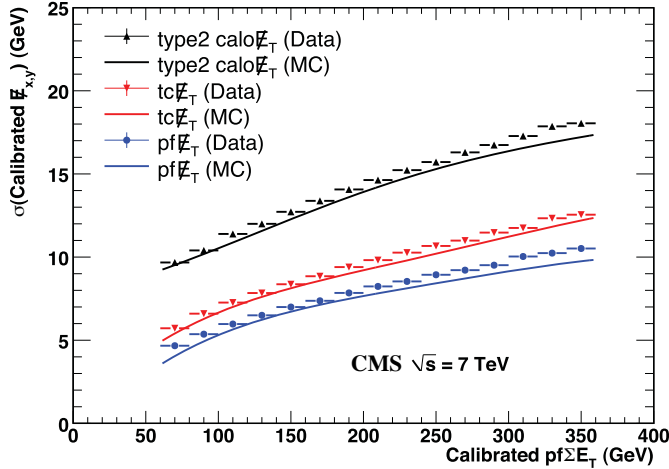


Figure 6.12: σ of a Gaussian fit to the x- and y-components of calibrated E_T vs. the calibrated PF E_T sum in a sample of events containing at least two jets with $p_T > 25$ GeV. σ is calibrated such that the E_T scale is equal for all three algorithms. PF $\sum E_T$ is corrected, on average, to the particle level using a Pythia v8 simulation [99]. The blue markers (data) and line (MC) refer to PF jets. Reprinted from Fig. 13 of ref. [97].

replacing the PF jets with their corrected energies (cf. Sec 6.1.3) and recalculating E_T . Only jets with electromagnetic fraction (EMF) below 90% and $p_T > 20$ GeV are replaced. This ensures that very electromagnetic jets (as well as isolated leptons, which also receive no correction), which consist chiefly of neutral pions and are measured accurately by the ECAL, do not receive a correction derived for jets with a large fraction of their energy in charged hadrons. In addition, the p_T cut guarantees that jet corrections are only applied where they are known to within a few percent. For this search, the level of agreement between the SM background estimate and the two-photon search sample in a low- E_T control region is the same regardless of whether the E_T is corrected or not, so for simplicity the Type-I E_T corrections are not used (see Sec. 7.4).

Figure 6.12 shows the σ of a Gaussian fit to the x- and y-components of calibrated E_T vs. the calibrated PF E_T sum in a sample of events containing at least two jets with $p_T > 25$ GeV. Again, PF E_T outperforms E_T constructed of calorimeter towers or track-corrected calorimeter deposits.

1496 **6.2 HLT**

1497 From the objects described in Sec. 6.1, four samples of events are formed:

- 1498 • $\gamma\gamma$ candidate sample, in which the two highest E_T objects are photons,
- 1499 • $e\gamma$ control sample, in which the two highest E_T objects are one electron and
1500 one photon,
- 1501 • ee control sample, in which the two highest E_T objects are electrons, and
- 1502 • ff control sample, in which the two highest E_T objects are fakes.

1503 In all samples, the leading EM object is required to have offline reconstructed $E_T > 40$
1504 GeV, while the trailing EM object is required to have offline reconstructed $E_T > 25$
1505 GeV. The high level triggers used to select the four samples, by run range, are listed
1506 in Table 6.3. No trigger is prescaled.

1507 Each piece of the HLT path name is defined as follows.

- 1508 • **Photon**: Energy deposit in the ECAL that fired an L1 trigger (cf. Sec. 5.2.1).
1509 For **Photon26_IsoVL_Photon18**, the L1 seed E_T threshold is 12 GeV, while for 1510 **Switched**
1511 all other triggers in Table 6.3 it is 20 GeV (cf. Sec. 5.2.1). 1512 **HLT**
1513 **path**
1514 **names**
1515 **to ver-**
1516 **batim**
1517 **font and**
1518 **added**
1519 **refer-**
1520 **ence**
1521 **to L1**
1522 **section**
- 1511 • Integer following the word **Photon**: E_T threshold in GeV for offline reconstructed
1512 photon, using the full photon reconstruction of Sec. 6.1.1 minus the laser cali-
1513 brations and assuming the primary vertex at (0, 0, 0).
- 1514 • **CaloIdL**: For EB photons, $H/E < 0.15$ and $\sigma_{inj} < 0.014$.
- 1515 • **IsoVL**: $I_{ECAL} < 0.012E_T + 6$ GeV, $I_{HCAL} < 0.005E_T + 4$ GeV, and $I_{track} <$
1516 $0.002E_T + 4$ GeV.
- 1517 • **R9Id**: $R9 > 0.8$.

Table 6.3: HLT paths triggered by the $\gamma\gamma$, $e\gamma$, ee , and ff samples, by run range. No triggers are prescaled.

Run range	$\gamma\gamma$	$e\gamma$	ee	ff
160404-163261	Photon26_ IsoVL_ Photon18	Photon26_ IsoVL_ Photon18	Photon26_ IsoVL_ Photon18	Photon26_ IsoVL_ Photon18
161216-166967	Photon36_ CaloIdL_ Photon22_ CaloIdL	Photon36_ CaloIdL_ Photon22_ CaloIdL	Photon36_ CaloIdL_ Photon22_ CaloIdL	Photon36_ CaloIdL_ Photon22_ CaloIdL
166347-180252	Photon36_ CaloIdL_ IsoVL_ Photon22_ CaloIdL_ IsoVL	Photon36_ CaloIdL_ IsoVL_ Photon22_ CaloIdL_ IsoVL	Photon36_ CaloIdL_ IsoVL_ Photon22_ CaloIdL_ IsoVL	Photon36_ CaloIdL_ IsoVL_ Photon22_ CaloIdL_ IsoVL Photon36_ CaloIdL_ IsoVL_ Photon22_ R9Id Photon36_ R9Id_ Photon22_ CaloIdL_ IsoVL Photon36_ R9Id_ Photon22_ R9Id

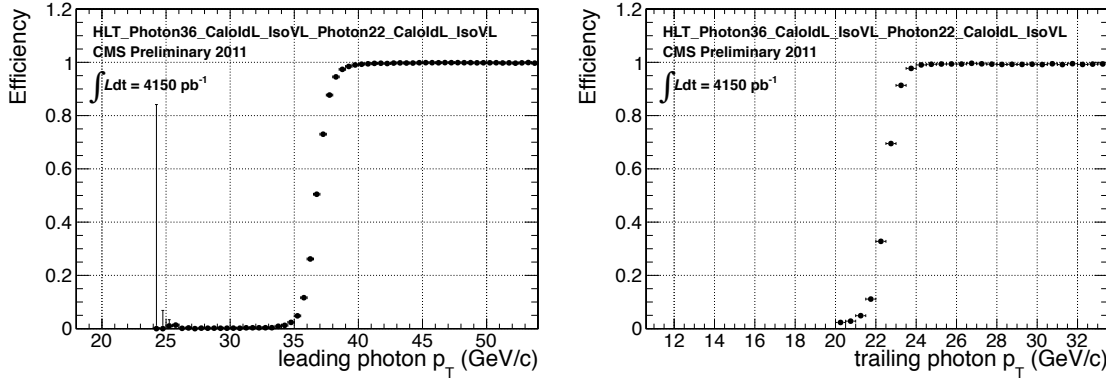


Figure 6.13: Efficiency of `HLT_Photon36_CaloIdL_IsoVL_Photon22_CaloIdL_IsoVL` for offline selected leading photon (left) and trailing photon (right) vs. photon p_T . Reprinted from Fig. 2 of ref. [85].

1518 In addition, the versions of `HLT_Photon26_IsoVL_Photon18` and
 1519 `Photon36_CaloIdL_Photon22_CaloIdL` that were active during runs 160404-163268
 1520 included a cut $E_{\max}/E_{5\times 5} < 0.98$ for spike rejection. E_{\max} is the energy in the highest
 1521 energy crystal of the EM cluster and $E_{5\times 5}$ is the energy in the 5×5 crystal matrix
 1522 around the seed crystal. For runs after 163268, Swiss cross spike rejection of individual
 1523 crystals from HLT quantities was performed (cf. Sec. 6.1.1). All information about the
 1524 evolution of the CMS HLT settings can be found in the HLT configuration browser
 1525 at <http://j2eeps.cern.ch/cms-project-confdb-hltdev/browser/>.

1526 As an example of the naming convention just described, the HLT path
 1527 `Photon36_CaloIdL_IsoVL_Photon22_R9Id` is fired if one photon is found with $E_T >$
 1528 36 GeV passing the CaloIdL and IsoVL requirements, and another is found with
 1529 $E_T > 22$ GeV passing the R9Id requirement.

1530 For the offline E_T cuts described in this section, the triggers are $> 99\%$ efficient,
 1531 as shown in Figure 6.13 [85]. The efficiencies are measured with respect to triggers
 1532 with lower E_T thresholds.

Switched
 HLT
 path
 names
 to ver-
 batim
 font
 Switched
 HLT
 path
 names
 to ver-
 batim
 font
 Added
 HLT ef-
 ficiency
 discus-
 sion

1533 6.3 Event Quality

1534 To suppress instrumental backgrounds, a set of event quality cuts are applied to the
 1535 $\gamma\gamma$, $e\gamma$, ee , and ff samples. First, all events are required to pass a good run selection,
 1536 as determined by the CMS Physics Validation Team [101]. The good run selection
 1537 excludes luminosity sections during which a sufficient part of the CMS detector was
 1538 unpowered or malfunctioning. Such conditions could occur if, for example, a high
 1539 voltage supply trips off in the middle of a run, or a DAQ error corrupts data quality
 1540 but is not spotted until after the data have been collected. The severity of a detec-
 1541 tor problem is judged by its effect on a wide range of analyses and reconstruction
 1542 algorithms. Of the $\sim 5 \text{ fb}^{-1}$ of integrated luminosity delivered by the LHC in 2011,
 1543 4.68 fb^{-1} passed the good run selection. This analysis is performed on the entire 2011
 1544 certified dataset.

1545 Second, all events must contain at least one good interaction vertex. The criteria
 1546 for a good vertex are:

- 1547 • $\chi^2 \neq 0$ OR $\text{ndof} \neq 0$ OR $N_{\text{tracks}} \neq 0$, where χ^2 and ndof are calculated for the
 1548 track fit to the vertex, and N_{tracks} is the number of tracks in the vertex fit
- 1549 • $\text{ndof} > 4$
- 1550 • $|z| < 24 \text{ cm}$, where z is the z -coordinate of the vertex position
- 1551 • $|\rho| < 2 \text{ cm}$, where ρ is the transverse displacement of the vertex position from
 1552 the beam line

1553 The good vertex requirement eliminates non-collision backgrounds such as beam
 1554 scraping, beam halo, cosmic muon interactions, and instrumental effects.

1555 Third, the two electromagnetic objects in the $\gamma\gamma$, $e\gamma$, ee , and ff events must
 1556 be separated in ϕ by at least 0.05. This requirement protects against beam halo
 1557 bremsstrahlung, in which a halo muon traveling parallel to the beam line radiates an

1558 energetic photon while itself depositing a large amount of energy in the ECAL. In
 1559 this case, the two ECAL hits would likely be at the same ϕ (and ρ).

1560 Fourth, the two EM objects must be separated in R by at least 0.6. Since the
 1561 isolation cone size used is 0.3, this ensures that the isolation energy of one EM object
 1562 cannot be in the veto strip (Fig. 6.6) of the other.

1563 Finally, the $\gamma\gamma$, $e\gamma$, ee , and ff events must pass an HCAL noise filter and ECAL
 1564 dead channel filter. The HCAL noise filter guarantees that all HCAL reconstructed
 1565 hits are inconsistent with any noise source. Noise sources [100] include:

- 1566 • Ion feedback in the HPDs absent any true incident photons, in which a thermal
 1567 electron ionizes a molecule in the HPD acceleration gap, faking a real signal
- 1568 • HPD discharge affecting nearly all channels in the same HPD [102], partially
 1569 explained by the effect of the 4 T CMS magnetic field on the flashover voltage
 1570 of the dielectric [104]
- 1571 • Concurrent signals in nearly all 72 channels of a single RBX, as yet unexplained
- 1572 • HF PMT window hits (as opposed to the usual quartz fiber hits)
- 1573 • ADC saturation

1574 Since HCAL noise may induce fake jets or E_T , events are rejected if any of the
 1575 following criteria are true:

- 1576 • Any HPD has > 17 hits
- 1577 • A single HPD has > 10 hits, but every other HPD has zero hits
- 1578 • An RBX has > 10 zero-ADC-count hits
- 1579 • Any HB/HE reconstructed hit corresponding to an RBX with > 50 GeV of
 1580 energy fails a two-dimensional cut defined by the variables $(TS4 - TS5)/(TS4 +$

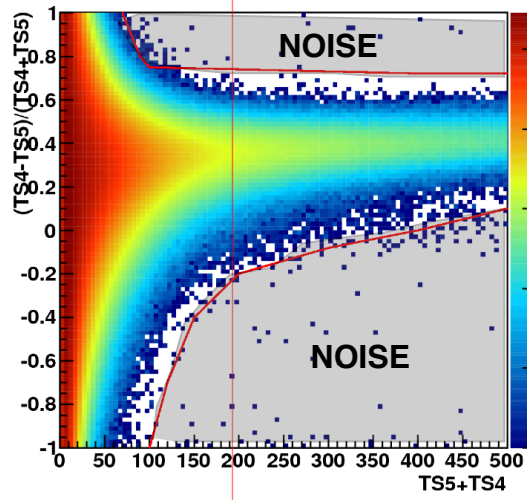


Figure 6.14: $(TS4 - TS5)/(TS4 + TS5)$ vs. $TS4 + TS5$ for a minimum bias sample. HB/HE hits are considered noisy if they lie in the sparsely populated gray region labeled "NOISE" defined by the curved red lines. Adapted from ref. [103].

1581 $TS5)$ vs. $TS4 + TS5$, where $TS4(TS5)$ is the hit amplitude in the fourth(fifth)
 1582 time sample read out for that hit. The cut is defined in Fig. 6.14.

1583 The ECAL dead channel filter is designed to flag events in which significant EM
 1584 energy was deposited in a masked region of the ECAL by using the trigger primitive
 1585 information for the corresponding trigger tower. Energy deposited in a masked region
 1586 of ECAL can cause fake \cancel{E}_T . Events are rejected if the trigger primitive E_T exceeds
 1587 the maximum value of 63.75 GeV in any trigger tower that is masked in the readout.

1588 6.4 Photon Identification Efficiency

1589 In order to determine the cross section (or cross section upper limit) for a GGM
 1590 signal, the photon identification efficiency is needed. Since no suitably large sample
 1591 of $Z \rightarrow \mu\mu\gamma$ events in CMS exists yet, the efficiency calculation relies on the similarity
 1592 between detector response to electrons and photons. A scale factor to correct the MC
 1593 photon ID efficiency to the real photon efficiency for the data is obtained from the
 1594 ratio of the electron efficiency from the data to the electron efficiency from MC.

1595 The different types of photon ID variables—calorimeter and track isolation, ratio of **Removed**
 1596 hadronic to electromagnetic energy of the shower, and transverse shower shape—are **refer-**
 1597 chosen so that their distributions for isolated electrons and photons are similar.³ **ence to**
 1598 The photon selection efficiency is **plots**

$$\epsilon_{\gamma} = \epsilon_{\gamma}^{\text{MC}} \times \frac{\epsilon_e^{\text{data}}}{\epsilon_e^{\text{MC}}} \quad (6.6)$$

1599 where

- 1600 • ϵ_{γ} is the photon ID efficiency in data,
- 1601 • $\epsilon_{\gamma}^{\text{MC}}$ is the photon ID efficiency in MC,
- 1602 • ϵ_e^{data} is the electron ID efficiency obtained using $Z \rightarrow ee$ electrons in the data
1603 that satisfy the photon ID cuts, and
- 1604 • ϵ_e^{data} is the electron ID efficiency obtained using $Z \rightarrow ee$ electrons in MC that
1605 satisfy the photon ID cuts.

1606 The ratio $\epsilon_e^{\text{data}}/\epsilon_e^{\text{MC}}$ is defined as the scale factor by which the GGM signal MC
 1607 photon ID efficiency must be multiplied to give an estimate of the photon ID efficiency
 1608 in data. The photon ID requirements of Table 6.1 plus the **IsoVL** HLT requirement
 1609 described in Sec. 6.2 and Table 6.3 are repeated in Table 6.4.

1610 6.4.1 Tag and Probe Method

1611 A *tag and probe* method using Z events is utilized to measure the efficiency of the
 1612 photon ID cuts in Table 6.1. The tag is a well-identified electron. The probe, by
 1613 contrast, is as loosely identified as possible, and all tags must pass the probe criteria

³ $R9$ differs between photons and radiating electrons, but the requirement $R9 < 1$ is loose enough not to introduce problems with the use of electrons to measure the photon ID efficiency.

1614 in addition to the stringent tag criteria. The tag and probe criteria used in this study
1615 are shown in Table 6.5.

1616 The invariant mass of the tag and probe are required to be within a narrow window
1617 around Z mass. Assuming that the probabilities of the tag and probe legs of the Z
1618 decay to pass the photon ID cuts are uncorrelated, the efficiency can be estimated as

$$\epsilon = \frac{N_{\text{tag-pass}}}{N_{\text{tag-pass}} + N_{\text{tag-fail}}} \quad (6.7)$$

1619 where $N_{\text{tag-pass}}$ is the number of tag-probe pairs in which the probe leg passes the
1620 photon ID cuts under study and $N_{\text{tag-fail}}$ is the number of tag-probe pairs in which
1621 the probe leg fails the cuts. Implicit in these definitions is a double counting of pairs
1622 in which both electrons pass the tag and probe criteria [106]. In addition, in the rare
1623 circumstance (less than 1% in MC [106]) that two or more probes may be matched
1624 to one tag, the pair with invariant mass closest to the Z mass is chosen.

1625 In practice, $N_{\text{tag-pass}}$ and $N_{\text{tag-fail}}$ are returned by a simultaneous unbinned maxi-
1626 mum likelihood fit to the invariant mass distributions of tag-pass and tag-fail events,
1627 with appropriate signal and background PDF assumptions. The fit form used is

Table 6.4: Candidate photon ID requirements.

Variable	Cut
I_{ECAL}	$< 0.012E_T + 6 \text{ GeV}$
I_{HCAL}	$< 0.005E_T + 4 \text{ GeV}$
I_{track}	$< 0.002E_T + 4 \text{ GeV}$
H/E	< 0.05
$\sigma_{i\eta i\eta}$	< 0.011
$I_{\text{ECAL}} - 0.0792\rho + I_{\text{HCAL}} - 0.0252\rho + I_{\text{track}}$	$< 6 \text{ GeV}$
$R9$	< 1

Table 6.5: Tag and probe criteria. The superscript 0.4 indicates that the isolation variable was calculated in a cone of $\Delta R = 0.4$ around the photon candidate. The isolations without superscripts use the standard $\Delta R = 0.3$ cones.

Variable	Cut	
	Tag	Probe
RECO object	photon	photon
HLT	HLT_Ele17_CaloIdVT_CaloIsoVT_TrkIdT_TrkIsoVT_SC8_Mass30_v* (must have fired the 17 GeV leg)	—
H/E	< 0.05	< 0.15
$I_{\text{ECAL}}^{0.4}$	$< 0.006E_T + 4.2 \text{ GeV}$	—
$I_{\text{HCAL}}^{0.4}$	$< 0.0025E_T + 2.2 \text{ GeV}$	—
$I_{\text{track}}^{0.4}$	$< 0.001E_T + 2.0 \text{ GeV}$	—
E_T	$> 25 \text{ GeV}$	—
SC E_T	—	$> 15 \text{ GeV}$
SC $ \eta $	< 1.4442	< 1.4442
$\sigma_{i\eta i\eta}$	< 0.009	—
Has pixel seed	Yes	—
Track match type	General track ^a	—
Track match ΔR	< 0.04	—
Track match p_T	$> 15 \text{ GeV}$	—
Track match $ \eta $	< 1.479	—

^aA general track is reconstructed with the CMS standard combinatorial track finder [105].

$$\begin{aligned} f_{\text{tag-pass}}(m_{\text{tag-pass}}) &= \epsilon N_S f_S^{\text{pass}}(m_{\text{tag-pass}}) + N_B^{\text{pass}} f_B^{\text{pass}}(m_{\text{tag-pass}}) \\ f_{\text{tag-fail}}(m_{\text{tag-fail}}) &= (1 - \epsilon) N_S f_S^{\text{fail}}(m_{\text{tag-fail}}) + N_B^{\text{fail}} f_B^{\text{fail}}(m_{\text{tag-fail}}) \end{aligned} \quad (6.8)$$

where $f_{\text{tag-pass}}(m_{\text{tag-pass}})$ and $f_{\text{tag-fail}}(m_{\text{tag-fail}})$ are the tag-pass and tag-fail PDFs, respectively; ϵ is the efficiency; N_S is the total number of Z signal events summed over both samples; $f_S^{\text{pass}}(m_{\text{tag-pass}})$ and $f_S^{\text{fail}}(m_{\text{tag-fail}})$ are the tag-pass and tag-fail signal PDFs, respectively; N_B^{pass} and N_B^{fail} are the numbers of background events in the tag-pass and tag-fail samples, respectively; and $f_B^{\text{pass}}(m_{\text{tag-pass}})$ and $f_B^{\text{fail}}(m_{\text{tag-fail}})$ are the tag-pass and tag-fail background PDFs, respectively. This particular implementation of the tag and probe methodology is based on tag `CMSSW_4_2_5` of the CMSSW package `PhysicsTools/TagAndProbe`, and uses the MINUIT2 [107] library, as coded in RooFit [108], for the likelihood maximization. For this study, CMSSWv4.2.8 was used.

For both samples, the signal shape is assumed to be a Crystal Ball function [109] convoluted with the Z generated lineshape, while the background shape is a PDF that describes the falling background as well as the kinematic turn-on at low invariant mass. The background PDF, called `RooCMSShape` [106], is given by

$$f_{\text{RooCMSShape}}(x) = \begin{cases} 1e20 & \text{for } (x - \mu)\gamma < -70 \\ 0 & \text{for } (x - \mu)\gamma > 70 \\ \text{erfc}((\alpha - x)\beta) \exp(-(x - \mu)\gamma) & \text{otherwise} \end{cases} \quad (6.9)$$

where α , β , γ , and μ are parameters of the fit, most of which are held fixed. In the three lowest E_T bins, all parameters of the tag-pass and tag-fail background PDFs are left floating, because the effect of the relaxed E_T cuts has a significant effect on

1645 the background shape. More details of the signal and background PDFs are given
 1646 in Table 6.6. The fixed signal and background parameter values were determined by
 1647 fitting a small sample ($0.0 \leq \eta < 0.25$) of Fall11 MC signal (DYJetsToLL) and back-
 1648 ground (QCD_Pt-20to30_BCtoE, QCD_Pt-30to80_BCtoE, QCD_Pt-80to170_BCtoE,
 1649 GJet_Pt-20_doubleEMEnriched, WJetsToLNu, TTJets) with parameters left float-
 1650 ing.⁴

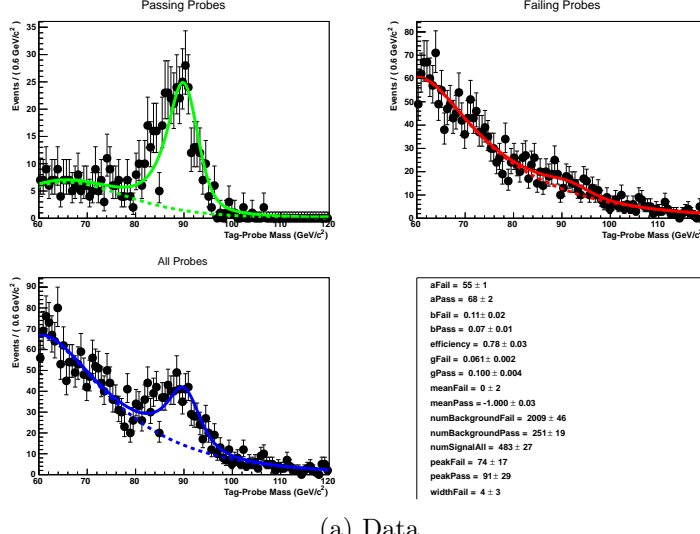
Table 6.6: Parameter values (parameter definitions are in the text) for the signal and background PDFs for the different samples. The background PDF applies to all efficiency bins except the four lowest E_T bins, which use a floating `RooCMSShape` background. When a bracketed range is given, the parameter is allowed to float within that range. When a constant is given, the parameter is fixed to that constant.

PDF	Crystal Ball fit parameters				RooCMSShape fit parameters			
	μ	σ	α	n	μ	α	β	γ
Tag-pass signal	[-1.0, 1.0]	[1.0, 3.0]	0.87	97.0	N/A	N/A	N/A	N/A
Tag-fail signal	[-1.0, 1.0]	[1.0, 3.0]	0.73	134.9	N/A	N/A	N/A	N/A
Tag-pass background	N/A	N/A	N/A	N/A	65.0	61.949	0.04750	0.01908
Tag-fail background	N/A	N/A	N/A	N/A	α	[50.0, 100.0]	0.065	0.048

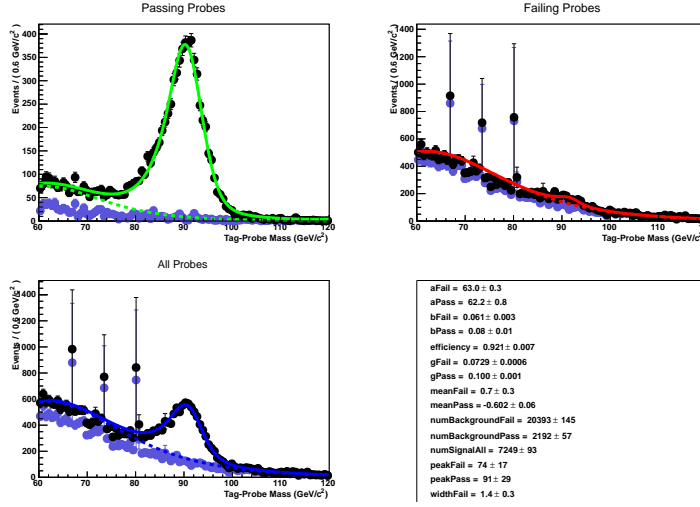
Added

1651 Some fit examples are shown in Figures 6.15 and 6.16. In Fig. 6.15, which shows fits
 1652 fits to data and MC for $15 \text{ GeV} \leq \text{probe } E_T < 20 \text{ GeV}$, the kinematic turn-on is below
 1653 the invariant mass range covered by the plot. The exponentially falling background
 1654 is easily seen underneath the signal, and is especially pronounced in the background-
 1655 dominated tag-fail sample.

⁴See Appendix A for a discussion of the MC samples.

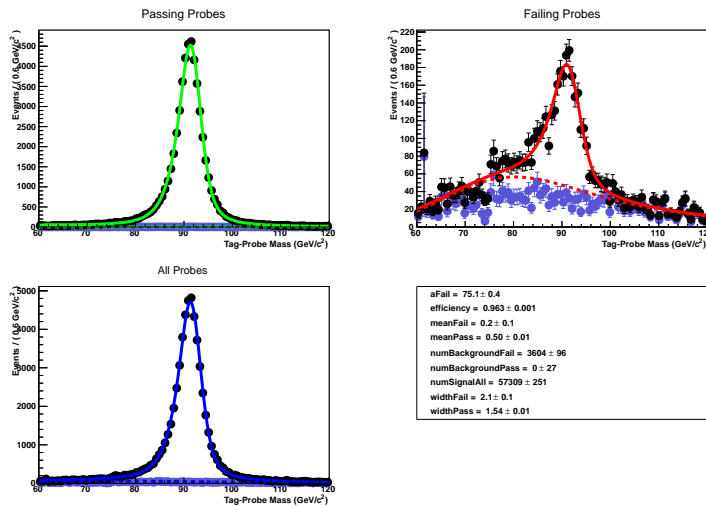
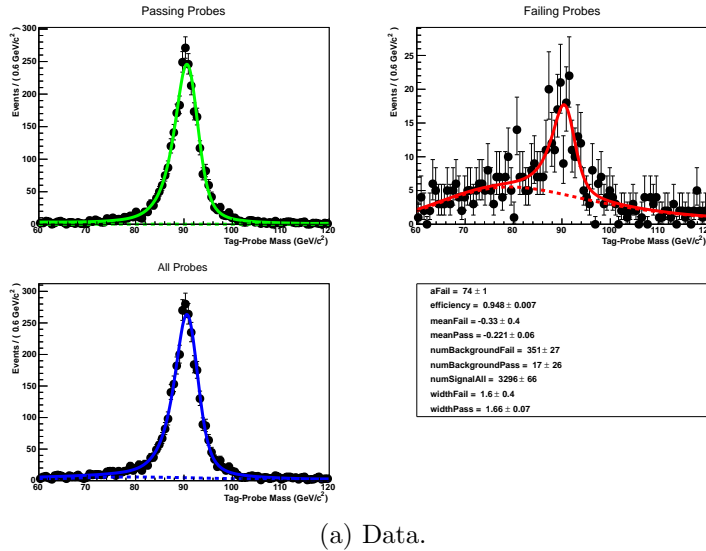


(a) Data.



(b) MC. The purple points are the background MC (photon + jet, W, QCD, and t̄t).

Figure 6.15: Tag and probe invariant mass fits for $15 \text{ GeV} \leq \text{probe } E_T < 20 \text{ GeV}$. Errors are statistical only. The tag-pass fit is shown in green in the upper-left-hand plot, the tag-fail fit in red in the upper-right-hand plot, and a fit to both samples in blue in the lower-left-hand plot. Dotted lines are the background components of the fits; solid lines are signal plus background.



(b) MC. The purple points are the background MC (photon + jet, W , QCD, and $t\bar{t}$).

Figure 6.16: Tag and probe invariant mass fits for $-0.25 \leq \text{probe } \eta < -0.5$. Errors are statistical only. The tag-pass fit is shown in green in the upper-left-hand plot, the tag-fail fit in red in the upper-right-hand plot, and a fit to both samples in blue in the lower-left-hand plot. Dotted lines are the background components of the fits; solid lines are signal plus background.

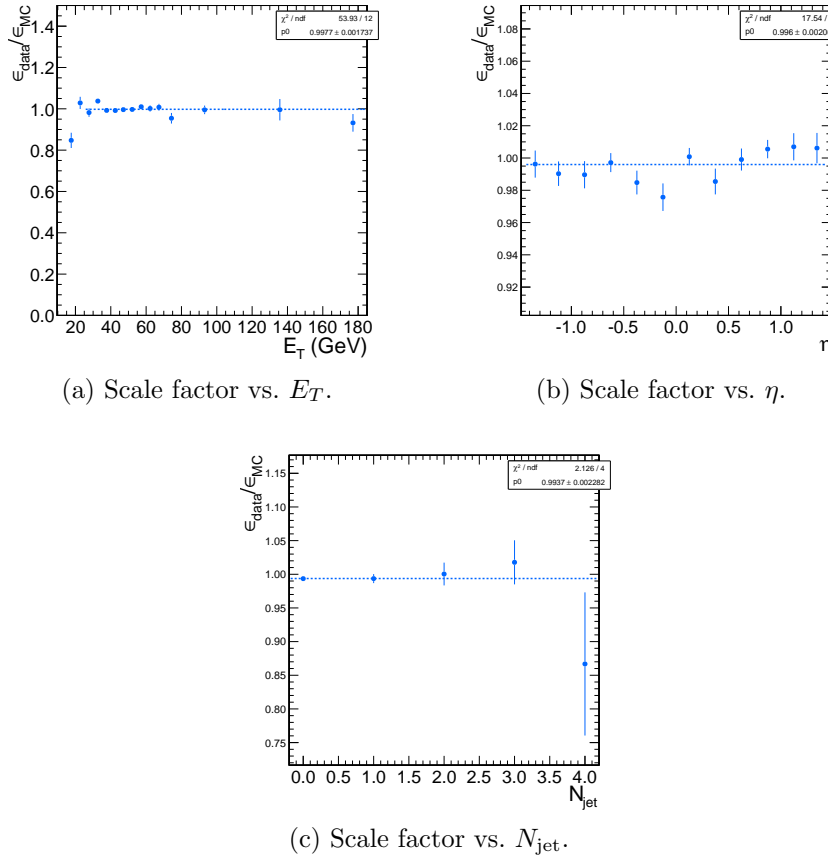


Figure 6.17: Dependence of the photon ID efficiency scale factor on some kinematic variables. Errors are statistical only.

1656 6.4.2 Photon Efficiency Scale Factor $\epsilon_e^{\text{data}}/\epsilon_e^{\text{MC}}$

1657 Figure 6.17 shows the dependence of the photon ID efficiency scale factor $\epsilon_e^{\text{data}}/\epsilon_e^{\text{MC}}$
 1658 on E_T , η , and N_{jet} , where jets are defined as in Table 6.2, but with only the two
 1659 Z electrons considered as candidates for overlap removal. Errors are statistical only.
 1660 There no significant dependence of the scale factor on these variables, so only one
 1661 scale factor is computed from the entire dataset.

1662 The effect of pileup is studied by comparing the efficiencies ϵ_e^{data} and ϵ_e^{MC} vs. the
 1663 number of primary vertices (N_{PV}) in the event. The efficiency only drops a few percent
 1664 for events with large N_{PV} after using pileup-corrected isolation cuts, as can be seen in
 1665 Figure 6.18a. The MC tracks the data, and the scale factor is flat vs. N_{PV} , as shown

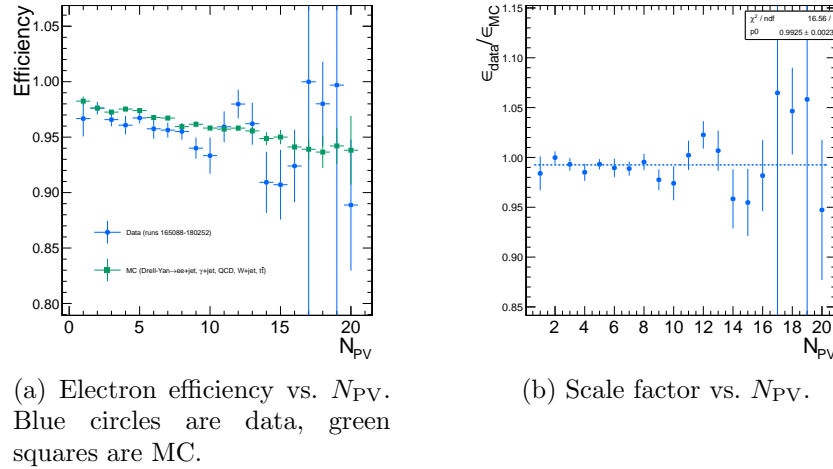


Figure 6.18: Dependence of the photon ID efficiency scale factor on the number of primary vertices per event. Errors are statistical only.

1666 in Fig. 6.18b.

1667 The scale factor is measured to be $\epsilon_e^{\text{data}}/\epsilon_e^{\text{MC}} = 0.994 \pm 0.002(\text{stat.}) \pm 0.035(\text{syst.})$. result
1668 Four main sources of systematic error, in addition to the statistical error of 0.2%, were uses this
1669 studied. syst.

1670 **Different behavior of electrons and photons in MC** Even though the photon
1671 ID cuts are designed to be similarly efficient for both electrons and photons,
1672 there might be a small difference in the performance between the two kinds
1673 of particles, e.g. because of electron bremsstrahlung. To check this effect, the
1674 MC electron ID efficiency was calculated using a $Z \rightarrow ee$ sample and the MC
1675 photon ID efficiency was calculated using a $\gamma + \text{jets}$ sample. Both samples were
1676 reconstructed in CMSSWv3.6. Half the difference between these two results,
1677 0.5%, was taken as an error on the scale factor.

1678 **Pileup** To account for the possibility that the MC simulation may not adequately some of
1679 reproduce the data in a high pileup environment, the data/MC scale factor these
1680 for events with 1-4 good reconstructed primary vertices was calculated, along bullets
1681 with the same for events with ≥ 5 good reconstructed primary vertices. The

1682 difference between the scale factors from both samples, 2.4%, was taken as an
 1683 error on the scale factor from pileup.

1684 **Signal fit over/underestimation** It was found that the signal fit slightly under-
 1685 estimates the data in the tag-pass sample, and slightly overestimates it in the
 1686 tag-fail sample. To cover this effect with a systematic error, the efficiencies in
 1687 data and MC, and then the scale factor, were recalculated using the background
 1688 (from fit) subtracted integrals of the tag-pass and tag-fail distributions, rather
 1689 than the fitted signal yields in those distributions. The difference between the
 1690 scale factor found in this way and the nominal scale factor, 1.9%, was taken as
 1691 an error on the scale factor.

1692 **Signal and background shape assumption** To assess the magnitude of the error
 1693 from the signal and background shape assumptions, the tag-pass and tag-fail
 1694 tail parameters (Crystal Ball α and n) were varied by $\pm 1\sigma$, and the background
 1695 shape was varied between `RooCMSShape`, exponential, power law, and quadratic.
 1696 All possible combinations of varied parameters were generated, and the data and
 1697 MC were refit and new scale factors generated according to those combinations.
 1698 The error was taken as the largest deviation of the scale factor from nominal,
 1699 1.8%.

1700 Finally, the pixel veto efficiency was estimated from MC to be 0.96 ± 0.005 (syst.),
 1701 with error due to varying assumptions of the tracker material distribution [110]. In
 1702 general, the photon ID selection used in this analysis is very efficient for GGM photons
 1703 and robust to pileup, and its efficiency is fairly well measured.

1704

Chapter 7

1705

Data Analysis

1706 The signature of GGM SUSY particle production in this search is an excess of two-
1707 photon events with high E_T above the Standard Model background. E_T is recon-
1708 structed using the particle flow algorithm as described in Sec. 6.1.3. Candidate two-
1709 photon events, as well as control events, are selected according to the offline object
1710 criteria presented in Secs. 6.1.1, 6.1.2, and 6.1.3; the event quality criteria in Sec. 6.3;
1711 and the trigger requirements in Sec. 6.2. These are summarized in Table 7.1.

Table 7.1: Selection criteria for $\gamma\gamma$, $e\gamma$, ee , and ff events.

Variable	Cut			
	$\gamma\gamma$	$e\gamma$	ee	ff
HLT match	IsoVL	IsoVL	IsoVL	IsoVL R9Id
E_T	$> 40/$ $> 25 \text{ GeV}$			
$\text{SC } \eta $	< 1.4442	< 1.4442	< 1.4442	< 1.4442
H/E	< 0.05	< 0.05	< 0.05	< 0.05
$R9$	< 1	< 1	< 1	< 1
Pixel seed	No/No	Yes/No	Yes/Yes	No/No
I_{comb} , $\sigma_{i\eta i\eta}$	$< 6 \text{ GeV} \&\&$ < 0.011	$< 6 \text{ GeV} \&\&$ < 0.011	$< 6 \text{ GeV} \&\&$ < 0.011	$< 20 \text{ GeV} \&\&$ $(\geq 6 \text{ GeV} \parallel$ $\geq 0.011)$
JSON	Yes	Yes	Yes	Yes
No. good PVs	≥ 1	≥ 1	≥ 1	≥ 1
ΔR_{EM}	> 0.6	> 0.6	> 0.6	> 0.6
$\Delta\phi_{\text{EM}}$	≥ 0.05	≥ 0.05	≥ 0.05	≥ 0.05

1712 This search utilizes 4.7 fb^{-1} of CMS data collected during the period April
1713 December 2011, corresponding to the following datasets [111]:

- 1714 • `/Photon/Run2011A-05Jul2011ReReco-ECAL-v1/AOD`
- 1715 • `/Photon/Run2011A-05Aug2011-v1/AOD`
- 1716 • `/Photon/Run2011A-03Oct2011-v1/AOD`
- 1717 • `/Photon/Run2011B-PromptReco-v1/AOD`

1718 The search strategy is to model the backgrounds to the GGM SUSY signal using
1719 \cancel{E}_T shape templates derived from the control samples, and then to look for a high- \cancel{E}_T
1720 excess above the estimated background in the $\gamma\gamma$ sample. There are two categories of
1721 backgrounds: QCD processes with no real \cancel{E}_T and electroweak processes with real \cancel{E}_T
1722 from neutrinos. The relevant QCD background processes are multijet production with
1723 at least two jets faking photons, photon + jet production with at least one jet faking
1724 a photon, and diphoton production. The relevant electroweak background processes,
1725 which are small compared to the QCD background, involve $W \rightarrow e\nu$ decay with a
1726 recoiling jet that fakes a photon or a real radiated photon (the W may come from
1727 the decay of a top quark in $t\bar{t}$ events). In both cases, the electron is misidentified
1728 as a photon due to a small inefficiency in reconstructing the electron pixel seed.
1729 The main diagrams contributing to the QCD(electroweak) backgrounds are shown in
1730 Figure 7.1(7.2).

1731 7.1 Control Samples

1732 Data control samples are used to model all of the backgrounds. The primary control
1733 sample used to model the QCD background is the ff sample, which is similar to the
1734 candidate $\gamma\gamma$ sample but with combined isolation or $\sigma_{inj\eta}$ cuts inverted. The cuts

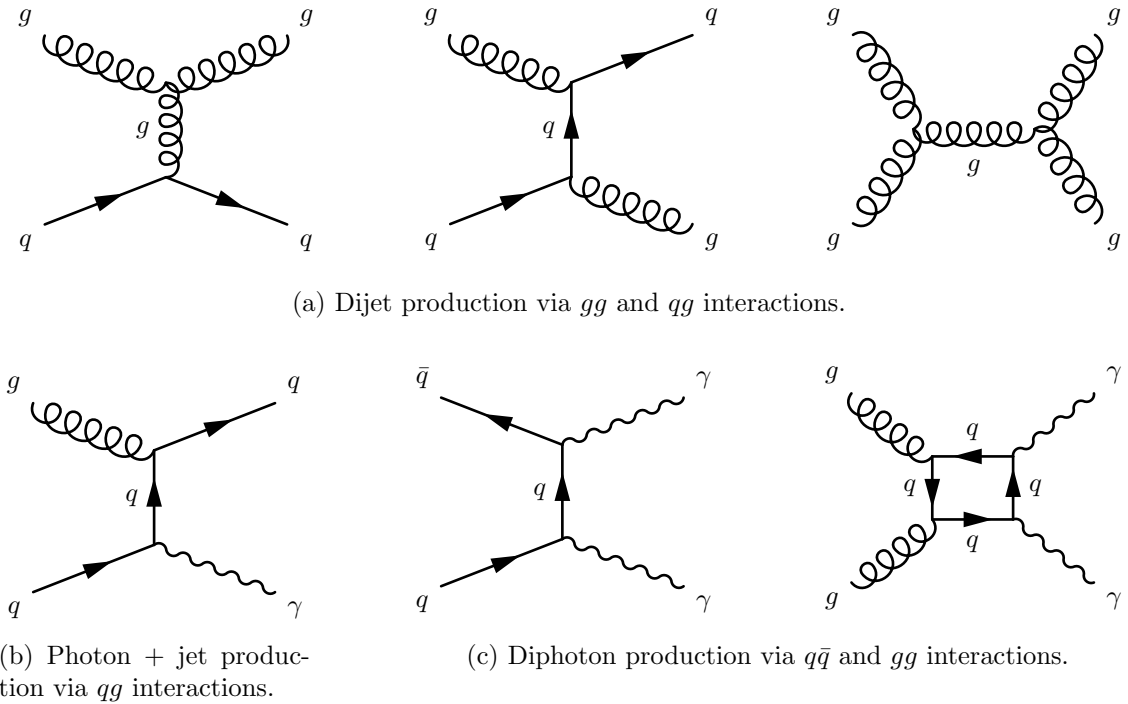


Figure 7.1: Representative Feynman diagrams of some QCD backgrounds to the GGM SUSY search.

1735 on these variables are used to distinguish between photons and jets, so by inverting
 1736 those cuts, the resulting ff sample becomes enriched with QCD dijets. Because the
 1737 fake photons are still required to pass a tight cut on H/E , they are guaranteed to be
 1738 very electromagnetic jets, with an EM energy scale and resolution similar to that of
 1739 the candidate photons. This insures that the resulting estimate of the \cancel{E}_T shape does
 1740 not have too long of a tail from severe HCAL mis-measurements that are actually
 1741 rare in the $\gamma\gamma$ sample.

1742 As a cross-check, the ee sample is also used to model the QCD background. This
 1743 sample of Z decays should have no true \cancel{E}_T , just like the ff sample, and the electron
 1744 definition (differing from the photon definition only in the presence of a pixel seed)
 1745 insures that the electron energy scale and resolution is similar to that of the photon.

1746 Finally, the $e\gamma$ sample is used to model the electroweak background from $W \rightarrow e\nu$
 1747 decays. The $e\gamma$ \cancel{E}_T distribution is scaled by the electron \rightarrow photon misidentification

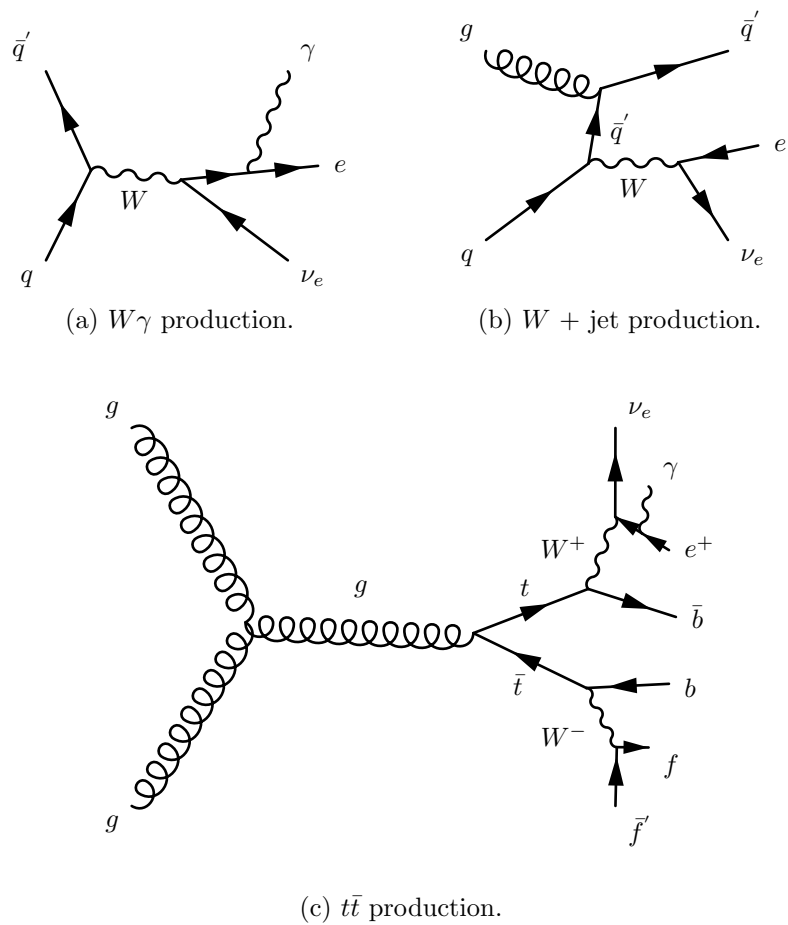


Figure 7.2: Representative Feynman diagrams of some electroweak backgrounds to the GGM SUSY search.

1748 rate to predict the number of $W\gamma$, $W + \text{jet}$, and $t\bar{t}$ events in the $\gamma\gamma$ sample.

1749 The remainder of this chapter describes the data analysis procedures and the final
1750 results of the search. Sec. 7.2 addresses the QCD background estimation. Sec. 7.3
1751 addresses the electroweak background estimation. The chapter concludes with a dis-
1752 cussion of systematic errors in Sec. 7.4 and a presentation of the final results in
1753 Sec. 7.5.

1754 7.2 Modeling the QCD Background

1755 7.2.1 Outline of the Procedure

1756 Due to the fact that the CMS ECAL energy resolution is much better than the
1757 HCAL energy resolution, the energies of the two candidate photons in the events of
1758 the $\gamma\gamma$ sample are typically measured to far greater accuracy and precision than the
1759 energy of the hadronic recoil in those events. Therefore, fake \cancel{E}_T in the $\gamma\gamma$ sample
1760 is almost entirely the result of hadronic mis-measurement in QCD dijet, photon +
1761 jet, and diphoton events. The strategy employed to model this background is to find
1762 a control sample in data consisting of two well-measured EM objects, just like the
1763 candidate $\gamma\gamma$ sample, and assign each event a weight to account for the underlying
1764 kinematic differences between the control and candidate samples. Once the reweighted
1765 \cancel{E}_T spectrum of the control sample is created, it is then normalized in the low- \cancel{E}_T
1766 region, the assumption being that GGM SUSY does not predict a significant amount
1767 of events at low \cancel{E}_T . There are three aspects of this QCD background estimation
1768 procedure that bear highlighting:

1769 **Choice of control sample** Since the underlying cause of \cancel{E}_T in the candidate sam-
1770 ple is mis-measured hadronic activity, a control sample with similar hadronic
1771 activity to the candidate sample should be chosen. Hadronic activity refers to
1772 number of jets, jet E_T , pileup, etc.

1773 **Reweighting** The control sample is reweighted so that its \cancel{E}_T spectrum appears as it
1774 would if the control sample had the same kinematic properties as the candidate
1775 $\gamma\gamma$ sample (i.e. particle p_T and η distributions, etc.). By choosing an appropriate
1776 control sample and reweighting it, the control \cancel{E}_T distribution should now match
1777 both the hadronic activity and the kinematics of the candidate sample.

1778 **Normalization** Finally, the control E_T distribution is normalized in a region of
1779 low \cancel{E}_T , where contamination from the expected GGM SUSY signal is small.
1780 This implies an extrapolation of the low- \cancel{E}_T QCD background prediction to the
1781 high- \cancel{E}_T signal region.

1782 As explained in the beginning of this chapter, the ff sample is used as the primary
1783 QCD control sample, while the ee sample is used as a cross-check. Both samples have
1784 two well-measured EM objects per event, no real \cancel{E}_T , and similar hadronic activity to
1785 the $\gamma\gamma$ sample. Figures 7.3- 7.8 show a comparison of the shapes of some distributions
1786 relevant to hadronic activity between the $\gamma\gamma$, ee , and ff samples. In general, the
1787 ee sample has less hadronic activity than the $\gamma\gamma$ and ff samples, as shown by the
1788 more steeply falling ee distributions in Figs. 7.3, 7.4, 7.5, and 7.6. In addition to the
1789 kinematic reweighting, there is also a reweighting by number of jets per event, which
1790 attempts to correct for this difference (see Sec. 7.2.2).

1791 7.2.2 Reweighting

1792 To reweight the control sample events to match the kinematics of the candidate sample
1793 events, a weight based on the p_T of the di-EM-object system and the number of jets
1794 in the event is used. As explained in Sec. 7.2.1, E_T in the $\gamma\gamma$, ff , and ee samples
1795 is due to the poorly measured hadronic recoil off the well-measured di-EM system.
1796 Therefore, the p_T of the di-EM system is a good handle on the true magnitude of
1797 the hadronic recoil, which affects the measured \cancel{E}_T . The di-EM system is depicted

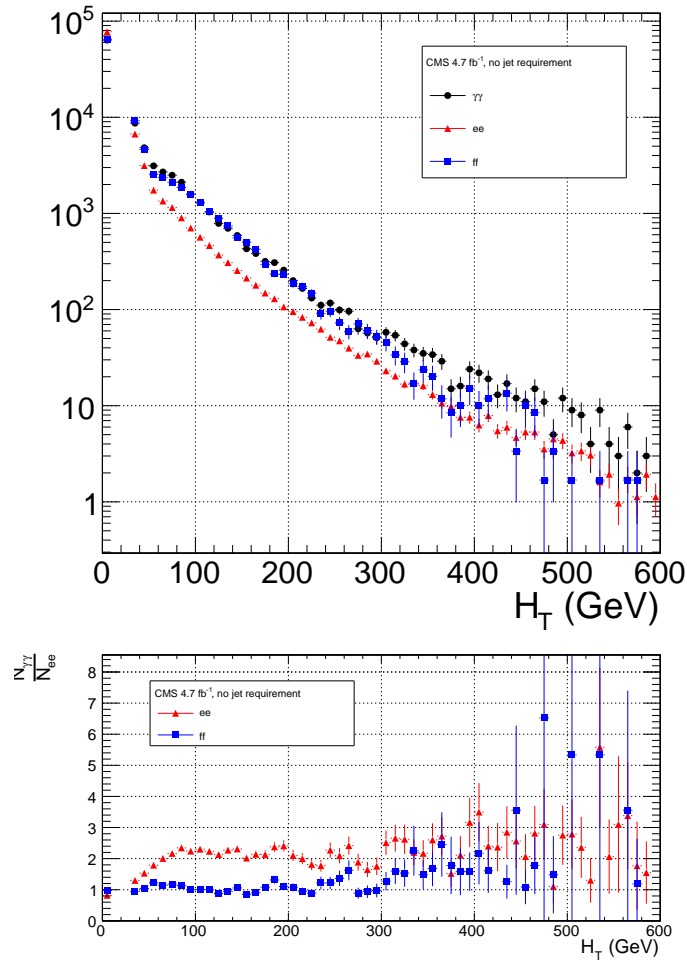


Figure 7.3: H_T , defined as the scalar sum of corrected jet E_T for jets defined as in Table 7.2. $\gamma\gamma$ is in black, ee ($81 \text{ GeV} \leq m_{ee} < 101 \text{ GeV}$) is in red, and ff is in blue. The ee and ff distributions are normalized to the number of events in the $\gamma\gamma$ distribution. Errors are statistical only.

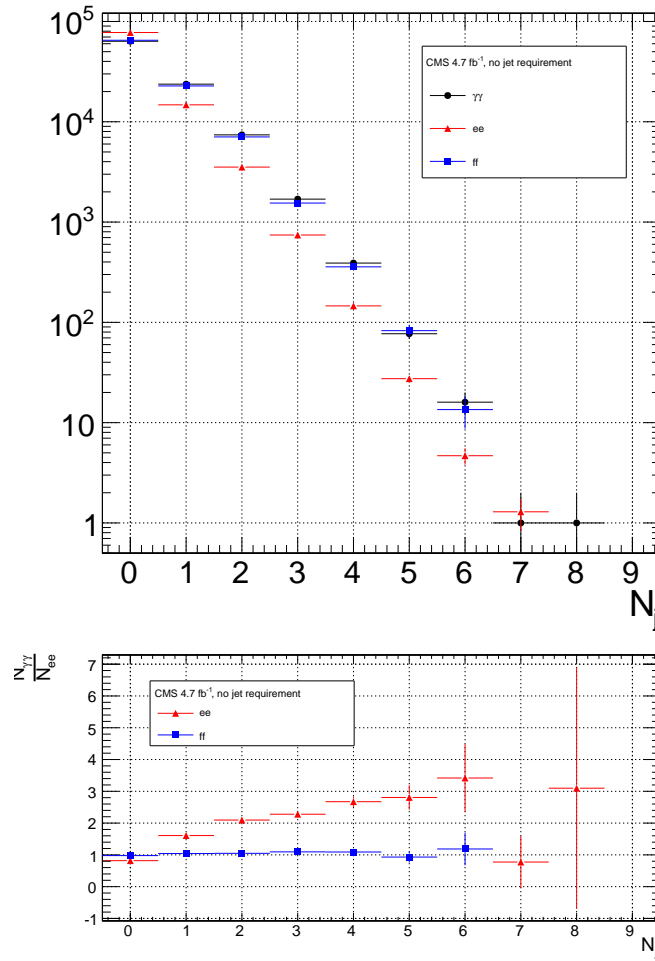


Figure 7.4: Number of jets per event for jets defined as in Table 7.2. $\gamma\gamma$ is in black, ee ($81 \text{ GeV} \leq m_{ee} < 101 \text{ GeV}$) is in red, and ff is in blue. The ee and ff distributions are normalized to the number of events in the $\gamma\gamma$ distribution. Errors are statistical only.

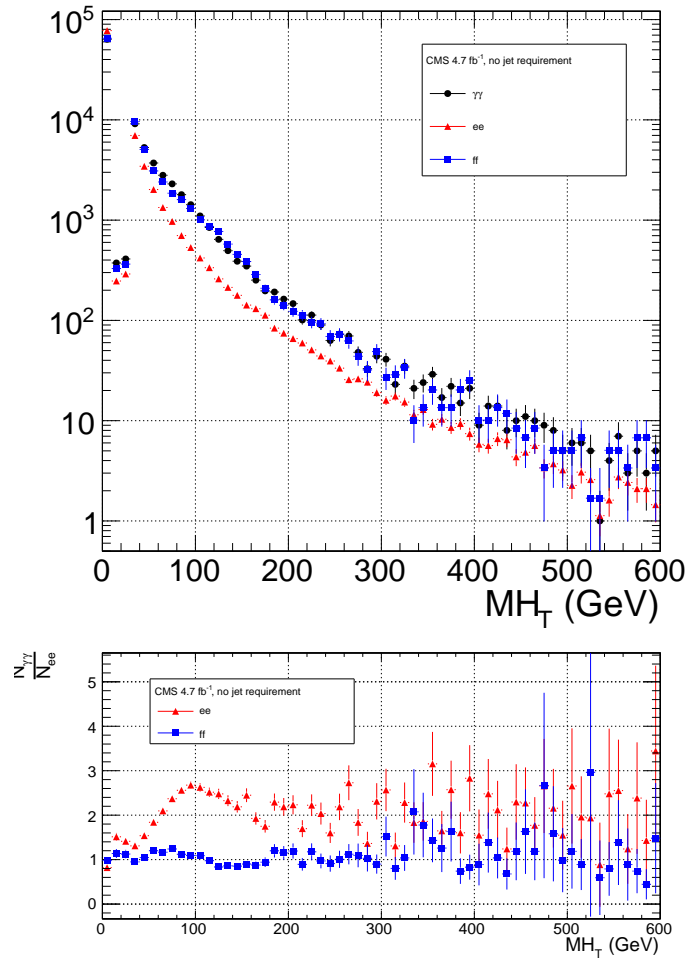


Figure 7.5: H_T , defined as the magnitude of the negative vectorial sum of corrected jet E_T for jets defined as in Table 7.2. $\gamma\gamma$ is in black, ee ($81 \text{ GeV} \leq m_{ee} < 101 \text{ GeV}$) is in red, and ff is in blue. The ee and ff distributions are normalized to the number of events in the $\gamma\gamma$ distribution. Errors are statistical only.

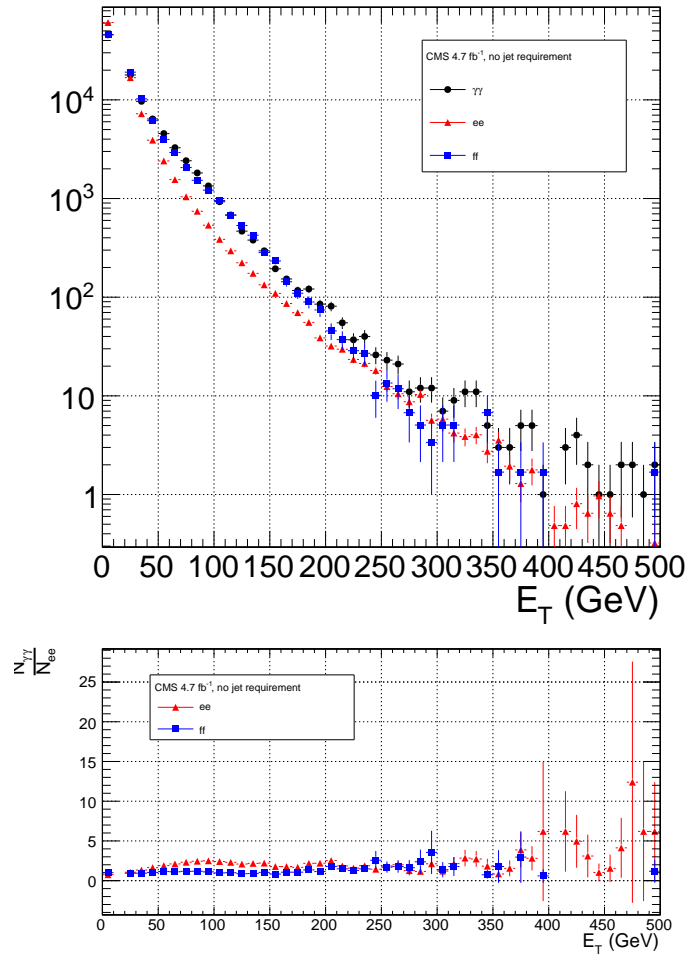


Figure 7.6: Corrected E_T for the jet with the largest corrected E_T per event, for jets defined as in Table 7.2 (excluding the p_T requirement). $\gamma\gamma$ is in black, ee ($81 \text{ GeV} \leq m_{ee} < 101 \text{ GeV}$) is in red, and ff is in blue. The ee and ff distributions are normalized to the number of events in the $\gamma\gamma$ distribution. Errors are statistical only.

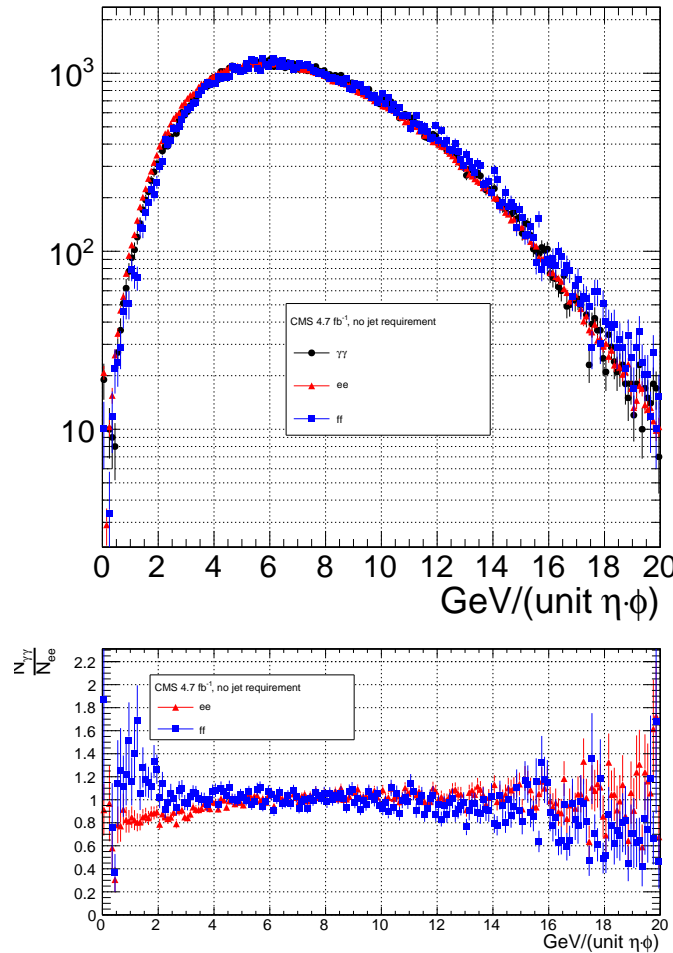


Figure 7.7: ρ (average pileup energy density in the calorimeters per unit $\eta \cdot \phi$, cf. Sec. 6.1.1). $\gamma\gamma$ is in black, ee ($81 \text{ GeV} \leq m_{ee} < 101 \text{ GeV}$) is in red, and ff is in blue. The ee and ff distributions are normalized to the number of events in the $\gamma\gamma$ distribution. Errors are statistical only.

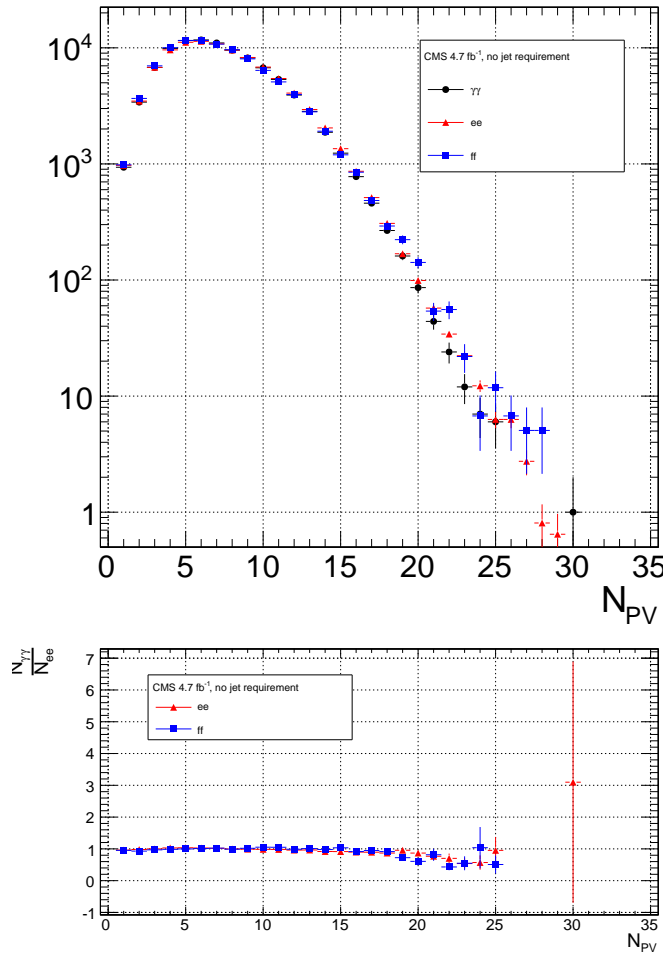


Figure 7.8: Number of good reconstructed primary vertices per event according to the criteria of Sec. 6.3. $\gamma\gamma$ is in black, ee ($81 \text{ GeV} \leq m_{ee} < 101 \text{ GeV}$) is in red, and ff is in blue. The ee and ff distributions are normalized to the number of events in the $\gamma\gamma$ distribution. Errors are statistical only.

Table 7.2: Definition of HB/HE/HF hadronic jets.

Variable	Cut
Algorithm	L1FastL2L3Residual corrected PF (cf. Sec. 6.1.3)
p_T	$> 30 \text{ GeV}$
$ \eta $	< 5.0
Neutral hadronic energy fraction	< 0.99
Neutral electromagnetic energy fraction	< 0.99
Number of constituents	> 1
Charged hadronic energy	$> 0.0 \text{ GeV}$ if $ \eta < 2.4$
Number of charged hadrons	> 0 if $ \eta < 2.4$
Charged electromagnetic energy fraction	< 0.99 if $ \eta < 2.4$
ΔR to nearest PF electron ^a , muon ^b , or one of the two primary EM objects	> 0.5

^aA PF electron is defined as an electron reconstructed with the PF algorithm [86] with $p_T > 15 \text{ GeV}$, $|\eta| < 2.6$, and $(I_{\text{charged}} + I_{\text{photon}} + I_{\text{neutral}})/p_T < 0.2$, where $I_{\text{charged}}(I_{\text{photon}})(I_{\text{neutral}})$ is the sum of PF charged hadron(PF photon)(PF neutral hadron) momenta in a $\Delta R = 0.4$ cone around the PF electron.

^bMuons are reconstructed [87] from a combination of muon station and inner tracker hits. Here, a muon must have track $\chi^2 < 10$, at least one good muon station hit, inner track transverse impact parameter $< 0.02 \text{ cm}$, inner track longitudinal impact parameter $< 0.5 \text{ cm}$, $p_T > 15 \text{ GeV}$, $|\eta| < 2.6$, and $(I_{\text{ECAL}} + I_{\text{HCAL}} + I_{\text{track}})/p_T < 0.2$, where $I_{\text{ECAL}}(I_{\text{HCAL}})(I_{\text{track}})$ is the sum of ECAL(HCAL)(track) momenta in a $\Delta R = 0.3$ cone around the muon.

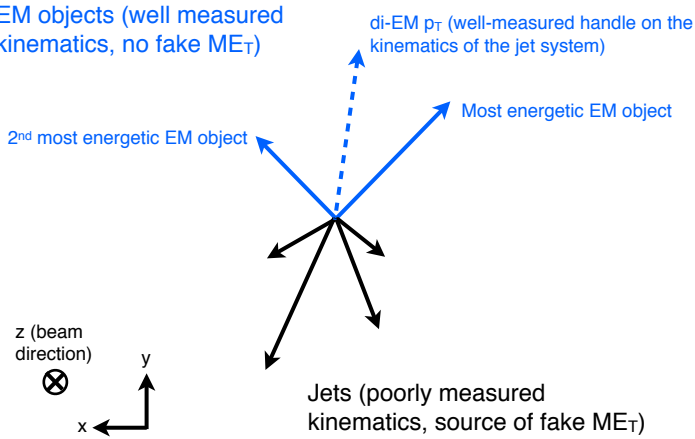
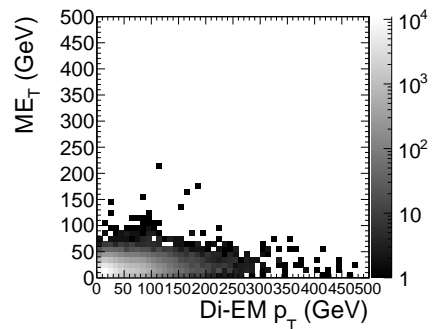
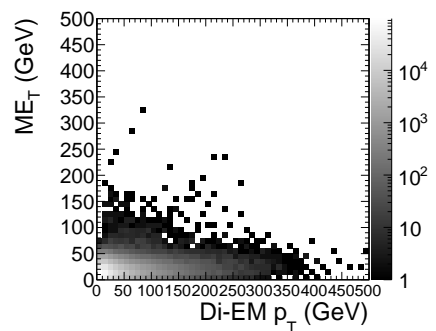
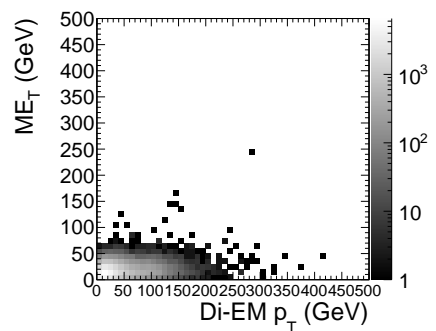


Figure 7.9: Cartoon showing the di-EM system in blue and the hadronic recoil in black. The di-EM p_T (dashed blue line) is used to reweight the control sample kinematic properties to match those of the candidate $\gamma\gamma$ sample.

1798 in Figure 7.9. As shown in Figure 7.10, E_T is largely uncorrelated with di-EM p_T , so
 1799 there is little danger of reweighting away a true signal excess.

1800 Whereas the di-EM p_T reweighting accounts for differences in production kine-
 1801 matics between the control and $\gamma\gamma$ samples, a simultaneous reweighting based on
 1802 the number of jets in the event accounts for differences in hadronic activity between
 1803 the samples, especially between ee and $\gamma\gamma$ (cf. Figs. 7.3- 7.8). Jets are defined as in
 1804 Table 6.2. Figure 7.11 shows the effect of reweighting by number of jets per event,
 1805 which is to increase(decrease) the tail of the ee (ff) E_T spectrum.

1806 Although the electron and photon energies are well measured by the ECAL, the
 1807 ECAL-only measurement of the fake photon energy (cf. Sec 6.1.1) is biased slightly
 1808 low due to the fact that fakes (which are really jets) tend to deposit some energy in
 1809 the HCAL. This can be seen in Figs. 7.12 and 7.13, which show the relative difference
 1810 between the ECAL-only E_T measurement and the PF E_T measurement vs. EMF for
 1811 electrons, photons, and fakes. PF E_T is defined as the L1Fast-corrected E_T of the
 1812 nearest PF jet with $p_T \geq 20$ GeV (i.e., the E_T of the PF jet object reconstructed from
 1813 the same ECAL shower as the fake photon). On average, the high-EMF fakes, which

(a) $\gamma\gamma$.(b) ee .(c) ff .Figure 7.10: E_T vs. di-EM p_T .

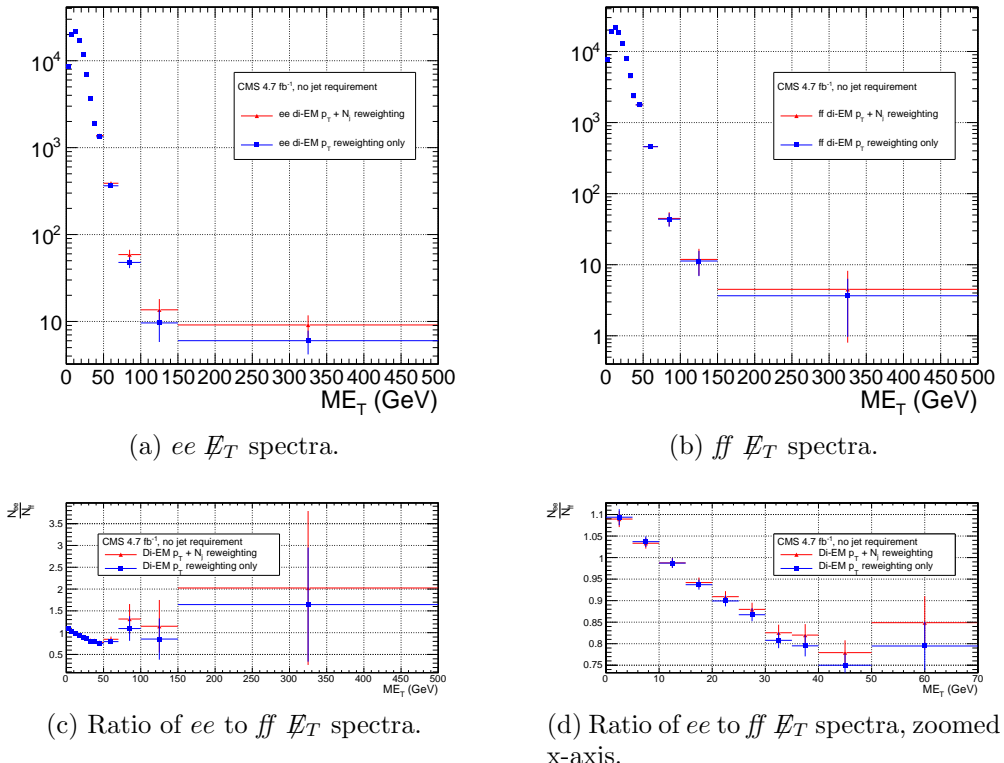


Figure 7.11: \cancel{E}_T spectra of the reweighted ee ($81 \text{ GeV} \leq m_{\text{ee}} < 101 \text{ GeV}$) and ff control samples. Blue squares indicate di-EM p_T reweighting only; red triangles indicate di-EM $p_T + \text{number of jets}$ reweighting. PF p_T (cf. p. 137) is used to calculate the di-EM p_T . The full normalization procedure is employed, along with ee sideband subtraction (discussed at the end of this section). Error bars are statistical only.

1814 make up the bulk of the sample, tend to deposit a few percent more energy in the
 1815 HCAL than the electrons or photons. This energy is recovered by the PF algorithm.
 1816 For this reason, the PF p_T is used in the calculation of di-EM p_T rather than the
 1817 ECAL-only p_T .¹ This leads to a modest improvement in the agreement between the
 1818 ee and ff \cancel{E}_T spectra, as shown in Figure 7.14.

1819 The control sample event weights are defined as

$$w_{ij} = \frac{N_{\text{control}}}{N_{\gamma\gamma}} \frac{N_{\gamma\gamma}^{ij}}{N_{\text{control}}^{ij}} \quad (7.1)$$

1820 where i runs over the number of di-EM p_T bins, j runs over the number of jet bins,
 1821 N_{control} is the total number of events in the control sample, $N_{\gamma\gamma}$ is the total number of
 1822 events in the $\gamma\gamma$ sample, $N_{\gamma\gamma}^{ij}$ is the number of $\gamma\gamma$ events in the i^{th} di-EM p_T bin and
 1823 j^{th} jet bin, and N_{control}^{ij} is the number of control sample events in the i^{th} di-EM p_T
 1824 bin and j^{th} jet bin. The effect of the reweighting is more significant for the ee sample
 1825 than for the ff sample, as shown in Figure 7.15.

1826 The ee sample contains a non-negligible background of $t\bar{t}$ events in which both
 1827 W bosons decay to electrons. These events have significant real \cancel{E}_T from the two
 1828 neutrinos (unlike the $\gamma\gamma$ events), and therefore inflate the background estimate at
 1829 high \cancel{E}_T . In order to remove the $t\bar{t}$ contribution from the ee sample, a sideband
 1830 subtraction method is employed.

1831 Only events in the ee sample with $81 \text{ GeV} \leq m_{ee} < 101 \text{ GeV}$, where m_{ee} is the
 1832 di-electron invariant mass, are used in the QCD background estimate. This choice
 1833 maximizes the ratio of Z signal to background. The sidebands used to estimate the
 1834 background contribution within the Z window are defined such that $71 \text{ GeV} \leq m_{ee} <$
 1835 81 GeV and $101 \text{ GeV} \leq m_{ee} < 111 \text{ GeV}$.

¹In the few events ($\mathcal{O}(10^{-3})$) in which two PF jet objects, corresponding to the two electrons or fakes, are not found, the ECAL-only p_T is used.

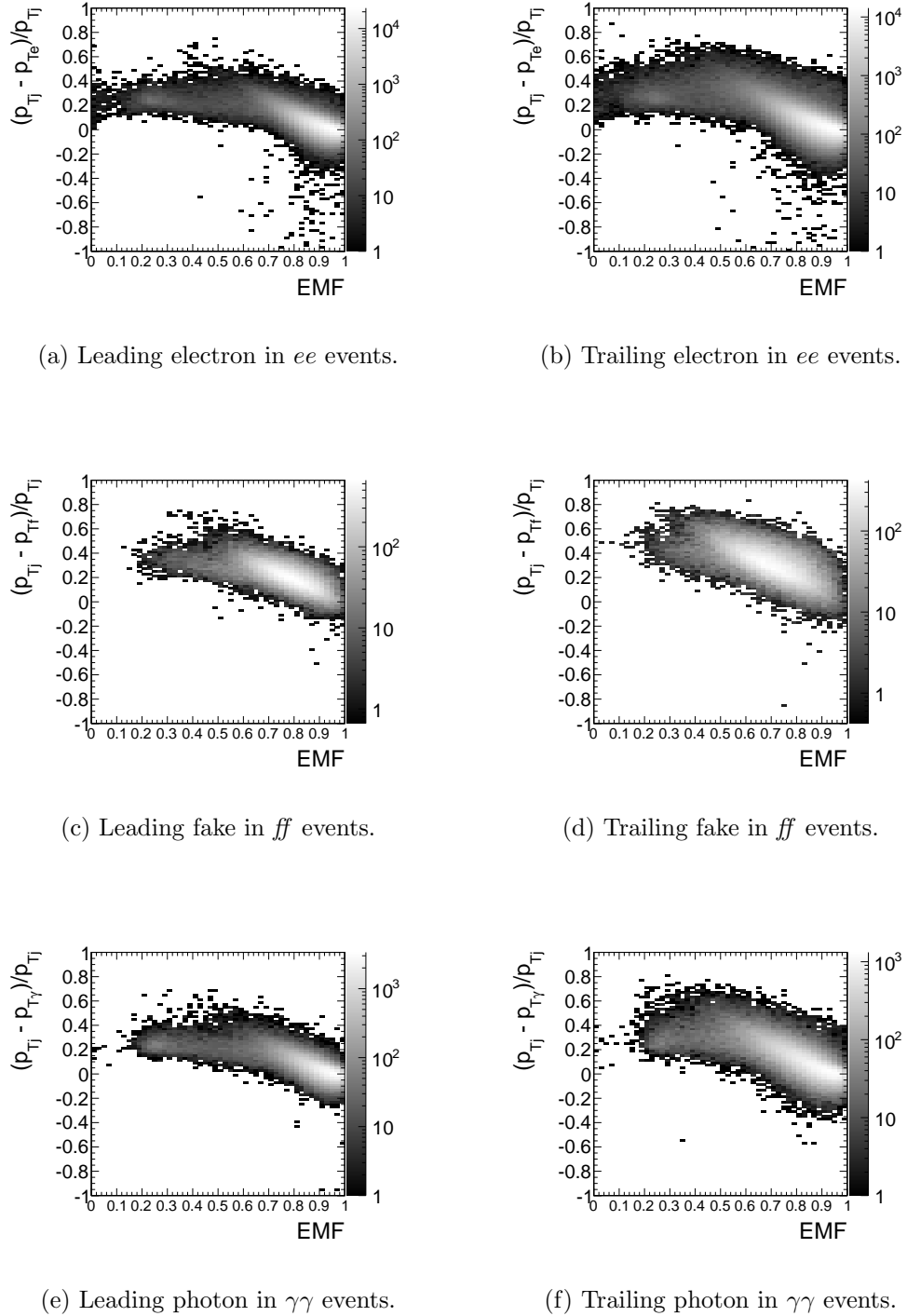


Figure 7.12: Relative difference between the ECAL-only E_T measurement and the PF E_T measurement vs. EMF. PF E_T is defined in the text.

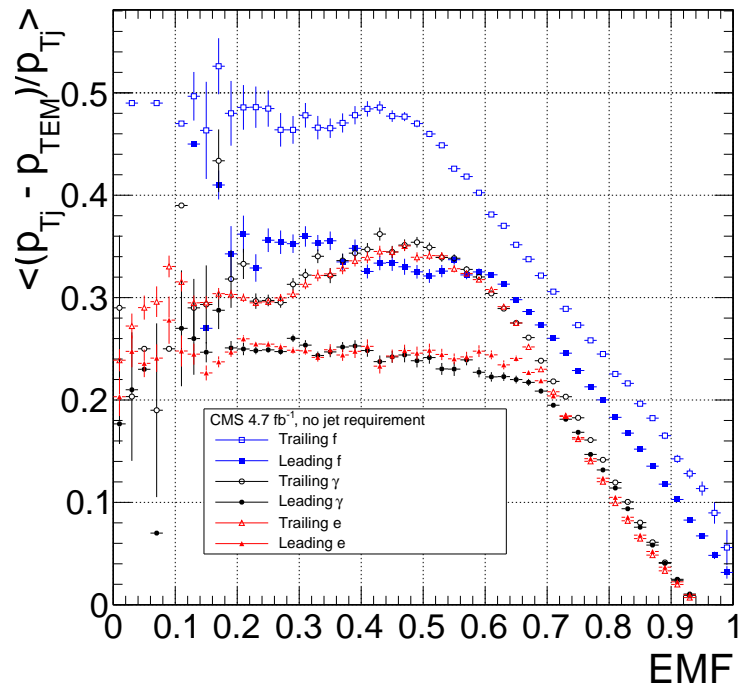


Figure 7.13: Average relative difference between the ECAL-only E_T measurement and the PF E_T measurement vs. EMF for the leading (filled marker) and trailing (open marker) electrons in ee events (red triangles), fakes in ff events (blue squares), and photons in $\gamma\gamma$ events (black circles). These are nothing more than profile histograms of Fig. 7.12. PF E_T is defined in the text. Error bars are statistical only.

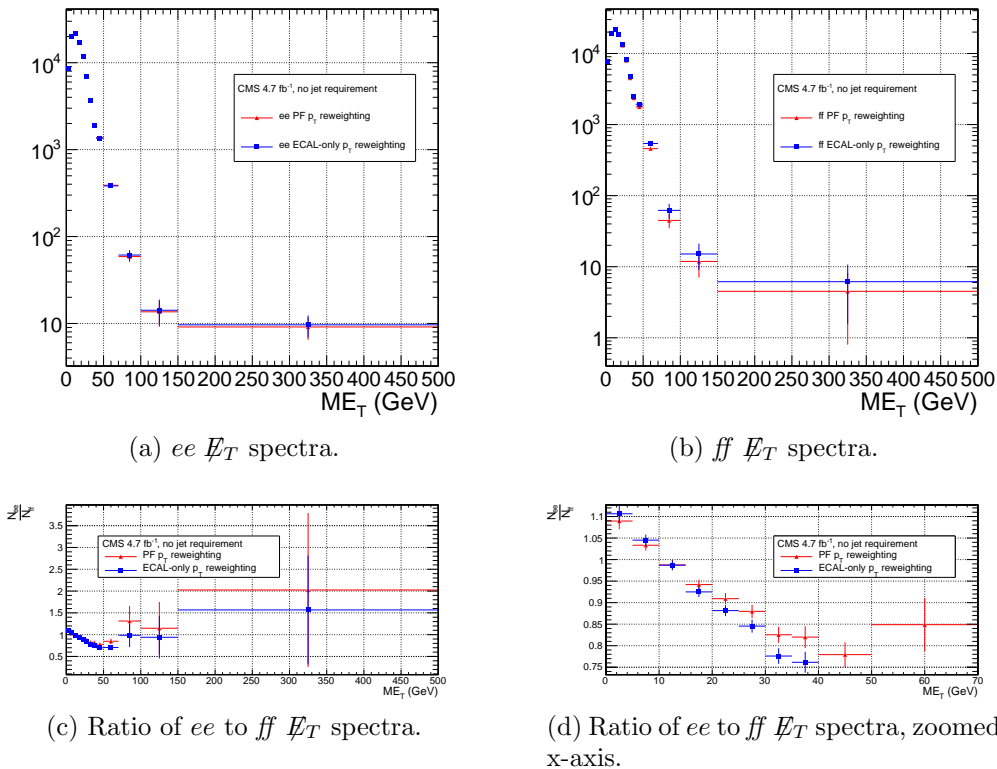


Figure 7.14: \cancel{E}_T spectra of the reweighted ee ($81 \text{ GeV} \leq m_{ee} < 101 \text{ GeV}$) and ff control samples. Blue squares indicate reweighting using the ECAL-only p_T estimate; red triangles indicate reweighting using the PF p_T estimate. The full reweighting and normalization procedure is employed, along with ee sideband subtraction (discussed at the end of this section). Error bars are statistical only.

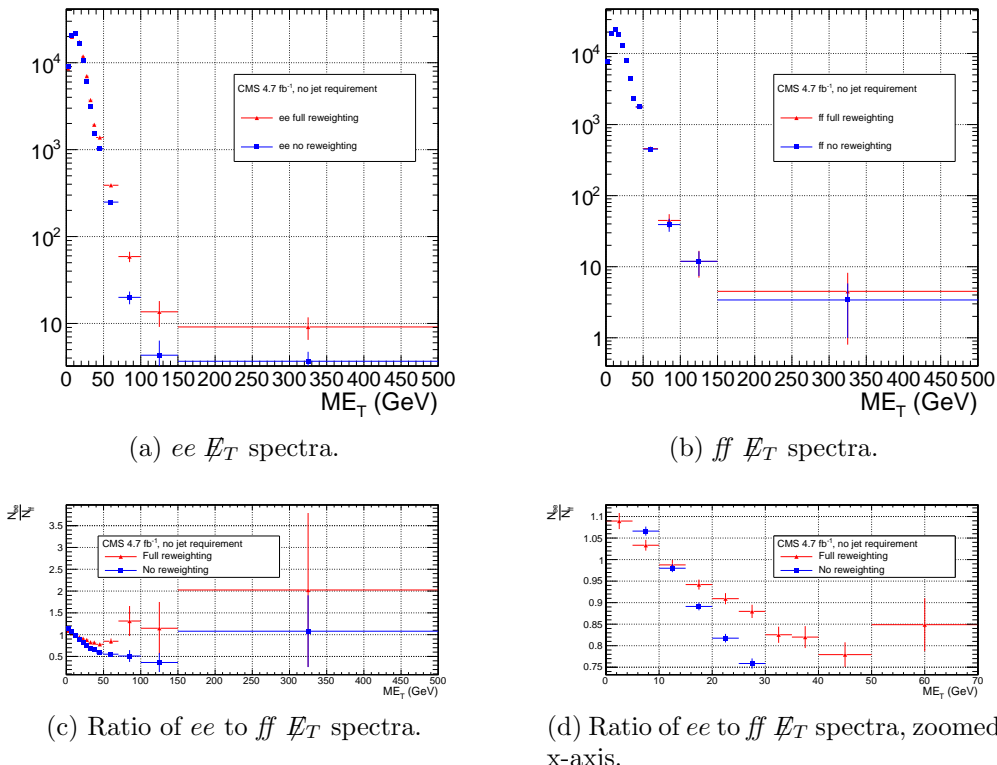


Figure 7.15: \cancel{E}_T spectra of the ee ($81 \text{ GeV} \leq m_{ee} < 101 \text{ GeV}$) and ff control samples. Red triangles indicate full di-EM $p_T +$ number of jets reweighting; blue squares indicate no reweighting. PF p_T (cf. p. 140) is used to calculate the di-EM p_T . The full normalization procedure is employed, along with ee sideband subtraction (discussed at the end of this section). Error bars are statistical only.

1836 The full reweighting procedure is applied to the Z signal region and the two
 1837 sideband regions independently. Only Z signal events are used in the calculation of
 1838 the di-EM p_T weights for the Z signal region, and likewise only the events within
 1839 a given sideband region are used in the calculation of the weights for that region.
 1840 Assuming a constant $t\bar{t}$ background shape, the resulting reweighted sideband \cancel{E}_T
 1841 distributions are added together and subtracted from the reweighted Z signal \cancel{E}_T
 1842 distribution. The sideband subtracted Z signal \cancel{E}_T distribution is then normalized
 1843 as discussed in Secs. 7.2.1 and 7.2.3. The statistical and reweighting error from the
 1844 sideband regions is propagated to the error on the final ee QCD \cancel{E}_T estimate.

1845 The di-EM p_T weights for the two ee sideband regions are shown in Figure 7.16.
 1846 The overall scale of the weights, as well as the trend with di-EM p_T , is similar for
 1847 the two regions (except at high di-EM p_T , where the statistics are poor anyway).
 1848 Figure 7.17 shows the \cancel{E}_T spectra for the two sideband regions and the Z signal
 1849 region after subtraction. The shapes of the spectra indicate that the high- \cancel{E}_T tail,
 1850 present in the sideband distributions, was successfully subtracted from the Z signal
 1851 distribution.

1852 The ee ($81 \text{ GeV} \leq m_{ee} < 101 \text{ GeV}$), ff , and $\gamma\gamma$ di-EM p_T spectra for events with
 1853 0, 1, or ≥ 2 jets (as in Table 6.2) are shown in Figure 7.18. Broad humps in the ff
 1854 and $\gamma\gamma$ spectra are due to kinematic ΔR and p_T turn-ons that are suppressed in the
 1855 ee sample due to the invariant mass cut. Figure 7.19 shows the weights applied to
 1856 the ee ($81 \text{ GeV} \leq m_{ee} < 101 \text{ GeV}$) and ff \cancel{E}_T spectra as a function of di-EM p_T and
 1857 number of jets per event.

1858 7.2.3 Normalization

1859 After reweighting, the \cancel{E}_T distributions of the QCD control samples are normalized
 1860 to the $\cancel{E}_T < 20 \text{ GeV}$ region of the candidate $\gamma\gamma$ \cancel{E}_T spectrum, where signal con-
 1861 tamination is low. The normalization factor is $(N_{\gamma\gamma}^{\cancel{E}_T < 20 \text{ GeV}} - N_{e\gamma}^{\cancel{E}_T < 20 \text{ GeV}})/N_{\text{control}}^{\cancel{E}_T < 20 \text{ GeV}}$,

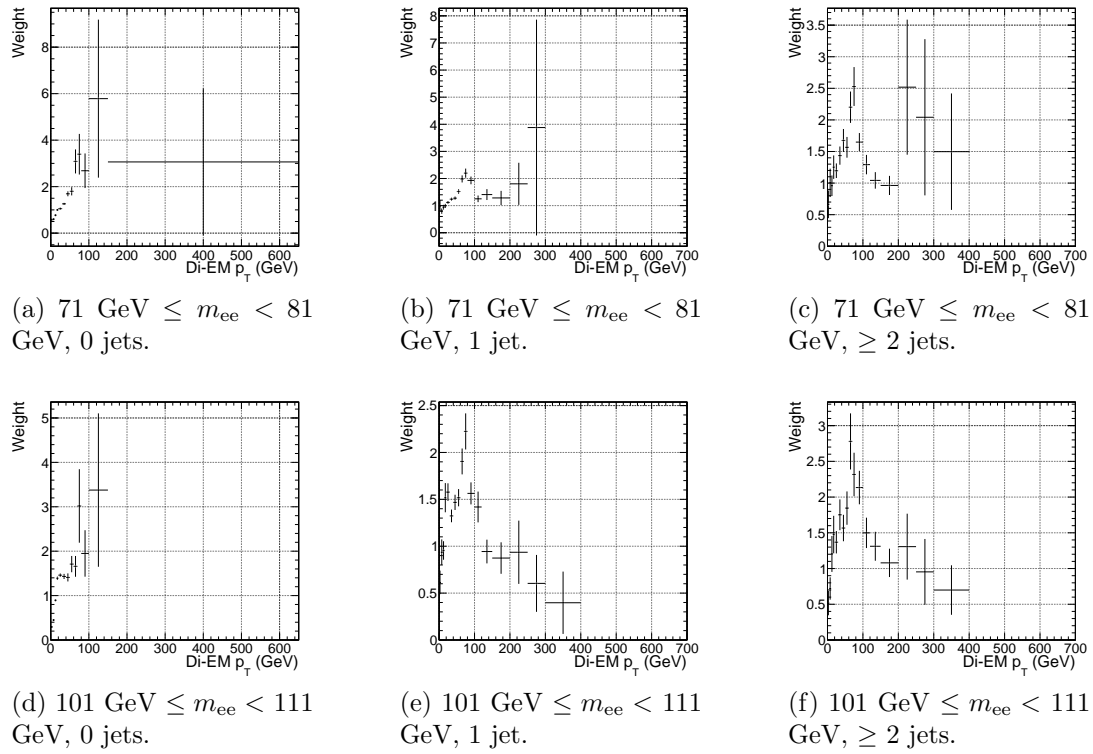


Figure 7.16: ee sideband di-EM p_T weights for events with 0, 1, or ≥ 2 jets (as in Table 6.2). Errors are statistical only.

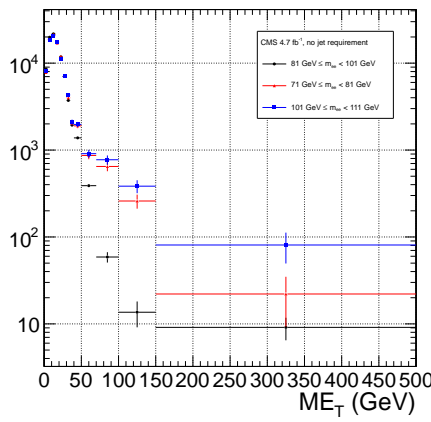
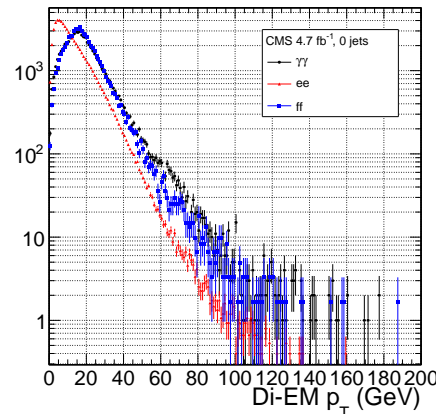
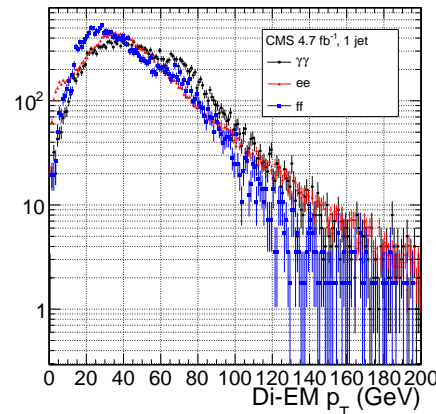


Figure 7.17: E_T spectra of the ee sample for $71 \text{ GeV} \leq m_{ee} < 81 \text{ GeV}$ (red triangles), $81 \text{ GeV} \leq m_{ee} < 101 \text{ GeV}$ (black circles), and $101 \text{ GeV} \leq m_{ee} < 111 \text{ GeV}$ (blue squares). The two sideband distributions (red and blue) and the Z signal distribution (black) are normalized to the total number of $\gamma\gamma$ events. Errors are statistical only.



(a) 0 jets.



(b) 1 jet.

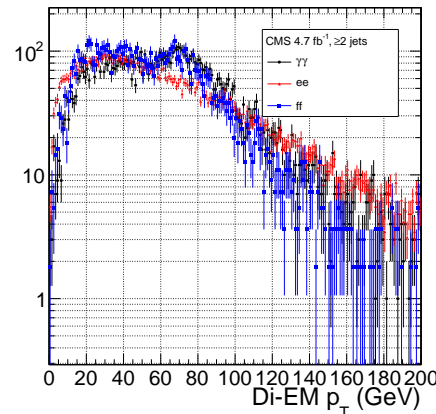
(c) ≥ 2 jets.

Figure 7.18: ee ($81 \text{ GeV} \leq m_{ee} < 101 \text{ GeV}$) (red triangles), ff (blue squares), and $\gamma\gamma$ (black circles) di-EM p_T spectra for events with 0, 1, or ≥ 2 jets (as in Table 6.2). Errors are statistical only.

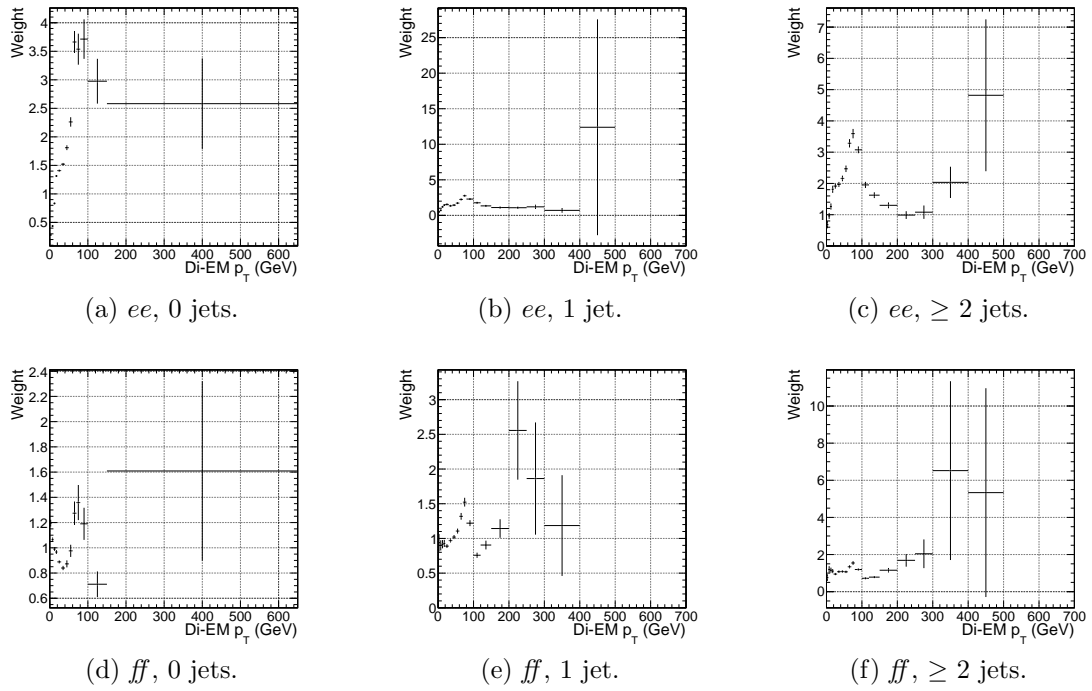


Figure 7.19: ee ($81 \text{ GeV} \leq m_{ee} < 101 \text{ GeV}$) and ff di-EM p_T weights for events with 0, 1, or ≥ 2 jets (as in Table 6.2). Errors are statistical only.

1862 where $N_{e\gamma}^{E_T < 20 \text{ GeV}}$ is the expected number of electroweak background events with E_T
 1863 $< 20 \text{ GeV}$ (discussed in Section 7.3). The error on the QCD background prediction
 1864 introduced by normalization is discussed in Sec. 7.4.

1865 7.3 Modeling the Electroweak Background

1866 $W\gamma$, $W + \text{jet}$, and $t\bar{t}$ processes in which the W decay electron is misidentified as a
 1867 photon (due to a failure to properly associate a pixel seed to the electron candidate)
 1868 can contribute significantly to the high- E_T tail of the $\gamma\gamma E_T$ spectrum. To estimate
 1869 this background, the $e\gamma$ sample, which is enriched in $W \rightarrow e\nu$ decays, is scaled by
 1870 $f_{e \rightarrow \gamma}/(1 - f_{e \rightarrow \gamma})$, where $f_{e \rightarrow \gamma}$ is the rate at which electrons are misidentified as photons.
 1871 The derivation of this scaling factor comes from the two equations

$$N_{e\gamma}^W = f_{e \rightarrow e} N_W \quad (7.2)$$

$$N_{\gamma\gamma}^W = (1 - f_{e \rightarrow e}) N_W \quad (7.3)$$

where $N_{e\gamma}^W$ is the number of W events in the $e\gamma$ sample in which the electron was correctly identified, $f_{e \rightarrow e}$ is the probability to correctly identify an electron, N_W is the true number of triggered $W \rightarrow e\nu$ events, and $N_{\gamma\gamma}^W$ is the number of W events in the $\gamma\gamma$ sample in which the electron was misidentified as a photon. The contribution from $Z \rightarrow ee$ can be neglected (i.e. $f_{e \rightarrow \gamma}$ is small and the Z contribution involves $f_{e \rightarrow \gamma}^2$, since both electrons have to be misidentified). Since $f_{e \rightarrow e} = 1 - f_{e \rightarrow \gamma}$, solving for $N_{\gamma\gamma}^W$ gives

$$N_{\gamma\gamma}^W = \frac{f_{e \rightarrow \gamma}}{1 - f_{e \rightarrow \gamma}} N_{e\gamma}^W \quad (7.4)$$

$f_{e \rightarrow \gamma}$ is measured by fitting the Z peaks in the ee and $e\gamma$ samples. The number of Z events fitted in the ee and $e\gamma$ samples, respectively, is given by

$$N_{ee}^Z = (1 - f_{e \rightarrow \gamma})^2 N_Z \quad (7.5)$$

$$N_{e\gamma}^Z = 2f_{e \rightarrow \gamma}(1 - f_{e \rightarrow \gamma}) N_Z \quad (7.6)$$

where N_Z is the true number of triggered $Z \rightarrow ee$ events. Solving for $f_{e \rightarrow \gamma}$ gives

$$f_{e \rightarrow \gamma} = \frac{N_{e\gamma}^Z}{2N_{ee}^Z + N_{e\gamma}^Z} \quad (7.7)$$

1882 A Crystal Ball function is used to model the Z signal shape in both the ee and
 1883 $e\gamma$ samples, while an exponential convoluted with an error function (`RooCMSShape`,
 1884 see Sec. 6.4.1) is used to model the background shape. The fixed fit parameters are
 1885 identical for the two samples, but the other parameters are allowed to float indepen-
 1886 dently. Table 7.3 shows the values and ranges of the fixed and floating fit parameters,
 1887 respectively.

Table 7.3: Parameter values for the signal and background PDFs for the ee and $e\gamma$ samples. When a bracketed range is given, the parameter is allowed to float within that range. When a constant is given, the parameter is fixed to that constant.

PDF	Crystal Ball fit parameters				<code>RooCMSShape</code> fit parameters			
	μ	σ	α	n	μ	α	β	γ
ee sig- nal	[86.2, 96.2]	[1.0, 5.0]	1.063	143.16	N/A	N/A	N/A	N/A
$e\gamma$ sig- nal	[86.2, 96.2]	[1.0, 5.0]	1.063	143.16	N/A	N/A	N/A	N/A
ee back- ground	N/A	N/A	N/A	N/A	58	97.0	0.0922	0.191
$e\gamma$ back- ground	N/A	N/A	N/A	N/A	56	72.02	0.098	0.0375

1888 Fits to the ee and $e\gamma$ invariant mass spectra are shown in Figure 7.20. Figure 7.21a
 1889 indicates that there is some dependence of $f_{e \rightarrow \gamma}$ on the electron p_T , but since the the
 1890 bulk of the electrons have $p_T \sim 45$ GeV, applying a p_T -dependent mis-identification
 1891 rate has a negligible effect on the final background estimate. (Note that all fit param-
 1892 eters are floating in the p_T -dependent fits.) The dependence on η is small, as shown
 1893 in Figure 7.21b. Therefore, a constant misidentification rate (derived from all ee and
 1894 $e\gamma$ events), rather than a p_T - and η -dependent misidentification rate, is used in the
 1895 final electroweak background estimate, with the difference between the constant rate
 1896 and the rate for electrons with p_T between 25 and 40 GeV (the range in which the
 1897 bulk of the trailing photons in the $\gamma\gamma$ sample lie) taken as a systematic error.

1898 Using the integrals of the Z fits shown in Fig. 7.20, Eq. 7.7, and the p_T systematic

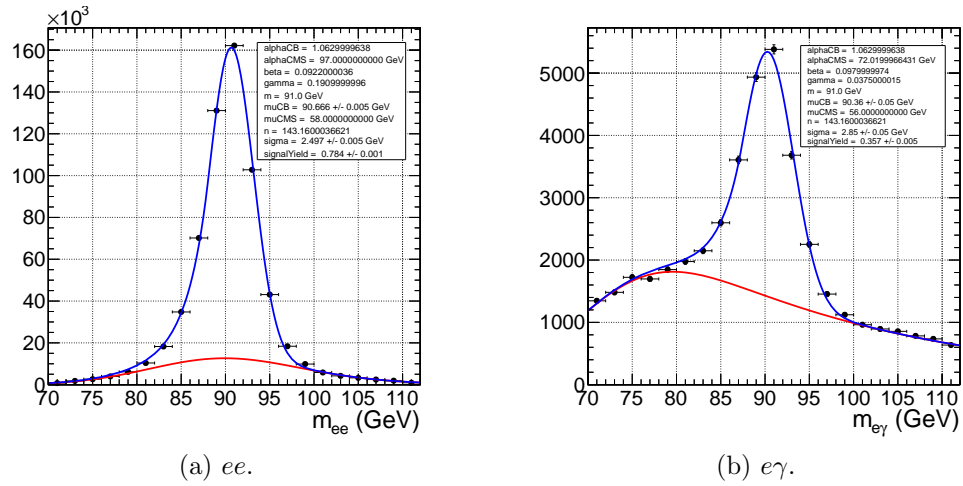
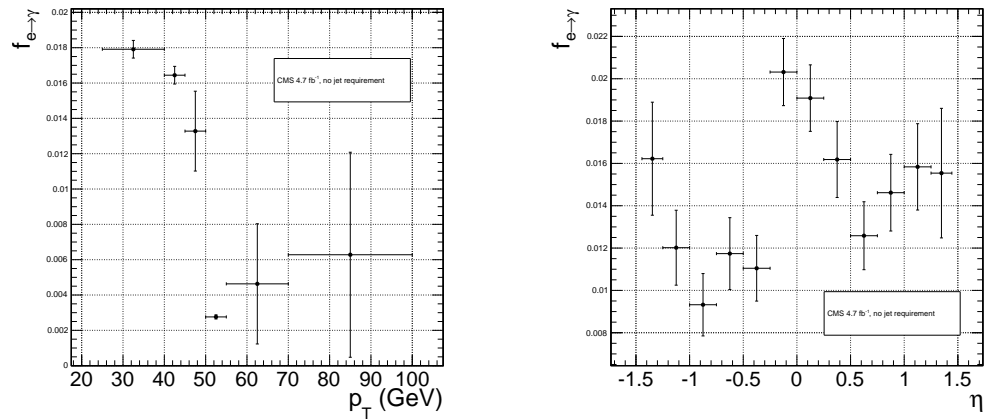


Figure 7.20: Fits to the ee and $e\gamma$ invariant mass spectra using the Crystal Ball RooCMSShape function described in the text and in Table 7.3. The total fit is shown in blue, while the background component is shown in red.



(a) $f_{e\rightarrow\gamma}$ vs. electron p_T . For the lowest p_T bin, the fit to the $e\gamma$ spectrum does not converge well, so the Z signal fraction is fixed to the value in Fig. 7.20b.

(b) $f_{e\rightarrow\gamma}$ vs. electron η .

Figure 7.21: $f_{e\rightarrow\gamma}$ vs. electron p_T and η .

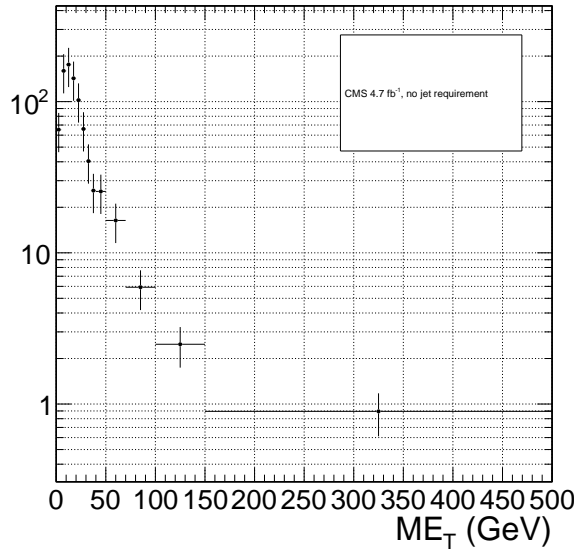


Figure 7.22: \cancel{E}_T spectrum of the $e\gamma$ sample after scaling by $f_{e\rightarrow\gamma}$. The total error on $f_{e\rightarrow\gamma}$ is propagated to the total error on the electroweak background estimate.

1899 discussed above, $f_{e\rightarrow\gamma}$ is calculated to be $0.014 \pm 0.000(\text{stat.}) \pm 0.004(\text{syst.})$. The
1900 scaled $e\gamma$ MET distribution is shown in Figure 7.22.

1901 In the 36 pb^{-1} version of this analysis [112], it was shown that the ee sample could
1902 accurately predict the QCD and real Z contribution to the $e\gamma$ sample at low \cancel{E}_T , and
1903 that the expectation from $W \rightarrow e\nu$ MC accounted for the remaining W contribution
1904 at high \cancel{E}_T . A plot of the \cancel{E}_T distributions of the 2010 $e\gamma$ sample and the predicted
1905 components is shown in Figure 7.23. This exercise helps to validate both the QCD
1906 and electroweak background prediction methods.

1907 7.4 Errors on the Background Prediction

1908 The statistical error on the final background estimate in a particular \cancel{E}_T bin comes
1909 from three sources: the number of control sample events collected in that bin, the
1910 statistical error on the weights applied to events in that bin, and the statistics of the
1911 normalization region. In the case of the ee control sample, there are contributions
1912 from the statistics of the m_{ee} sidebands as well.

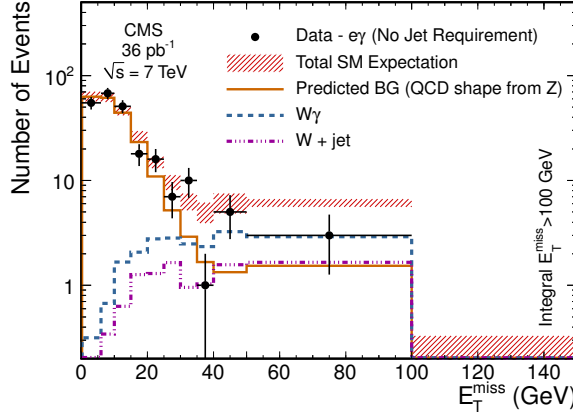


Figure 7.23: E_T spectrum of the $e\gamma$ sample in 35 pb^{-1} of 2010 LHC data scaled by the 2010 measured $f_{e \rightarrow \gamma}$ (black dots), QCD and real Z predicted background from the 2010 ee sample (solid orange line), MC $W + \text{jet}$ estimate (dash-dotted purple line), and MC $W\gamma$ estimate (dashed blue line). The total $e\gamma$ prediction (red band) is the sum of the ee , $W + \text{jet}$, and $W\gamma$ predictions. Reprinted from Fig. 2 of ref. [112].

1913 In order to propagate the statistical error due to the reweighting procedure to
 1914 the shape of the final QCD E_T distribution, 1000 toy sets of weights are generated.
 1915 Each set includes a weight for each (di-EM p_T , N_j) bin, with the values picked from a
 1916 Gaussian distribution with mean and standard deviation equal to the observed weight
 1917 for that bin and its statistical error. The effect of reweighting error is not correlated
 1918 between E_T bins. For each of the 1000 experiments, the control sample data are
 1919 reweighted according to the generated weights, and the background estimates are
 1920 calculated for each E_T bin. Since the distribution of the toy background estimates
 1921 follows a Gaussian distribution in each E_T bin, the RMS spread of the estimates is
 1922 taken as the statistical error due to reweighting. This procedure is carried out for the
 1923 ff , ee , low sideband ee , and high sideband ee samples.

1924 The total statistical error on the background estimate per E_T bin is given by

$$\sigma_{\text{stat}}^2 = \sigma_{\text{stat,QCD}}^2 + \sigma_{\text{stat,EW}}^2 \quad (7.8)$$

1925 where $\sigma_{\text{stat,QCD}}^2$ is the square of the total statistical error on the QCD prediction in
 1926 the \cancel{E}_T bin

$$\sigma_{\text{stat,QCD}}^2 = \sigma_{\text{stat},s}^2 + \sigma_{\text{Poisson,QCD}}^2 + \sigma_{\text{reweight},s}^2 + \sigma_{\text{reweight,QCD}}^2 \quad (7.9)$$

1927 and $\sigma_{\text{stat,EW}}$ is the Poisson error on the number of $e\gamma$ events in the \cancel{E}_T bin ($= \sqrt{N_{e\gamma}}$,
 1928 where $N_{e\gamma}$ is the prediction in the \cancel{E}_T bin after scaling by $f_{e\rightarrow\gamma}$). The contributions
 1929 to $\sigma_{\text{stat,QCD}}^2$ are discussed below.

- 1930 • $\sigma_{\text{stat},s}^2$ is the statistical error contributed by the normalization factor s (i.e. from
 1931 Poisson error in the normalization region $\cancel{E}_T < 20$ GeV):

$$\begin{aligned} \sigma_{\text{stat},s}^2 = & \frac{N_{\text{control}}^2}{(N_{\gamma\gamma}^{\text{norm}} - N_{e\gamma}^{\text{norm}})^2} ([\sigma_{\text{Poisson},\gamma\gamma}^{\text{norm}}]^2 + [\sigma_{\text{Poisson},e\gamma}^{\text{norm}}]^2) + \\ & \frac{N_{\text{control}}^2}{(N_{\text{control}}^{\text{norm}})^2} (\sigma_{\text{Poisson,control}}^{\text{norm}})^2 \end{aligned} \quad (7.10)$$

1932 where N_{control} is the number of reweighted, normalized events in the \cancel{E}_T bin,
 1933 $N_{\gamma\gamma}^{\text{norm}}$ is the number of $\gamma\gamma$ events in the normalization region, $N_{e\gamma}^{\text{norm}}$ is the num-
 1934 ber of $e\gamma$ events in the normalization region (after scaling by $f_{e\rightarrow\gamma}$), $\sigma_{\text{Poisson},\gamma\gamma}^{\text{norm}}$
 1935 is the Poisson error on the number of $\gamma\gamma$ events in the normalization region
 1936 ($= \sqrt{N_{\gamma\gamma}^{\text{norm}}}$), $\sigma_{\text{Poisson},e\gamma}^{\text{norm}}$ is the Poisson error on the number of $e\gamma$ events in the
 1937 normalization region ($= \sqrt{N_{e\gamma}^{\text{norm}}}$), $N_{\text{control}}^{\text{norm}}$ is the number of QCD control (ee
 1938 or ff) events in the normalization region, and $\sigma_{\text{Poisson,control}}^{\text{norm}}$ is the Poisson error
 1939 on the number of QCD control (ee or ff) events in the normalization region
 1940 ($= \sqrt{\sum_{i=1}^{N_{\text{control}}^{\text{norm}}} w_i^2}$, where w_i is the di-EM p_T weight applied to event i). For
 1941 the ee control region, N_{control} and $N_{\text{control},\text{norm}}$ are sideband subtracted, and
 1942 $\sigma_{\text{Poisson,control}}^{\text{norm}}$ includes the Poisson error on the number of sideband events.

- 1943 • $\sigma_{\text{Poisson,QCD}}$ is the Poisson error due to the number of QCD control (ee or ff)
1944 events in the \cancel{E}_T bin, equal to $\sqrt{\sum_{i=1}^{N_{\text{control}}} w_i^2}$, where w_i is the di-EM p_T weight
1945 applied to event i . For the ee control region, $\sigma_{\text{Poisson,QCD}}$ includes the Poisson
1946 error on the number of subtracted sideband events.

- 1947 • $\sigma_{\text{reweight},s}$ is the error contributed by the control sample reweighting in the nor-
1948 malization region ($= \frac{N_{\text{control}}^2}{(N_{\text{control}}^{\text{norm}})^2} \sigma_{\text{reweight,control}}^{\text{norm}}$). $\sigma_{\text{reweight,control}}^{\text{norm}}$ is the quadrature
1949 sum of the RMS of the 1000 toy reweighting experiments for each \cancel{E}_T bin in the
1950 normalization region. For the ee control sample, it also includes (in quadrature)
1951 the RMS of the toys in the sideband samples.

- 1952 • $\sigma_{\text{reweight,QCD}}$ is the error contributed by the control sample reweighting in the \cancel{E}_T
1953 bin ($= s \sigma_{\text{reweight,control}}$). $\sigma_{\text{reweight,control}}$ is the RMS of the 1000 toy reweighting
1954 experiments for the E_T bin. For the ee control sample, it also includes (in
1955 quadrature) the RMS of the toys in the sideband samples.

1956 The difference in hadronic activity between the ee , ff , and $\gamma\gamma$ samples results in
1957 a small bias (~ 1 GeV) of the ee \cancel{E}_T distribution towards lower values with respect
1958 to the ff and $\gamma\gamma$ samples, as shown in Figure 7.24. Therefore, the ff sample is used
1959 as the primary QCD background estimator, and the difference between the ee and ff
1960 predictions is assigned as an error on the knowledge of the hadronic activity. For \cancel{E}_T
1961 > 100 GeV, this error amounts to 43% of the total QCD + electroweak background
1962 estimate, and is the dominant source of systematic error.

1963 The second largest source of systematic error comes from the p_T dependence of the
1964 $e \rightarrow \gamma$ misidentification rate (see 7.3). For $\cancel{E}_T > 100$ GeV, the expected electroweak
1965 background is 3.4 ± 1.0 events, so this error amounts to 4.8% of the total QCD +
1966 electroweak background estimate.

1967 The assumption of a constant $t\bar{t}$ and $W + \text{jets}$ background shape under the Z
1968 peak in the ee sample induces a systematic error on the ee sideband-subtracted back-

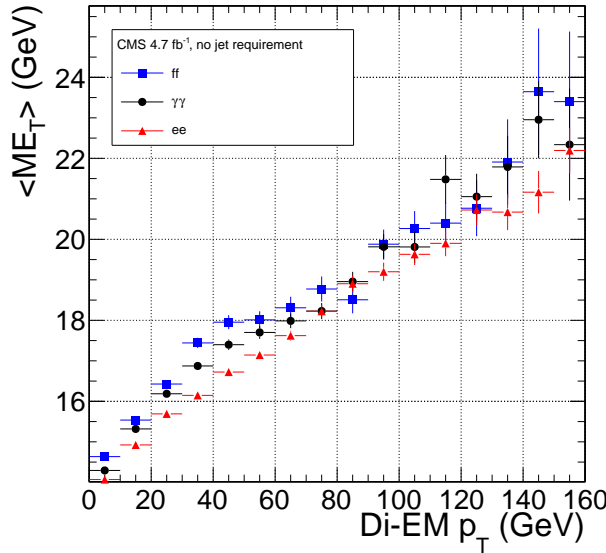


Figure 7.24: Average \cancel{E}_T vs. di-EM p_T for the ff (blue squares), ee (red triangles), and $\gamma\gamma$ (black circles) samples.

1969 ground prediction. To assess the magnitude of this error, the sideband subtraction
 1970 (see Sec. 7.2.2) is performed once using only the prediction from the high sideband,
 1971 and once using only the prediction from the low sideband. In each of these cases, the
 1972 prediction is weighted by a factor of two, to account for the fact that the sideband
 1973 regions are only half as wide (10 GeV) as the signal region (20 GeV). The maximum
 1974 variation from the nominal ee estimate is taken as the error, which amounts to 11%
 1975 for $\cancel{E}_T > 100$ GeV. \cancel{E}_T distributions using the nominal ee sideband subtraction, the
 1976 low-sideband-only subtraction, and the high-sideband-only subtraction are shown in
 1977 Figure 7.25.

Added

1978 Finally, the few percent error on the jet energy correction factors introduces an this
 1979 error on the final background estimate through (a) the use of the PF p_T to measure para-
 1980 the di-EM p_T , (b) the counting of jets passing a 30 GeV p_T threshold for placement of graph
 1981 the event in an N_j bin for reweighting, and (c) the counting of jets above threshold for
 1982 the ≥ 1 -jet version of the selection. To estimate this error, 100 pseudo-experiments
 1983 are generated with identical properties as the true data sample, except with corrected
 1984 jet energies (in all events) all shifted by an amount $r\sigma(p_T, \eta)$. r is a random number

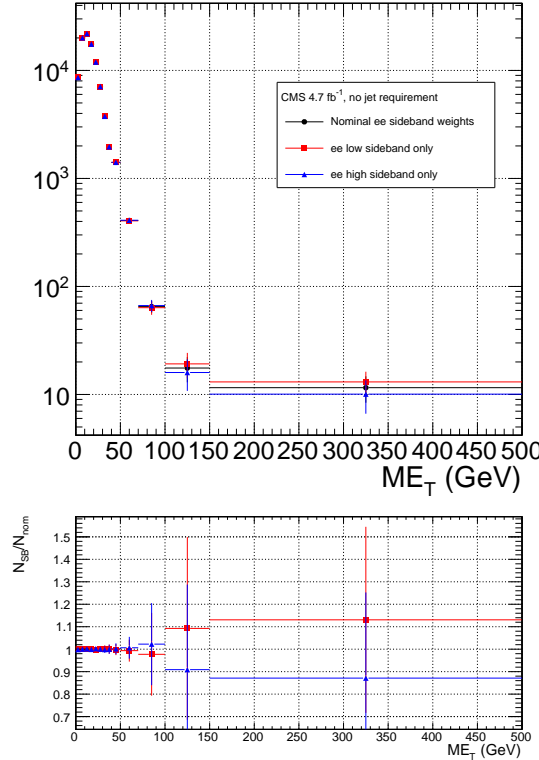


Figure 7.25: ee \cancel{E}_T distributions using the nominal sideband subtraction (black circles), low sideband only (red squares), and high sideband only (blue triangles). The bottom plot shows the ratio of the low sideband distribution to the nominal (red squares) and the ratio of the high sideband distribution to the nominal (blue triangles).

1985 drawn from a Gaussian distribution with mean 0 and width 1, and $\sigma(p_T, \eta)$ is the
 1986 uncertainty on the jet energy correction factor (which, like the correction factor itself,
 1987 is a function of p_T and η). The same factor r is applied to all jets in all events in the
 1988 pseudo-experiment because the jet energy correction errors are correlated from jet to
 1989 jet (they result from e.g. uncertainties in MC simulation or uncertainties in ECAL
 1990 energy scale [91]). The standard error of the mean of the 100 resulting background
 1991 estimates in each relevant \cancel{E}_T bin is taken as the error. The error in each \cancel{E}_T bin is
 1992 assumed to be uncorrelated. This process is repeated for both the inclusive and ≥ 1 -
 1993 jet selections. For $\cancel{E}_T \geq 100$ GeV, the jet energy correction uncertainty is 1.5% (2.2%)
 1994 of the total background for the inclusive (≥ 1 -jet) selection.

1995 The uncertainty in how to define the (di-EM p_T , N_j) bins, especially at high di-

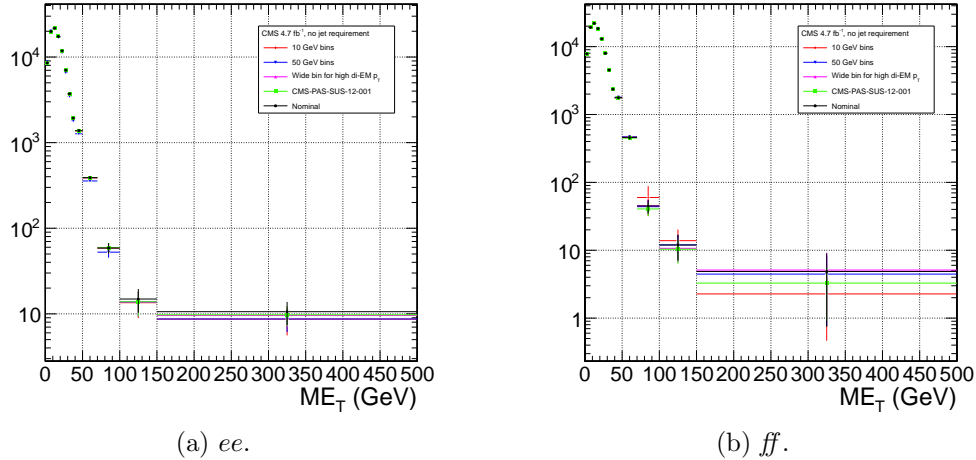


Figure 7.26: Comparison of \cancel{E}_T distributions for five different di-EM p_T bin definitions: uniform bins of width 10 GeV (red diamonds); uniform bins of width 50 GeV (blue downward-pointing triangles); bins with lower edges $\{0.0, 5.0, 10.0, 15.0, 20.0, 30.0, 40.0, 50.0, 60.0, 70.0, 80.0, 100.0, 750.0\}$ GeV for 0-jet events and $\{0.0, 5.0, 10.0, 15.0, 20.0, 30.0, 40.0, 50.0, 60.0, 70.0, 80.0, 100.0, 150.0\}$ GeV for ≥ 1 -jet events (magenta upward-pointing triangles), i.e. a single wide bin at high di-EM p_T ; bins with lower edges $\{0.0, 5.0, 10.0, 15.0, 20.0, 30.0, 40.0, 50.0, 60.0, 70.0, 80.0, 100.0, 150.0\}$ GeV for 0-jet events and $\{0.0, 5.0, 10.0, 15.0, 20.0, 30.0, 40.0, 50.0, 60.0, 70.0, 80.0, 100.0, 120.0, 150.0, 200.0, 700.0\}$ GeV for ≥ 1 -jet events (green squares), i.e. the bins used in ref. [29]; and the nominal bin definitions shown in Fig. 7.19 (black circles).

1996 EM p_T where the statistics are low, is covered by the 1000-toys procedure as long as
 1997 the bins are not too coarse. This is shown in Figure 7.26. If the bins are too coarse,
 1998 the details of the shape of the di-EM p_T spectra are lost, and the reweighting has a
 1999 smaller effect.

2000 The use of uncorrected instead of corrected PF \cancel{E}_T (see Sec. 6.1.3) makes no
 2001 difference in the agreement of the background predictions and the search sample in
 2002 a control region at low \cancel{E}_T , as shown in Figure 7.27. Since the control samples are
 2003 derived from the same data as the search sample, any biases in the \cancel{E}_T reconstruction
 2004 due to jet energy scale are present equally in both samples.

2005 Tables 7.4 and 7.5 list all the errors on the ee and ff QCD background predictions,
 2006 respectively, for the \cancel{E}_T bins used in the search. Table 7.6 lists the errors on the

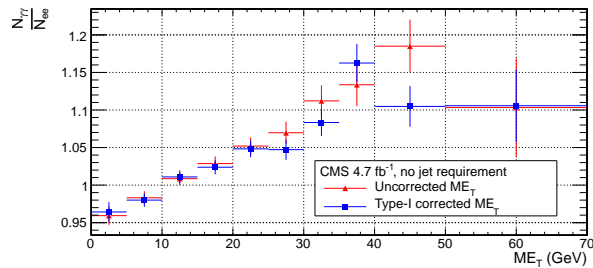
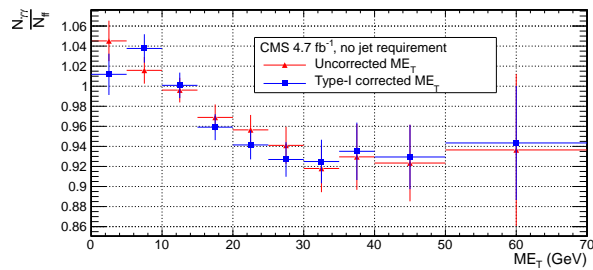
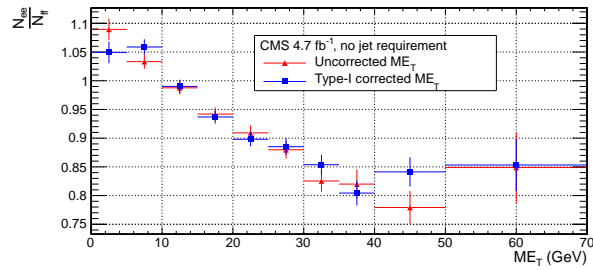
(a) Ratio of $\gamma\gamma$ to ee \cancel{E}_T distributions.(b) Ratio of $\gamma\gamma$ to ff \cancel{E}_T distributions.(c) Ratio of ee to ff \cancel{E}_T distributions.

Figure 7.27: Agreement between $\gamma\gamma$, ee , and ff samples for uncorrected (red triangles) and corrected (blue squares) \cancel{E}_T .

2007 electroweak background prediction. Finally, Table 7.7 shows the errors on the total
 2008 QCD + electroweak background prediction, broken down by origin (statistical or
 2009 systematic) and QCD background estimation sample (ee or ff). In the final result,
 2010 only the ff QCD estimate is used.

Table 7.4: Errors on the ee QCD background prediction as a fraction of the ee pre-diction.

Source of error	Fractional uncertainty (%)				
	[50, 60)	[60, 70)	[70, 80)	[80, 100)	≥ 100
Total	3.9	8.1	16	25	25
Statistics	3.6	7.8	16	24	22
No. events	3.6	7.7	15	24	20
In norm. region	0.43	0.44	0.46	0.55	0.51
In this E_T bin	3.5	7.7	15	24	20
Reweighting	0.73	1.2	3.5	4.3	7.7
In norm. region	0.19	0.19	0.2	0.24	0.23
In this E_T bin	0.71	1.2	3.5	4.3	7.7
Systematics	2.6	4.4	1.2	7.5	14
$f_{e \rightarrow \gamma}$ (in norm. region)	0.0012	0.0012	0.0013	0.0015	0.0014
m_{ee} background shape	1.4	2	0.72	5.5	12
Jet energy scale	2.2	3.9	0.96	5.1	6.9

2011 7.5 Results

2012 Figure 7.28(7.29) shows the E_T distribution of the inclusive(≥ 1 -jet) $\gamma\gamma$ search sample
 2013 along with the predicted E_T distributions of the QCD and electroweak backgrounds.
 2014 The observed number of two-photon events, ee and ff background estimates and
 2015 their errors, and expected number of inclusive(≥ 1 -jet) two-photon events from two
 2016 representative GGM SUSY models are listed in Table 7.8(7.9). (Details of the SUSY
 2017 MC production are given in Chapter 8.) The ee estimate is shown for comparison;
 2018 the ff estimate is the official result used in the interpretation. No deviation from the
 2019 Standard Model prediction is observed in the $\gamma\gamma$ search sample.

Table 7.5: Errors on the ff QCD background prediction as a fraction of the ff prediction.

Source of error	Fractional uncertainty (%)				
	[50, 60)	[60, 70)	[70, 80)	[80, 100)	≥ 100
Total	15	25	61	34	64
Statistics	7.2	14	30	33	38
No. events	7.1	14	29	33	36
In norm. region	0.64	0.64	0.64	0.64	0.64
In this E_T bin	7.1	14	29	33	36
Reweighting	0.85	2.7	5.1	6.9	13
In norm. region	0.27	0.27	0.27	0.27	0.27
In this E_T bin	0.81	2.6	5.1	6.9	13
Systematics	13	21	53	6.6	52
ee/ff difference	13	21	53	5.5	52
$f_{e \rightarrow \gamma}$ (in norm. region)	0.0012	0.0012	0.0012	0.0012	0.0012
Jet energy scale	0.099	1.7	1.8	3.5	1.8

Table 7.6: Errors on the $e\gamma$ electroweak background prediction as a fraction of the $e\gamma$ prediction.

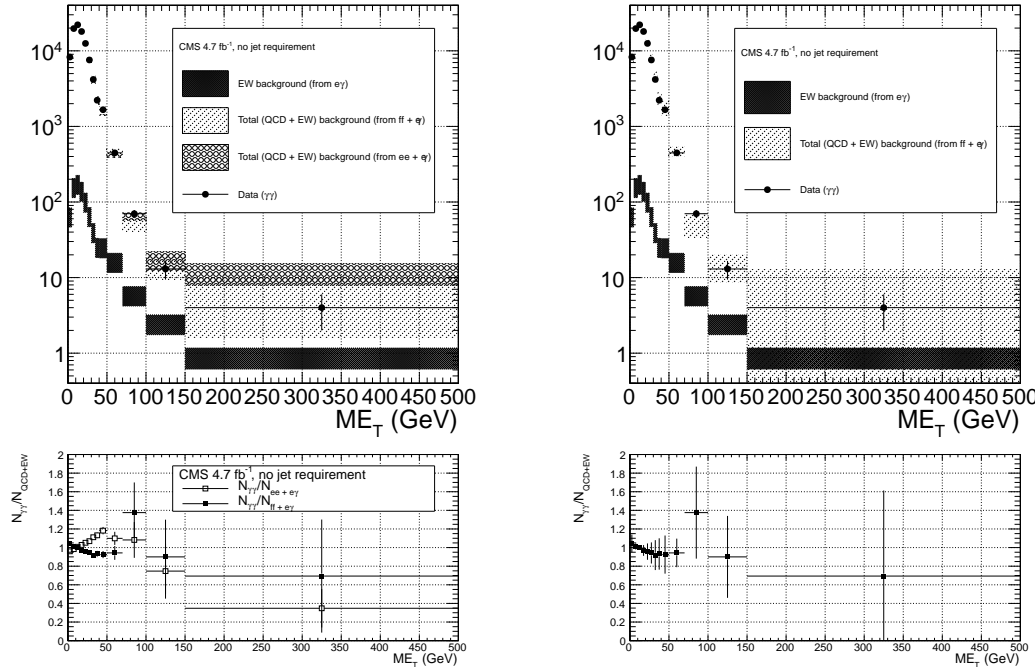
Source of error	Fractional uncertainty (%)				
	[50, 60)	[60, 70)	[70, 80)	[80, 100)	≥ 100
Total	29	29	30	30	30
Statistics	3.6	5.2	6.7	7.2	6.5
Systematics ($f_{e \rightarrow \gamma}$)	29	29	29	29	29

Table 7.7: Errors on the total QCD + electroweak background prediction as a fraction of the total prediction.

Source of error	Fractional uncertainty (%)				
	[50, 60)	[60, 70)	[70, 80)	[80, 100)	≥ 100
Total ($ee + e\gamma$)	3.9	7.8	15	22	22
Statistics	3.4	7.3	14	21	18
QCD	3.4	7.3	14	21	18
Electroweak	0.13	0.3	0.53	0.79	0.76
Systematics	2.7	4.5	2.6	7.4	13
QCD	2.5	4.1	1.1	6.7	12
Electroweak	1	1.7	2.3	3.2	3.4
Total ($ff + e\gamma$)	14	24	54	30	54
Statistics	6.9	13	26	29	30
QCD	6.9	13	26	29	30
Electroweak	0.11	0.24	0.79	0.83	1.1
Systematics	12	20	47	6.7	43
QCD	12	20	47	5.8	43
Electroweak	0.9	1.3	3.4	3.4	4.8

Table 7.8: Observed numbers of two-photon events, ee and ff background estimates and their errors, and expected numbers of two-photon events from two representative GGM SUSY models (details of MC simulation given in Chapter 8) for the E_T bins used in the search. The ee estimate is shown for comparison; the ff estimate is the official result used in the interpretation. Errors on the background estimates are detailed in Tables 7.4, 7.5, 7.6, and 7.7. Errors on the expected numbers of GGM events are purely statistical.

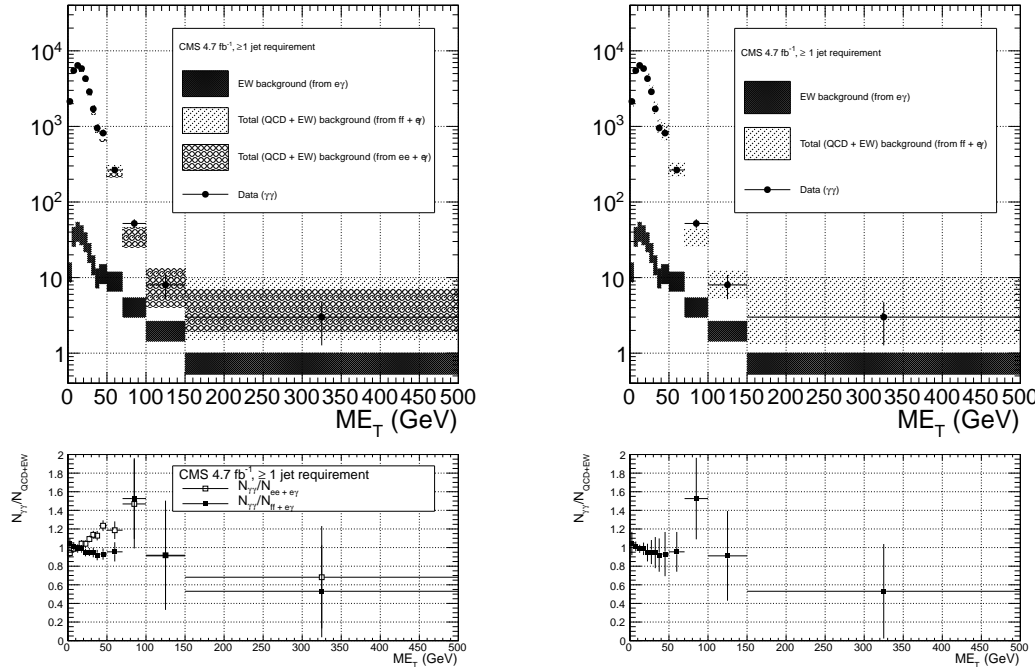
Source	No. events				
	[50, 60)	[60, 70)	[70, 80)	[80, 100)	≥ 100
Observation ($\gamma\gamma$)	354	93	37	33	17
Predicted background ($ff + e\gamma$)	361 ± 51.5	113 ± 27.1	26.9 ± 14.5	23.9 ± 7.23	20.2 ± 10.9
Predicted background ($ee + e\gamma$)	317 ± 14.1	90.2 ± 7.77	39.6 ± 5.75	25.1 ± 5.66	28.9 ± 6.70
$m_{\tilde{q}} = 720$ GeV $M_3 = 720$ GeV $M_1 = 375$ GeV	13.3 ± 2.13	17.7 ± 2.46	15.3 ± 2.33	42.9 ± 3.82	966 ± 18.3
$m_{\tilde{q}} = 1440$ GeV $M_3 = 1440$ GeV $M_1 = 375$ GeV	0.008 ± 0.003	0.009 ± 0.003	0.012 ± 0.003	0.030 ± 0.005	1.92 ± 0.04



(a) $ee + e\gamma$ and $ff + e\gamma$. The widths of the bands correspond to the errors given in Table 7.7, excluding the error associated with the difference between the ee and ff QCD estimates for the $ff + e\gamma$ E_T distribution.

(b) $ff + e\gamma$. The widths of the bands correspond to the errors given in Table 7.7, including the error associated with the difference between the ee and ff QCD estimates.

Figure 7.28: E_T distribution of the $\gamma\gamma$ search sample (black circles) along with the predicted E_T distributions of the QCD and electroweak backgrounds (small circle band for ee QCD prediction + electroweak prediction, slanted dashed band for ff QCD prediction + electroweak prediction). The electroweak background prediction is shown in the crosshatched band. The bottom plots show the ratio of the $\gamma\gamma$ E_T distribution to the $ee + e\gamma$ background distribution (open squares) and $ff + e\gamma$ background distribution (filled squares).



(a) $ee + e\gamma$ and $ff + e\gamma$. The widths of the bands correspond to the errors given in Table 7.7, excluding the error associated with the difference between the ee and ff QCD estimates for the $ff + e\gamma$ E_T distribution.

(b) $ff + e\gamma$. The widths of the bands correspond to the errors given in Table 7.7, including the error associated with the difference between the ee and ff QCD estimates.

Figure 7.29: \cancel{E}_T distribution of the $\gamma\gamma + \geq 1$ jet search sample (black circles) along with the predicted \cancel{E}_T distributions of the QCD and electroweak backgrounds (small circle band for ee QCD prediction + electroweak prediction, slanted dashed band for ff QCD prediction + electroweak prediction). The electroweak background prediction is shown in the crosshatched band. The bottom plots show the ratio of the $\gamma\gamma$ \cancel{E}_T distribution to the $ee + e\gamma$ background distribution (open squares) and $ff + e\gamma$ background distribution (filled squares).

Table 7.9: Observed numbers of two-photon + ≥ 1 -jet events, ee and ff background estimates and their errors, and expected numbers of two-photon + ≥ 1 -jet events from two representative GGM SUSY models (details of MC simulation given in Chapter 8) for the E_T bins used in the search. The ee estimate is shown for comparison; the ff estimate is the official result used in the interpretation. Errors on the background estimates are detailed in Tables 7.4, 7.5, 7.6, and 7.7. Errors on the expected numbers of GGM events are purely statistical.

Source	No. events				
	[50, 60)	[60, 70)	[70, 80)	[80, 100)	≥ 100
Observation ($\gamma\gamma + \geq 1$ jet)	202	63	27	25	11
Predicted background ($ff + e\gamma$)	200 ± 35.4	77.7 ± 28.1	19.4 ± 8.55	14.7 ± 7.04	14.4 ± 5.59
Predicted background ($ee + e\gamma$)	171 ± 10.2	52.7 ± 5.74	25.1 ± 4.76	10.2 ± 5.04	13.1 ± 5.74
$m_{\tilde{q}} = 720$ GeV $M_3 = 720$ GeV $M_1 = 375$ GeV	13.3 ± 2.13	17.7 ± 2.46	15.3 ± 2.33	42.9 ± 3.82	965 ± 18.3
$m_{\tilde{q}} = 1440$ GeV $M_3 = 1440$ GeV $M_1 = 375$ GeV	0.008 ± 0.003	0.009 ± 0.003	0.012 ± 0.003	0.031 ± 0.004	1.92 ± 0.04

2020 **Chapter 8**

2021 **Interpretation of Results in Terms
2022 of GMSB Models**

2023 As shown in Figs. 7.28 and 7.29 and Tables 7.8 and 7.9, no excess of events above
2024 the Standard Model expectation is found in either the ≥ 0 - or ≥ 1 -jet analyses for the
2025 GMSB-sensitive region $\cancel{E}_T \geq 50$ GeV. Therefore, upper limits on the production cross
2026 sections of various GMSB models are calculated and then translated into statements of
2027 exclusion. Section 8.1 describes the GMSB models that were generated with MC and
2028 tested for exclusion. The upper limit calculation and translation to model exclusions
2029 is laid out in Section 8.2. The upper limits themselves are presented in Section 8.3,
2030 and, finally, the exclusions are presented in Section 8.4.

2031 **8.1 Simplified Models**

2032 The exclusion reach of the two-photon search is presented for three different two-
2033 dimensional scans in GMSB parameter space. The first scan covers the bino NLSP
2034 scenario of Sec. 3.5. In this scan, M_2 , which controls the amount of wino mixing, is
2035 set to 3.5 TeV. M_1 , which controls the amount of bino mixing, is set to 375 GeV.
2036 This insures that all gauginos except the lightest neutralino are too heavy to be pro-

2037 duced in significant numbers at the LHC. All other mass parameters except for M_3
 2038 (\sim gluino mass) and $m_{\tilde{q}}$ (\sim first- and second-generation squark mass) are set to 3.5
 2039 TeV, which insures that squark/gluino decay to intermediate states such as third-
 2040 generation squarks or any flavor of lepton is strongly suppressed. Every mass param-
 2041 eter except for M_1 , M_3 , and $m_{\tilde{q}}$ is set so large that it has essentially no effect on
 2042 the sparticle dynamics that can be observed in LHC collisions, which are completely
 2043 determined by M_1 , M_3 , and $m_{\tilde{q}}$. The high-mass parameters are decoupled from the
 2044 relevant part of the spectrum. M_3 and $m_{\tilde{q}}$ are scanned over from $M_3 = m_{\tilde{q}} = 400$ GeV
 2045 to $M_3 = m_{\tilde{q}} = 2$ TeV in 80-GeV steps. The resulting simplified model consists only
 2046 of a gluino, first- and second-generation squarks, and the lightest neutralino and its
 2047 decay products (the gravitino is forced to be the LSP). The scan in M_3 - $m_{\tilde{q}}$ space illu-
 2048 minates the sensitivity of the two-photon search to different levels of signal hadronic
 2049 activity.

2050 The second scan is identical to the first except that the values of M_1 and M_2 are
 2051 inverted ($M_1 = 3.5$ TeV and $M_2 = 375$ GeV). In this case, M_1 is decoupled from
 2052 the relevant part of the spectrum. This corresponds to the wino NLSP scenario of
 2053 Sec. 3.5. Now, both the lightest neutralino and the lightest chargino have masses of
 2054 order 375 GeV, and are therefore produced with approximately equal frequency in
 2055 the gluino and squark decays. The chargino decays to $W + \tilde{G}$, so final states in this
 2056 scan often include leptons or large jet multiplicity. Since there is no guarantee that
 2057 two neutralinos will be produced and will decay to two photons, this search is not
 2058 well optimized for the wino NLSP scenario. However, a related CMS search with one
 2059 photon and ≥ 3 jets has an exclusion reach of ~ 1 TeV in M_3 and $m_{\tilde{q}}$ for this scenario
 2060 [29].

2061 The third scan is M_3 vs. M_1 for $m_{\tilde{q}}$, M_2 , and all other mass parameters equal to
 2062 2.5 TeV (decoupled). M_3 is scanned from 160 GeV to 2 TeV in 80-GeV steps, while
 2063 M_1 is scanned from 150 GeV to 1050 GeV in 100-GeV steps. $M_3 < M_1$ is not allowed,

as this would imply that the gluino, not the lightest neutralino, is the NLSP. This scan highlights the performance of the two-photon search as a function of M_1 (i.e. as a function of decays open to the neutralino), whereas the previous two scans keep M_1 fixed.

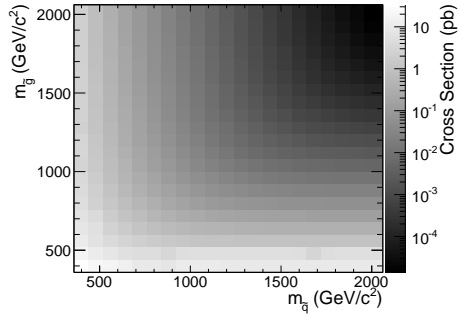
For each scan, the sparticle mass spectrum is generated with SuSpect 2.41 [123] and the decay widths with SDECAY 1.3 [124]. The event data (including production, unstable particle decay, parton showering, and hadronization) is generated with Pythia 6.422 [130], using the sparticle mass spectra and decay widths as inputs. The gravitino is always forced to be the LSP. The simulated data are reconstructed with CMSSWv4.2.2, which uses a detector simulation based on GEANT 4 [125]. Next to leading order cross sections are calculated with PROSPINO 2.1 [126], and shown in Figure 8.1 for the three signal MC scenarios.

8.2 Upper Limit Calculation and Model Exclusion

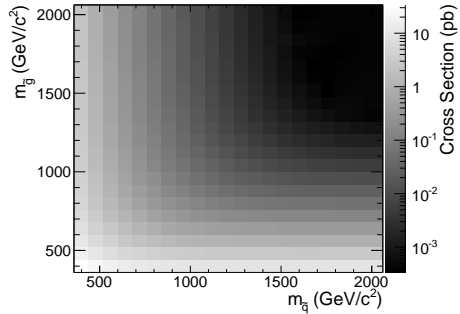
The upper limits are calculated according to the prescription followed for the 2011 ATLAS + CMS Higgs limit combination [113]. This prescription utilizes the frequentist CL_s method [114] with profile likelihood test statistic [115]. The CL_s method and the profile likelihood are explained in Section 8.2.2, using specific signal MC points to illustrate the procedure. First, however, the signal MC acceptance \times efficiency, which is an input to the limit setting procedure, is presented in Section 8.2.1.

8.2.1 Signal Acceptance \times Efficiency

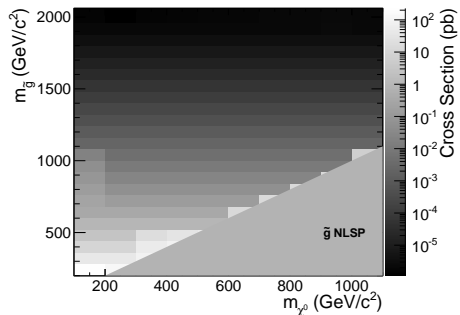
The signal acceptance \times efficiency (denoted $\mathcal{A} \times \epsilon$), defined for each signal point as the number of $\gamma\gamma$ events selected with $\cancel{E}_T \geq 50$ GeV divided by the total number of events generated, is shown in Figure 8.2 for the three different scenarios described in Sec. 8.1. Acceptance refers to the fraction of true events that can be detected given



(a) M_2 decoupled ($M_2 = 3.5$ TeV), $M_1 = 375$ GeV, M_3 vs. $m_{\tilde{q}}$.



(b) M_1 decoupled ($M_1 = 3.5$ TeV), $M_2 = 375$ GeV, M_3 vs. $m_{\tilde{q}}$.



(c) $m_{\tilde{q}}$ decoupled ($m_{\tilde{q}} = 2.5$ TeV), M_3 vs. M_1 .

Figure 8.1: Next to leading order cross sections for the three different MC scenarios described in the text.

2088 the fiducial extent of the detector and the E_T cuts on the photons. Efficiency denotes
 2089 the fraction of accepted events (i.e. those events passing the E_T and η cuts) that have
 2090 two photons passing the photon identification criteria.

2091 In Figs. 8.2a and 8.2b, the large drop in $\mathcal{A} \times \epsilon$ for $m_{\tilde{q}} > M_3$ is due to an increase
 2092 in the number of jets produced per event and a consequent reduction in the number
 2093 of photons that pass the $I_{\text{comb}} < 6$ GeV cut. For $m_{\tilde{q}} > M_3$, there is more phase space
 2094 available to produce gluinos in the hard scatter than squarks. However, since gluinos
 2095 must decay via squarks, and in these models all squarks are heavier than the gluino,
 2096 only the two-jet decay $\tilde{g} \rightarrow q\tilde{q}\chi^0$ is available. Conversely, when $m_{\tilde{q}} < M_3$, there is
 2097 more phase space available to produce squarks, which may then decay via one jet as
 2098 $\tilde{q} \rightarrow q\tilde{\chi}^0$. Jets in SUSY events may be very close to the neutralino decay photons,
 2099 and as a result the photons may fail the strict isolation requirements, leading to lower
 2100 $\mathcal{A} \times \epsilon$ for jet-rich events. The worsened acceptance along $M_3 = 400$ GeV and $m_{\tilde{q}} = 400$
 2101 GeV in Fig. 8.2b is due to efficiency of the jet cut, which decreases drastically as M_3
 2102 and $m_{\tilde{q}}$ approach M_1 because of shrinking phase space to produce hard jets in the
 2103 squark and gluino decays to neutralinos.

2104 The broad peak in $\mathcal{A} \times \epsilon$ shown in Fig. 8.2a for $m_{\tilde{q}} < M_3$ and ~ 600 GeV $< m_{\tilde{q}} <$
 2105 ~ 1600 GeV is due to the $\cancel{E}_T > 50$ GeV cut. The efficiency of the cut decreases
 2106 as $m_{\tilde{q}}$ decreases because of the fixed M_1 of 375 GeV. If the squark-neutralino mass
 2107 splitting gets too small, the likelihood of producing an energetic enough gravitino to
 2108 pass the \cancel{E}_T cut decreases.

2109 $\mathcal{A} \times \epsilon$ is generally much lower for the $M_2 = 375$ GeV grid (Figs. 8.2c and 8.2d)
 2110 due to the larger contribution from chargino decays to $W + \tilde{G}$, which do not give rise
 2111 to photons in the final state. The increased acceptance for $M_3 > m_{\tilde{q}}$ is due to the
 2112 same jet multiplicity issue affecting the $M_1 = 375$ GeV grid. As M_3 and $m_{\tilde{q}}$ increase
 2113 relative to the fixed M_2 , the jets from squark and gluino decay get more energetic,
 2114 increasing the chance that they will overlap with the neutralino decay photon and

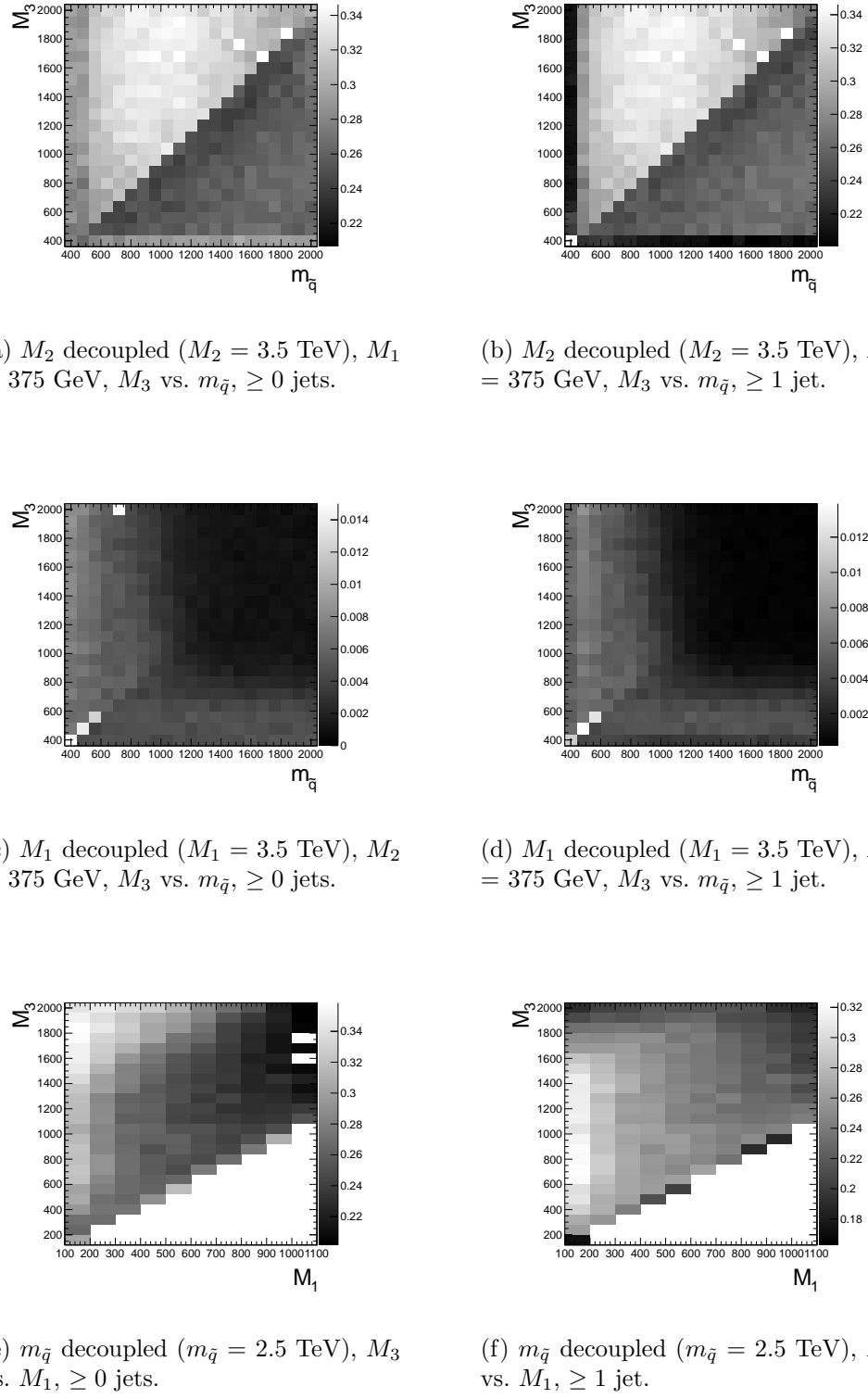


Figure 8.2: Signal acceptance \times efficiency (defined in the text) for the three different scenarios described in Sec. 8.1.

cause it to fail the isolation cut. For $m_{\tilde{q}} \gtrsim 1$ TeV and $M_3 \gtrsim 800$ GeV, the acceptance is so low that not enough events were simulated to see the acceptance decrease over the statistical error.

In Fig. 8.2e, the neutralino is always heavy enough to guarantee decay to a photon that can pass the 40 GeV p_T cut. $\mathcal{A} \times \epsilon$ increases as M_3 increases because the larger gluino-neutralino mass splitting gives the neutralino a larger kinetic energy, increasing the chance that it will decay to a photon with 40 GeV p_T or higher. After the bino mass increases beyond the threshold needed to produce high p_T photons, $\mathcal{A} \times \epsilon$ decreases with increasing M_1 , independent of gluino mass, because higher M_1 means more phase space is open to decays of the form $\tilde{\chi}_1^0 \rightarrow Z\tilde{G}$ and $\tilde{\chi}_1^0 \rightarrow H\tilde{G}$. The two-photon search is naturally not as efficient for these decays.

Added

There is a small chance that some real GMSB signal events could be reconstructed as ff events in the data. To correct the signal acceptance for this effect, the number of signal events reconstructed as ff events is subtracted from the number of signal $\gamma\gamma$ events, effectively reducing the signal acceptance. This is generally a small correction ($\sim 5\%$).

8.2.2 CL_s and the Profile Likelihood Test Statistic

The process of setting a cross section upper limit entails (1) defining a test statistic, (2) generating a distribution for that test statistic under the signal + background and background-only hypotheses, and (3) deciding whether or not the observed value of the test statistic is more compatible with the signal + background (i.e. weaker upper limit) or background-only (i.e. stronger upper limit) hypotheses by considering where it falls within the test statistic distributions. An important requirement on the choice of test statistic is that it be able to effectively discriminate between the signal + background and background-only hypotheses, i.e. the shape of its distribution for these two hypotheses should be different. The procedure for determining the exclud-

ability of a particular model given the value of the test statistic observed should not give rise to pathological behavior in the presence of small signals, low statistics, or weak sensitivity to models, as is commonly the case in high energy physics. These demands on the test statistic and the limit setting procedure itself dictate the choice of the profile likelihood test statistic and CL_s procedure.

In the remainder of this section, the notation is taken from ref. [113].

Profile Likelihood

For a specific model of GMSB, the limit setting procedure concerns the question of whether to reject the signal + background hypothesis $\mu s + b$ in favor of the background-only (Standard Model) hypothesis of b ($\mu = 0$). μ is a dimensionless signal strength parameter. s is the expected number of signal events, calculated from MC simulated signal events as in Secs. 8.1 and 8.2.1. b is the expected number of background events, estimated in Chap. 7. By the Neyman-Pearson lemma [116], the ratio of the likelihood of $\mu s + b$ to the likelihood of b is the test statistic with the highest power to reject $\mu s + b$ at whatever confidence level is desired. In practice, this means that the likelihood ratio is the best discriminator between the GMSB and Standard Model hypotheses.

The likelihood of the signal + background hypothesis as a function of the data (either real or generated) is defined as

$$\mathcal{L}(\text{data}|\mu, \theta) = \prod_{i=1}^N \frac{(\mu s_i(\theta) + b_i(\theta))^{n_i}}{n_i!} e^{-\mu s_i(\theta) - b_i(\theta)} p(\tilde{\theta}|\theta) \quad (8.1)$$

where $N = 5$ is the number of E_T bins used in the analysis ([50, 60) GeV, [60, 70) GeV, [70, 80) GeV, [80, 100) GeV, and [100, ∞) GeV); $s_i(\theta)$ and $b_i(\theta)$ are the expected number of signal and background events in E_T bin i , respectively; n_i is the number of events observed in E_T bin i ; and θ represents all the nuisance parameters

(uncertainties). $p(\tilde{\theta}|\theta)$ represents the product of probability distribution functions (PDFs) for the nuisance parameters, where $\tilde{\theta}$ is the default value of the nuisance parameter. In this analysis, there are eight experimental nuisance parameters per E_T bin, given here as relative errors on the expected number of signal events:

- Uncertainty on the measured integrated luminosity (4.5% in all bins) [117]
- Uncertainty on the signal acceptance due to $\epsilon_e^{\text{data}}/\epsilon_e^{\text{MC}}$ and the pixel veto efficiency error (cf. Sec. 6.4.2) (8% in all bins)
- Uncertainty on the signal acceptance due to imperfect pileup simulation (2.6% in all bins)
- Systematic uncertainty on QCD background prediction due to difference between ff and ee estimates (5.5%-53% of the QCD background depending on bin)
- Systematic uncertainty on electroweak background prediction due to p_T dependence of $f_{e \rightarrow \gamma}$ (29%-30% of the electroweak background depending on bin)
- Statistical uncertainty on the signal acceptance (1.8%-100% depending on model and bin)
- Statistical uncertainty on the QCD background prediction (7.2%-38% of the QCD background depending on bin)
- Statistical uncertainty on the electroweak background prediction (3.6%-7.2% of the electroweak background depending on bin)

and one very small theoretical nuisance parameter: the uncertainty on the signal acceptance due to underlying parton distribution function (PDF) uncertainties. In the limit-setting code, the uncertainties on signal acceptance due to photon efficiency and PDF errors are added in quadrature and treated as one. The uncertainty on the

2187 signal acceptance due to jet energy correction uncertainties is negligible, due to the
 2188 presence of many hard jets in GMSB signal events. The uncertainties on integrated
 2189 luminosity and pileup are 100% correlated between E_T bins, and the uncertainty on
 2190 signal acceptance can usually be treated similarly because the error on $\epsilon_e^{\text{data}}/\epsilon_e^{\text{MC}}$ often
 2191 dominates the PDF error on acceptance (although these three uncertainties are 0%
 2192 correlated with each other).

2193 To estimate the uncertainty due to imperfect simulation of LHC pileup, the square
 2194 of the average data efficiency for photons over the range 1-15 reconstructed primary
 2195 vertices (see Fig. 6.18a), weighted by the number of $\gamma\gamma$ events per primary vertex bin,
 2196 is calculated. The efficiency per primary vertex bin is estimated from a linear fit to
 2197 Fig. 6.18a. The process is repeated for MC using the entire range of primary vertices
 2198 in Fig. 6.18a (all MC signal points have the same pileup simulation). The error is
 2199 taken as $2 \times |\text{avg. data efficiency squared} - \text{avg. MC efficiency squared}| / (\text{avg. data}$
 2200 efficiency squared + avg. MC efficiency squared).

2201 Each nuisance parameter PDF is modeled by a log-normal distribution:

$$p(\tilde{\theta}|\theta) = \frac{1}{\sqrt{2\pi} \ln \kappa} \exp\left(-\frac{(\ln \tilde{\theta}/\theta)^2}{2(\ln \kappa)^2}\right) \frac{1}{\tilde{\theta}} \quad (8.2)$$

2202 where $\tilde{\theta} = 1$ and $\kappa = 1 + \text{the one-standard-deviation relative error on the nuisance}$
 2203 parameter (e.g. for the 4.5% error due to integrated luminosity, $\kappa = 1.045$).

2204 Similarly, the likelihood of the background-only hypothesis as a function of the
 2205 data (either real or generated) is defined as

$$\mathcal{L}(\text{data}|0, \theta) = \prod_{i=1}^N \frac{b_i(\theta)^{n_i}}{n_i!} e^{-b_i(\theta)} p(\tilde{\theta}|\theta) \quad (8.3)$$

2206 The profile likelihood test statistic is defined as

$$\tilde{q}_\mu = -2 \ln \frac{\mathcal{L}(\text{data}|\mu, \hat{\theta}_\mu)}{\mathcal{L}(\text{data}|\hat{\mu}, \hat{\theta})}, 0 \leq \hat{\mu} \leq \mu \quad (8.4)$$

where the $\hat{\theta}_\mu$ maximize $\mathcal{L}(\text{data}|\mu, \hat{\theta}_\mu)$ when it is evaluated at a particular μ , and $\hat{\mu}$ and $\hat{\theta}$ are the global maximum likelihood estimators of μ and θ . The condition $\hat{\mu} \leq \mu$ insures that the obtained cross section upper limit is one-sided, i.e. there is no possibility to find a lower limit on the cross section. The profile likelihood test statistic has the nice property that in the asymptotic (large statistics) limit its PDF can be approximated by analytic formulae, eliminating the need to generate multiple toy experiments to get the PDF. However, the approximation breaks down for small numbers of observed events, so in practice the asymptotic limit is only used as a first guess at the location of the true limit.

The PDFs $f(\tilde{q}_\mu|\mu, \hat{\theta}_\mu^{\text{obs}})$ and $f(\tilde{q}_\mu|0, \hat{\theta}_0^{\text{obs}})$ for the profile likelihood test statistic under the signal + background and background-only hypotheses, respectively, are obtained by generating toy MC pseudo-experiments. $\hat{\theta}_\mu^{\text{obs}}$ and $\hat{\theta}_0^{\text{obs}}$ maximize Eqs. 8.1 and 8.3, respectively, when they are evaluated for the observed data. For each μ (and the background-only hypothesis $\mu = 0$), the pseudo-experiments are generated by picking random values of s and b from a Poisson distribution with the θ fixed as just described.

CL_s

In the classical frequentist approach, a signal model may be excluded at the 95% confidence level (CL) if the probability of any measurement of the test statistic to be greater than or equal to the observed value given the signal + background hypothesis is 5%. This means that the observed value of the test statistic is so incompatible with what one would expect to observe if the signal model were true that, under the

assumption that the signal model *is* true, the chance of observing a test statistic even further afield from the signal expectation is only 5%. Mathematically,

$$\begin{aligned} p_\mu &\equiv P(\tilde{q}_\mu \geq \tilde{q}_\mu^{\text{obs}} | \mu s + b) = \int_{\tilde{q}_\mu^{\text{obs}}}^{\infty} f(\tilde{q}_\mu | \mu, \hat{\theta}_\mu^{\text{obs}}) d\tilde{q}_\mu \\ p_\mu &\leq 0.05 \Rightarrow \text{exclude } \mu \end{aligned} \quad (8.5)$$

where $\tilde{q}_\mu^{\text{obs}}$ is the observed value of the test statistic and p_μ is the p-value. As indicated in Eq. 8.5, the p-value is simply the integral of the PDF of \tilde{q}_μ from $\tilde{q}_\mu^{\text{obs}}$ to infinity.

By construction, the classical 95% CL frequentist approach described above will reject a true signal + background hypothesis 5% of the time. This can happen if the experiment gets “unlucky” and the observation fluctuates low, causing $\tilde{q}_\mu^{\text{obs}}$ to fall in the tail of the \tilde{q}_μ distribution. This poses a problem for the case of very weak signals ($\mu \sim 0$), because it will lead to spurious exclusions of models to which the experiment has little sensitivity. To avoid this pitfall, the CL_s limit setting method is used.

In the CL_s method, the classical frequentist p-value of Eq. 8.5 is simply divided by one minus the p-value of the background-only hypothesis, and it is this ratio, rather than the p-value of the signal + background hypothesis alone, that is required to be ≤ 0.05 . Mathematically,

$$1 - p_0 \equiv P(\tilde{q}_\mu \geq \tilde{q}_\mu^{\text{obs}} | b) = \int_{\tilde{q}_\mu^{\text{obs}}}^{\infty} f(\tilde{q}_\mu | 0, \hat{\theta}_0^{\text{obs}}) d\tilde{q}_\mu \quad (8.6)$$

$$\text{CL}_s(\mu) \equiv \frac{p_\mu}{1 - p_0} \quad (8.7)$$

$$\text{CL}_s(\mu) \leq 0.05 \Rightarrow \text{exclude } \mu$$

where p_0 is the p-value for the background-only hypothesis ($\mu = 0$). In the case of low sensitivity to μ , $p_\mu \lesssim 1 - p_0$, so $\text{CL}_s(\mu) \lesssim 1$ and μ will not be excluded. On the

contrary, for high sensitivity to μ ($\mu s \gg \sigma_b$), $p_\mu \ll 1 - p_0$, so models that can be excluded by the criterion $p_\mu \leq 0.05$ will also be excluded by the criterion $\text{CL}_s \leq 0.05$. Compared to the classical frequentist method, CL_s limits can be a little stronger in the case of low signal sensitivity [113].

To determine the upper limit on the cross section of a particular model, the lowest value of μ for which $\text{CL}_s(\mu) \leq 0.05$, denoted $\mu^{95\% \text{ CL}}$, is found. The cross section upper limit of that model is then simply $\mu^{95\% \text{ CL}}$ multiplied by the expected cross section of the model (cf. Fig. 8.1).

In contrast to the observed upper limit, the expected upper limit is calculated from an ensemble of background-only MC pseudo-experiments. The distribution $f(\mu_{\text{pseudo}}^{95\% \text{ CL}})$ is plotted (one entry per pseudo-experiment). The median expected upper limits and $\pm 1\sigma$ and $\pm 2\sigma$ bands are defined as

$$0.5 = \int_0^{\mu_{\text{exp}}^{95\% \text{ CL}}} f(\mu_{\text{pseudo}}^{95\% \text{ CL}}) d\mu_{\text{pseudo}}^{95\% \text{ CL}} \quad (8.8)$$

$$0.16 = \int_0^{\mu_{-1\sigma,\text{exp}}^{95\% \text{ CL}}} f(\mu_{\text{pseudo}}^{95\% \text{ CL}}) d\mu_{\text{pseudo}}^{95\% \text{ CL}} \quad (8.9)$$

$$0.84 = \int_0^{\mu_{+1\sigma,\text{exp}}^{95\% \text{ CL}}} f(\mu_{\text{pseudo}}^{95\% \text{ CL}}) d\mu_{\text{pseudo}}^{95\% \text{ CL}} \quad (8.10)$$

$$0.025 = \int_0^{\mu_{-2\sigma,\text{exp}}^{95\% \text{ CL}}} f(\mu_{\text{pseudo}}^{95\% \text{ CL}}) d\mu_{\text{pseudo}}^{95\% \text{ CL}} \quad (8.11)$$

$$0.975 = \int_0^{\mu_{+2\sigma,\text{exp}}^{95\% \text{ CL}}} f(\mu_{\text{pseudo}}^{95\% \text{ CL}}) d\mu_{\text{pseudo}}^{95\% \text{ CL}} \quad (8.12)$$

The technical procedure followed to calculate the 95% CL cross section upper limits for each GMSB model tested is given below.

1. Calculate a guess for the median expected limit and $\pm 2\sigma$ error bands ($\mu_{\pm 2\sigma, \text{guess}}^{95\% \text{ CL}}$) using the asymptotic formulae for $f(\tilde{q}_\mu | 0, \hat{\theta}_0^{\text{obs}})$.

2. Calculate observed ($\mu_{\text{obs,asym}}^{95\% \text{ CL}}$), median expected ($\mu_{\text{exp,asym}}^{95\% \text{ CL}}$), and $\pm 1\sigma$ ($\mu_{\pm 1\sigma, \text{asym}}^{95\% \text{ CL}}$)

2262 and $\pm 2\sigma$ ($\mu_{\pm 2\sigma, \text{asym}}^{\text{95\%CL}}$) expected CL_s limits using the asymptotic formulae for
 2263 $f(\tilde{q}_\mu | \mu, \hat{\theta}_\mu^{\text{obs}})$ and $f(\tilde{q}_\mu | 0, \hat{\theta}_0^{\text{obs}})$. Restrict the range of $\mu_{\text{obs,asym}}^{\text{95\%CL}}$ and $\mu_{\text{exp,asym}}^{\text{95\%CL}}$ to
 2264 $[0, 5 \times \mu_{\pm 2\sigma, \text{guess}}^{\text{95\%CL}}]$ (this avoids pathological behavior of the limit-setting code
 2265 when the expected number of signal events is much greater than the observed
 2266 number of events and only introduces a $\sim 5\%$ upward bias in the observed limit,
 2267 well within the $\pm 1\sigma$ error bands).

- 2268 3. Calculate median expected ($\mu_{\text{exp}}^{\text{95\%CL}}$) and $\pm 1\sigma$ ($\mu_{\pm 1\sigma}^{\text{95\%CL}}$) and $\pm 2\sigma$ ($\mu_{\pm 2\sigma}^{\text{95\%CL}}$) ex-
 2269 pected CL_s limits using 100 toy MC pseudo-experiments to generate $f(\tilde{q}_\mu | \mu, \hat{\theta}_\mu^{\text{obs}})$
 2270 and $f(\tilde{q}_\mu | 0, \hat{\theta}_0^{\text{obs}})$. Restrict the range of $\mu_{\text{exp}}^{\text{95\%CL}}$ to $[0, 5 \times \mu_{\pm 2\sigma, \text{guess}}^{\text{95\%CL}}]$.
- 2271 4. If $\mu_{\pm 2\sigma}^{\text{95\%CL}}$ could not be calculated, set $\mu_{\pm 2\sigma}^{\text{95\%CL}} = \mu_{\pm 2\sigma, \text{asym}}^{\text{95\%CL}}$ instead.
- 2272 5. If $\mu_{+2\sigma}^{\text{95\%CL}} \neq \mu_{-2\sigma}^{\text{95\%CL}}$ and $\mu_{\text{obs,asym}}^{\text{95\%CL}} > 0.0001$:
 - 2273 • If $\mu_{\text{obs,asym}}^{\text{95\%CL}} > \mu_{+2\sigma}^{\text{95\%CL}}$, set $\mu_{+2\sigma}^{\text{95\%CL}} = 1.3 \times \mu_{\text{obs,asym}}^{\text{95\%CL}}$.
 - 2274 • If $\mu_{\text{obs,asym}}^{\text{95\%CL}} < \mu_{-2\sigma}^{\text{95\%CL}}$, set $\mu_{-2\sigma}^{\text{95\%CL}} = 0.7 \times \mu_{\text{obs,asym}}^{\text{95\%CL}}$.
- 2275 6. If $\mu_{+2\sigma}^{\text{95\%CL}} = \mu_{-2\sigma}^{\text{95\%CL}}$, set $\mu_{\pm 2\sigma}^{\text{95\%CL}} = \mu_{\pm 2\sigma, \text{asym}}^{\text{95\%CL}}$ instead.
- 2276 7. Scan over 100 equally spaced test values of μ between $\mu_{-2\sigma}^{\text{95\%CL}}$ and $\mu_{+2\sigma}^{\text{95\%CL}}$ and,
 2277 if $\mu > 0.0001$, calculate the CL_s p-value (p_μ) for this test value of μ to 10^{-6}
 2278 precision using a minimum of 500 toy experiments to generate $f(\tilde{q}_\mu | \mu, \hat{\theta}_\mu^{\text{obs}})$ and
 2279 $f(\tilde{q}_\mu | 0, \hat{\theta}_0^{\text{obs}})$.
- 2280 8. Determine the observed ($\mu_{\text{obs,scan}}^{\text{95\%CL}}$), median expected ($\mu_{\text{exp,scan}}^{\text{95\%CL}}$), and $\pm 1\sigma$ ($\mu_{\pm 1\sigma, \text{scan}}^{\text{95\%CL}}$)
 2281 and $\pm 2\sigma$ ($\mu_{\pm 2\sigma, \text{scan}}^{\text{95\%CL}}$) expected CL_s limits from the scan p-values for the signal
 2282 + background and background-only pseudo-experiments.

2283 Finally, a particular GMSB model is excluded if the upper limit on the cross
 2284 section for that model is less than the expected theoretical cross section.

2285 8.3 Cross Section Upper Limits

2286 Figure 8.3 shows the observed upper limits on the cross sections for the models de-
 2287 scribed in Sec. 8.1. In some ($\mathcal{O}(10^{-3})$) cases, the upper limit is zero due to a compu-
 2288 tational failure. The upper limit for these points is estimated from the average of the
 2289 upper limits of the four neighboring points, as shown in Figure 8.4. If any of the four
 2290 points is also missing a valid upper limit, it is dropped from the average. The errors
 2291 on the individual upper limits used in the estimate are propagated to the error on
 2292 the average.

2293 8.4 Exclusion Contours

2294 Exclusion contours for the GMSB models discussed above are shown in Figure 8.5. The
 2295 contours are derived from plots of predicted cross section minus cross section upper
 2296 limit ($\sigma \times (1 - \mu^{95\%CL})$), where σ is the nominal value of the predicted cross section
 2297 for a given GMSB model) vs. the two model parameters of interest, so the values are
 2298 either negative (not excluded) or positive (excluded). Sometimes, a particular point
 2299 may have a different sign than its four same-sign neighbors (cf. Fig. 8.4) due to a
 2300 fluctuation. In these cases, $\sigma \times (1 - \mu^{95\%CL})$ for the anomalous point is estimated
 2301 as the average $\sigma \times (1 - \mu^{95\%CL})$ of the four neighboring points. The errors on the
 2302 individual values of $\sigma \times (1 - \mu^{95\%CL})$ used in the estimate are propagated to the error
 2303 on the average.

2304 In the plots in Fig. 8.5, the expected limit (i.e. the contour derived from $\sigma \times (1 -$
 2305 $\mu_{\text{exp,scan}}^{95\%CL})$) is drawn in dark orange and the 1σ experimental band around the expected
 2306 limit (i.e. the shaded region between the contours derived from $\sigma \times (1 - \mu_{\pm 1\sigma, \text{scan}}^{95\%CL})$) is
 2307 drawn in light orange. The values of $\mu_{\text{exp,scan}}^{95\%CL}$ and $\mu_{\pm 1\sigma, \text{scan}}^{95\%CL}$ only reflect the experimental
 2308 uncertainties given in Sec. 8.2.2.

2309 The observed limits (derived from $\sigma \times (1 - \mu_{\text{obs,scan}}^{95\%CL})$) and 1σ theoretical error

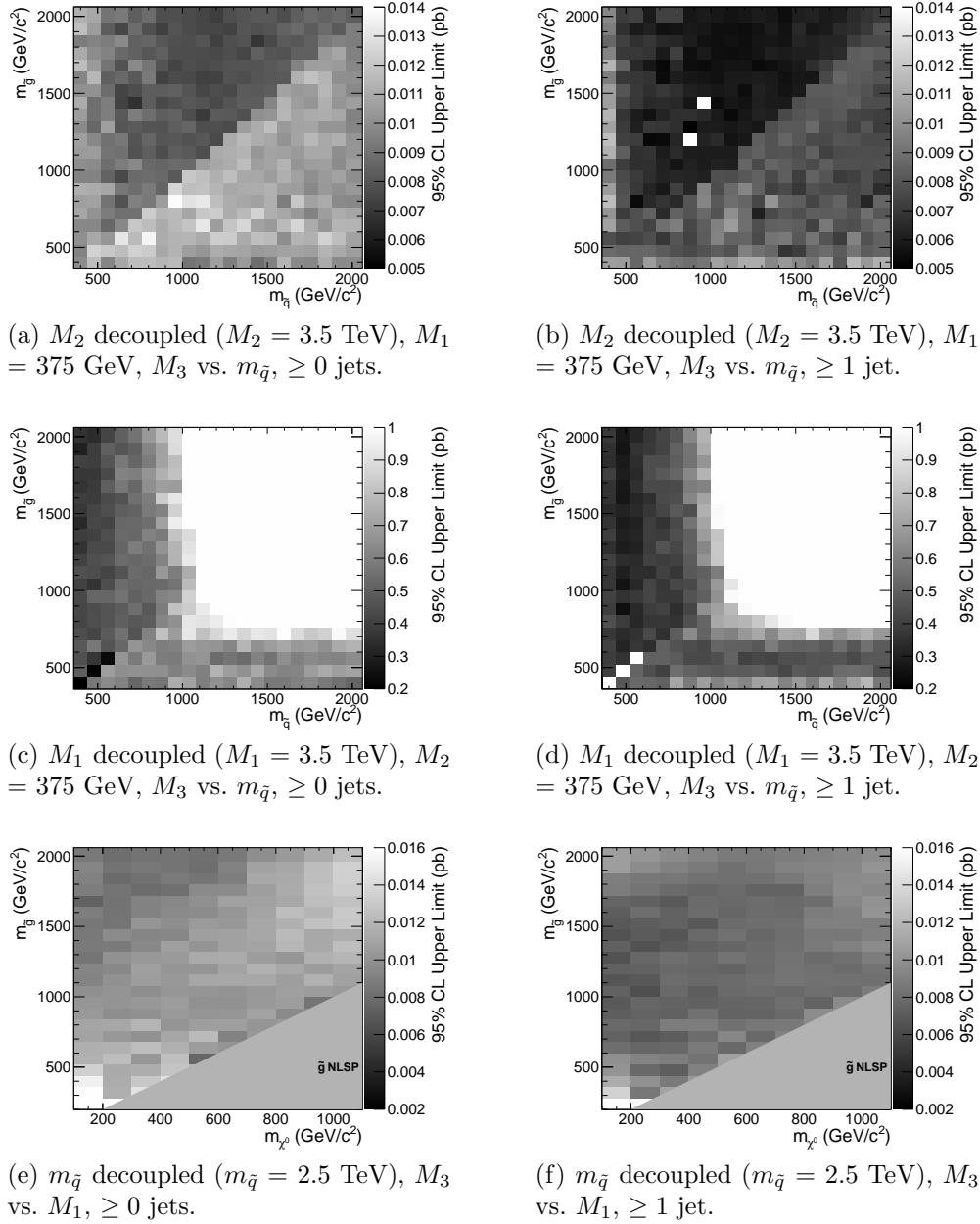


Figure 8.3: Cross section upper limits for the three different scenarios described in Sec. 8.1.

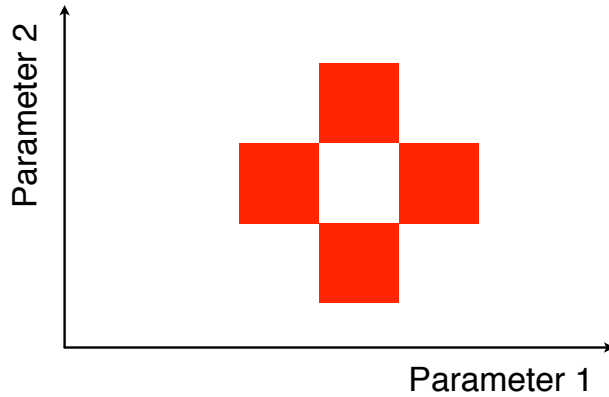


Figure 8.4: Diagram of the points (red squares) used in the estimation of an upper limit when a computational failure occurs (middle white square).

bands around the observed limits in Fig. 8.5 are drawn in blue. The contours that define this band are derived from $\pm(\sigma_{\pm 1\sigma} - \sigma\mu_{\text{obs,scan}}^{95\% \text{CL}})$, where $\sigma_{\pm 1\sigma}$ is the nominal value of the predicted cross section \pm the one-standard-deviation theoretical error on the predicted cross section. In this way, the experimental and theoretical errors, the latter due to imperfect knowledge of the predicted cross section, are shown separately. Comparing with Fig. 8.1, one can easily see that the shapes of the exclusion curves are driven by the contours in the expected cross section plane. In all the plots, the observed limit is slightly higher than the expected limit, reflecting the fact that the background prediction is slightly higher than the observation.

The dominant theoretical uncertainties on the GMSB cross sections are due to:

- PDF uncertainty (4%-100% depending on model)
- Renormalization scale uncertainty (0.036%-25% depending on model)

The PDF4LHC [118] recommendations are used to calculate the effect of these uncertainties on the GMSB cross sections. The recommendations state that PDF sets

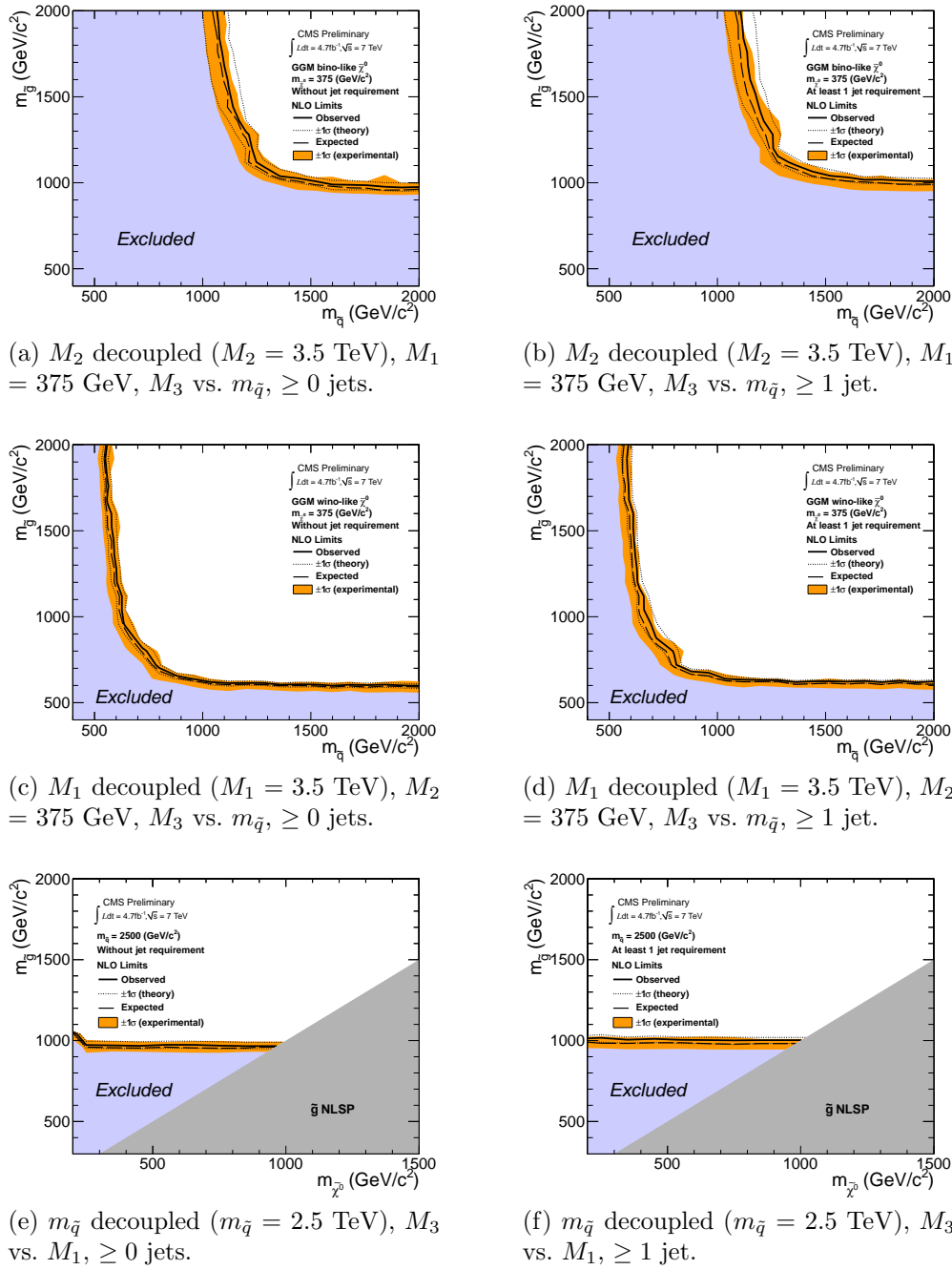


Figure 8.5: Exclusion contours for the three different scenarios described in Sec. 8.1.

from MSTW08 [119], CTEQ6.6 [120], and NNPDF2.0 [121] should be considered in the determination of the PDF uncertainties, because these three PDF sets include constraints from the Tevatron and from fixed target experiments, as well as from HERA [?], and are thus the most complete.

Each collaboration's PDF prediction comes from a global fit to experimental data with a certain number of free parameters. The best fit parameters come from minimizing the χ^2 ; increasing the χ^2 by one from its minimum can be written in terms of the N -dimensional Hessian error matrix [?] where N is the number of free parameters. To form the i^{th} pair of members of the PDF set, the PDF is evaluated once at the parameter values given by the i^{th} eigenvector of the Hessian matrix, and then again at the parameter values given by the negative of the i^{th} eigenvector. Each PDF set therefore contains $2N$ members, corresponding to the positive and negative values of the N eigenvectors [122].

To calculate the PDF uncertainties for a given GMSB model, the leading order Pythia cross section is reweighted by a factor of the error PDF divided by the leading order PDF with which the model was generated. This is repeated for each error PDF in a given PDF set. The $\pm 1\sigma$ deviations are proportional to the maximum difference between cross sections obtained this way. The actual equation for the $\pm 1\sigma$ errors is Eq. (43) of ref. [122]. In the same way, the $\pm 1\sigma$ errors are calculated for the CTEQ6.6, MSTW08, and NNPDF2.0 PDF sets. The total error is given by the half the difference between the largest $+1\sigma$ deviation and the smallest -1σ deviation [118].

The uncertainties on the signal cross sections due to the choice of renormalization/factorization scale ($\alpha_S(M_Z)$) are evaluated by calculating the PROSPINO next to leading order cross section once with $\alpha_S(M_Z)$ halved, then once with $\alpha_S(M_Z)$ doubled. The lower error on the cross section is taken as the absolute difference between the nominal and halved-scale values of the cross section, while the upper error is taken as the absolute difference between the nominal and doubled-scale values. The PDF

2351 and α_S uncertainties are added in quadrature to give the total PDF uncertainty.

2352 Note that the quoted GMSB cross sections are evaluated at next to leading order
2353 using PROSPINO, but it is the leading order Pythia cross sections that are reweighted
2354 to the next to leading order MSTW08, CTEQ6.6, and NNPDF2.0 PDFs to get the
2355 error bands. In addition, since to a good approximation the GMSB production cross
2356 sections for the M_3 - $m_{\tilde{q}}$ scans only depend on M_3 and $m_{\tilde{q}}$, the same PDF errors per
2357 point are used for the \tilde{B} -like and \tilde{W} -like grids.

2358

Chapter 9

2359

Conclusion

2360 The results of a search for evidence of new particle production via final states with
2361 2 photons, large \cancel{E}_T , and ≥ 0 or ≥ 1 jet in pp collisions at $\sqrt{s} = 7$ TeV have been
2362 presented. No deviation in the production rate from that predicted by the Standard
2363 Model has been found. The null results were used to constrain general models of
2364 gauge mediated supersymmetry breaking. In these types of models, gluinos and first-
2365 and second-generation squarks are restricted to masses above ~ 1 TeV.

2366 These bounds on supersymmetry do not exclude it completely. The gluinos and
2367 first- and second-generation squarks can be a little bit heavier (but not too much
2368 heavier than a few TeV) and still imply an elegant supersymmetric solution to the
2369 hierarchy problem. More importantly, the bounds on the first- and second-generation
2370 squarks say nothing about the stop squark, which is intimately connected to the Higgs
2371 mass. At one loop order in the supersymmetric Standard Model, the lightest Higgs
2372 mass is given by [127]

$$m_h^2 \lesssim m_Z^2 + \frac{3g^2 m_t^4}{8\pi^2 m_W^2} \left[\ln \frac{M_S^2}{m_t^2} + \frac{X_t^2}{M_S^2} \left(1 - \frac{X_t^2}{12M_S^2} \right) \right] \quad (9.1)$$

2373 where g is the $SU(2)_L$ coupling constant, M_S^2 is the average of the two observable

2374 stop squared masses, and X_t is a parameter that characterizes stop mixing. The Higgs
 2375 mass is directly sensitive to the stop mass, for which the only current lower bound of
 2376 330 GeV [128] is much weaker than for the first- and second-generation squarks (and
 2377 highly model dependent). The current hints of a Higgs with mass ~ 125 GeV [15, 16]
 2378 point to a stop mass below 2 TeV if SUSY is really a symmetry of nature, depending
 2379 on model.

2380 Future searches for GMSB could look for either direct pair production of stops
 2381 decaying via top quarks to neutralinos that then decay to photons, or for stops pro-
 2382 duced in the decay of a heavier pair-produced particle like the gluino. Looking for a
 2383 final state containing a top, antitop, and ≥ 1 photon may be advantageous because
 2384 the expected SM background should be small.

2385 Top quark reconstruction depends heavily on b jet identification. The same b tag-
 2386 ging techniques needed to find stops could also be applied to a search for a Higgsino-
 2387 like neutralino decaying primarily to $b\bar{b}$. If gaugino mixing were in a certain corner of
 2388 parameter space, then photon + $b\bar{b}$ events might provide a window onto GMSB.

2389 There are a number of interesting possibilities for future GMSB searches in ad-
 2390 dition to those just outlined. SUSY searches will likely remain a fruitful avenue of
 2391 investigation throughout the lifetime of the LHC.

2392 **Appendix A**

2393 **Monte Carlo Samples**

2394 A number of MC samples are utilized in this analysis and referred to throughout the
2395 text. Below is a list of the MC samples used and an explanation of what the sample
2396 names mean.

2397 **A.1 List of Samples**

2398 1. Drell-Yan + up to 2 hard jets:

2399 /DYJetsToLL_TuneZ2_M-50_7TeV-madgraph-tauola/
2400 Fall11-PU_S6_START42_V14B-v1/AODSIM

2401 2. QCD enriched with B and D meson decays to electrons:

2402 /QCD_Pt-20to30_BCtoE_TuneZ2_7TeV-pythia6/
2403 Fall11-PU_S6_START42_V14B-v1/AODSIM,
2404 /QCD_Pt-30to80_BCtoE_TuneZ2_7TeV-pythia6/
2405 Fall11-PU_S6_START42_V14B-v1/AODSIM,
2406 /QCD_Pt-80to170_BCtoE_TuneZ2_7TeV-pythia6/
2407 Fall11-PU_S6_START42_V14B-v1/AODSIM

2408 3. Photon + jet doubly enriched with jets passing an EM filter:

2409 /GJet_Pt-20_doubleEMEnriched_TuneZ2_7TeV-pythia6/
 2410 Fall11-PU_S6_START42_V14B-v1/AODSIM

2411 4. W leptonic decays + up to 2 hard jets:

2412 /WJetsToLNu_TuneZ2_7TeV-madgraph-tauola/
 2413 Fall11-PU_S6_START42_V14B-v1/AODSIM

2414 5. $t\bar{t}$ + up to 2 hard jets:

2415 /TTJets_TuneZ2_7TeV-madgraph-tauola/
 2416 Fall11-PU_S6_START42_V14B-v2/AODSIM

2417 A.2 Explanation of Naming Conventions

2418 • L: charged lepton

2419 • B: B hadron

2420 • C: D , or charmed, hadron

2421 • E: electron or positron

2422 • G: photon

2423 • W: W boson

2424 • Nu: neutrino

2425 • T: top quark

2426 • TuneZ2: Pythia tune incorporating 2010 LHC data with CTEQ6L1 [120] PDFs
 2427 [129]

2428 • M-50: Generated l^+l^- invariant mass threshold of 50 GeV

2429 • 7TeV: Generated center-of-mass energy 7 TeV

- 2430 ● **pythia6**: Parton showering and hadronization simulated with Pythia v6.424
- 2431 [130]
- 2432 ● **madgraph**: Hard interaction generated with MadGraph 5 [131]
- 2433 ● **tauola**: τ decays generated with Tauola [132]
- 2434 ● **PU_S6**: Generated with S6 pileup scenario, which has a mean between 6 and
- 2435 7 interactions per crossing, and includes pileup from the neighboring bunch
- 2436 crossings according to a Poisson distribution with mean equal to the number of
- 2437 interactions in the in-time crossing [133]
- 2438 ● **START42_V14B**: Reconstructed with best alignment and calibration constants
- 2439 and magnetic field conditions as of August 3, 2011
- 2440 ● **Pt_XtoY**: $X \leq$ generated $\hat{p}_T < Y$
- 2441 ● **BCToE**: Only keeps events if they contain at least one electron with $E_T > 10$
- 2442 GeV in $|\eta| < 2.5$ that came from a b or c quark
- 2443 ● **doubleEMEnriched**: Enriched in photons, electrons, electrons from b/c decay,
- 2444 and electromagnetic jets [134]
- 2445 ● **AODSIM**: Run through full CMS reconstruction algorithm based on a GEANT 4
- 2446 [125] detector simulation; AOD data tier, including generator-level information

2447

Bibliography

- 2448 [1] <http://cms.web.cern.ch/news/cms-detector-design> (2011).
- 2449 [2] S.L. Glashow, J. Iliopoulos, and L. Maiani, *Phys. Rev. D* **2** (1970) 1285; S.L. Glashow, *Nucl. Phys.* **22(4)** (1961) 579; J. Goldstone, A. Salam, and S. Weinberg, *Phys. Rev.* **127** (1962) 965; S. Weinberg, *Phys. Rev. Lett.* **19** (1967) 1264; A. Salam and J.C. Ward, *Phys. Lett.* **13(2)** (1964) 168.
- 2450 [3] M. Gell-Mann, *Phys. Lett.* **8** (1964) 214; G. Zweig, *CERN 8419/TH. 412* (1964) (unpublished).
- 2451 [4] J. Drees, *Int. J. Mod. Phys.* **A17** (2002) 3259.
- 2452 [5] P.W. Higgs, *Phys. Lett.* **12(2)** (1964) 132; P.W. Higgs, *Phys. Rev. Lett.* **13** (1964) 508; P.W. Higgs, *Phys. Rev.* **145** (1966) 1156.
- 2453 [6] I. Aitchison, *Supersymmetry in Particle Physics: An Elementary Introduction* (Cambridge University Press, Cambridge 2007), p. 4.
- 2454 [7] C. Quigg, in *Flavor Physics for the Millennium: TASI 2000, Boulder, 2000*, edit by J. L. Rosner (World Scientific, Singapore, 2001), p. 3.
- 2455 [8] L. Álvarez-Gaumé and J. Ellis, *Nature Phys.* **7** (2011) 2.
- 2456 [9] G. Arnison et al. (UA1 Collaboration), *Phys. Lett.* **B122** (1983) 103.
- 2457 [10] G. Arnison et al. (UA1 Collaboration), *Phys. Lett.* **B126** (1983) 398.

- ²⁴⁶⁵ [11] J. Gunion, H.E. Haber, G. L. Kane, and S. Dawson, *The Higgs Hunter's Guide*,
²⁴⁶⁶ (Addison-Wesley, Redwood City, 1990).
- ²⁴⁶⁷ [12] S. P. Martin, *A Supersymmetry Primer* **v4** (2006) 86. [arXiv:hep-ph/9709356](#).
- ²⁴⁶⁸ [13] K. Nakamura et al. (Particle Data Group), *J. Phys.* **G37** (2010) 075021.
- ²⁴⁶⁹ [14] G. Jungman, M. Kamionkowski, and K. Griest, *SU* **4240-605** (1995).
- ²⁴⁷⁰ [15] S. Chatrchyan et al. (CMS Collaboration), *Phys. Lett.* **B710** (2012) 26.
- ²⁴⁷¹ [16] G. Aad et al. (ATLAS Collaboration), *Phys. Lett.* **B710** (2012) 49.
- ²⁴⁷² [17] M. Dine and W. Fischler, *Phys. Lett.* **B110** (1982) 227; C.R. Nappi and B.A.
²⁴⁷³ Ovrut, *Phys. Lett.* **B113** (1982) 175; L. Alvarez-Gaumé, M. Claudson, and M.B.
²⁴⁷⁴ Wise, *Nucl. Phys.* **B207** (1982) 96; M. Dine and A.E. Nelson, *Phys. Rev.* **D48**
²⁴⁷⁵ (1993) 1277; M. Dine, A.E. Nelson, and Y. Shirman, *Phys. Rev.* **D51** (1995)
²⁴⁷⁶ 1362; M. Dine, A.E. Nelson, Y. Nir, and Y. Shirman, *Phys. Rev.* **D53** (1996)
²⁴⁷⁷ 2658.
- ²⁴⁷⁸ [18] A.H. Chamseddine, R. Arnowitt, and P. Nath, *Phys. Rev. Lett.* **49** (1982) 970; R.
²⁴⁷⁹ Barbieri, S. Ferrara, and C.A. Savoy, *Phys. Lett.* **B119** (1982) 343; L.E. Ibáñez,
²⁴⁸⁰ *Phys. Lett.* **B118** (1982) 73; L.J. Hall, J.D. Lykken, and S. Weinberg, *Phys. Rev.*
²⁴⁸¹ **D27** (1983) 2359; N. Ohta, *Prog. Theor. Phys.* **70** (1983) 542; J. Ellis, D.V.
²⁴⁸² Nanopoulos, and K. Tamvakis, *Phys. Lett.* **B121** (1983) 123; L. Alvarez-Gaumé,
²⁴⁸³ J. Polchinski, and M. Wise, *Nucl. Phys.* **B221** (1983) 495.
- ²⁴⁸⁴ [19] P. Meade, N. Seiberg, and D. Shih, *Progr. Theor. Phys. Suppl.* **177** (2009) 143.
- ²⁴⁸⁵ [20] G. Aad et al., *CERN-PH-EP-2011-160* (2011).
- ²⁴⁸⁶ [21] T. Aaltonen et al., *Phys. Rev. Lett.* **104** (2010) 011801.
- ²⁴⁸⁷ [22] CMS Collaboration, *CMS-PAS-SUS-11-009* (2011).

- 2488 [23] <http://en.wikipedia.org/wiki/Tevatron>.
- 2489 [24] E. Fernandez et al., *Phys. Rev. Lett.* **54** (1985) 1118; E. Fernandex et al., *Phys.*
 2490 *Rev.* **D35** (1987) 374; D. Decamp et al., *Phys. Lett.* **B237(2)** (1990) 291; F.
 2491 Abe et al., *Phys. Rev. Lett.* **75** (1995) 613; S. Abachi et al., *Phys. Rev. Lett.* **75**
 2492 (1995) 618; G. Alexander et al., *Phys. Lett.* **B377(4)** (1996) 273; S. Aid et al.,
 2493 *Z. Phys.* **C71(2)** (1996) 211; S. Aid et al., *Phys. Lett.* **B380(3-4)** (1996) 461; B.
 2494 Aubert et al., *Phys. Rev. Lett.* **95** (2005) 041802.
- 2495 [25] O. Buchmueller et al., *CERN-PH-TH/2011-220* (2011).
- 2496 [26] <https://twiki.cern.ch/twiki/bin/view/CMSPublic/PhysicsResultsSUS>.
- 2497 [27] G. Aad et al., *JINST* **3** (2008) S08003.
- 2498 [28] B.C. Allanach et al., *Eur. Phys. J.* **C25** (2002) 113.
- 2499 [29] CMS Collaboration, *CMS-PAS-SUS-12-001* (2012).
- 2500 [30] A. Boyarsky, J. Lesgourges, O. Ruchayskiy, and M. Viel, *CERN-PH-TH/2008-*
 2501 *234* (2009).
- 2502 [31] E. Komatsu et al., *Astrophys. J. Suppl. Ser.* **180** (2009) 330.
- 2503 [32] C.-H. Chen and J.F. Gunion, *Physical Review* **D58** (1998) 075005.
- 2504 [33] F. Staub, W. Porod, J. Niemeyer, *JHEP* **1001** (2010) 058.
- 2505 [34] L. Evans and P. Bryant (eds.), *JINST* **3** (2008) S08001.
- 2506 [35] <http://cms.web.cern.ch/news/summary-2011-p-p-running> (2011).
- 2507 [36] <http://public.web.cern.ch/public/en/lhc/Facts-en.html> (2008).
- 2508 [37] CERN, <http://cdsweb.cern.ch/record/833187> (2005).

- 2509 [38] RGBStock.com, <http://www.rgbstock.com/photo/n7EsabW/Airplane> (2011).
- 2510 [39] R. Flükiger, S. Y. Hariharan, R. Küntzler, H. L. Luo, F. Weiss, T. Wolf, and J.
2511 Q. Xu, in *Landolt-Börnstein: Numerical Data and Functional Relationships in*
2512 *Science and Technology*, edited by R. Flükiger and W. Klose (Springer, 2012).
- 2513 [40] Y.-P. Sun, F. Zimmermann, and R. Tomás, in Proceedings of the 23rd Particle Ac-
2514 celerator Conference, Vancouver, 2009, <http://accnet.web.cern.ch/accnet/>
2515 Literature/2009/TH5PFP016-Sunpdf.pdf (unpublished).
- 2516 [41] O.S. Brüning et al. (eds.), *CERN-2004-003-V-1*, <http://lhc.web.cern.ch/lhc/LHC-DesignReport.html> (2004).
- 2518 [42] CERN, <http://cdsweb.cern.ch/record/841568/files/> (1993).
- 2519 [43] P. Komorowski and D. Tommasini, in *Proceedings of the 1998 International*
2520 *Computational Accelerator Physics Conference, Monterey, 1998*, edited by K.
2521 Ko and R. Ryne (SLAC, Stanford, 1998), p. 192, http://www.slac.stanford.edu/econf/C980914/papers/ICAP98_eConf.pdf.
- 2523 [44] <http://lhc-machine-outreach.web.cern.ch/lhc-machine-outreach/components/magnets.htm> (2008).
- 2525 [45] S. Chatrchyan et al. (CMS Collaboration), *JINST* **3** (2008) S08004.
- 2526 [46] G.L. Bayatian et al. (CMS Collaboration), *CERN/LHCC 2006-001*, edited by
2527 D. Acosta (2006).
- 2528 [47] M. Ivova, talk given at the Swiss Ph.D. School on Particle and Astroparticle
2529 Physics (CHIPP), Monte Verita' (2010).
- 2530 [48] G. Bolla et al., *Nucl. Instr. Meth. Res.* **A461** (2001) 182.

- 2531 [49] https://twiki.cern.ch/twiki/pub/CMSPublic/DPGResultsTRK/_imgf9e0ee48ebca770d7774454532b4b4ee.png (2011).
- 2532
- 2533 [50] https://twiki.cern.ch/twiki/pub/CMSPublic/DPGResultsTRK/_img7569b7652b3f7c15030a11a4223e631c.png (2011).
- 2534
- 2535 [51] https://twiki.cern.ch/twiki/pub//CMSPublic/DPGResultsTRK/hv11_d1.png (2011).
- 2536
- 2537 [52] https://twiki.cern.ch/twiki/pub/CMSPublic/DPGResultsTRK/_imga571742cbed3a14a9e2581ae95efa54c.gif (2011).
- 2538
- 2539 [53] <https://twiki.cern.ch/twiki/pub//CMSPublic/DPGResultsTRK/StripHitRes2.gif> (2011).
- 2540
- 2541 [54] https://twiki.cern.ch/twiki/pub//CMSPublic/EcalDPGResults/histories2_laser.png (2012).
- 2542
- 2543 [55] https://twiki.cern.ch/twiki/pub//CMSPublic/EcalDPGResults/electronres_eb_inclusive.png (2012).
- 2544
- 2545 [56] https://twiki.cern.ch/twiki/pub//CMSPublic/EcalDPGResults/electronres_ee_inclusive.png (2012).
- 2546
- 2547 [57] <https://twiki.cern.ch/twiki/pub//CMSPublic/EcalDPGResults/seed-time.EEEE.png> (2012).
- 2548
- 2549 [58] N. Akchurin and R. Wigmans, *Rev. Sci. Instrum.* **74** (2003) 2955.
- 2550 [59] CMS Collaboration, *CMS-DP 2010-025* (2010).
- 2551 [60] https://twiki.cern.ch/twiki/pub/CMSPublic/PhysicsResultsMUO/dimuMass_2011Run_1fb_20July2011.pdf (2011).
- 2552
- 2553 [61] S. Chatrchyan et al. (CMS Collaboration), *JHEP* **4** (2012) 33.

- 2554 [62] W.H. Smith, P. Chumney, S. Dasu, F. Di Lodovico, M. Jaworski, J.R. Lackey, and
 2555 P. Robl in *Proceedings of the 7th Workshop on Electronics for LHC Experiments,*
 2556 *Stockholm, 2001*, edited by C. Isabella (CERN, Geneva, 2001), p. 238.
- 2557 [63] R. Alemany et al., *IEEE Trans. Nucl. Sci.* **52**(5) (2005) 1918.
- 2558 [64] R. Brun and F. Rademakers, *Nucl. Inst. Meth. Res.* **A389** (1997) 81. See also
 2559 <http://root.cern.ch/>.
- 2560 [65] J. Gutleber and L. Orsini, *Cluster Comput.* **5** (2002) 55.
- 2561 [66] D. Box, D. Ehnebuske, G. Kakivaya, A. Layman, N. Mendelsohn, H.F.
 2562 Nielsen, S. Thatte, and D. Winer, *W3C Note 08*, <http://www.w3.org/TR/2000/NOTE-SOAP-20000508/> (2000).
- 2563 [67] R. Arcidiacono et al., talk given at the 10th ICAL-EPCS International Conference
 2564 on Accelerator and Large Experiment Physics Control Systems, Geneva (2005).
- 2565 [68] J. Knobloch et al., *CERN-LHCC-2005-024* (2005).
- 2566 [69] R. Brunelière, *Nucl. Instr. Meth. Res.* **A572** (2007) 33.
- 2567 [70] S. Chatrchyan et al. (CMS Collaboration), *JINST* **5** (2010) T03011.
- 2568 [71] CMS Collaboration, *CMS PAS EGM-10-002* (2010).
- 2569 [72] P. Meridiani and C. Seez, *CMS IN-2011/002* (2011).
- 2570 [73] P. Adzic et al. (CMS Electromagnetic Calorimeter Group), *Eur. Phys. J.* **C44S2**
 2571 (2006) 1.
- 2572 [74] P. Adzic et al. (CMS Electromagnetic Calorimeter Group), *JINST* **3** (2008)
 2573 P10007.

- 2575 [75] M. Malberti, *Nuc. Sci. Symposium Conference Record NSS/MIC IEEE* (2009)
 2576 2264.
- 2577 [76] S. Chatrchyan et al. (CMS Collaboration), *JINST* **5** (2010) T03010.
- 2578 [77] R. Paramatti, *J. Phys. Conf. Ser.* **293** (2011) 012045.
- 2579 [78] Y. Yang, http://www.hep.caltech.edu/cms/posters/Pi0Poster_CMSWeekDec2011.pdf (2011).
- 2580
- 2581 [79] M. Anderson, A. Askew, A.F. Barfuss, D. Evans, F. Ferri, K. Kaadze, Y. Maravin,
 2582 P. Meridiani, and C. Seez, *CMS IN-2010/008* (2010).
- 2583 [80] <https://twiki.cern.ch/twiki/bin/view/CMS/ECALEnergyScaleCorrections>.
- 2584 [81] The $H \rightarrow \gamma\gamma$ working group, *CMS AN-2011/426* (2011).
- 2585 [82] M. Cacciari, *LPTHE-P06-04* (2006).
- 2586 [83] M. Cacciari, G.P. Salam, and G. Soyez, *CERN-PH-TH-2011-297* (2011).
- 2587 [84] S. Chatrchyan et al. (CMS Collaboration), *Phys. Rev. Lett.* **106** (2011) 082001.
- 2588 [85] A. Askew, B. Cox, D. Elvira, Y. Gershtein, M. Hildreth, D. Jang, Y.-F. Liu, D.
 2589 Mason, D. Morse, U. Nauenberg, M. Paulini, R. Stringer, R. Yohay, and S.L.
 2590 Zang, *CMS AN-2011/515* (2011).
- 2591 [86] F. Beaudette, D. Benedetti, P. Janot, and M. Pioppi, *CMS AN-2010/034* (2010).
- 2592 [87] M. Konecki, in Proceedings of the European Physical Society Europhysics Con-
 2593 ference on High Energy Physics, Krakow, 2009, Eur. Phys.Soc. Mulhouse (ed.)
 2594 (unpublished).
- 2595 [88] W. Adam, R. Früwirth, A. Strandlie, and T. Todorov, *J. Phys.* **G31** No. 9 (2005).
- 2596 [89] CMS Collaboration, *CMS PAS PFT-09-001* (2009).

- 2597 [90] CMS Collaboration, *CMS PAS PFT-10-002* (2010).
- 2598 [91] S. Chatrchyan et al., *JINST* **6** (2011) P11002.
- 2599 [92] CMS Collaboration, *CERN-PH-EP 2011-102* (2011).
- 2600 [93] M. Cacciari, G.P. Salam, and G. Soyez, *JHEP* **0804** (2008) 063.
- 2601 [94] G. Salam, talk given at CERN Theory Institute: SM and BSM Physics at the
2602 LHC (2009).
- 2603 [95] C.W. Fabjan and R. Wigmans, *Rep. Prog. Phys.* **52** (1989) 1519.
- 2604 [96] <http://www-cdf.fnal.gov/physics/new/top/2004/jets/cdfpublic.html>
2605 (visited on 16 January 2011).
- 2606 [97] S. Chatrchyan et al. (CMS Collaboration), *JINST* **6** (2011) P09001.
- 2607 [98] CMS Collaboration, *CMS PAS JME-09-002* (2009).
- 2608 [99] T. Sjöstrand, S. Mrenna, and P. Z. Skands, *Comput. Phys. Commun.* **178** (2008)
2609 852.
- 2610 [100] S. Chatrchyan et al. (CMS Collaboration), *JINST* **5** (2010) T03014.
- 2611 [101] <https://twiki.cern.ch/twiki/bin/view/CMS/PVTMain> (2011).
- 2612 [102] J. P. Chou, S. Eno, S. Kunori, S. Sharma, and J. Wang, *CMS IN-2010/006*
2613 (2010).
- 2614 [103] Y. Chen, talk given at a meeting of the CMS JetMET group (2011).
- 2615 [104] R. Korzekwa et al., *iEEE Trans. Elec. Dev.* **38** (1991) 745.
- 2616 [105] W. Adam, Th. Speer, B. Mangano, and T.Todorov, *CMS NOTE 2006/041*
2617 (2006).

- 2618 [106] G. Daskalakis, D. Evans, C.S. Hill, J. Jackson, P. Vanlaer, J. Berryhill, J. Haupt,
 2619 D. Futyan, C. Seez, C. Timlin, and D. Wardrope, *CMS AN-2007/019* (2007).
- 2620 [107] F. James and M. Roos, *Comput. Phys. Commun.* **10** (1975) 343.
- 2621 [108] W. Verkerke and D.P. Kirkby, *CHEP-2003-MOLT007* (2003).
- 2622 [109] J.E. Gaiser, Ph.D. thesis, Stanford University (1982).
- 2623 [110] A. Askew, S. Arora, Y. Gershtein, S. Thomas, G. Hanson, R. Stringer, W.
 2624 Flanagan, B. Heyburn, U. Nauenberg, S.L. Zang, R. Nandi, D. Elvira, D. Mason,
 2625 M. Balazs, B. Cox, B. Francis, A. Ledovskoy, and R. Yohay, *CMS AN* **2010/271**
 2626 (2010).
- 2627 [111] Information about all CMS datasets is available from the CMS Data Aggrega-
 2628 tion System (DAS), located at the URL <https://cmsweb.cern.ch/das/>.
- 2629 [112] S. Chatrchyan et al., *Phys. Rev. Lett.* **106** (2011) 211802.
- 2630 [113] G. Aad et al. (ATLAS Collaboration), S. Chatrchyan et al. (CMS Collabora-
 2631 tion), and LHC Higgs Combination Group, *CMS-NOTE-2011/005* (2011).
- 2632 [114] A.L. Read, in *Proceedings of the First Workshop on Confidence Limits, Geneva,*
 2633 *2000*, edited by L. Lyons, Y. Perrin, and F.E. James (CERN, Geneva, 2000), p.
 2634 81.
- 2635 [115] G. Cowan, K. Cranmer, E. Gross, and O. Vitells, *Eur. Phys. J.* **C71** (2011)
 2636 1554.
- 2637 [116] J. Neyman and E.S. Pearson, *Phil. Trans. R. Soc. Lond.* **A231** (1933) 289.
- 2638 [117] CMS Collaboration, *CMS PAS EWK-11-001* (2011).

- 2639 [118] S. Alekhin et al. (The PDF4LHC Working Group), arXiv:1101.0536 [hep-ph];
 2640 M. Botje et al. (The PDF4LHC Working Group), arXiv:1101.0538 [hep-ph];
 2641 <http://www.hep.ucl.ac.uk/pdf4lhc/index.html>.
- 2642 [119] A.D. Martin, W.J. Stirling, R.S. Thorne, and G. Watt, *Eur. Phys. J.* **C63**
 2643 (2009) 189.
- 2644 [120] P. M. Nadolsky, H.-L. Lai, Q.-H. Cao, J. Huston, J. Pumplin, D. Stump, W.-K.
 2645 Tung, and C.-P. Yuan, *Phys. Rev.* **D78** (2008) 013004.
- 2646 [121] R.D. Ball, L. Del Debbio, S. Forte, A. Guffanti, J.I. Latorre, J. Rojo, and M.
 2647 Ubiali, *Nucl. Phys.* **B838** (2010) 136.
- 2648 [122] J.M. Campbell, J.W. Huston, and W.J. Stirling, *Rep. Prog. Phys.* **70** (2007) 89.
- 2649 [123] A. Djouadi, J.-L. Kneur, G. Moultaka, arXiv:hep-ph/0211331 (2005).
- 2650 [124] M. Muhlleitner, A. Djouadi, Y. Mambrini, *Comput. Phys. Commun.* **168** (2005)
 2651 46.
- 2652 [125] J. Allison et al., *IEEE Trans. Nucl. Sci.* **53**(1) (2006) 270.
- 2653 [126] W. Beenakker, R. Hoepker, M. Spira, arXiv:hep-ph/9611232 (1996).
- 2654 [127] M. Carena, J.S. Conway, H.E. Haber, and J.D. Hobbs, *FERMILAB-Conf-00*
 2655 **279-T** (2000). arXiv:hep-ph/0010338
- 2656 [128] ATLAS Collaboration, *ATLAS-CONF 2012-036* (2012).
- 2657 [129] R. Field, talk given at LHC Physics Centre at CERN Minimum Bias and Un-
 2658 derlying Event Working Group Meeting (2011).
- 2659 [130] T. Sjöstrand, S. Mrenna, and P. Z. Skands, *JHEP* **0605** (2006) 026.

- 2660 [131] J. Alwall, M. Herquet, F. Maltoni, O. Mattelaer, and T. Stelzer, *JHEP* **1106**
2661 (2011) 128.
- 2662 [132] Z. Was, *Nucl. Phys. Proc. Suppl.* **98** (2001) 96.
- 2663 [133] <http://cmslxr.fnal.gov/lxr/source/SimGeneral/MixingModule/python/>
2664 `mix_E7TeV_Fall2011_Reprocess_50ns_PoissonOOTPU_cfi.py` (2011).
- 2665 [134] <http://cmslxr.fnal.gov/lxr/source/GeneratorInterface/GenFilters/>
2666 `src/doubleEMEnrichingFilterAlgo.cc` (2011).